Liquid Metal Corrosion Studies on Ferritic/Martensitic Steels in Lead Lithium Eutectic for Fusion Energy Applications

By

POULAMI CHAKRABORTY

Enrolment No: - ENGG01201304040

Bhabha Atomic Research Centre

A thesis submitted to the

Board of Studies in Engineering Sciences

In partial fulfillment of requirements
for the Degree of
DOCTOR OF PHILOSOPHY
of
HOMI BHABHA NATIONAL INSTITUTE

July, 2018

Homi Bhabha National Institute[1]

Recommendations of the Viva Voce Committee

As members of the Viva Voce Committee, we certify that we have read the dissertation prepared by Poulami Chakraborty entitled Liquid Metal Corrosion Studies on Ferritic/Martensitic Steels in Lead Lithium Eutectic for Fusion Energy Applications and recommend that it may be accepted as fulfilling the thesis requirement for the award of Degree of Doctor of Philosophy.

Chairman – Dr. S. Banerjee Srikumar Banerjee **Date:** 14.12.2018

Guide / Convener – Dr. V. Kain **Date:** Dec. 14, 2018

Co-guide - Dr. G. K. Dey Gautam Kumar Dey **Date:** 14/12/18

Examiner – Dr. C. K. Behera **Date:** 14/12/18

Member 1- Dr. D. K. Maity **Date:** 14/12/18

Member 2- Dr. S. B. Roy **Date:**

Member 2- Dr. N. K. Maheshwari Naresh Kr Mahesh. **Date:** 14/12/18

Final approval and acceptance of this thesis is contingent upon the candidate's submission of the final copies of the thesis to HBNI.

I/We hereby certify that I/we have read this thesis prepared under my/our direction and recommend that it may be accepted as fulfilling the thesis requirement.

Date: Dec. 14, 2018

Place: Mumbai

Gautam Kumar Dey
<Signature>
Dr. G. K. Dey

<Signature>
Dr. V. Kain

---

[1] This page is to be included only for final submission after successful completion of viva voce.

STATEMENT BY AUTHOR

This dissertation has been submitted in partial fulfillment of requirements for an advanced degree at Homi Bhabha National Institute (HBNI) and is deposited in the Library to be made available to borrowers under rules of the HBNI.

Brief quotations from this dissertation are allowable without special permission, provided that accurate acknowledgement of source is made. Requests for permission for extended quotation from or reproduction of this manuscript in whole or in part may be granted by the Competent Authority of HBNI when in his or her judgment the proposed use of the material is in the interests of scholarship. In all other instances, however, permission must be obtained from the author.

Poulami Chakraborty

Poulami Chakraborty

DECLARATION

I, hereby declare that the investigation presented in the thesis has been carried out by me. The work is original and has not been submitted earlier as a whole or in part for a degree / diploma at this or any other Institution / University.

Poulami Chakraborty

Poulami Chakraborty

List of Publications arising from the thesis

Journal

1. P. Chakraborty, V. Kain, R. Tewari, G. K. Dey, "Corrosion of an India produced RAFM steel in flowing lead-lithium eutectic", Fusion Engineering and Design 123 (2017) 269-276.
2. P. Chakraborty, V. Kain, P. K. Pradhan, R. K. Fotedar, N. Krishnamurthy, G. K. Dey, "Corrosion of Indian RAFMS in Pb-17Li in a Rotating Disc Corrosion Test Facility at 773 K", Fusion Engineering and Design 100 (2015) 181–189.
3. P. Chakraborty, V. Kain, P. K. Pradhan, R. K. Fotedar and N. Krishnamurthy,"Corrosion of Modified 9Cr-1Mo Steel and Indian RAFMS in Static Pb-17Li at 773 K", The Journal of Fusion Energy, 34, (2015) 293-297
4. P. Chakraborty, V. Kain, P. K. Pradhan, R. K. Fotedar and N. Krishnamurthy, "Corrosion of modified 9Cr-1Mo steel in Pb-17Li in a rotating disc experiment at 773 K", The Journal of Fusion Energy 34 (2015) 371-378
5. A. Sarada Sree, T. Kamble, P. Chakraborty, R. K. Fotedar, E. Rajendra Kumar, A. K. Suri, Platicis E., Ziks A., Poznjak A., Shisko A., "Preliminary Corrosion Studies on Structural Material P-91 in Lead-Lithium for Indian LLCB TBM", Nuclear Fusion 54 (2014) 083029 (9pp).

Paper in Conference/Symposium proceedings:

1. P. Chakraborty, V. Kain, and G. K. Dey, "Compatibility of Indian RAFMS with molten Pb-17Li at 773 K", The Third Joint IAEA-ITER Meeting on ITER Materials and Technologies", IAEA Headquarters, Vienna, November (2015).
2. P. Chakraborty, V. Kain, N. Krishnamurthy, "Establishing the compatibility of Indian Reduced Activation Ferritic-Martensitic Steel (IN-RAFMS) with Pb-17Li eutectic", The Karlsruhe International School of Fusion Technologies, Germany, September, (2014).

Poulami Chakraborty

Poulami Chakraborty

DEDICATED
TO
MY
FATHER

ACKNOWLEDGEMENTS

- I would like to express my deep and sincere gratitude to my guide, Dr. Vivekanand Kain, for being a great teacher and source of inspiration to me. It was because of his constant encouragement, involvement and all round support that led to the successful completion of this work.
- I would like to thank my co-guide, Dr. G. K. Dey for his cooperation at each stage of research. The work could not have been carried out smoothly without his involvement and problem solving ability. Sincere thanks to Dr. M. Krishnan, Head, MSD and AD, Materials Group for his facilitation and encouragement. I would also express my heartfelt gratitude to Dr. R. Tewari for his immense support, guidance and understanding which has always been a pillar of strength for me.
- I would like to thank all the members of the members of Doctoral committee for their critical reviews and suggestions throughout the work. I feel blessed to have been associated with Dr. S. Bannerjee (Chairman, Doc. Com.) through my PhD.
- I would like to thank Dr. N. Krishnamurthy, Shri R. K. Fotedar and Shri P. K.Pradhan who had been my mentors at different stages of this work and have always facilitated me in their best possible ability. I would specially thank Dr. N. K. Maheshwari for helping me with the CFD analysis and Shri S. Malhotra for providing the magnets for corrosion studies. My heartfelt thanks go to Shri S. Bysakh from CGCRI, Kolkata for allowing me to carry out the XPS analysis. Special thanks to Shri E.R. Kumar and Dr. R. Bhattacharya from IPR, Gandhinagar.
- I would like to express my gratitude to Dr. J. Konys (Karlsruhe Institute of Technology, Germany) and Dr. J. Freibergs (Institute of Physics, Latvia) for allowing us to test our samples at their lead lithium loops.
- I would like to thank Mr. Vishal Singh for helping me in carrying out most of the SEM-EDS analysis. I would also like to thank Shri Sunil K. Bonagni for all the technical discussion and doubt clearing sessions which helped me a lot at various points of thesis writing.
- I also express my sincere thanks to all the technical staff of Materials Group, BARC, especially Shri B. Suman for their extensive cooperation and support during the tenure of the project work.
- Finally, I would like to thank my parents for their blessings and encouragement during the entire course of the project. My father, Dr. Dipankar Chakraborty, who have been a source of inspiration in all my academic endeavors. Heartfelt thanks to my mother, Smt. Nandini Chakraborty, whose limitless love and care for my baby, allowed me to concentrate on my PhD work and complete it in time. Thanks to my husband, Shri Abhishek Srivastava, who has always believed in me, supported and motivated me at each and every step of my progress. Finally, thanks to Almighty for blessing with our baby boy, Arghadeep, whose smiling face makes me face every challenge with a smile.

(Poulami Chakraborty)

TABLE OF CONTENTS

Abstract

Reduced activation ferritic/martensitic steels (RAFMS) are considered as the most promising structural materials for nuclear fusion reactors mainly because of their stability under high energy fusion neutrons. However, the corrosion compatibility of these steels with the coolant, lead-lithium eutectic (Pb-Li) is a major concern. In the present research work, under different operating conditions, the corrosion behavior of the Indian RAFMS (IN RAFMS: 9Cr-1.4W) and its surrogate material, modified 9Cr-1Mo steel (P91) in molten Pb-Li has been investigated. For this purpose, a number of specialized test facilities (like static, rotating disc and loop) offering isothermal, non isothermal under static and flowing conditions were developed. Based on the test set-ups and operating conditions, different geometries of corrosion coupons were designed. The temperature of exposure in Pb-Li was varied from 773 K to 823 K while the Pb-Li flow velocity considered for dynamic experiments was kept in the range of 0.01 to 1.5 m/s. In addition, the effect of magnetic field (0.5 to 1.8 T) on the corrosion process of IN RAFMS and P91 was also studied. The Pb-Li exposure experiments have been carried out up to time duration ranging from 350 h - 10, 000 h. Through these experiments it has been demonstrated that in liquid Pb-Li IN RAFMS is more corrosion resistant in comparison to P91. This high corrosion resistant property in IN RAFMS was established due to the presence of tungsten which has been shown to create a difference in surface oxide chemistry in addition to providing solid solution strengthening. It has also been shown that the corrosion of both, IN RAFMS and P91, generally initiates with the dissolution of is oxide layer consisting of oxides of iron and chromium ($(Cr,Fe)_2O_3$ /FeO) as well as tungsten oxide (WO_2, WO_3) in the case of IN RAFMS. Dissolution of this layer occurs mainly due to reduction by lithium and this creates an initial period of reduced corrosion rate (incubation period); which is as long as ~ 3000 h for IN RAFMS. It has been shown that the grain boundary attack also take place during the incubation period due to a comparatively weaker passive layer on grain boundary regions when Fe and Cr from the entire matrix dissolve through the grain boundary channels of penetrating Pb-Li. Such attacks lead to carbide dropping from grain boundaries (and martensitic laths). It has also been shown that after complete dissolution of the oxide layer, the corrosion mechanism changed and uniform depletion of Fe and Cr occurred from entire surface. It has been shown that during this period, the diffusion of iron across the Pb-Li boundary layer is the rate controlling step. The corrosion attack by Pb-Li has been also found to be grossly non-uniform in nature. It has also been shown that increasing temperature of exposure, flow velocity and introduction of temperature gradient increase the corrosion rate. The effects of these factors on the corrosion mechanism have been discussed in detail in the present study. Although the increase in flow velocity does not affect the original corrosion mechanism, very high flow velocities (>1 m/s) can cause grain dropping. The presence of a magnetic field has also been shown to increase the corrosion rate and significantly affect the corrosion mechanism possibly due to its interaction with Pb-Li flow. Many of these variables have been studied in detail and observed property variations have been rationalized by proposing a corrosion mechanism explaining the synergistic effects.

LIST OF ABBREVIATIONS

Abbreviations	Full Form
ADSS	Accelerator Driven Subcritical System
BARC	Bhabha Atomic Research Centre
CFD	Computational Fluid Dynamics
CLAM	China Low Activation Martensitic steel
DAE	Department of Atomic Energy
DC	Direct Current
DEMO	Demonstration Fusion Power Plant
EBSD	Electron Back Scattered Diffraction
EDM	Electric Discharge Machine
EDS	Energy Dispersive Spectroscopy
EMPPIL	Electro-Magnetic Pump driven Pb-Li Loop
EMPPIL-M	Modified Electro-Magnetic Pump driven Pb-Li Loop
EUROFER or EUROFER 97	European Ferritic/Martensitic Steel
F/M steel or FMS	Ferritic/Martensitic Steel
GDOES	Glow Discharge Optical Emission Spectroscopy
HV	High Vacuum
IAEA	International Atomic Energy Agency
ICP-AES	Inductively Coupled Plasma - Atomic Emission Spectroscopy
IN RAFMS	Indian Reduced Activation Ferritic/Martensitic Steel
IPUL	Institute of Physics , University of Latvia
ISO	Indian Standard Organization
ITER	International Thermonuclear Experimental Reactor
JET	Joint European Torus
KIT	Karlsruhe Institute of Technology, Germany
LAFMS	Low Activation Ferritic/Martensitic Steel

LASER	Light Amplification by Stimulated Emission of Radiation
LLCB	Lead Lithium Cooled Ceramic Breeder
MHD	Magneto-hydrodynamics
MIDHANI	Mishra Dhatu Nigam
ODS	Oxide Dispersion Strengthened
ORNL	Oak Ridge National Laboratory
P91	Modified 9Cr-1Mo steel
PAG	Prior Austenite Grains
Pb-Li	Lead-Lithium Eutectic
RAFMS	Reduced Activation Ferritic/Martensitic Steel
RDCTF	Rotating Disc Corrosion Test Facility
RDCTF	Rotating Disc Corrosion Test Facility
RPM	Revolutions per Minute
SEM	Secondary Electron Microscope
SST-1	Steady-State Tokamak-1
TBM	Test Blanket Modules
TEM	Transmission Electron Microscope (TEM)
VFD	Variable Frequency Drive
XPS	X ray Photoelectron Spectroscopy
XRD	X-Ray Diffraction

LIST OF FIGURES

LIST OF TABLES

CHAPTER 1

INTRODUCTION

1.1. Background

In the recent past, liquid metals like lead (Pb) and its alloys e.g. lead-bismuth eutectic (Pb-Bi) and lead-lithium eutectic (Pb-Li) have been proposed as potential coolants for advanced nuclear energy systems [1-2]. The attractiveness of these metals/alloys as reactor coolants arises from their low melting points, low vapor pressures, high heat transport capabilities and compatibility with water [3]. Systems using lead or its alloys as coolants include advanced nuclear fission reactors like the Accelerator Driven Subcritical system (ADSS), Lead cooled fast reactors, etc as well as the nuclear fusion reactors [3-4]. However, the compatibility of such coolants with the structural and / or cladding materials remains as one of the major challenges in the deployment of lead/lead-alloy-cooled nuclear reactors [5]. In comparison to the corrosion by an aqueous solution which is an electro-chemical process, the corrosion by liquid metal does not involve electron transfer in the liquid and is a physical–chemical process [6]. Due to its unconventional nature, liquid-metal corrosion has been a topic of research for more than three decades and in most practical cases simply depends on the difference in chemical potential (concentration gradient) between the solid and liquid and the extent of solubility of the solid metal in the liquid metal [7].

In the 1950s, on the eve of the second IAEA conference on Peaceful uses of Atomic Energy, the possibility of employing nuclear fusion for meeting global energy requirements was noted. Although the use of controlled nuclear fusion as an energy source presents major scientific and engineering challenges, the successful demonstration of the engineering feasibility of a fusion reactor is expected to be a solution to the energy crisis issue in near future [8]. One of the ways to achieve the controlled nuclear fusion of light elements like deuterium and tritium is by magnetic confinement of the fusion plasma which is achieved in a device called the Tokamak (Figure 1.1) [9].

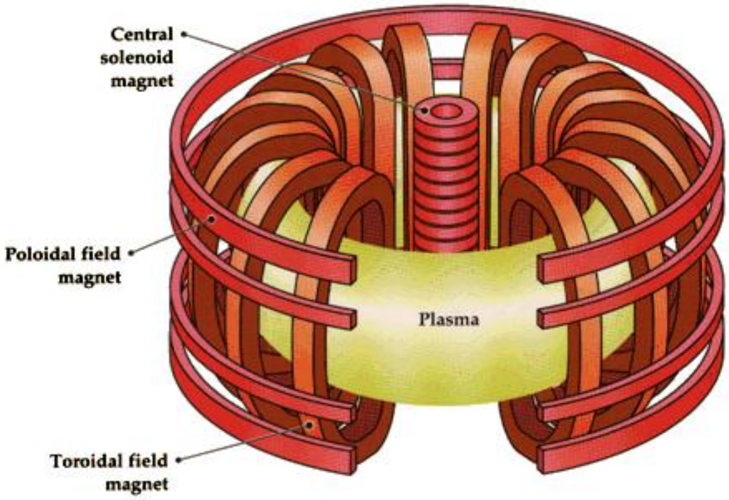

Fig. 1.1: A TOKAMAK type of Fusion Reactor [9].

Due to limited availability, the tritium required to fuel the fusion reactor is generally bred in-situ in a process called Tritium Breeding [10]. The International Thermonuclear Experimental Reactor (ITER) is an international research and engineering project which is currently building the world's largest and most advanced experimental Tokamak or Fusion Reactor at France [11]. Along with the other dedicated assignments towards the ITER itself; the participating countries including India are involved in designing their own Test Blanket Modules (TBMs) with the main aim of effective breeding of tritium from Li or its alloy/compound [12-13]. In this regard, liquid metal breeders such as Lithium or the Lead-Lithium eutectic alloy (Pb-Li) have the potential for constituting attractive breeding blankets, especially if the liquid metal serves as breeder and coolant [14]. Since the eutectic alloy (Pb-Li) is generally preferred for safety reasons because it is much less chemical reactive with air, water, or concrete, the same has been proposed by India as the coolant, tritium breeder and neutron multiplier for its Lead Lithium Cooled Ceramic Breeder (LLCB) concept [15].

However, a number of challenges present themselves towards the successful demonstration of a lead lithium cooled blanket / reactor and one of the key challenges concerns structural materials to be used [16]. These include corrosion compatibility with the coolant, high temperature strength, stability under irradiation, etc [17]. Since late 1970s, ferritic/martensitic steels are candidate structural materials for fast and fusion reactors because of their higher swelling resistance, higher thermal conductivity and lower thermal expansion than austenitic steels [18-19]. However, keeping in mind the damaging capacity of the high energy fusion neutrons (14 MeV); the reduced activation ferritic/martensitic (RAFM) steels are presently considered to be the most promising structural materials [20]. RAFM steels including the Indian RAFMS (IN RAFMS) have now achieved a sufficient level of technical maturity; i.e. qualified fabrication routes, welding technology and a general industrial experience is already available [21-22]. The IN RAFMS (composition: 9Cr–1.4W–0.06Ta–0.1C) have been produced by slightly varying the composition of the conventional modified 9Cr-1Mo steel (P91) [23-24]. The microstructure of IN RAFMS has been established through standard heat treatment of normalizing and tempering and the steel was found to have a tempered martensitic microstructure with coarse $M_{23}C_6$ carbides, rich in Cr and W on the lath boundary and fine intralath Ta and V rich MX precipitates [25]. The physical, thermodynamic and mechanical properties of IN RAFMS have been studied in detail while different fabrication processes like machining, Hot Isostatic Pressing (HIP) and welding have also been investigated [24-26]. However, the corrosion compatibility of IN RAFMS with Pb-Li under various test conditions still remains a gap area and has not been reported in literature so far. Moreover, with exception to a few studies, the detailed corrosion mechanism of ferritic/martensitic steels in Pb-Li and its dependence on the duration of exposure, especially in terms of micro-structural effects is still an unexplored territory.

- Thus, the compatibility of IN RAFMS material in molten Pb-Li needs to be investigated taking into account the effect of operating parameters like temperatures, temperature gradient, flow velocities and magnetic field.
- Moreover, the mechanism of corrosion of IN RAFMS and similar materials in molten Pb-Li needs to be established considering the role of various alloying elements and operating conditions so as to predict their behavior under any other unknown/unexpected circumstances.

1.2. Objective of the study

Keeping these aforementioned gap areas in mind, the major objectives of the proposed research work are:-

1. To investigate the corrosion compatibility of IN RAFMS and compare it with its surrogate material, P91 steel in molten Pb-Li under static and dynamic conditions and establish the effect of duration of exposure on the corrosion behavior.
2. To establish the effect of temperature and flow velocity on the corrosion of IN RAFMS and P91 in Pb-Li under isothermal static and dynamic conditions.
3. To study the effect of temperature gradient and magnetic field on the corrosion behavior of IN RAFMS and P91 in Pb-Li under non-isothermal flow conditions.
4. To establish the corrosion mechanism of IN RAFMS and P91 in Pb-Li in the presence and absence of magnetic field and establish the role of surface oxides, alloying elements and microstructure in detail.

1.3. Structure of the thesis

The thesis of the present work has been broadly divided into eight chapters. Chapter 1 introduces the topic, the gap areas and the objectives of the present work. A detailed literature survey on fusion reactor materials, especially with reference to ferritic / martensitic (F/M) steels, liquid metal corrosion and the present R& D on compatibility of F/M steels with Pb-Li, are summarized in Chapter 2. Chapter 3 deals with the design basis and description of various experimental facilities developed during the present work for corrosion studies as well as the basis of selection of operating parameters. Details of materials used for corrosion study, the plan of work and the actual experiments performed are described in Chapter 4. Chapters 5and 6 present the results obtained from corrosion studies on IN RAFMS and P91 material under different conditions of temperature, flow and magnetic field and interpretations on the results obtained. An overall discussion on the outcome of different experiments is given in Chapter 7 while the final conclusions are listed in Chapter 8.

CHAPTER 2

LITERATURE SURVEY

2.1. Nuclear Fusion

A nuclear reaction is a process in which atoms collide with other atoms and lose some of their original mass [27]. According to the principle of energy conservation as shown in Equation 2.1 (i.e. Einstein's equation); even a little bit of lost mass (m); results in generation of a very large amount of energy (E).

$$E = mc^2 \quad \ldots \quad 2.1$$

Where 'c' is the velocity of light.

In a fission reaction, a heavy atomic nucleus is split into smaller nuclei, other particles and radiation. In a typical reaction, an atom of uranium 235 absorbs a neutron and splits into two lighter atoms, barium and krypton, emitting radiation and neutrons as shown in Figure 2.1. When critical mass is attained, the emitted neutrons can split further atoms, producing a very fast chain reaction[27].

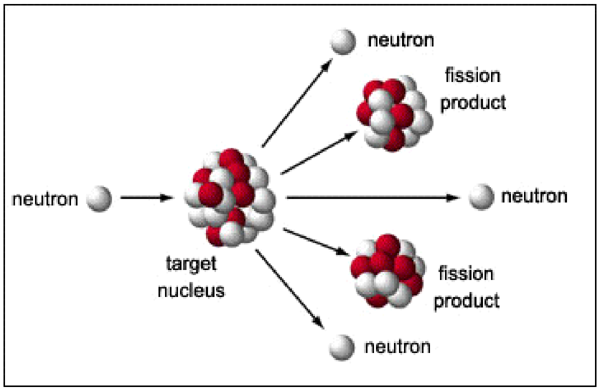

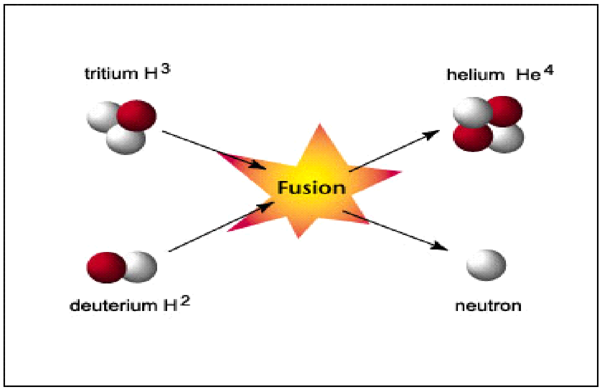

Fig. 2.1: Nuclear fission reaction [28]. **Fig. 2.2: Nuclear fusion reaction [28].**

Nuclear fusion is the process by which two or more atomic nuclei join together, or "fuse", to form a single heavier nucleus [29]. This is usually accompanied by the release or absorption of large quantities of energy. Fusion is the process at the core of our Sun and all other stars of our universe, where gravitational forces have created the necessary conditions for fusion. Over billions of years, gravity gathered the Hydrogen clouds of the early universe into massive stellar bodies. In the extreme density and temperature of their cores, fusion of hydrogen occurs in Sun and the temperatures reach to 15,000,000 °C [30]. The mass of the resulting Helium atom is not the exact sum of the two initial atoms, however: from the mass that is lost; great amounts of energy is gained. In similar manner, the fusion of the two isotopes of hydrogen i.e. Deuterium and Tritium will result in formation of a Helium atom and one neutron along with the release of fusion energy as shown in Figure 2.2 [29].

2.1.1. Fusion Fuels

Although different isotopes of light elements can be paired to achieve fusion, the deuterium - tritium system makes fusion attainable at lowest plasma temperature as shown in Figure 2.3 [29-31]. Deuterium can be distilled from all forms of water and is a widely available [32]. Tritium is a fast-decaying radioelement of hydrogen which occurs only in trace quantities in nature. In the Deuterium-Tritium (D-T) fusion reaction, high energy neutrons are released along with Helium atoms as shown in Figure 2.4 [33]. The electrically-neutral neutrons escape the plasma generally contained within the magnetic fields and is absorbed by the surrounding walls [34-35]. If these walls have containment for Lithium, the incoming neutron is absorbed by the Lithium atom, which recombines into an atom of Tritium and an atom of Helium. The Tritium can then be removed from the blanket and recycled into the plasma as fuel.

2.1.2. Tritium Breeding

Lithium can be contained inside the fusion reactor in the form of liquid or solid tritium breeders in test blanket modules (TBM) [12]. The liquid breeders include pure Li, lead-lithium eutectic and molten salts like FLIBE which will flow in a closed circuit while solid breeders could be Li_2O, Li_2TiO_3 or $LiSiO_2$ in the form of ceramic pebbles [35].

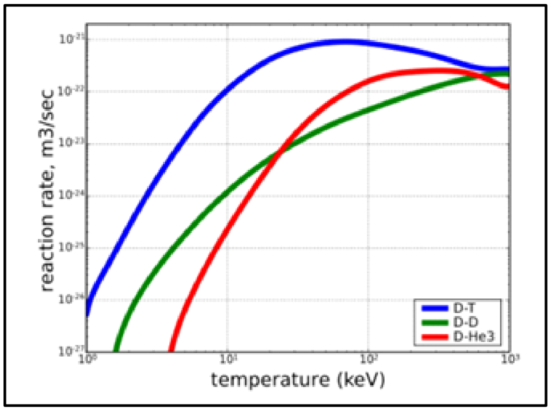

Fig 2.3: Fusion reaction rate for various fuel combinations [33].

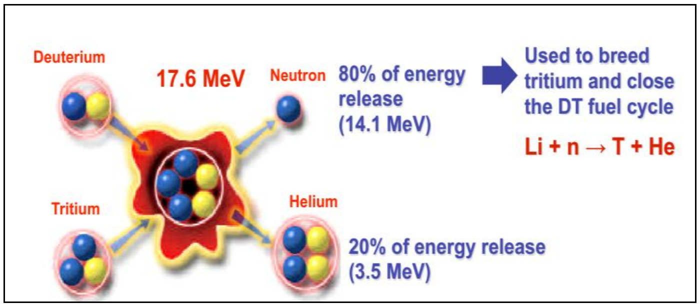

Fig 2.4: The Deuterium-Tritium Fusion Reaction [36].

Natural lithium contains 92.5% ^{7}Li and 7.5% ^{6}Li and tritium can be produced from lithium isotopes by using neutron capture reactions shown in Equation 2.2 and 2.3 for ^{6}Li and ^{7}Li respectively.

$^{6}_{3}Li+^{1}_{0}n \rightarrow ^{4}_{2}\alpha+^{3}_{1}T+4.784\ MeV$ ………………………………………………………….... 2.2

$^{7}_{3}Li+^{1}_{0}n \rightarrow ^{4}_{2}\alpha+^{3}_{1}T+^{1}_{0}n - 2.467\ MeV$ ……………………………………………………….... 2.3

However, the cross-section of the reaction using ^{6}Li is much higher (for neutrons in the range of MeV as produced in fusion reaction i.e. 14 MeV) than the reaction using ^{7}Li [37]. Natural lithium has an absorption cross-section for thermal neutrons of 71 barns the Lithium-6 isotope has an absorption cross-section of 945 barns [38]. Moreover, The $^{7}Li\ (n;\ n'\alpha)^{3}_{1}T$ reaction is endothermic with an energy threshold of 2.8 MeV. Thus; it is much more favorable to use ^{6}Li in the blankets than ^{7}Li which in turn demands for enrichment of ^{6}Li in the tritium breeders. The enrichment will be around 30 % in solid breeders while may go upto 90 % for liquid breeders [39].

2.2. The Fusion Reactor

To cause fusion on Earth, the atoms to be fused must be in the form of PLASMA [33]. Attainment of stable plasma to achieve fusion depends largely on the temperature, density and confinement technique [34]. Researchers around the world have worked vigorously and are now in a position to obtain effective plasmas with the help of high magnetic confinement in a special torus (doughnut) shaped vessel known as TOKAMAK [40]. In the recent past, the D-T plasma could be held for about 5 seconds in a TOAKAMAK called the Joint European Torus (JET) at UK resulting in fusion power of over 15 MW [41]. Such achievements gave impetus for setting up of the International Thermonuclear Experimental Reactor (ITER) to obtain fusion power of 500 MW (from a 50 MW input) for up to 500 seconds [42]. Seven countries, including India, are participating in it. The machine is expected to generate more energy (ten times) out of the fusion process than is used to initiate it. The next step would be to build an actual plant that will generate electricity from fusion, now tentatively known as the DEMO plant. Figure 2.5 gives a view of the different components of the ITER machine. In the recent past, India joined as an equal partner in the ITER program at Cadarache, France, in which the commitment of the country lies in delivering a large inventory of sophisticated components [43].

2.2.1. Test Blanket Module

Breeding blankets represent one of the major technological breakthroughs required for passing from ITER to the next step DEMO [13]. The fusion reactor plasma is confined by magnetic fields and the heat generated due to the fusion in the plasma is extracted by an appropriate coolant, the He gas and/or a eutectic alloy liquid flowing in the blanket modules that are sitting close to the plasma. The heat is transported to the coolant through the walls of the TBMs by both electromagnetic radiation from plasma and the electrically neutral 14.1 MeV neutrons that escape from the plasma into the walls of the TBMs and the functional materials in TBMs. Also, since the blanket consists of ^{6}Li either in the form of a ceramic compound or liquid metal (pure lithium or lead-lithium eutectic alloy), it transmutes to tritium by (n, α) reaction giving rise to additional heat to the coolant.

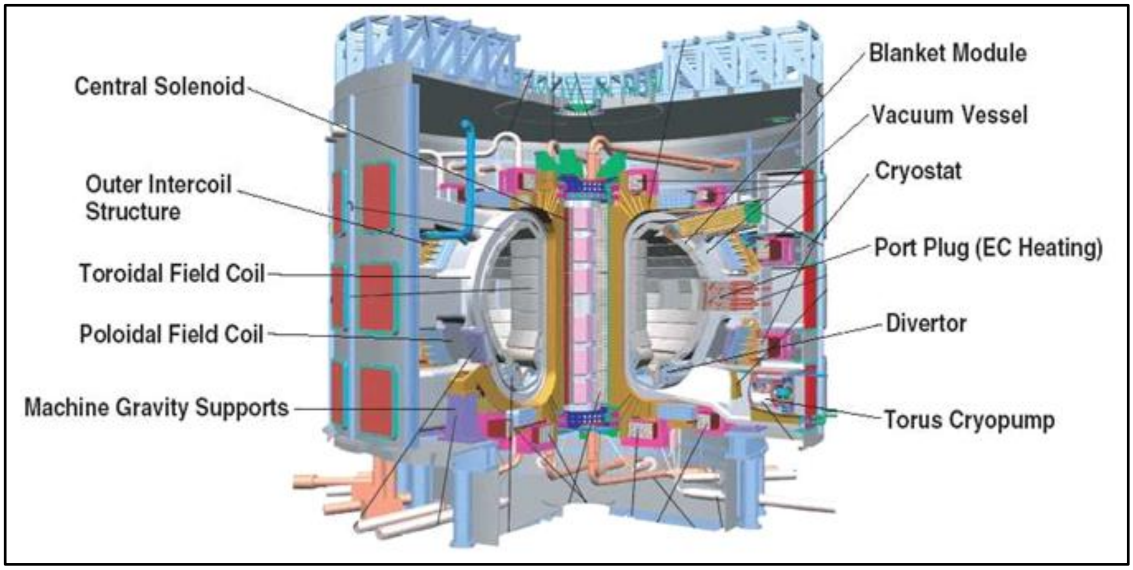

Fig 2.5: Main components in ITER [36].

However, when the 14.1 MeV neutrons escaping from the plasma enter the walls of the TBM, complications arise due to the radiation damage (displacements and transmutations) of lattice atoms caused by them [16]. Moreover, because of the high cross-section of these high energy neutrons to cause the (n, α) and the (n, p) reactions with almost all elements, atoms constituting the walls of the TBMs undergo these reactions leading to the formation of both helium and hydrogen in them at high rates causing serious damage to the structural material. On the other hand, the corrosion behavior of the TBM structural material with the coolant/liquid breeder under high temperature, magnetic field and irradiation is also a deciding factor while estimating the service life [19].

Taking the above issues into consideration while developing a sustainable blanket, various participating countries are designing their own test blanket modules to test their effectiveness at

ITER [12]. Each TBM has its distinct design and materials under use. There are differences in coolants, structural materials, neutron reflectors and other major components. The major design parameters of some of the ITER relevant test blanket module proposed by various participating countries have been listed in Table 2.1[14].

Table 2.1: Design parameters of various ITER relevant TBMs [14].

	European	China		U.S.A	Russian	Korea	India
		1	2				
Structural material	EUROFER	CLAM	CLAM	F82H or EUROFER	V-Cr-Ti	RAFM	IN RAFMS
Breeder	Pb-Li	Pb-Li	Pb-Li	Pb-Li	Li	Li	Pb-Li and Li_2TiO_3
Neutron multiplier	NA	NA	NA	NA	Be or none	NA or Be	NA
Flow channel insert	NA	SiC_f/SiC	NA	SiC_f/SiC or metallic	NA	NA	NA
MHD insulation	NA	NA	Al_2O_3/ other choice	NA	Different options	NA	(Al_2O_3 TBD)
Primary Coolant	He	He + PbLi	He	He + PbLi	Li	He	He and PbLi
Primary Coolant Parameters							
Inlet/ Outlet temperatures, °C	300/500 (He) 300/480 (PbLi)	340/402 (He) 480/700 (PbLi)	340/420 (He) ~450 (PbLi)	350/420 (He) 360/470 (PbLi)	Varies (He) 250/450,350/550 (Li)	300/406 (He)- 340/411 (Li)	350/460 (He) 370/480 (PbLi)
Pressure, MPa	8 (He), <1 (PbLi)	8 (He), 1(PbLi)	8 (He), ~	8 (He), 2 (PbLi)	0.5 (Li)	8 (He)	8 (He), <1.2 (PbLi)
Temp. max, FW, °C at 0.5 MW/m^2 ˚C	546	534	547	554	~675	614	550
T. max, breeder, °C	568	700	480	500	550	458	480
T. max, breeder/structural material interface	548	434	478	<480	590	<500	~450

°C							
Breeder mass flow rate, Kg/s	0.22-2.2	5.2	0.1-1	21	1.07	0.011	42
Breeder max flow velocity, m/s	<0.001	0.014	<0.003	0.1	0.002-0.004	<0.5	1.0

2.2.2. The Indian Test Blanket Module

India has proposed a unique *'hybrid'* blanket known as Lead Lithium cooled Ceramic Breeder (LLCB) for its Test Blanket Module (TBM) for testing at ITER which contains a solid breeder as well as a liquid breeder [15-44]. The parameters of the Indian LLCB TBM are already listed in Table 2.1. The Pb-Li acts as the secondary coolant while helium gas at 80 bars with inlet temperature of 573 K (300°C) and outlet temperature of 823 K (550°C) acts as the primary coolant for the structural material. The Indian variety of Reduced Activation Ferritic -Martensitic Steel (Indian RAFMS) has been proposed as the structural material for the LLCB TBM [24]. Al_2O_3 coating on the inner walls of the TBM box has been proposed which will helps to reduce the MHD drag and prevents corrosion as well as tritium permeation into the structural steel [45]. The schematic of the Indian LLCB TBM is shown in Figure 2.6

2.3. Structural Materials for Fusion Reactor

For the construction of a 'TOKAMAK' type fusion reactor and its 'Tritium Breeding Blanket', a number of materials – both structural and functional – are required to be developed. The structural materials need to have the sufficient radiation resistance apart from other properties and the functional materials should have the required level of integrity under the operating conditions i.e. high energy neutron environment as well as strong mechanical, electromagnetic and heat loads [47]. A schematic view of the materials layout around the fusion plasma is shown in Figure 2.7. The plasma facing material over the first wall experiences high radiation damage due to the high energy neutrons apart from the high heat flux. To avoid sputtering of plasma facing material, an element that either does not sputter due to the neutrons hitting it or, else, it does not quench the plasma despite the fact that it sputters, is selected. High Z (atomic number) elements (e.g. W) fall in the 1st category and the low Z elements (e.g Be) form the 2^nd^ one. [48]

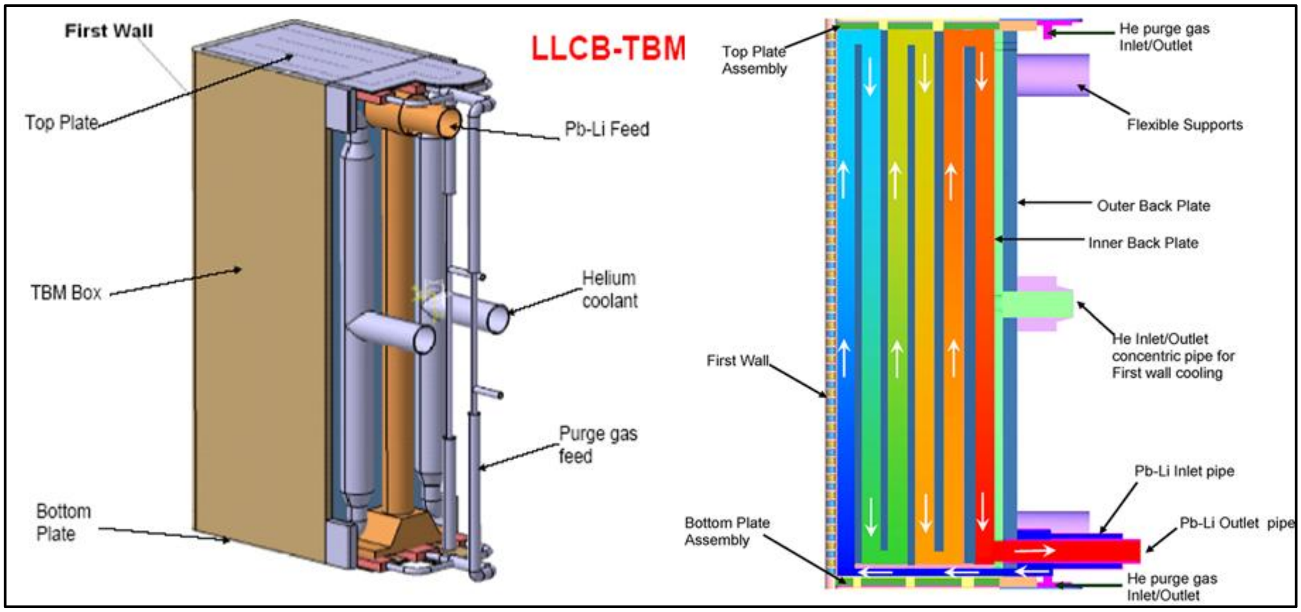

Fig 2.6: The schematic of Indian LLCB TBM [46].

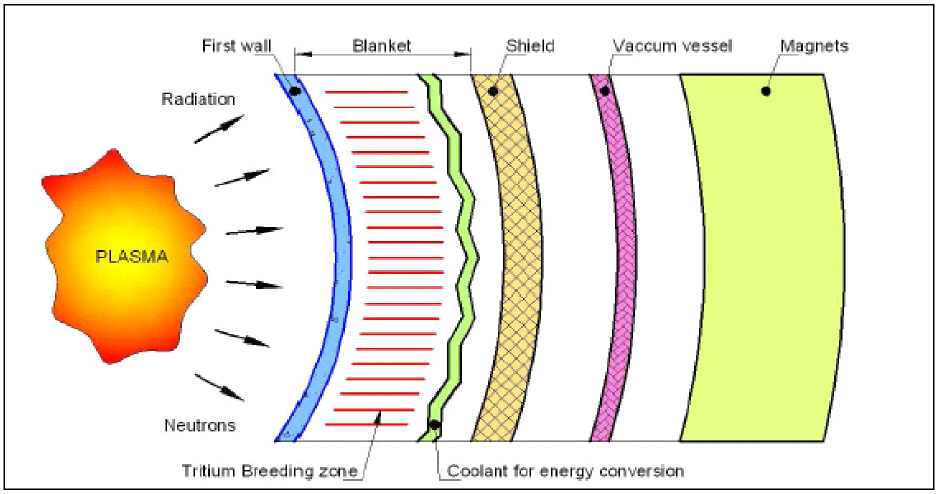

Fig.2.7: Schematic view of the arrangement of materials in a TOKAMAK [49].

Next to the plasma facing material in the first wall is a material that can act as a heat sink and carrier of heat away from the first wall to avoid its excessive heating. This generally is OFHC (oxygen free high conductivity copper) alloyed with a little bit of Cr (< 1 wt %) to give the Cu the required tensile strength and even a lesser content of Zr (<0.1 wt %) to impart the required fatigue strength [50].

Next to the plasma facing material or to the heat sink (as the situation may demand), and bonded to it, is the first wall structural material. Initially, austenitic stainless steel 316 was selected as the first wall structural material and continues to be material of construction for the first wall of ITER in the form of low activation 316 LN (IG), IG meaning the ITER grade [16]. However, because of its tendency to swell more under irradiation as compared to the ferritic steels and unacceptable fatigue life above 600 ^{0}C, especially with He (generated due to (n, α) reactions) in it, the material of choice for the first wall now for the DEMO reactors is the low activation Ferritic/Martensitic (F/M) steel (FMS). However vanadium alloys and SiC are also some of the available options.

2.3.1. First Wall Structural Materials

a. Steels

As discussed earlier, RAFM steels are one of the proposed candidates for first wall structure. Reduced activation is achieved by selection of appropriate alloying elements and control of substitutional and interstitial impurities [51]. The alloying elements and the impurities in the steel have to be such that, due to the neutron irradiation, they do not transform to their respective long half-life radio-active isotopes. They are actually derivatives of the commercially available modified 9Cr-1Mo steel where constituents producing radioisotopes having long half lives (eg. Mo, Nb) have been replaced by relatively less active counterparts (like W, Ta) [20].

The typical compositions of the various RAFM steels developed in different countries (including India) and proposed as structural material for the first wall are given in Table 2.2. In order to have sustained irradiation resistance beyond 30 years, nano-structured RAFM steels have been also developed which are capable of distributing the He into small bubbles by nucleating them on the surfaces of Ti-Y-O complexes introduced in the steel. This steel is known as the oxide dispersion strengthened (ODS) F/M steel [52].

Table 2.2: Typical compositions of the various RAFM steels for the first wall of ITER-TBMs [53, 24].

	IN RAFMS	EUROFER	F82H	CLAM	JLF-1	ORNL9Cr–2WVTa
Origin	India	European Union	USA	China	Japan	USA
Cr	9.04	8.5	8.0	9.0	9.0	8.75
C	0.08	0.11	0.10	0.1	0.1	0.1
Mn	0.55	0.5	0.5	0.45	0.45	0.45
P	0.002	<0.005	<0.02	<0.003	-	-
S	0.002	<0.005	<0.01	<0.002	-	-
B	0.0005	0.005	0.003	-	-	-
N	0.0022	0.03	<0.001	<0.02	0.05	-
W	1.00	1-1.2	2.0	1.5	2.0	2.0
Ta	0.06	0.08	0.04	1.15	0.7	0.07
Si	0.09	<0.005	0.1	<0.01	<0.1	0.2
V	0.22	0.25	0.2	0.2	-	0.25

b. Vanadium Alloys

Vanadium-based alloys, mainly V-4Cr-4Ti and V- 5Cr-5Ti, are very attractive for the structural part of the first wall due to their low activation, good high temperature strength and surface heat capability [54]. However, they have strong affinity for solutes such as oxygen, carbon and nitrogen, which leads to matrix embrittlement and reduced compatibility with liquid Li. Also, they have high solubility, diffusivity and permeability of tritium, which can lead to embrittlement at low temperatures [54].

c. SiC_f/SiC Composites

SiC_f/SiC ceramic composites have attractive properties for both structural as well as functional applications. They have the ability to operate with acceptable mechanical properties up to almost 1100 °C [55]. The SiC_f/SiC composites also have very good tolerance against neutron irradiation up to very high temperatures and an inherent low level of long-lived radioisotopes. However, they have low surface heat capability and are quite brittle. Also, the production rates of hydrogen and helium in these composites due to the (n,α) reactions are extremely high and there is also a possibility of leakage of helium gas coolant into the fusion plasma through the porous SiC_f/SiC ceramic composites [16].

A comparison of the properties of the three types of first wall structural materials is made in Table 2.3. Presently, the best choice is to go for F/M steels as the industrial experience of fabrication and joining of vanadium and its alloys is not as much developed and because of inherent brittleness, the bulk SiC and SiC_f-SiC composites still do not qualify for use. As far as the operating temperature range in concerned; the upper temperature limit for structural materials in fusion reactors may be controlled by: Thermal creep, high temperature helium embrittlement, void swelling, and compatibility/corrosion issues [56]. Void swelling is not anticipated to be significant in ferritic-martensitic steel [57] or V-Cr-Ti alloys 10 [54] up to damage levels in excess of 100 dpa. Chemical compatibility issues can also reduce the maximum operating temperature for a particular fusion blanket system. Due to a high density of matrix sinks, ferritic/martensitic steel are quite resistant to helium embrittlement [58].

The lower temperature limits for the ferritic/martensitic steel are based on fracture toughness embrittlement associated with low temperature neutron irradiation. The radiation hardening in BCC alloys at low temperatures (<0.3 TM) is generally pronounced even for doses as low as ~1 dpa [59]. The amount of radiation hardening typically decreases rapidly with irradiation temperature above $0.3T_M$, and radiation-induced increases in the DBTT may be anticipated to be acceptable at temperatures above ~0.3 T_M(where T_M is the melting point) [59].

Table 2.3: Comparison between the properties of various structural materials for the first wall [56].

Property/Material	FMS	V-4Cr-4Ti	SiC_f/SiC
Temperature Window, ^0C	300-600	400-700	700-1000
Surface Heat Capability, kW/K.m	4.32-2.74	4.61-4.63	1.05
Thermal Expansion, 10^{-6}/K	11.1-12.3	10.3-11.4	2.5
Thermal Conductivity, W/K.m	33.4-32.3	31.3-33.8	12.5
DBTT*, ^0C	<20	250-300	Brittle

2.3.2. Materials for Test Blanket Modules

The structural material for the first wall and therefore the TBM box has been discussed earlier and is at the moment proposed to be the ferritic/martensitic steels. If the tritium breeder (basically, Li^6) inside the TBM is in the form of a solid ceramic compound, it is solid breeder TBM and, if the breeder is in liquid state (as pure Li liquid or eutectic Pb-Li alloy liquid), it is called a liquid breeder TBM [12].

In the case of a solid TBM, the coolant is generally helium [12]. To have enough neutrons for the breeding reaction, berillium or beryllide is to be inserted in the solid TBM as a neutron multiplier [60]. The solid TBM thus consists of the structural material (low activation F/M steel), the ceramic breeder (lithium titanate or lithium silicate), the neutron multiplier (Be or beryllide) and the coolant, He. In case of liquid breeder TBM, the coolant may be liquid lithium, lead-lithium eutectic (Pb-Li) or Li^6 based salt (eg. LiF-KF i.e. FLINAK) [14]. When Pb-Li is used in a liquid breeder TBM, Li works as the breeder and Pb as the neutron multiplier. The entire liquid itself acts as the coolant (primary or secondary). As a coolant, it creates the extra issue of Magneto-Hydro-Dynamic (MHD) drag on its own flow in the TBM, which raises further requirements in terms of electrically insulating coatings on steel [61]. However, there is no need to insert Berillium or Beryllide for neutron multiplication in this case.

2.4. The Lead-Lithium eutectic

Due to various problems of handling and usage of pure lithium, the lead- lithium eutectic (Pb-Li) has been proposed as one of the best possible coolant in such conditions [62]. Moreover, the eutectic does not show vigorous chemical reactions with air or water which is an important criterion in the choice of breeder materials [63, 64]. Possible disadvantages are related to high density, lesser compatibility with steels as compared to Li, tritium containment problems (due to its very low solubility) and melting temperature which is higher than that of Li [62, 65]. Table 2.4 lists some of the empirical relations to calculate the physical properties of Pb-17atom %Li eutectic (Pb-17Li) while Table 2.5 compare the actual values with that of other potential coolants like lead bismuth eutectic (Pb-Bi), lithium and water.

2.4.1. The eutectic composition

The lithium concentration of the lead lithium eutectic is a very important parameter. Lithium determines the eutectic's chemical activity and a fine variation of Li concentration can significantly vary the physical-chemical and solute transport properties [68]. Quality assurance of Pb-Li eutectic is intimately related with the accurate determination of the eutectic chemical composition with the analysis technique certifying at 0.1% Li and the eutectic production technique guaranteeing its short-scale homogeneity (in order to avoid Li aggregation) [66]. Hansen and Anderko had initially published data pertinent to the lead-rich section of the Pb-Li phase diagram (Li<25 at%) in their book where they reviewed the previous work and recommended the most extensive and comprehensive data which was for 17 at% Li (denoted as Pb-17Li) at melting point 235 °C [69]. Hence Pb-17Li became the choice of alternative breeder material for the blanket designs.

Table 2.4: Physical properties of Pb-17Li [66, 67].

Property	Expression	Temperature range
Melting Temperature: T_m	507 K	
Density , ρ (kg/m3)	10.45 ´ 10^{-3} (1 - 161 ´ 10-^{6} T)	508-625 K
Specific heat [1] C_P [J/kg-K]	195 - 9.116 ´ 10^{-3} T	508-800 K
Thermal Conductivity K_{th} (W/m-K)	1.95 + 0.0195 T	508-625 K
Electrical resistivity (nW-m)	10.23 + 0.00426 T	508-933 K
Surface tension (N/m)	0.52 - 0.11´ 10^{-3} T	520-1000 K
Dynamic viscosity (Pa - s)	0.187 ´ 10^{-3}exp [1400./T]	521-900 K
Vapor pressure (Pa)	1.5 x 1010 exp (-22900/T)	550-1000 K

Metallurgical studies on lead-lithium alloys had also started long back in the 1950s. At the suggestion of the Neutron Physics Division of the Oak Ridge National Laboratory, the Metallurgy Division initiated a research program to determine the potential application of a lead-lithium alloy as a combination neutron and gamma-ray shielding material for both instruments and reactors [38]. Under this program the alloying, casting and joining of Pb-Li alloys were studied. It was established that the use of eutectic composition was necessary in order to avoid unnecessary segregation associated with the slow cooling rates encountered in large, relatively thick castings. It was observed at that time from the phase diagram of Pb-Li in Figure 2.8, the eutectic alloy contains 0.69 wt % lithium (17 at %) and melts at 235˚C (508 K).

Table 2.5: Comparison of physical properties of various coolants [68].

Properties	Unit	LBE	Pb-Li	Lithium	Water
Melting Point at 1 bar	˚C	125	235	180.5	0
Boiling Point at 1bar	˚C	2516	~1700	1317	100
		At 300 ˚C	At 300 ˚C	At 300 ˚C	At 300 ˚C
Density	Kg/m^3	10325	9988	505	1000
Heat capacity	J/(Kg.K)	146.33	200.22	4279	4180
Kinematic Viscosity	[m^2/s].10^7	1.754	1.3	9	9.1
Heat Conductivity	W/(m.K)	12.68	45.2	29.2	0.6
Electrical Conductivity	[A/(V.m)].10^5	8.48	12.67	33.5	2.10^{-4} (tap)
Thermal Expansion Coefficient	K^{-1}.10^6	6.7	41.2	43.6	6
Surface Tension	[N/m].10^{-3}	410	430	421	52 (tap)

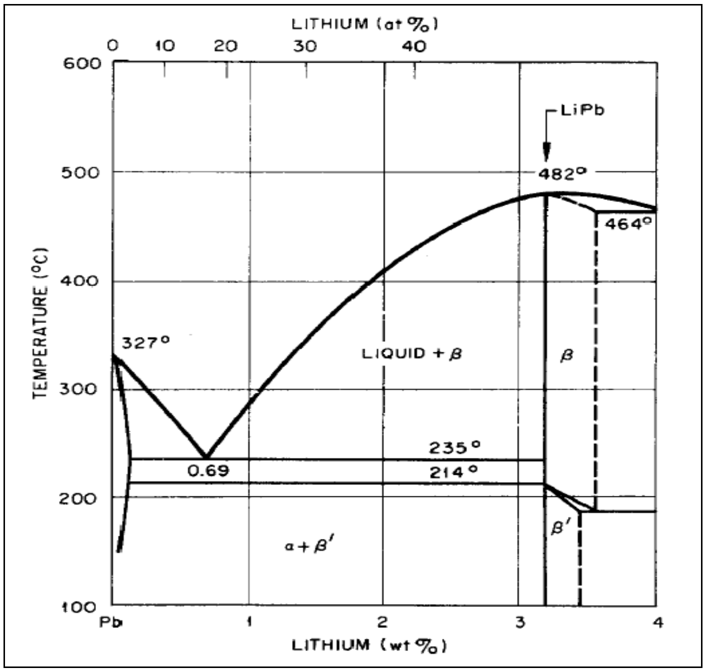

Fig. 2.8: The lead-lithium phase diagram [38].

At that time, liquidus temperatures were conventionally determined by thermal analysis methods. These methods, however, were unreliable since they suffered from the fact that, being non-equilibrium methods, they were still used to determine equilibrium data. In 1992, Hubberstey and Sample [70] developed a new technique to re-determine the composition of Pb-Li eutectic. The measurement of electrical resistance as a function of temperature under equilibrium condition overcomes such problem, since the plots relating these two parameters, which are readily determined with a high degree of accuracy, exhibit an abrupt change in gradient at the liquidus and a sharp discontinuity at the eutectic. In their work, the eutectic composition corresponded to 15.7 ± 0.2 at% (denoted as Pb-15.7Li) at melting point 235 ± 1 °C [70]. As a result the Pb-17Li alloy which was chosen for the most of conceptual designs of breeder blankets or experimental loops had been shown to lie slightly away from the eutectic point. However, although this chemical composition differs a little from the eutectic one (Pb-15.7Li), it is not of great importance in practice and the alloy (Pb-17Li) is still suitable for the operation of a blanket [71-72]. Nevertheless, for the newest design proposal for Indian LLCB TBM, the reference lead-lithium alloy is Pb-16atom %Li (Pb-16Li) [73-74]. For the sake of understanding, lead-lithium eutectic has been generally denoted as Pb-Li in this thesis.

2.4.2. Crystal structure of Pb-Li

Pb-Li is theoretically reported to be a rhombohedral phase, with a slightly distorted CsCl structure [75]. It has been reported as the Pb-Li phase is heated; it changes from a complex rhombohedral phase to a simple cubic phase [76]. Moreover calculation from space group theory shows that Pb-Li and Pb should have similar cubic phases. It may be highly possible that the PbLi phase retains its cubic structure at room temperature, and hence not always visible in the X-Ray Diffraction (XRD) pattern of the alloy [77]. Figure 2.9 shows the micrograph of Pb-17Li ((etched in nitric Acid: glacial acetic acid: glycol =1:1:10) where the lamellar eutectic structure could be clearly seen. The lead in lithium-lead eutectic activates by neutron irradiation and forms Polonium which is an alpha emitter with a 130 day half life [62]. This happens through a two-step reaction as given in equation 2.4 and 2.5. Bismuth is either an original impurity of lead or a buildup from lead during irradiation.

$^{208}Pb(n, \gamma)\ ^{209}Pb$ ---- (3h) → ^{209}Bi ……………………………………………………………2.4

$^{209}Bi(n, \gamma)\ ^{210}Bi$ ----(5h)→ ^{210}Po → α ……………………………………………………………….2.5

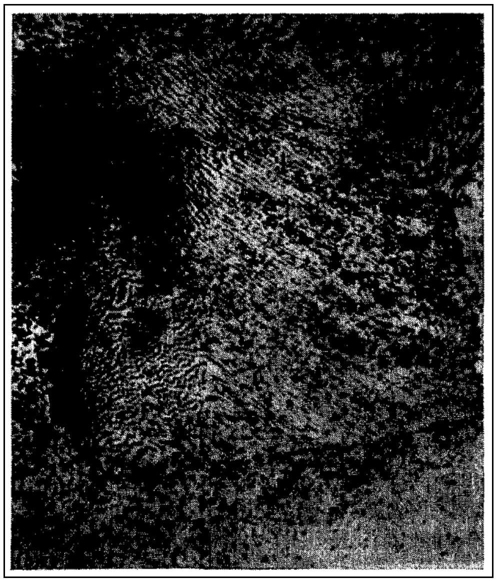

Fig. 2.9: Micrograph of Pb-17Li at 1, 000 x [38].

2.5. The Ferritic/Martensitic Steels

Since the late 1970s, ferritic/ martensitic Cr-Mo steels have been considered alternate candidate structural materials to austenitic stainless steels for first wall and blanket structure applications for fusion reactors [78]. This choice followed irradiation studies I fast reactors that showed these steels to be more swelling resistant than austenitic steels. The steels also have higher thermal conductivity and lower thermal expansion than the austenitic steels, which provide improved resistance to thermal stresses for a reactor operating in a pulsed mode [18].

2.5.1. Microstructural Evolution of Ferritic/Martensitic Steels:-

The first Cr-Mo steels were used for conventional power-generation applications in the 1920s. The 2¼Cr-1Mo (nominally Fe-2.25Cr-1.0 Mo-0.3Si-0.45Mn-0.12C) steel, designated by ASTM as Grade 22, was introduced in the 1940s and is still widely used today [79]. Along with Grade 22, 9Cr-1Mo (T9 was an early development, the additional chromium added for corrosion resistance [18]. Since then, there has been a continual push to increase operating temperatures of conventional fossil-fired power-generation systems. This led to the development of several “generations” of steels with improved elevated-temperature strengths (Table 2.6) begining with T22 and T9 (zeroth generation) with 100,000 h creep-rupture strengths at 600 ºC of about 40 MPa [80].

Steels beyond the zeroth generation contained mainly 9–12% Cr for improved corrosion and oxidation resistance for elevated-temperature operating conditions. The first generation, in addition to increased chromium, involved primarily the addition of the carbide formers vanadium and niobium to T22 and T9 compositions to add precipitate strengthening. In some cases, a small tungsten addition was made for further solid solution strengthening, in addition to that provided by molybdenum. These steels, introduced in the 1960s for applications to 565 ºC, included 2¼Cr-1MoV, HT9 (Fe- 12.0Cr-1.0Mo-0.25V-0.5Ni-0.5W-0.6Mn-0.4Si-0.2C), HT91 (Fe-12.0Cr-1.0Mo-0.25V- 0.5Ni-0.6Mn-0.4Si-0.2C), and EM12 (Fe-9.5Cr-2.0Mo-0.30V-0.40Nb-1.1Mn-0.4Si- 0.10C) [79]. These steels, which included those later considered for fast reactor applications in the 1970s, had increased 10^5 h rupture strengths at 600ºC of up to 60 MPa.

Generally, the microstructures of the 9 and 12% Cr steels are designed by balancing austenite and ferrite stabilizers to produce 100% austenite during austenitization and 100% martensite during a normalizing (air cooling) or quenching treatment following austenitization, although a small amount ofδ-ferrite (<1%) may be present in some cases, especially in the 12% Cr steels. For the second generation, developed in 1970–1985, carbon, niobium, and vanadium were optimized, nitrogen (0.03–0.05%) was added, and the maximum operating temperature increased to 593ºC [81]. The new steels included modified 9Cr-1Mo, designated T91 (Fe-9.0Cr-1.0Mo-0.0.2V-0.08Nb-0.05N-0.40Mn-0.40Si-0.10C) and HCM12 (Fe-12.0Cr-1.0Mo-1.0W-0.25V-0.05Nb-0.55Mn-0.30Si-0.03N-0.10C), which has a duplex structure (tempered martensite and δ-ferrite). These steels have 10^5 h rupture strengths at 600 °C of about 100 MPa [79]. Of these latter steels, T91 has been used most extensively in the power-generation industry throughout the world.

Table 2.6: Evolution of Ferritic/Martensitic Steels for the power generation industry [79].

Generation	Years	Steel Modification	Steels	10^5 h Rupture Strength, 600 °C (MPa)	Maximum Temperature of Use (˚C)
0	1940-60	Basic Cr-Mo steels	T22,T9		520-538
1	1960-70	Addition of Mo, Nb, V to simple Cr-Mo steels	EM12,HCM9N, HT9,HT91	40	565
2	1970-85	Optimization of C, Nb, V, N	HCM12,T91, HCM2S	60	593
3	1985-95	Partial Substitution of W for Mo and addition of Cu, N, B	NF616,E911, HCM12A	100	620
4	After 1996	Increase in W and addition of Co	NF12,SAVE12	140	650

The third generation of steels was developed based on the previous generation, primarily by the substitution of tungsten for some of the molybdenum, although boron and nitrogen were also utilized. These steels include NF616 (Fe-9.0Cr-1.8W-0.5Mo-0.20V-0.05Nb-0.45Mn-0.06Si-

0.06N-0.004B- 0.07C), designated Grade 92, E911 (Fe-9.0Cr-1.0Mo-1.0W-0.20V-0.08Nb-0.40Mn- 0.40Si-0.07N-0.11C), etc [79]. They were developed and introduced in the 1990s for 620º C operations with 10^5h creep rupture strengths at 600ºC of 140 MPa.

Finally, the next generation of steels is being developed at present, where the intention is to push operating temperatures to 650ºC. These fourth-generation steels, SAVE12 (Fe-11.0Cr-3.0W-3.0Co-0.20V-0.07Nb-0.30Mn-0.30Si-0.04N-0.07Ta-0.04Nd- 0.10C) and NF12 (Fe-11.0Cr-2.6W-2.5Co-0.2Mo-0.2V-0.07Nb-0.50Mn-0.20Si-0.06N 12 0.004B-0.08C), differ from the previous generation primarily by the use of up to 3.0% cobalt; they have projected 105 h creep-rupture strengths at 600ºC of 180 MPa [82].

The *reduced activation steel compositions* were patterned after the existing conventional steels being used or developed at the time the reduced-activation steels were being developed. The ORNL 9Cr-2WVTa, for example, was patterned after modified 9Cr-1Mo steel, with the molybdenum replaced by tungsten and niobium replaced by tantalum [83]. As a result, most of these steels should, at best, be ranked as second generation although they generally have creep properties similar to those of modified 9Cr- 1Mo (T91) [84]. The possible exception is the EUROFER composition, which was developed most recently; the composition has characteristics of third-generation steels, in that it contains boron and nitrogen (Table 2) [85].

It should be noted that the replacement of molybdenum by tungsten was also used to develop T23 which is an advanced 2¼Cr steel (Fe-2.25Cr-1.6W-0.1Mo-0.25V-0.05Nb- 0.45Mn-0.20Si-0.003B-0.06C) [86]. The 100,000 h creep-rupture strength at 600ºC of this steel is above that of first generation steels, and it can exceed that of T91 under some conditions.

2.5.2. Normalized and Tempered Microstructure

The strength of the 9–12% Cr steels generally depends on the tempered martensite microstructure and the precipitates therein [87]. The general microstructures (prior-austenite grain boundaries, lath/sub-grain boundaries, dislocations, and precipitates) of most of the new 9%Cr and 12%Cr steels are similar [19, 21]. Strengthening mechanisms in these steels include Solid-Solution Strengthening, Dislocation-Particle Interactions, Dislocation-Dislocation Interactions and Dislocation-grain boundary interactions [79].

In the normalized or quenched conditions, martensite laths with a high dislocation density are observed as shown in the transmission electron micrographs of 12Cr-1MoVW (HT9) steel in normalized condition in Figure 2.10(a). When tempered, the dislocation structure recovers, and the laths become elongated sub-grains with a typical average width of 0.25–0.5 μm [Figure 2.10(b)]. Laths are contained within the prior-austenite grain boundaries, and they still contain a relatively high dislocation density (10^{13}–10^{14} m^{-2}), depending on the tempering conditions [88]. The dominant precipitates are large (60–150 nm) $M_{23}C_6$ particles that are mainly on lath boundaries and prior-austenite grain boundaries [891]. If V and Nb are present in the composition, there will also be a fine distribution of small (20–80 nm) MX particles that have generally been concluded to be vanadium nitrides and/or niobium/tantalum carbonitrides, depending on the composition [90]. Small amounts of M_2X (a high chromium, high-nitrogen precipitate) are also found in some cases. The $M_{23}C_6$ helps stabilize the lath boundaries during elevated-temperature exposure, and the MX particles pin the dislocations, both processes helping to retard recovery. For RAFM steels, the Nb is replaced by Ta in MX and M_2X types precipitates [23].

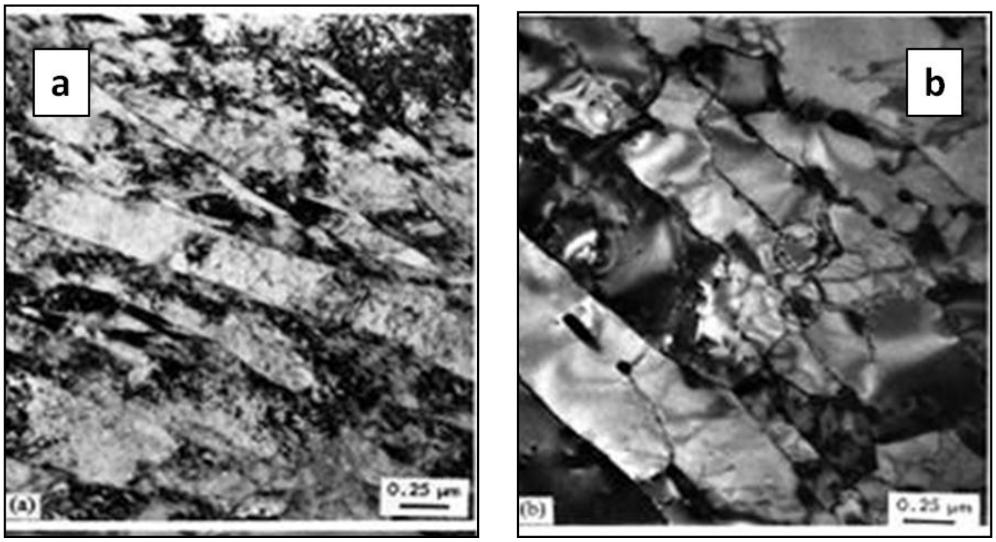

Fig. 2.10: TEM images of 12Cr-1MoVW (HT9) steel in (a) normalized and (b) normalized-and-tempered conditions [79].

2.5.3. Effect of Elevated Temperature on Microstructure

Significant microstructural changes of the 9–12% Cr ferritic/martensitic steels occur when exposed to elevated temperatures during service, thermal aging, or in a creep test at typical service temperatures of 550–650ºC, with the of rate changes increasing with increasing temperature [91]. Elevated-temperature exposure causes a reduction in the dislocation density, with the reduction generally greater during a creep test than for thermal aging without a stress [92]. Along with the reduction in dislocation density, the $M_{23}C_6$ particles coarsen, allowing the martensite laths to transform to more equiaxed sub-grains, with the sub-grains being fully recovered in a crept specimen after about 30,000 h at 600ºC [79]. Along with the coarsening of the $M_{23}C_6$, there is also a coarsening in the MX precipitate distribution, although these particles coarsen much more slowly than $M_{23}C_6$. During coarsening, changes occur in the composition of the M (e.g., enrichment in chromium in the $M_{23}C_6$, etc.) in the precipitates as equilibrium is approached [93]. In addition to the coarsening of $M_{23}C_6$ and MX, another important effect of elevated temperature exposure is the formation of Laves phase, $(FeCr)_2(Mo,W)$ [94]. Laves phase forms during thermal aging and creep, and at 600ºC and above, it quickly coarsens, with the coarsening proceeding more quickly under stress [95]. Laves phase formation is important because it removes the solid-solution strengthening elements tungsten and molybdenum from solution. Thus, elevated-temperature exposure pushes the evolution of the microstructure toward equilibrium, which will consist of large, relatively equiaxed sub-grains within the prior austenite grain boundaries. The interior of the sub-grains will contain a very low dislocation density [96]. This general microstructural evolution applies to all 9–12% Cr-Mo-W-V steels containing small amounts of Nb, B, N, etc.

2.5.4. Effect of Composition on Microstructure

Although the overall microstructures of the 9–12% Cr steels are quite similar for most compositions that have been developed, it is the compositional changes made over the years that have resulted in the improved properties. Generally, the developers of the new steels have used modified 9Cr-1Mo, T91 (9Cr-1MoVNb), as a benchmark for comparison [84].

a. Carbon and Nitrogen

Carbon and nitrogen are strong austenite stabilizers with a relatively large solubility in austenite. They have a very small solubility in ferrite, which gives rise to the formation of carbides, nitrides, and carbonitrides [79].

b. Effect of Chromium

Chromium is a ferrite-stabilizing element that is generally added to steels for oxidation and corrosion resistance. It provides slight solid-solution strengthening when added to iron [97]. Chromium reacts with carbon to form carbides; the chromium-rich carbides usually encountered in the 2–12% Cr steels are M_7C_3 and $M_{23}C_6$. The latter carbide dominates in the 9–12% Cr steels; it forms during tempering and remains present throughout the elevated-temperature exposure [89].

c. Effect of Tungsten and Molybdenum

In developing steels beyond T91, tungsten was added to the modified 9Cr-1Mo composition (E911, HCM12) or substituted for part of the molybdenum (NF616, T23, TB12) [98]. Independent of the above work and at about the same time, molybdenum was replaced by tungsten for nuclear considerations in the development of reduced-activation steels for fusion applications [51]. In this case, tungsten was a natural choice to replace molybdenum because it was in the same column of the periodic Table and behaved similarly in steel (formed similar-type carbides, etc.). Molybdenum and tungsten are ferrite stabilizers, and depending on other ferrite stabilizers (i.e., Cr, V, Si, Nb) and austenite stabilizers (i.e., C, N, Ni, Co, and Cu) present in steel, the amount must be limited to avoid δ-ferrite [99]. In the tempered condition, Mo and W are distributed between the solid solution and also incorporated in the $M_{23}C_6$ and MX. The two elements provide relatively high solid-solution strengthening of iron [79]. ***Tungsten diffuses more slowly than molybdenum, which slows recovery and Laves precipitation processes*** [100]. The elements generally do not form carbides or nitrides in the 9–12% Cr steels, although M_2C (Mo_2C or W_2C) does form in low-chromium steels (e.g., Mo_2C in 2¼Cr-1Mo) [101]. A molybdenum equivalent, Moeq, defined as Mo+0.5W (concentrations in wt. %) in solid solution, has been established, and because of Laves precipitation, it has been stated that at equilibrium the Moeq cannot be expected to exceed 1% [79].

d. Effect of Vanadium, Niobium, and Tantalum

Vanadium and niobium are strong carbide, nitride, and carbonitride formers, and in the 9–12 %Cr steels, they are expected to form MX, where V and Nb are enriched in the M, and X is either carbon, nitrogen, or a combination of the two, resulting in carbides (MC), nitrides (MN), or carbonitrides [M(C, N)] [89, 102]. At one time it was believed that strengthening by vanadium was caused by the formation of vanadium carbide. More recent work indicated that the vanadium-rich MX is rich in nitrogen [79]. Niobium carbides are extremely stable, and it is necessary to heat to temperatures beyond normal austenitizing temperatures for them to dissolve completely. However, undissolved niobium carbides restrict grain growth during austenitization, thus producing a refined prior-austenite grain size relative to steel without niobium [89]. *Tantalum is generally expected to behave like niobium. However, TEM analyses indicated that for the normalized-and-tempered 9Cr-2WVTa steel, 75– 90% of the tantalum unexpectedly remained in solution after normalization* [103]. Nevertheless, the tantalum does produce austenite grain refinement, similar to what is observed for niobium-containing steels [104].

2.6. The modified 9Cr-1Mo steel (P91)

In order to achieve the dual-phase ferritic-martensitic (F/M) structure as compared to the fully martensitic steels; the carbon content in F/M steels was reduced and other compensating minor elements were added. The phase diagram of low C Fe-Cr system is shown in Figure 2.11[105]. Compared with the Fe-Cr-C diagram, in low-C Fe-Cr- 2Mo system, the ($\alpha + \gamma$) region shifts to lower Cr concentration [106]. This is also affected by the C content. Therefore, it would be easier to get dual phases in low-C 9Cr-2Mo steels than in 9Cr-1Mo steel [107]. Nevertheless if the niobium content is higher and (carbon + nitrogen) content is lower, in that case dual phases are observed even in 9Cr-1Mo system [106]. The microstructure of dual-phase steels actually consists of tempered martensite and δ ferrite. Both fine carbides $M_{23}C_6$ and MC are observed in martensitegrains and much less carbides are observed in ferrite grains. In the martensite phase, the dislocation density is very high, but dislocation density is lower in ferritic phases [106-109].

The modified 9Cr—1Mo steel or P91 was developed by increasing the nitrogen content of the basic 9Cr-1Mo (P9) composition and adding small amounts of vanadium (V) and niobium (Nb) [110]. The composition of both type of steels i.e. P9 and P91; is shown in Table 2.7.The optical microstructures of the P9 and P91 steels shown in Figures 2.12 (a) and (b) reveal tempered martensite structure. The Transmission Electron Microscope (TEM) micrographs, Fig. 2.12(c) and (d), show the precipitates formed after tempering. Energy Dispersive X-ray Spectroscopy (EDS) analysis showed that both P9 and P91 have $M_{23}C_6$precipitates on grain and lath boundaries, while P91 contained in addition MX particles inside the grains that were rich in V and/or Nb [106].

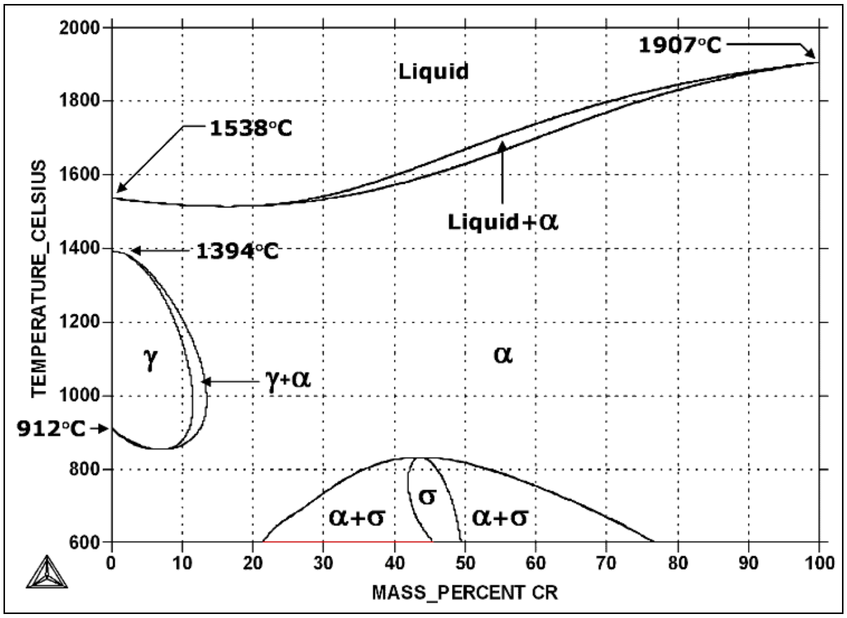

Fig. 2.11: The iron chromium phase diagram [105].

Table 2.7: Composition of P9 and P91steel [110].

	C	Si	Mn	Cr	Mo	V	Nb	Ni
P9 (9Cr-1Mo)	0.07	0.26	0.35	8.24	0.95	-	-	-
P91 (modified 9Cr-1Mo)	0.08	0.5	0.39	9.4	1.0	0.25	0.09	0.13

2.7. Reduced Activation Ferritic Martensitic Steels (RAFMS)

One of the main technological requirements for the fabrication of blanket components is the development and qualification of structural materials which would be able to withstand severe conditions comprising of 14MeV neutrons, neutral and charged plasma particles, high surface heat flux and very strong magnetic fields [111]. Although the conventional 9Cr–1Mo Ferritic–martensitic steels and its variants meet most of the requirements for applications below 773 K in liquid metal cooled fast fission reactors; the development of fusion power plants has put forward a demand to for superior grades of steels, which are not only resistant to neutron irradiation of higher energy but also pose a reduced hazard from the induced radioactivity arising due to transmutation reactions [16]. This has led to an extensive research and development program worldwide on fusion reactor materials leading to the development of low or Reduced Activation Ferritic– Martensitic steels (RAFM) [51].

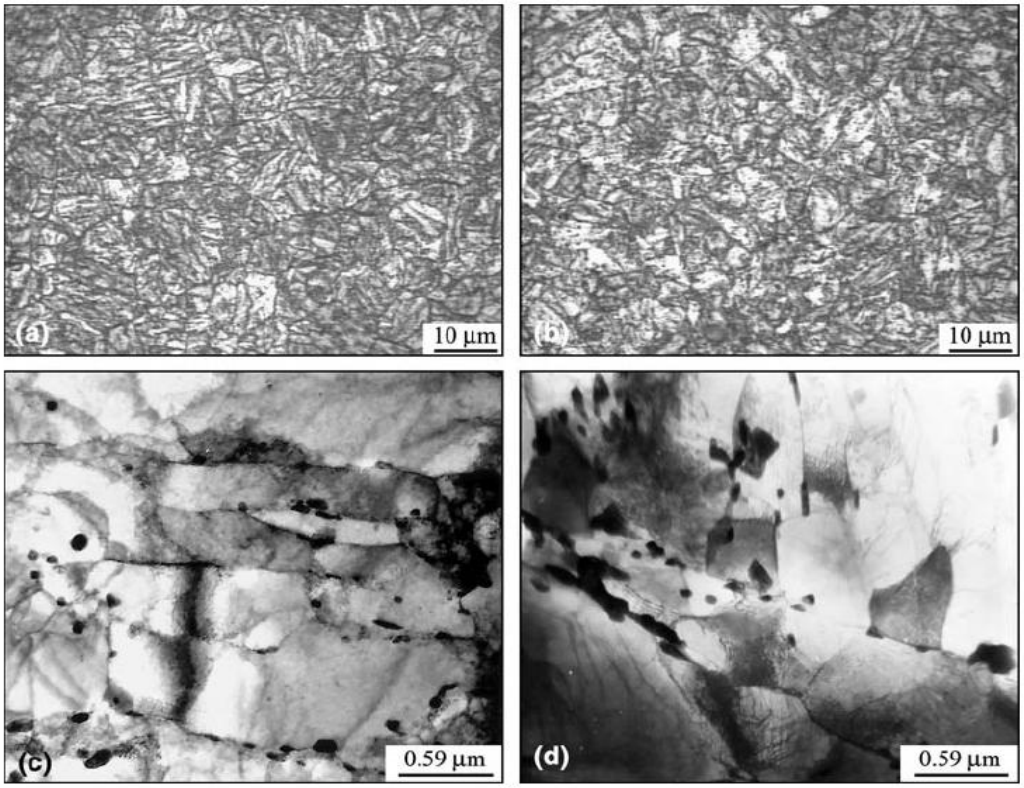

Fig. 2.12: Optical Micrographs of (a) P9, (b) P91 and TEM images of (c) P9 and (d) P91 [110].

The design principles for the RAFM steels are essentially same as that of conventional 9Cr–1Mo steel, but with a major difference with respect to elements producing long half-life transmutation products like Ni, Mo, Nb, Cu, Co, Al, N, etc [112]. These elements are largely substituted by their comparatively lower activation counterparts, such as Mn, W, V, Ta, and C, so that the RAFM steel at the end of its useful lifespan of about 100 years can be safely handled after a shorter cooling period, rather than a cooling time of over 1000 years, which would have been the case with conventional Cr–Mo–Ni–Nb containing ferritic/martensitic steels [113].

Different varieties of RAFM steel are now being developed around the world particularly in the countries participating in ITER [21, 114]. These steels have now achieved technology maturity with respect to fabrication routes, welding technology and general industrial experience. The temperature range for use of RAFM steels is presently about 623–823 K, the lower value being limited by irradiation-induced embrittlement effects and the upper value by a strong reduction in mechanical strength [56]. Notable among the different kinds of RAFM steels developed include the Japanese F82H steel and JLF-1 steel, the European EUROFER-97 steel, the Chinese low activation martensitic (CLAM) steel and the ORNL 9Cr–2WVTa steel developed in ORNL, USA [22, 92, 114, 115, 116,]. India has also proposed is own specific RAFM steel called as the Indian RAFMS which matches quite closely in composition to EUROFER 97 [B. Raj et al., 2011]. The composition of these steels wt% has been already given Table 2.2.

2.8 The Indian RAFM steel

In order to develop the India specific RAFM steel; four heats of the 9Cr–W–Ta–0.2V RAFM steel having the combinations of tungsten and tantalum contents as 1 wt% tungsten with 0.06 wt% tantalum, 1.4 wt% tungsten with 0.06 wt% tantalum, 2 wt% tungsten with 0.06 wt% tantalum, and 1 wt% tungsten with 0.14 wt% tantalum have been initially produced [B. Raj et al., 2010, S. Saroja et al., 2011]. These steels are designated as 1W–0.06Ta, 1.4W–0.06Ta, 2W–0.06Ta and 1W–0.14Ta respectively, based on their tungsten and tantalum contents [117].

Chemical compositions of the four steels are shown in Table 2.8. The steels were produced by selection of proper raw materials and employing vacuum induction melting and vacuum arc refining routes with stringent control over the thermo-mechanical processing parameters during forging, rolling and heat treatment [24,117]. Strict control has also been exercised on the amount of radioactive tramp elements (Mo, Nb, B, Cu, Ni, Al, Co and Ti) and on the elements that promote embrittlement (S, P, As, Sb, Sn, Zr and O). These elements have been restricted to ppm levels, as given in Table 2.8.

Based on the detailed mechanical properties evaluation of these RAFM steels having tungsten content in the range 1–2 wt.% and tantalum content in the range 0.06–0.14 wt.%, the chemical composition of India-specific RAFM steel has been established as 9Cr–1.4W–0.06Ta–V, having optimum combination of strength and toughness and is designated as Indian Reduced Activation Ferritic Martensitic (IN RAFM) steel [24].

In 2010, the fresh batch of IN RAFM steel (9Cr–1.4W–0.06Ta), meeting the stringent chemical composition requirements with respect to radiologically undesirable elements as well as trace and tramp elements, was produced by vacuum induction melting followed by vacuum are refining [23]. Detailed investigations on the microstructure, including thermodynamic and kinetic features of phase transformations, and tensile, creep and ductile–brittle transition behavior of this steel indicate that the Indian RAFMS has the required microstructure, phase stability, creep rupture strength, elevated temperature tensile strength as well as low ductile-to-brittle transition temperature for fusion reactor/TBM applications [25, 118].

The optimum combination of normalizing and tempering heat treatment for Indian RAFMS were arrived at based on the variation of prior austenite grain size and hardness with austenitising heat treatment temperature and with duration of tempering heat treatment [23]. The comparison of the heat treatment schedule of IN RAFMS with EUROFER-97 material has been shown in Table 2.9. The optical micrograph of the normalized and tempered IN RAFM steel (Fig. 2.13(a)) show a tempered martensite structure [23,117]. TEM analysis reveals the formation of lath structure with precipitation of carbides onlath boundaries and within the laths (Fig. 2.13(b)) [23,117]. The coarse carbides present on the lath boundaries were identified as$M_{23}C_6$ by electron diffraction. These carbides are rich in chromium with a large solubility for tungsten. Using a combination of electron diffraction and energy dispersive analysis of X-rays, the fine carbides on the dislocations inside the laths have been identified as tantalum- and vanadium-rich MX type of precipitates.

Table 2.8: Major constituents of the first heats of RAFM steels produced in India [24].

Steel/Alloying Elements	1W-0.06Ta	1.4W-0.06Ta	2W-0.06Ta	1W-0.14Ta
Cr	9.04	9.03	8.99	9.13
C	0.08	0.126	0.12	0.12
Mn	0.55	0.56	0.65	0.57
V	0.22	0.24	0.24	0.22
Ta	0.06	0.06	0.06	0.135
N	0.02	0.03	0.02	0.03
Si	0.06	0.06	0.06	0.06

Table 2.9:- Heat Treatment of Ferritic/Martensitic steels [23, 115].

	EUROFER	**IN RAFMS**	**P91**
Normalizing	1255 K/27 min /air cooling	1325K/15 min air cooling	1315K/40 min air cooling
Tempering	1035 K/1.5 h/ air cooling	1035 K/45 min air cooling	1015 K/ 2 h air cooling.

The ductile-to-brittle transition temperature (DBTT) estimated on the basis of 68 joule criterion was found to be below 203 K, as has been also reported for EUROFER 97 [25]. The Yield Strength (YS) and Ultimate Tensile Strength (UTS) of the Indian RAFM steel are comparable to those of EUROFER 97 and F82H steels as shown in Figure 2.14. Both the YS and UTS have been found to decrease with increase in temperature, with the rate of decrease being slower in the intermediate temperature range of 450–650 K [117]. Creep properties of the pilot scale RAFM steel studied in air over a wide stress range at 773 K, 823K and 873 K, showed creep rupture strength comparable to EUROFER 97 steel. However, the Indian RAFM material has creep rupture strength lower than that of Grade 91 ferritic steel [24,118].

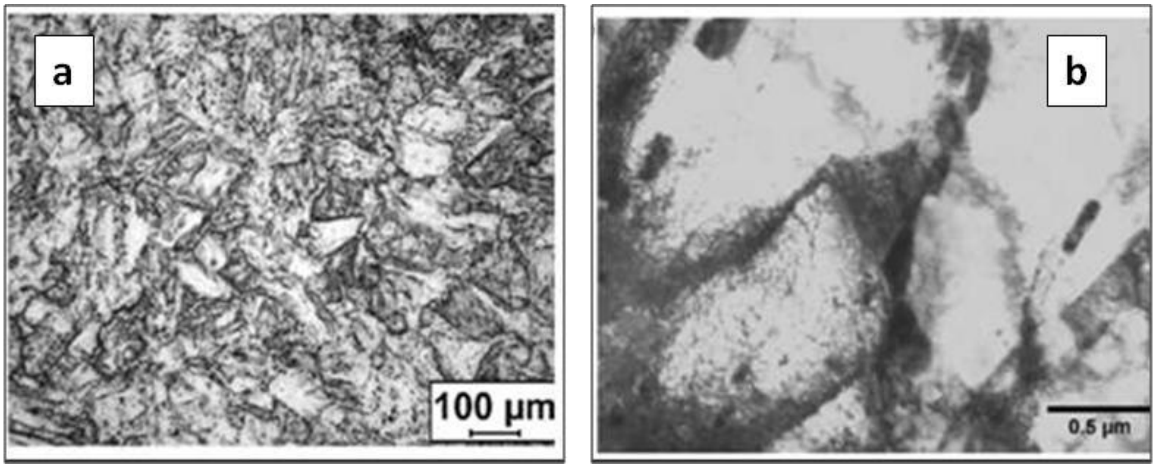

Fig 2.13: Microstructure of 1253 K/2 h normalized and 1033 K/30 min tempered IN RAFMS (a) optical micrograph showing tempered martensitic structure; and (b) TEM micrograph showing lath structure with coarse intra- and inter-lath carbides [117].

2.9. Liquid Metal Corrosion

Corrosion has been defined by U. R. Evans' as "destruction of metal by chemical or electrochemical action"; a familiar example being the rusting of iron [119]. Thus, corrosion by this definition denotes the transfer of electrons. But this is not usually the case in liquid metal attack, and, therefore, to define "the destruction of a solid metal by a liquid metal" as corrosion, the above definition must be broadened in order to allow for the solution or solubility of a solid metal in a liquid metal wherein ***no transfer of electrons is involved*** **[**120]. Compared with corrosion by aqueous solution which is known as an electro-chemical process, the corrosion by liquid metal does not involve electron transfer in the liquid and can be recognized as a physical–chemical process [121].

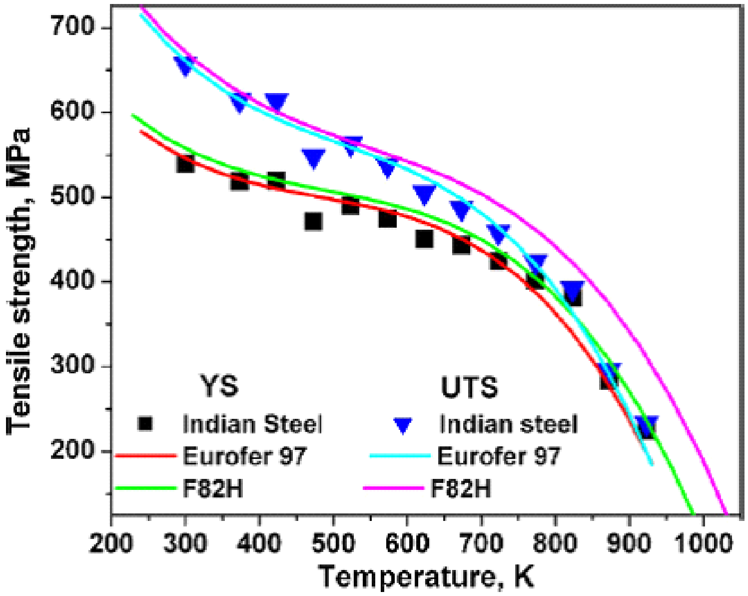

Fig 2.14: Variation of Yield strength and Tensile strength of IN RAFMS, EUROFER 97 and F82H steels with temperature [22].

Liquid-metal corrosion in most cases simply depends on the difference in chemical potential (concentration gradient) between the solid and liquid and the extent of solubility of the solid metal in the liquid metal. However, many other factors **[**120] can influence the solution rate or the attainment of the solubility like:-

- Temperature.
- Temperature gradients and cyclic temperature fluctuations.
- Surface area to volume ratio.
- Flow velocity or Reynolds number.

- Number of materials in contact with the same liquid metal.
- Formation of surface intermetallic compounds and oxide or nitride films
- Impurities in the liquid metals which can increase the solution rate.

Concentration gradient—In order to attain equilibrium in a multicomponent, multiphase system; the chemical potential of each component in any given phase has to be equal to its chemical potential in every other phase. A redistribution of the components between the phases of the system thus tends to occur creating dissolution of solid metals into liquid metals until their **solubility limit** at a particular temperature is reached. The driving force for this process, thus, is associated with the equalization of the chemical potentials, which results in a decrease of the free energy of the system [122].

Temperature is one of the most important variables, because the higher the temperature the higher the solubility of the solid metal in the liquid metal [123]. Also, as the temperature increases, diffusion rates increase, which is quite important in certain types of liquid-metal corrosion. When a **temperature gradient** exists in a liquid metal system, the difference in solubility of the dissolved metal in the liquid metal in the hot and cold parts of the system gives rise to temperature gradient mass transfer **[**120]. Thus, at the high temperature, material goes into solution and subsequently at the lower temperature comes out of solution and precipitates in the bulk liquid, or forms dendrites, or forms a uniform layer on the container wall.

The flow velocity, or Reynolds number, is only important in a closed loop; where in a decrease in the thickness of the lamellar layer in the flow channel occurs as the flow velocity increases [124]. Thus, when metal atoms pass from the hot region to the cold region of the loop, the diffusion paths between channel wall and bulk liquid are shorter.

The **ratio of the exposed metallic surface area to the volume of liquid metal** is a controlling factor in the amount of corrosion experienced in a solid metal container in a static system since the metal will corrode sufficiently to saturate the liquid metal at the operating temperature; therefore, as the ratio of surface area to volume decreases, the amount of corrosion increases [125].

Purity of the liquid metal can have quite an effect on the rate at which the solubility limit is reached and can markedly affect the wetting tendency of the liquid metal on the solid metal [126].

When two or more solid metals are in contact with a liquid metal, the phenomenon of **dissimilar metal mass transfer**, or concentration mass transfer, should be considered even when the temperature is constant [127].

2.9.1. Types of Liquid Metal Corrosion

In all liquid-metal corrosion tests, these variables must be considered and controlled to obtain information that will be useful in the over-all understanding of the suitability of solid metals as containers for various liquid metals. Depending on the presence or absence of the above factors, various kinds of liquid metal corrosion is defined:

a. Simple solution type attack

In the case of a pure metal, solution type attack will lead to the even removal of metal from the surface till the liquid is saturated. In the case of an alloy the attack can also be a simple solution type similar to the decarburizing action of lithium over type 430 stainless steel after 40 h at 1000 °C as shown in the Figure 2.15 [120]. If all the phase diagrams of liquid-metal-solid metal systems were available, an ascertainment could be made of the depth of attack that would occur in a static system as a result of simple solution by examining the solubility limit of the solid metal in the liquid metal at the operating temperature. However, there would be no idea about the rate at which the solubility limit was achieved since it can be influenced greatly by other variables, such as impurities in the system.

b. Attack due to alloying

In order to form an alloy between the liquid and solid metal; there must be some solubility of the liquid metal in the solid metal. The Ag-Pb system is an example in which the liquid metal is soluble in the solid metal which is observed from the phase diagram shown in Figure 2.16 (a). In some experiments the liquid metal dissolves considerably in the solid metal with the formation of an intermetallic compound [122]. When SS 446 was tested in lead at 1000°C, it is found that after 400 h lead has diffused into the alloy predominantly at the grain boundaries and has formed a compound (Fig. 2.16 (b)).

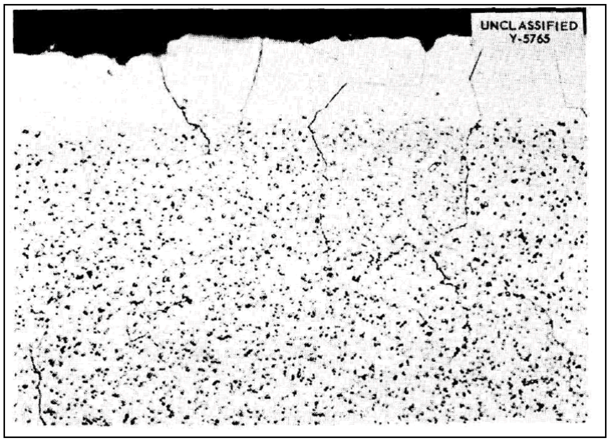

Fig 2.15: Decarburizing by lithium over type 430 stainless steel after 40 h at 1000 °C [20].

c. Attack due to selective leaching

One of the more serious types of liquid metal corrosion that can occur is the deep intergranular penetration brought about by the removal of one constituent from an alloy. The selective removal of nickel from a 75% Ni-25% Mo alloy also occurred in a sample from the hot leg of a thermal-convection loop which operated for 200 hr with lead at 800 °C and with a 300 °C temperature gradient (Fig. 2.17). In this case the nickel was preferentially removed from the hot zone and deposited in the cold zone of the Loop.

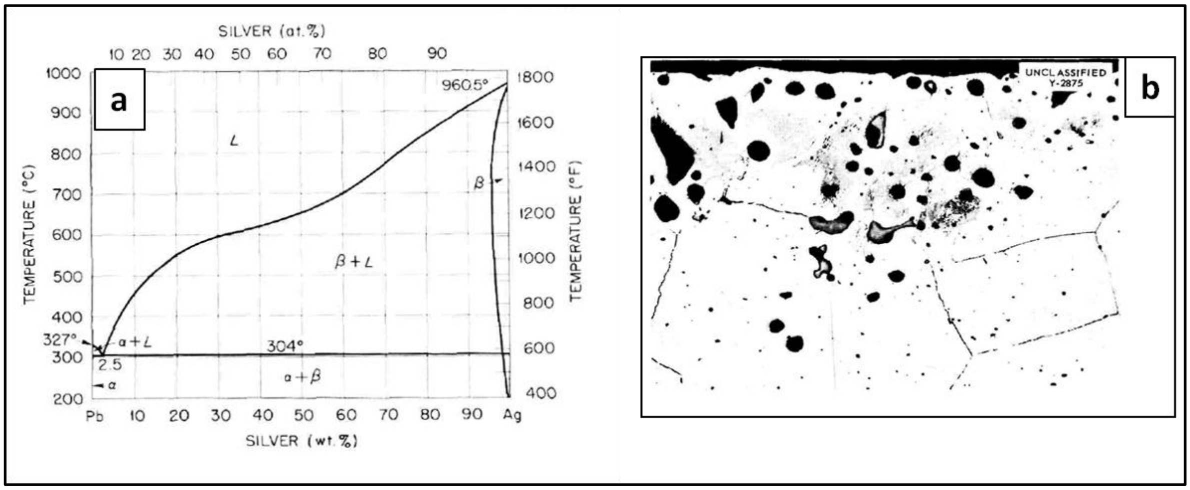

Fig 2.16: (a) The Ag-Pb phase diagram and (b) Diffusion of lead in the grain boundaries of SS 446 when tested at 1000 °C for 400 h [120].

d. Liquid metal corrosion due to the presence of impurities

In liquid metals, impurities, such as oxygen, nitrogen, and carbon, can have an appreciable effect upon the rate of attack, and in some cases the whole mode of attack can be changed because of the effect of the impurity on the surface tension or because of the reactivity of the impurity [126]. For e.g. a shallow attack is produced by pure lithium in SS316L steel wall at 800^{o}C in 100 h **[**120]. However, if the lithium is contaminated with a small quantity of nitrogen, the complete tube wall will be penetrated by the lithium during the same type of test. This is due to the fact that nitrogen-contaminated lithium reacts with the carbides that form the grain boundary network when the testing temperature was above the solution temperature of the carbides **[**20]

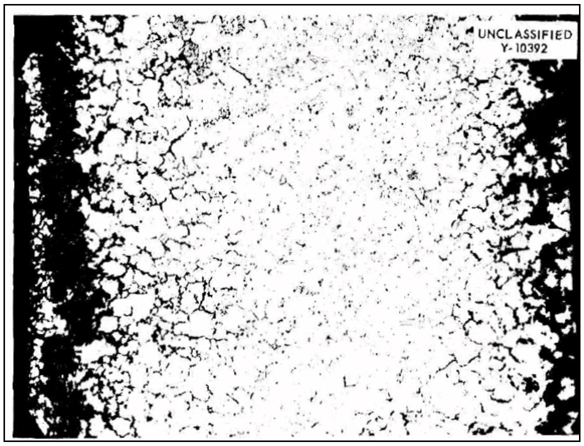

Fig. 2.17: Selective removal of Ni from 75% Ni-25% Mo alloy in lead thermal-convection loop [120].

e. Temperature gradient mass transfer

The most damaging type of corrosion is the temperature gradient mass transfer. This is of great significance in nuclear reactor systems where the coolant flows in a closed loop having a temperature gradient between the zones closer to the reactor core and those outside the core. The removal of a slight amount of material will not cause a large variation in the liquid metal/alloy properties. However, precipitation of this removed material will cause chocking of the cooler regions like heat exchanger and complete cessation of flow. The driving force for temperature gradient mass transfer is the difference in solubility of the dissolved metal in the liquid alloy at two different temperature extremes of the flowing system [128]. The various steps through which metallic atoms go through during temperature gradient mass transfer are shown in Figure 2.18.

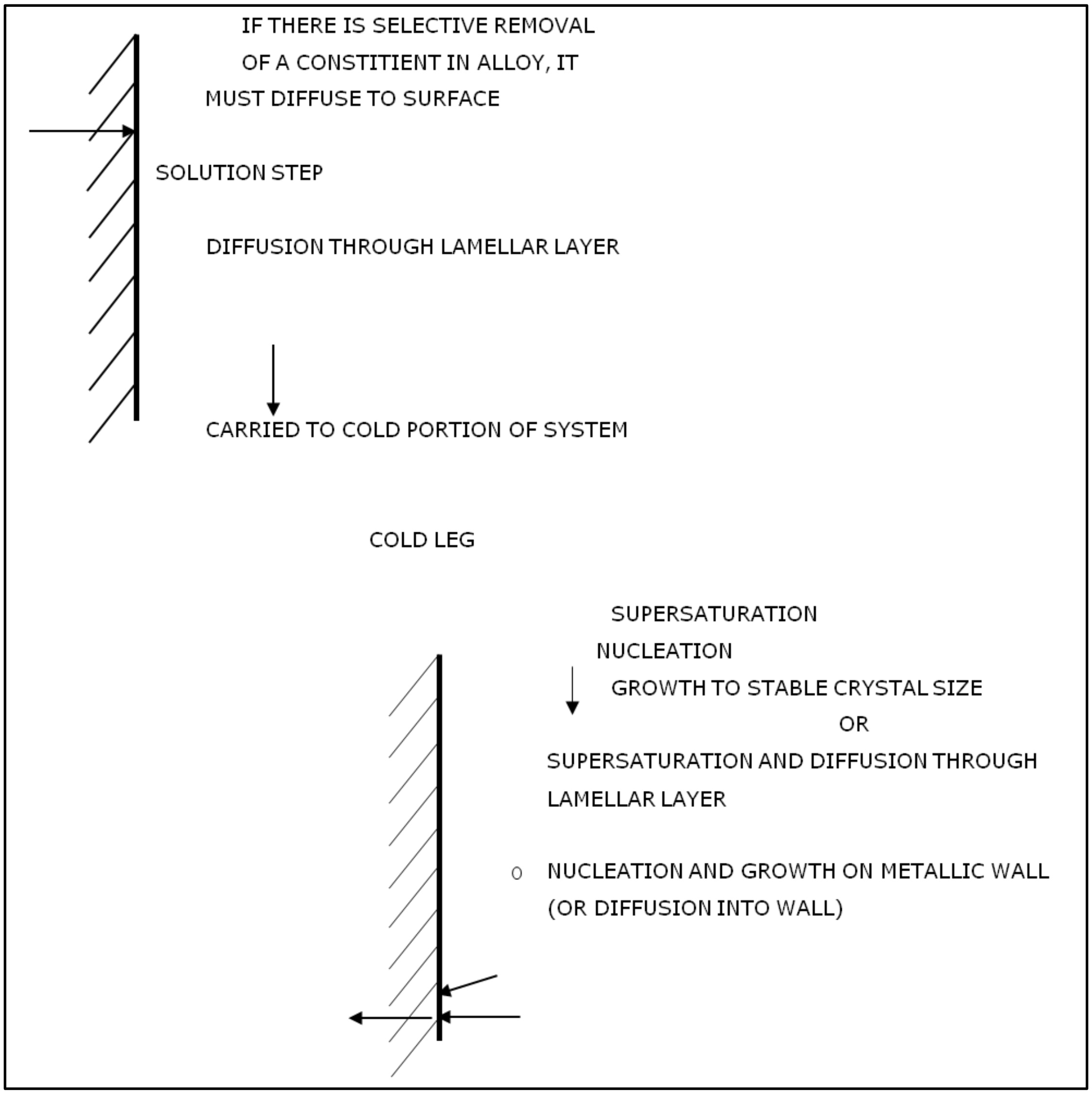

Fig: 2. 18: Various steps in Temperature Gradient Mass Transfer [120].

f. Dissimilar metal mass transfer dissimilar-metal mass transfer or concentration-gradient mass transfer

A schematic view of the manner in which dissimilar-metal mass transfer takes place is seen in Figure 2.19**.** In this case atoms of metal A go into solution and move to the surface of metal B either by diffusion and/or by movement of the liquid. On reaching the surface of metal B they come out of solution, alloy with metal B**,** and diffuse inward. The driving force for dissimilar-metal transfer is the decrease in the free energy that is achieved through the alloying of the two metals [127]. The greater the difference in the chemical potentials of A in the two solid phases, the greater will be the driving force for the occurrence of mass transfer. The rate of mass transfer is dependent on the temperature since an increase in temperature will increase the diffusion rate in both the liquid and the solid phases. When a molybdenum sample was being tested in sodium contained in a nickel crucible at ORNL; it was observed after 100 h at 1000 °C that a sufficient quantity of nickel had transferred through the sodium and deposited and alloyed on the molybdenum surface to produce the Ni-Mo intermetallic as shown in Figure 2.10.

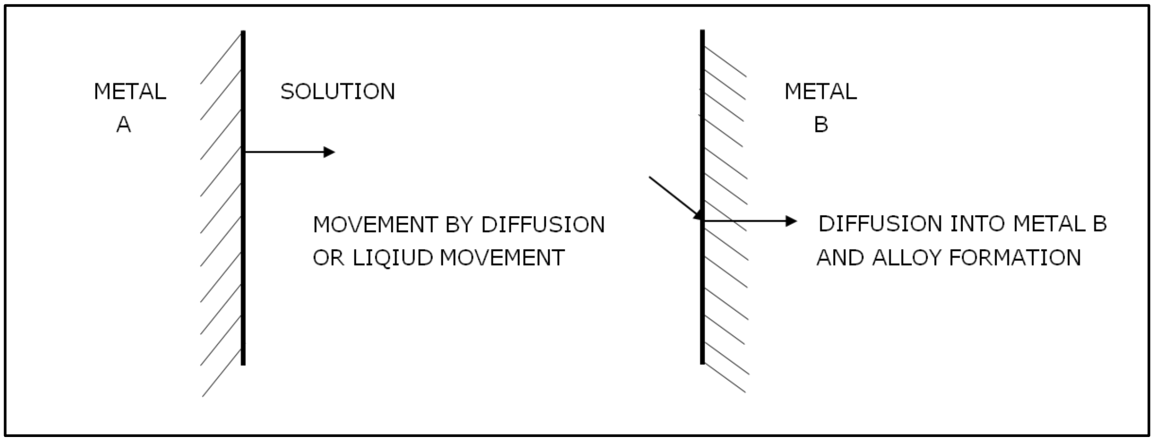

Fig. 2.19: Schematic view of the mechanism of Dissimilar Metal or Concentration gradient Mass Transfer [120].

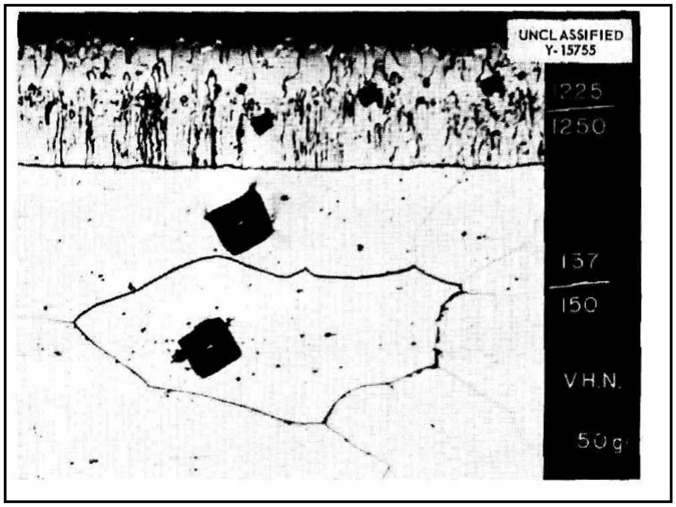

Fig. 2.20: lnter-alloying Between Molybdenum and Nickel by Dissimilar Mass Transfer after 100 h at 1000 °C [120].

2.9.2 .Mechanism of Liquid metal/alloy corrosion in nuclear reactor systems

Liquid metal corrosion is one of the key factors that have to be considered when using liquid metal as a heat transfer medium such as the primary coolant in advanced nuclear reactors [120-130]. The processes can be simply shown as in Fig. 2.21 which describes three significant steps:

(1) Transport in the solid (metal or alloy),

(2) Dissolution of the steel constituents into the liquid, or mass exchange at the solid/liquid interface, and

(3) Transport of the corrosion products and impurities in the liquid.

The first step is governed by the movability of mass in the solid materials, and the second step is governed by dissolution/chemical reactions at the liquid/solid interface, while the third step is controlled by both mass convection and diffusion in the liquid.

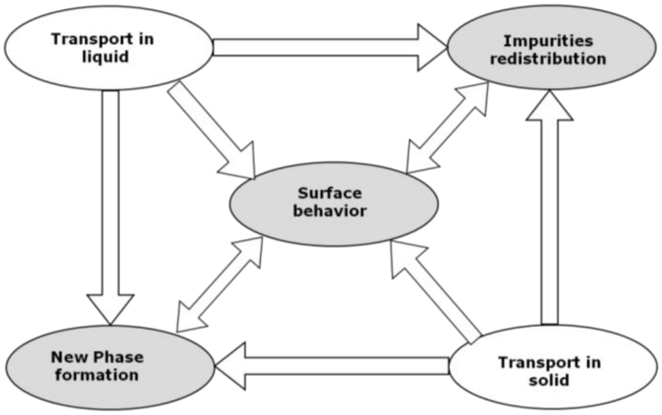

Fig 2.21: Simple view of liquid metal corrosion process in nuclear reactor system [131].

The transport processes in liquid and solid are coupled with each other at solid/liquid interface through mass exchange. The overall mass transfer has been classified into two categories [132]:-

1. *Concentration Gradient or Dissimilar metal mass transfer*: due to the thermodynamic requirement that all element chemical potentials should be equivalent in all phases

2. *Thermal gradient mass transfer*: due to the temperature dependent solubility in the liquid of all corrosion products.

In an ***isothermal liquid metal closed loop system***, the corrosion may finally stop because of saturation of the corrosion products, while in a ***non-isothermal system such as the primary coolant loop system*** of a nuclear reactor, the final state is a kinetic equilibrium in which the amount of corrosion is balanced by the amount of the precipitation all through the loop. It is the precipitation that sustains the corrosion in a non-isothermal liquid metal loop [133]. The precipitating corrosion product may be in the form of layers tightly adhering on the pipe wall or particles suspending in the liquid [134]. In the second case, the two phase flow with solid particles may result in mechanical erosion which can damage the structural materials seriously.

2.9.2. a. Surface Recession or Wall thinning: - Liquid metal corrosion may or may not result in surface recession of structural materials, depending on the transport of corrosion product in the solid and liquid phases, and the dissolution reaction at the interface. Corrosion is grossly governed by the **mass transfer rate in the liquid or the dissolution rate (reaction rate) at the interface**. If the corrosion rate is controlled by mass transfer rate, it is called as ***Mass transfer controlled corrosion,*** and for the other case, it is called as ***Activation controlled or dissolution controlled corrosion*** [131**].** The slower among the two controls the overall corrosion rate. If the diffusion rate in the solid is fast enough to balance the mass transfer rate in liquid, there will be no surface recession. However, such ideal case does not occur in a practical system because the diffusion in the solid phase is always the slowest process.

2.9.2. b. Role of Oxygen in Lead –bismuth and Lead –lithium systems: -Liquid metal corrosion not only depends on the liquid metal itself and but also on the impurities present in it. If liquid lead or lead–bismuth is selected as the primary coolant of a nuclear reactor, then oxygen is added deliberately into it to serve as a protective method for mitigating the corrosion of structural materials. The oxygen concentration in the liquid is controlled in a certain range in order to form a protective oxide layer on structural material surfaces and to avoid the precipitation of the lead oxide from the liquid [135-136]. Under low oxygen conditions (below the controlled range); the amount of solid oxides formed over the structural material is too small in order to form a continuous protective layer whereas under high oxygen conditions; lead and bismuth starts to oxide creating chocking possibilities although the steel surface is protected by a continuous oxide layer. Thus there is a transition zone in the oxygen potential in lead/ lead bismuth which is the ideal condition for preventing liquid metal corrosion as well as oxidation as shown in the Figure 2.22 [137].

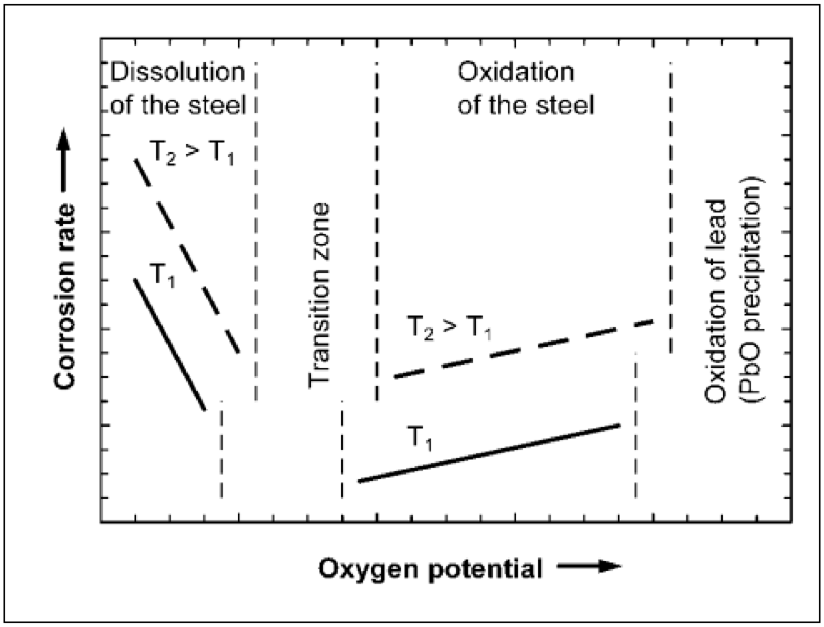

Fig. 2.22: Transition zone in the oxygen potential in lead/ lead bismuth showing ideal condition for preventing liquid metal corrosion [137].

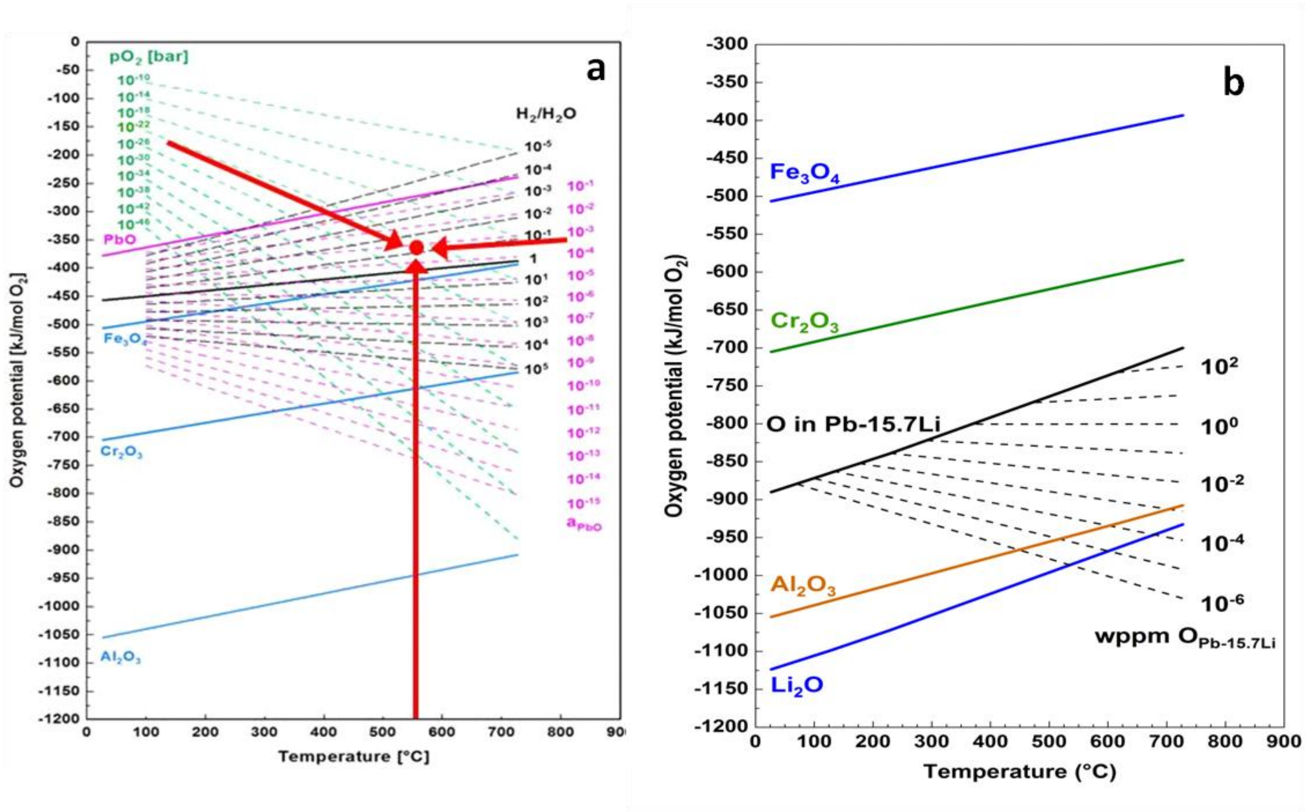

Fig. 2.23: Ellingham diagram for oxides of iron, chromium and aluminum showing the position of (a) Lead oxide and (b) Lithium oxide [138].

However; this approach does not hold true for liquid lead lithium systems. From the Ellingham diagrams of various metallic oxides shown in Fig 2.23 (a) and (b); it is clear that the oxides of major steel elements like iron and chromium are much more stable than lead oxide at 500 °C to 600 °C (Fig 2.23 (a)). The line for bismuth oxide lies quite close to that of lead oxide and thus behaves similarly. Therefore when oxygen is introduced in a Pb-Bi system; the steel will oxidize much earlier than lead or bismuth and thus the steel will be protected from liquid metal corrosion [135].

However; in case of lead lithium eutectic; the oxidation tendency of lithium is much greater than iron or chromium oxides as shown in Fig 2.23 (b). Therefore even the slightest oxygen introduced into the system will lead to oxidation of Li while the steel surface would remain available for liquid metal corrosion [138]. Oxidation of Li would lead to a shift in the Pb-Li composition leading to a change in melting point and also cause segregation of solid lithium oxide having high melting point. Thus, oxygen needs to avoid in the lead lithium system. The position of aluminum oxides has been indicated in both the above diagrams in order to indicate the stability of the proposed Al_2O_3 coatings for corrosion resistance. It could be seen clearly that at very pure Pb-Li (dissolved oxygen $< 10^{-6}$ wppm), even aluminum oxide will be attacked by Pb-Li at >450°C, but never iron and/or chromium oxide [139]

2.9.2. c. Liquid Metal Corrosion in a dynamic system.

Characteristics of the system: - Conventionally, the characteristics of hydrodynamic system are defined by dimensionless numbers like Reynolds number, Scmidts number and Sherwood number. The **Reynolds number** expresses the ratio of inertial forces acting of the liquid to the viscous forces as given in equation 2.6.

$Re = v.d/\nu$ …………………………………………..…………………………………. 2.6

Where v is the flow velocity (m/s), d is the characteristic length/ hydraulic diameter (m) and ν is the dynamic viscosity of the system (m^2/s) [140]. For velocities lower than a critical value (Re_{crit}); the flow remains laminar while otherwise the flow becomes turbulent. The critical value is defined by the nature of the corrosion system (rotating disc; rotating cylinder; pipe flow etc) [141]. In case of a turbulent flow; various regimes of velocity distribution may occur inside a test system:-

a. A thin laminar sub-layer of thickness δ_h resulting from viscous drag is present close to the pipe surface where the flow is laminar.

b. A diffusion boundary layer of thickness “δ_d” across which there exists a concentration gradient if mass transport occurs.

c. A buffer layer between diffusion boundary layer and turbulent zone.

d. A fully turbulent region where highest velocities are obtained.

The relationship between the thickness of laminar boundary layer and the diffusion boundary layer is given by the **Schmidt number** and expressed by Equation 2.7.

$S_c = \nu/D$ …………………………………………..…………………………………... 2.7

where D is the diffusion coefficient of the relevant species (m^2/s).The higher the value of S_c, the thinner will be the diffusion layer and the faster will be its formation [140].

Mass transfer is the process of transporting material from a surface to the bulk of a flowing fluid. The overall transport to the surface consists of diffusion at the interface solid–liquid and bulk convection. The mass transfer rate can be expressed according to Equation 2.8

Rate of reaction (R) = k. (Δc) …………………………………………...…….………….. 2.8

Where, where K (ms^{-1}) is an empirical mass transfer coefficient depending on hydrodynamic factors and Δc is the concentration gradient between the solid–liquid interface and the bulk [142].

In some cases, the mass transfer coefficient is considered to be the ratio $D/(\delta d)$ where D is the diffusion coefficient (m^2/s) and δd (m) is the thickness of the diffusion boundary layer. The thickness of the diffusion boundary layer is a function of the fluid velocity, the geometry of the installation and the physicochemical properties of the fluid. Mass transfer rates can also be expressed in a dimensionless form by the **Sherwood number (**S_h) as given in Equation 2.9.

$S_h = Kd/D$ ……………………………...…………………………...…….………….. 2.9

where K is the mass transfer coefficient (m s−1), d is the characteristic specimen length (m) and D is the diffusion coefficient of the relevant species (m^2/s). It can be shown by dimensional analysis that Sh is a function of Re and Sc [140].

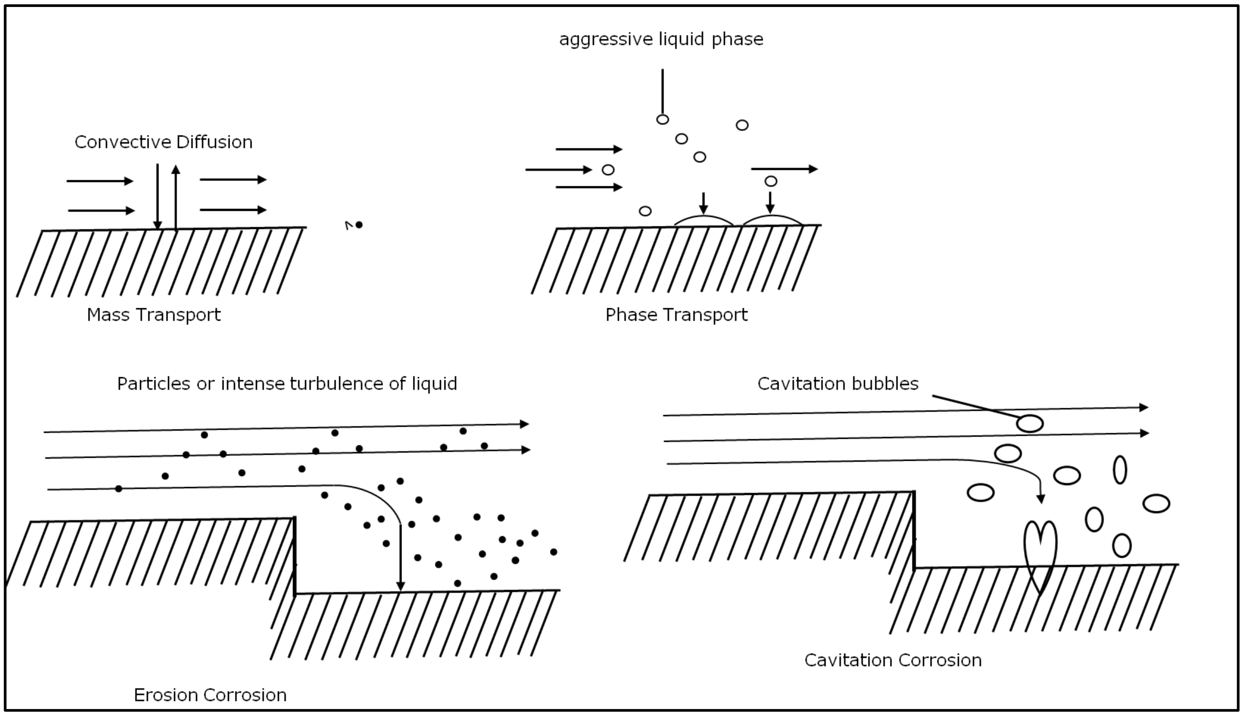

Fig. 2.24: Representation of the four main types of flow-induced corrosion [142].

Momentum transfer is the physical force within the fluid acting through turbulence at the solid metal surface. It is measured by the **wall shear stress** τ ($N.m^{-2}$) [143]. This parameter is a direct measurement of the viscous energy loss within the turbulent boundary layer and it is related to the intensity of turbulence in the fluid acting on the wall. Wall shear stress can be expressed as equation 2.10.

$$\tau = f.\ 2.v^2.\rho \quad \ldots\ldots \quad 2.10$$

Where f is the dimensionless Fanning friction factor determined from Blausious equation, v is the fluid velocity ($m.s^{-1}$) and ρ is the fluid density ($kg.m^{-3}$) [140]

Different forms of flow induced corrosion: The different mechanisms of combined action of flow and corrosion lead to four types of flow-induced corrosion: mass transport-controlled corrosion, phase transport-controlled corrosion, erosion–corrosion and cavitation–corrosion [142].These are represented on Fig. 2.24.

To study flow-induced corrosion at wide range of velocities various techniques like the pipe flow tests, the rotating specimens test (disc, cylinder) or the jet impingement tests are generally used [140,144]. The effects of flow velocity may be summarized as follows [145]:

- At flow velocities close to zero, i.e., in the absence of induced convection, natural convection alone is involved in mass transfer.
- Under the influence of moderate induced convection, mass transfer increases but mechanical flow effects are absent.
- When the system is subjected to forced convection with high flow velocities leading to mechanical flow effects, protective films (passive films, layers of corrosion products) and, in extreme cases, the metallic substrate itself may suffer from mechanically induced damage.

In a liquid metal environment where corrosion occurs by direct dissolution [140], the corrosion mechanism can be divided into two steps:

(i) The dissolution reaction at the surface of the solid metal.

(ii) The transport by convective diffusion of the dissolved metal from the solid–liquid interface to the bulk i.e. mass transfer.

The effects of flow velocity on the above processes are indicated in Figure 2.25. At low velocities, the corrosion rate is completely or partially mass transfer controlled [140]. In such a case, the global dissolution at the solid–liquid interface is at the equilibrium and the corrosion process is thus limited by the diffusion of the dissolved species in the laminar sub-layer from the solid–liquid interface to the bulk (the corrosion rate corresponds to the mass transfer rate or diffusion flux). The thickness of the laminar sub layer depends on the hydrodynamic regime (geometry, fluid velocity and fluid physicochemical properties). Therefore, when the corrosion process is mass transfer controlled, the corrosion rate increases with increasing velocity (phase A: "mass transfer controlled" – Fig. 2.25) [146]. At high velocities, the dissolution reaction at the solid–liquid interface becomes the limiting step. In this region, the corrosion rate is independent of the fluid velocity and, in principle, also of the geometry (phase B: "activation controlled" – Fig. 2.25). At much higher velocities, erosion–corrosion may occur if the surface shear stress is high enough to strip a protective film from the surface (phase C: "Breakaway Corrosion" – Fig. 2.25) [146]. For heavy liquid metals, cavitation–corrosion is also likely to occur at high velocities due to their high density.

2.10. Compatibility of Ferritic/Martensitic Steels with Pb-Li

Corrosion testing of various potential fusion reactors structural materials, especially steels in Pb–Li with correlation to fusion technology started roughly three decades ago [147-148]. Experiments have been carried out in both static and dynamic conditions [144]. The techniques for compatibility evaluation can be classified into static pot, stirred pot, thermal convection loop and forced convection loop as listed in Table 2.10. The stirred pot or the rotating disk system is designed to investigate the effect of flow conditions on the corrosion without temperature gradient. The flow velocity for the test is higher than the velocity in the thermal convection loop which may accelerate the diffusion of the element dissolved from the specimen surface and create a shear stress on the specimen surface which can cause erosion/corrosion [149]. After the all types of corrosion tests; the tested samples are usually analyzed by measuring metal loss or length/diameter change, standard metallographic technique with optical microscopy, and by applying SEM (Scanning Electron Microscopy) and EDS.

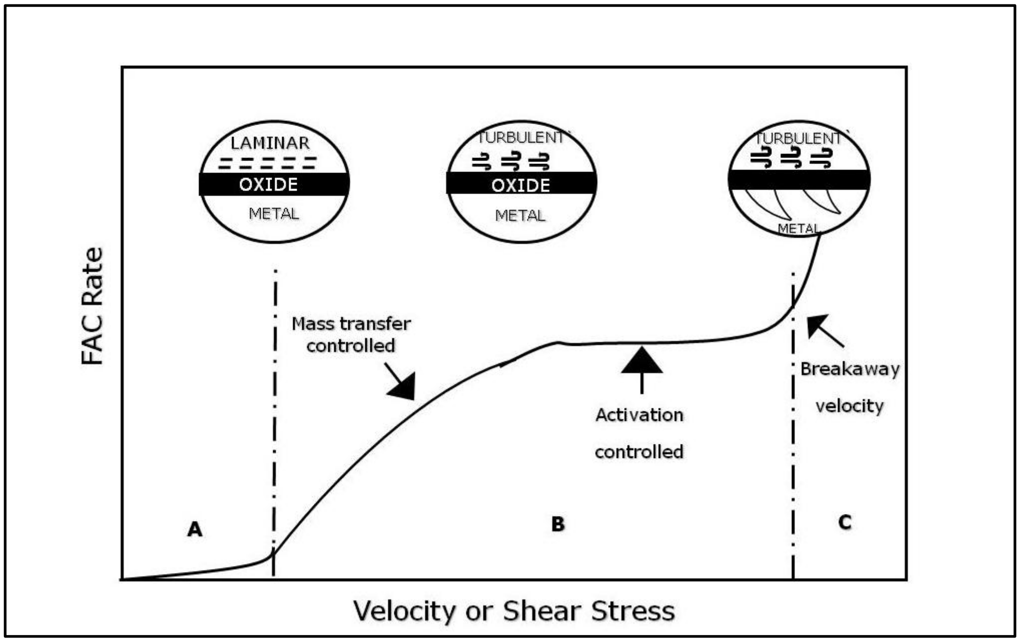

Fig. 2.25: Variation of the mechanism of flow accelerated corrosion (FAC) as a function of the fluid velocity [146].

The initial compatibly tests in Pb-Li were performed under static conditions or in thermal convectional loops [150-152]. Near 1986, first results were reported on corrosion behavior of AISI 304 and AISI 316L steel in a small pumped Pb–17Li loop [153]. Other groups also started activities in the field of Pb-Li corrosion analyses during that time [151, 154], however corrosion testing was in the beginning was limited to moderate temperatures near 400˚C. The corrosion mechanism was described as a leaching-out process, preferably of Ni, with linear kinetics and that austenitic surface scales were converted to porous ferritic ones [153]. End of the 1980s ferritic–martensitic steels were integrated into the test programs and a homogeneous dissolution was mentioned as corrosion long-term mechanism [155-158]. Incubation effects observed at short-term exposed samples were also reported [158-159]. The performed tests showed that temperature and flow velocity have an important effect on corrosion rate [155,173]. Since 1990s, interest changed concerning corrosion behavior to low activation steels like MANET I, F82H-mod, Optifer IV and later on EUROFER 97, F82H, CLAM, etc [72, 161-164]. Most of the compatibility tests were performed at temperatures of 500°C or below [165]. In the last 10 years some, test conditions were modified in order to analyze the behavior at higher test temperatures (≤550°C) to approach test scenarios towards realistic ITER conditions (e.g. HCCB TBM) and to generate a data base for development of modeling tools [125, 138, 166-167]

Table 2.10: Various techniques for liquid metal corrosion tests [149].

Name	Objective and Characteristic	Parameter Control	
		Flow	Temperature Gradient
Static pot	Saturated condition achievable Surface corrosion trend studied Easy handling and compact	No	No
Stirred pot	Saturated condition achievable Surface corrosion and effect of flow studied Easy handling and compact	Yes	Generally No
Forced Convection Loop	Unsaturated condition achievable Effect of flow and erosion corrosion studied Complicated handing and Robust	Yes	Yes

- **Corrosion of conventional steels (Austenitic &Ferritic/Martensitic)**

In static experiments, samples of have been exposed in lead lithium baths under different conditions of temperature and environment. In 1982, static corrosion experiments up to 6000 h were conducted with AISI 316L in Pb-17Li by V. Coen et al [155]. Results showed that in the temperature range 723-873 K, the corrosion layers formed revealed strong nickel depletion giving rise to structural changes and Pb and Li penetration in the matrix. On the other hand, no corrosion was observed at 673K even after 6000 hrs [155].

In 1984, Chopra and Tortorelli conducted a review of corrosion and environmental effects on the mechanical properties of austenitic and ferritic steels for use with liquid metals in fusion reactors [148]. The mechanisms and kinetics of the corrosion processes in liquid Li and Pb-17Li systems were examined and their influence on degradation of structural material was discussed. The review indicated that the dissolution rates of austenitic and ferritic steels in Pb-17Li are an order of magnitude greater than in Li. Limited data indicated that an increase in flow velocity or temperature gradient of the system increased the rates of dissolution of structural steels [148].

In 1992, J. Sannier et al reported that in a semi-stagnant condition i.e. a low Pb-17Li velocity, a significant thermal gradient and a short distance between hot and cold zones - corrosion kinetics of both 316L and 1.4914 F/M steels are linear and about three times lower compared to turbulent flow condition. From the amount of recovered deposits, the mass transfer of 316L at 723 K is equivalent to that of 1.4914 steel at 748 K [168].

In 1988, V. Coen et al conducted experiments to study the effect of Pb-17Li on the tensile properties of steels considered as candidate structural materials in fusion reactor [169]. The possibility of liquid metal embrittlement (LME), in Pb-17Li at various strain rates and temperatures, were explored out on the steels AISI 316 L and the martensitic steel DIN 1.4914. It may be necessary to mention here that Liquid metal embrittlement (also known as liquid metal induced embrittlement) is a phenomenon of practical importance, where certain ductile metals experience drastic loss in tensile ductility or undergo brittle fracture when tested in the presence of specific liquid metals [170]. In general, a tensile stress; externally applied or internally present, is needed to induce this embrittlement. Presence of an oxide layer on the solid metal surface also prevents good contact between the two metals and stops LME. The results of the aforesaid work indicated that both austenitic steels (AISI 316L) and ferritic steels (DIN 1.4914) are not subjected to LME in presence of Pb-17Li. Moreover, after a heat treatment of 1500 hrs, in the liquid alloy, at 873 K, the effect of corrosion is irrelevant on the bulk tensile properties [169].

Dynamic experiments with lead-lithium eutectic have been conducted in liquid metal loops. Both natural circulation and forced circulation types have been extensively used for the study of the corrosion behavior of structural materials in liquid lead -lithium at high operating temperatures (i.e. 673 K to 823 K) [138, 159] . A natural circulation/thermal convection loop circulates liquid metal with the help of the buoyancy force generated from the temperature difference of liquid maintained at two different locations in the loop [171]. They are simple to operate and do not require any external force for driving the liquid. The velocities obtained in such loops are generally low i.e.in the range of (1-10 cm/s).

In 1986, Tortorelli and Devan [152] conducted Pb-17Li compatibility experiments in a thermal convection loop at a maximum temperature of 773 K. Type 316 stainless steel and Fe-12Cr-1Mo-V-W steel were exposed for more than 6000 hrs. Results showed that at 773 K, severe, non uniform attack of SS 316resulted in the formation of extensive ferritic corrosion layers. In contrast, the Fe-12Cr-1MoVW steel exhibited uniform corrosion. The presence of the ferritic layer on the type 316 stainless steel and the effects of specimen cleaning on its integrity, were shown to be important considerations in evaluating the corrosion data for this steel and in comparing corrosion losses for the two types of alloys [152].

Liquid metal corrosion tests at higher flow velocities can be conducted in a forced circulation loop driven by pump [161-163, 172]. Such a loop usually consists of a number of important components like test section for holding the samples and the heat exchanger for lowering the temperature before the pump [172]. The electromagnetic pump for liquid metals provides the driving force for fluid flow and velocities as high as 30 cm/s can be obtained [163]. Other than these, the flow meter and pressure transducer helps in maintaining the required parameters like flow velocity and pressure head. A cold trap is installed in the low temperature region to allow corrosion products to precipitate and avoid plugging. Corrosion tests at different flow velocities can be conducted in a forced circulation loop just by changing the rotation speed of the pump. A pump driven loop named PICOLO (Figure 3.22) has been installed at Karlsruhe Institute of Technology, Germany. This loop has been used for corrosion study of various structural materials in Pb-17Li [161-162].

The results from one of the experiments conducted in this facility revealed that the extent of material loss of the martensitic steel; MANET (10.6 Cr - 0.77 Mo) in flowing liquid Pb-17Li alloy at both 773 K and 823 K, at a flow velocity of 0.3 m/s; can limit its maximum usage temperature to 723 K in a fusion reactor environment [173]. The upper temperature limit for the austenitic steel SS 316 L (N) under similar conditions will be 50 K lesser [174]. In the year 2000, the corrosion of three ferritic- martensitic steels were examined in Pb-17Li in the PICOLO loop at 753 K [161]. Two different processes were found responsible for the corrosive attack. Firstly, the passive oxide layer on the steel surface was dissolved. This so-called incubation period was dependent on temperature and on the flow velocity of the melt. The second step was the dissolution of the steel matrix which was characterized by a strong depletion of iron. Alloying elements, which have a high solubility in Pb-17Li, were partly leached out of the matrix. Elements which have a low solubility in Pb -17Li (e.g., Mo, W, V) remained in matrix enriching the surface compared to the bulk steel composition [161].

The corrosion behavior of the martensitic steel DIN 1.4914 was tested at the PICOLO loop in flowing liquid Pb-17Li at 823 K at a velocity of 0.3 m/s for 3, 700 h duration [176]. The weight loss of the exposed specimens was recorded after cleaning them in a bath of molten sodium maintained at 423 K**.** This resulted in a corrosion rate of 0.37 mm/y which was three times lower than that for austenitic steels [175].

- **Corrosion of EUROFER 97**

N. I. Loginov et al. also tested the corrosion resistivity of EUROFER 97 against liquid Pb-Li in static and dynamic (stirring) conditions at 873 K up to 3000 h. The dynamic tests were carried out by rotating disc method [176]. The average velocity of samples was 0.5±0.15 m/s as a result of three velocity components: radial, tangential and axial by means of Navier-Stocks equation. The loss of thickness δ as a function of loss of mass was found to follow the Equation 2.11:

$$\delta = \Delta m / F . \rho \quad \text{2.11}$$

Where F is the area of sample surface contacting lead-lithium alloy and ρ is the density of EUROFER 97. EUROFER samples corroded at the rate of 430µm/y at a velocity of 0.14 m/s when exposed for 3000 h. Ten times lesser corrosion rate was demonstrated by EUROFER in static Pb-Li for similar test parameters.

In 2002, Benamati et.al exposed the corrosion and tensile samples of the EUROFER 97 steel to Pb–17Li in the LIFUS II loop at 753 K [177]. During the tests, the liquid metal flow velocity in the test section was about 10^{-2} m/s. The specimens were extracted after 1, 500, 3, 000 and 4, 500 h exposure for weight change measurements and metallurgical analysis was performed while tensile tests were performed at 753 K. The results showed that EUROFER 97 underwent uniform corrosion at a rate of 40 µm/y and the mechanical properties seemed to be unaffected or only slightly affected by the liquid metal [177].

Karel Splichal and Milan Zmitko examined the corrosion resistance of EUROFER 97 in flowing Pb–17Li melt at the temperature of 773 K for 2500 h [178]. The experiments have shown that the surface corrosive attack is revealed only after a certain incubation period. During this period, the protective oxide layers do not enable a direct attack of the surface by the melt though diffusion of elements like iron and chromium from bulk to the liquid through the surface take place slowly. At longer exposure times, these layer no longer remains and do not prevent dissolutions of steel components which take place at an accelerated rate than earlier. Concentration profiles of steel components near the steel surface were examined by EDX line-scan and point analyses where slight decrease in highly soluble steel components in Pb–17Li like Cr and Fe was found. The increase of W content, as a component with lower solubility in liquid metals, was observed near the steel surface.

J. Konys et. al conducted the corrosion testing of bare EUROFER 97 samples was performed in flowing Pb–17Li with a flow velocity of 0.22 m/s in the PICOLO-loop. They observed that at a lead lithium flow velocity of 0.22 m/s, the corrosion rates increases by a factor of five when the temperature of exposure was increased from 753 K to 823 K [163,179] while it decreased to 400 μm/y at 823 K when the velocity was reduced to 0.22 m/s at 823 K [167]. This imposes a dangerous design concern for a reactor in that if it overheats only by a small margin, the corrosion rates would increase by almost 5 times. This means that the lifetime of a reactor blanket could be drastically reduced by a small increase in temperature, at least in the hottest section of the loop. For a realistic estimation of material loss, one of the reports published by the above group uses Sannier's correlation to correlate the material loss (ML) in the form of dissolution depth per year with the flow velocity (v) is the velocity, temperature (T) and hydraulic diameter (d) [124]. The Sanniers correlation is given in equation 2.12 [180].

$ML = 8 * 10_8 * \exp [-25690/1.98T] * v^{0.875} * d_h^{-0.125}$ [μm/a] 2.12

Figure 2.26 shows the dependence of metal loss obtained from Sannier's correlation on temperature at three flow Pb-Li flow velocities i.e. 0.22, 0.05, 0.005 m/s. Out of this, 0.22 m/s was the experimental flow velocity for most of the tests on RAFM steels in the PICOLO loop. Therefore the experimental data of metal loss from these tests have also been included in Figure 2.26 and shows good agreement with Sannier's correlation [124].

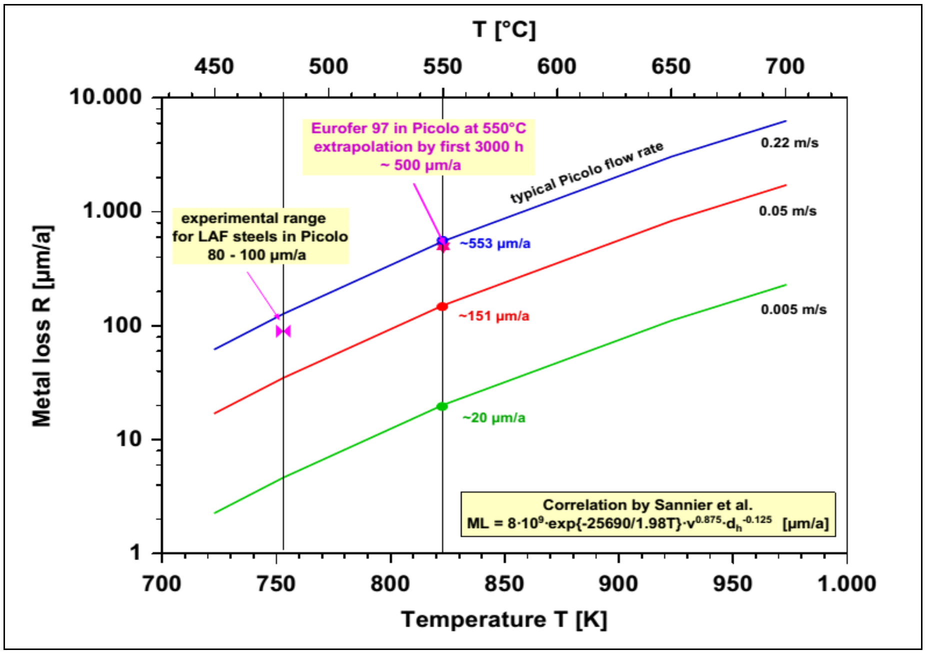

Fig. 2.26: Corrosion of RAFM steels given using Sannier's correlation in dependence of temperature and flow velocity including the values of PICOLO testing of EUROFER [124].

Figure 2.27 (a) shows the cross-section of the EUROFER sample exposed to Pb-Li in PICOLO loop at 550° C (823 K) after 1025 h [167]. The adherent Pb-Li scale could be seen over the sample surface and non-uniform corrosion attack upto the extent of 41 µm is observed. Figure 2.27 (b) shows the path of elemental line scans of alloying elements and lead taken across the boundary while the actual line scans are shown in Figure 2.28. Depletion of iron and chromium at a very thin region close to the boundary (3-4 µm) is noted although ingress of lead was not confirmed [167].

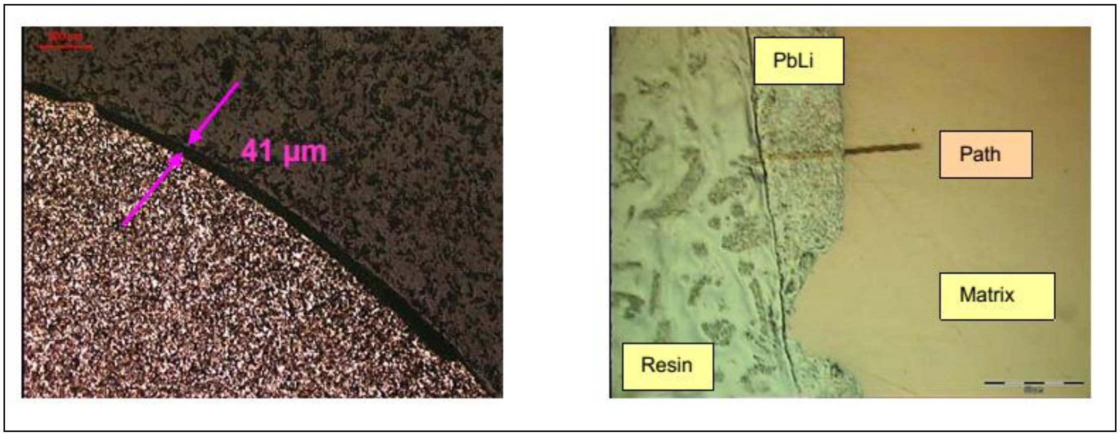

Fig. 2.27: (a) Cross-section of EUROFER 97 exposed to Pb-Li at 823 K; (b) path of EDS line scan across the exposed boundary [167].

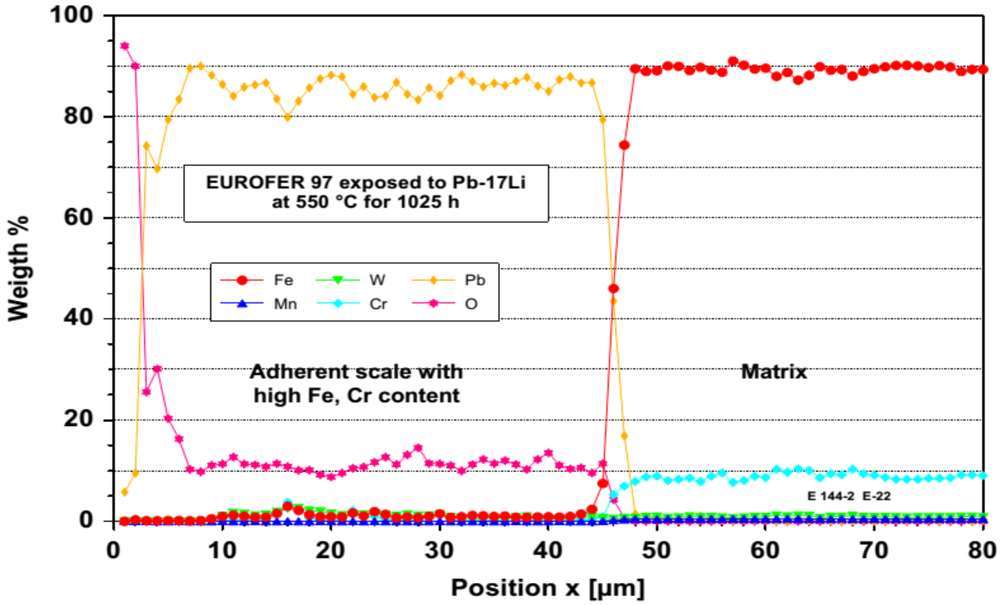

Fig. 2.28: EDS composition profile of Fe, Cr, Mn, W, Pb and O across the exposed surface after 1025 h [167].

It was reported that due to the high corrosion attack at 823 K, large amount of precipitates were also present in the PICOLO loop which led to plugging after about 3000 h of operation [181]. Both, experimental and analytical analyses indicated that safe operation of Pb–Li systems without the risk of line plugging may need corrosion resistant coatings to bring down corrosion and precipitation behavior at high operation temperatures to a manageable level also at small flow velocities [181]. Experiments with EUROFER 97 in PICOLO loop also revealed that the

Pb-Li attack was stronger at prior austenitic grain boundaries and at positions with a high density of grain boundaries [163]. Therefore, it could be assumed that different microstructures on the surface of steel probably lead to corrosion attack at different time or speed and delayed wetting. Based on the results from PICOLO loop, code named MATLIM [166] have been developed at KIT to calculate the mass transfer in liquid metal loops based on dissolution mechanism. The authors have indicated extrapolation of short term corrosion data would not be a relevant guide to predict the lifetime of a reactor due to delayed wetting and decrease in flow velocity at later stages due to wall thinning as shown in the Figure 2.29 [181]. Therefore, actual long term exposure data points are absolutely necessary.

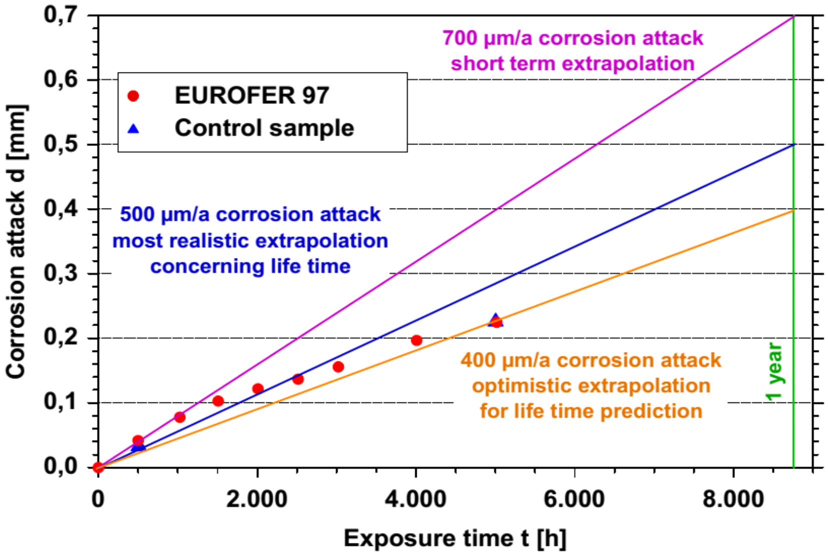

Fig. 2.29: Corrosion attack of EUROFER 97 in PICOLO loop showing the importance of long exposure data for realistic prediction of corrosion rate [181].

The effect of magnetic field on the corrosion of EUROFER-97 by Pb-17Li was studied in a forced circulation loop under a magnetic field of 1.7 T at Institute of Physics, University of Latvia [182]. It was observed that at a maximum flow velocity of 823 K and an average flow velocity of 5 cm/s; the magnetic field increased the rate of corrosion by more than 2 times of the value observed without magnetic field. The samples exposed under magnetic field showed prominent parallel (wavy) lines on their surface in the direction of flow after 2, 000 h of exposure [182, 183].

R. Morreu et al. [184] investigated the corrosion on EUROFER steel on the samples from the above experiments in Latvia. They predicted some possible mechanisms for the above observation. According to them, the key phenomenon behind corrosion was the dissolution of iron into Pb–17Li, without any lead re-deposition. Theoretical analysis predicted that the above wavy-shape develops extremely slowly, whose wavelength depends of the inclination of the wave-vector with respect to the flow axis. The electric current, which short-circuits the humps within the wall, contributes to the corrosion by a mechanism, which has been called electro-dissolution and is expressed in terms of the electro-dissolution number.

- **Corrosion of JLF-1 steel**

The compatibility of JLF-1, a RAFM steel from Japan, with static and flowing lithium (Li) was investigated in 2008 [185]. The weight losses of JLF-1specimens in static Li systems showed saturation at the temperature of 773 K and 873 K. This is reported to be due to the saturation of Fe, Cr in bulk Li or formation of saturated layer of dissolved elements in liquid Li near the specimen surface. In the corrosion test in a thermal convection loop, the corrosion rate at 773 K for 250 h was significantly larger than that obtained in the static test in an identical condition [186, 187]. After Li exposure the phase transformation from martensite to ferrite was found on the exposed surface due to depletion of carbon from the steel specimens. [185,187]. Figure 2.30 (a) shows the details of tempered martensite structure in RAFM steels while Figure 2.30 (b) depicts the phase transition after Li exposure from martensite (BCT) to ferrite (BCC) due to carbon depletion [125]. At the same time, selective depletion of alloy elements, such as Cr was detected by EDS on the surface [186]. The flowing Li enhanced the weight loss, phase change and hardness reduction due to the mass transfer process [186].

On the other hand, the exposure of JLF-1 to Pb-17Li in static condition at 873 K showed a lot of pits on the specimen surface after the immersion for 750 h [125]. The specimen surface after a similar test for 3000 h test revealed the preferential attack to the boundaries as the connection of the pits, which were observed after 750 h exposure. The weight loss of the specimen increased with the exposure time reaching a maximum of 1.3 g/m^2 after 3200 h. The depletion of Cr on the specimen surface was reported in the initial stage of the corrosion although the total corrosion loss was determined by the dissolution of Fe at an isothermal condition [125].

The compatibility test of JLF-1 with Pb-17Li in flowing condition was performed by immersion to an impeller induced stirring pot at 873 K as shown in Fig 2.31 [125, 188]. The rotating flow included only small upward and downward flow components produced by the rotating impeller, so the liquid metal is well mixed with near constant concentration of impurities throughout the liquid volume [125]. The flow velocity can be roughly estimated as inertial flow with the flow velocity equal to the speed of the impeller. The velocity of the samples (located just over the periphery of the impeller on both sides) is given by the Equation 2.13

$v = \Pi dn$ ………………………………………………………………………………...2.13

where ‘v’ is the flow velocity at the specimen surface in m/s, ‘d’ is the width of the impeller in m and ‘n’ is rotating speed in s^{-1}.

Unlike the specimen exposed to the static Pb–17Li, the surface exposed to flowing Pb-17Li had a granular-like microstructure [125]. The formation of granular microstructure was explained to be due to the erosion-corrosion of JLF-1 specimen which was caused by the exfoliation of the corroded surface by the flow [125]. First, the liquid Pb-17Li penetrated into the boundary of the microstructure. Then, the bonding between the sub-grains became loose. Thus the grains were peeled off by the flow and could not be coarsened without available sufficient time [125]. The surface of JLF 1 specimen after exposure to Pb-Li in static and flowing condition at 873 K is shown in fig 2.32 while the mechanism of flow accelerated corrosion in flowing Li or Pb-Li is explained in Fig 2.33.

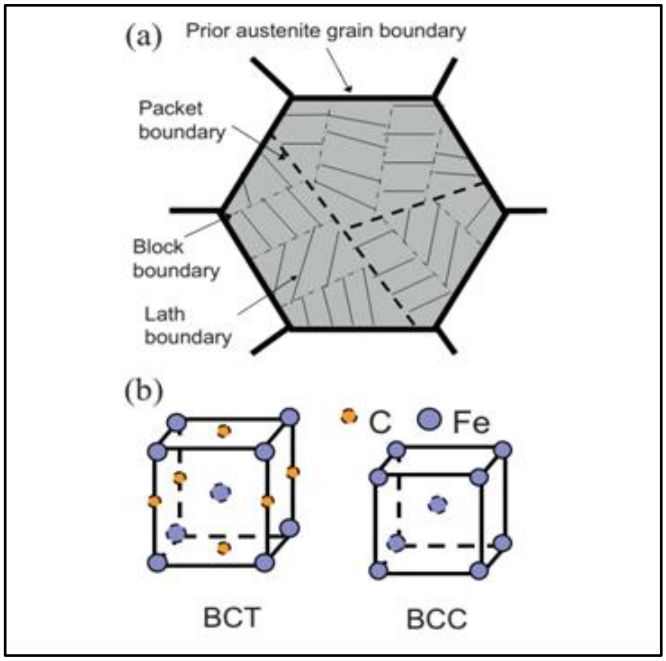

Fig. 2.30: (a) Schematic illustration of tempered martensite structure; (b) phase transformation from BCT to BCC due to carbon depletion [125].

- **Corrosion of F82H steel**

The corrosion of F82H (Fe-8Cr-2WVTa-0.1C) produced by Japan was studied in flowing Pb-Li at 823 K and penetration of both lead and lithium was observed [189]. The exposed specimen exhibits local pitting corrosion and a Cr-depleted layer at the surface with an approximate maximum depth of 10 µm after 500 h was observed. In addition, Cr-rich phases were observed in the substrate region, where $M_{23}C_6$ had probably disappeared into the Cr-depleted layer. The depth profile of the constituents of F82H and Pb and Li into the exposed surface after 300 h as obtained by Radio Frequency Glow Discharge Optical Emission Spectroscopy (rf GDOES) is shown in Figure 2.34.

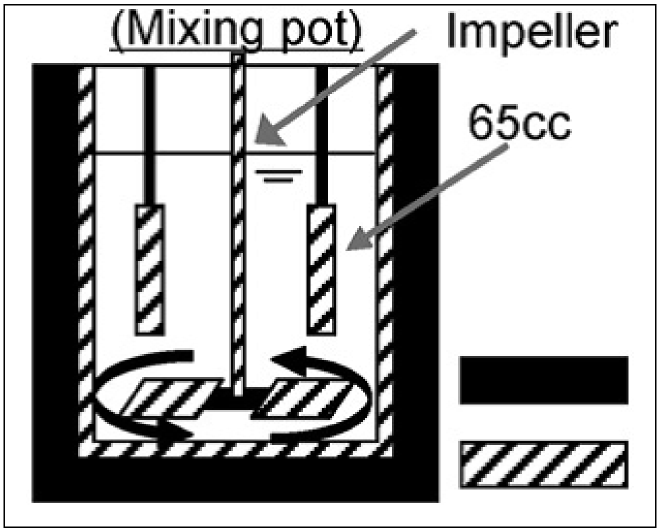

Fig. 2.31: Corrosion test set-up with Impeller Induced Flow [125].

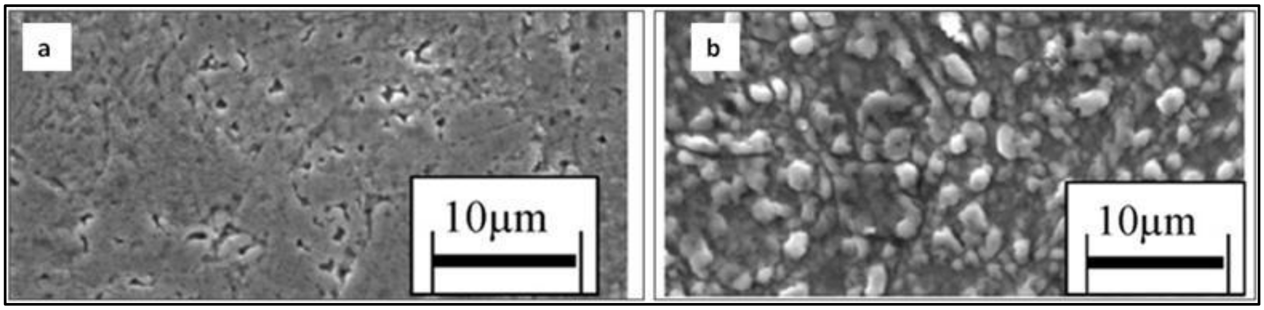

Fig. 2.32: (a) Surface of JLF 1 exposed to Pb–17Li at 823 K in static condition for 750 h, (b) Surface of JLF 1 exposed Pb–17Li at 823 K in flowing condition for 250 h [125].

- **Corrosion of CLAM steel**

An experimental campaign with Pb-17Li was launched in China through construction and operation of the DRAGON series of lead-lithium experimental loops dedicated towards corrosion compatibility studies of CLAM steel under various operating conditions. [190,191].

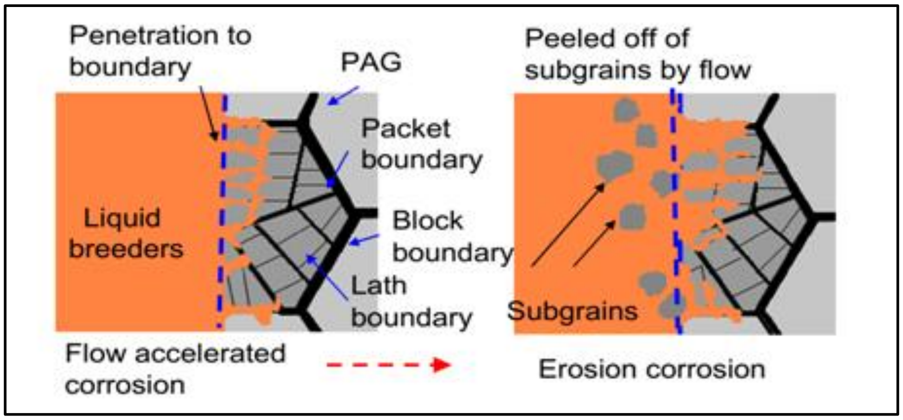

Fig. 2.33: Flow accelerated corrosion of JLF-1 steel in Li or Pb-Li [125].

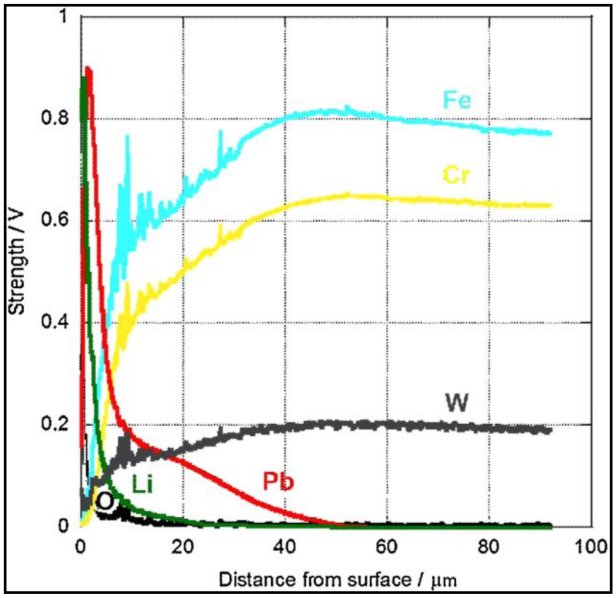

Fig 2.34: Depth-profile of elements of F82H after 300 h in Pb–17Li obtained by rf-GD-OES [189].

The examination of the corrosion behavior for CLAM steel in flowing Pb-Li was carried out at 753 K in the DRAGON-I loop in China, up to duration of 8000 h [164]. At the beginning of the exposure, the specimen surface was protected by the passive oxides Cr_2O_3 or $(Fe_xCr_{1-x})_2O_3$ (determined by X ray Photoelectron Spectroscopy i.e XPS) and local corrosion was caused by the reaction of Fe_3O_4 and Pb. After 6000 h of exposure, the whole surface of the specimen suffered corrosion attack due to the leaching out of steel elements; and after that, a spongy corrosion zone was formed. The corrosion rate was determined by evaluating the depth of the corrosion layer after 8000 h of exposure, and was about 17μm/y.

This literature survey brings out that the first stage in the liquid-metal attack over ferritic martensitic steels involves dissolving the passive oxide layer on the steel surface [161,164]. Such a layer is usually formed during the thermal treatment of steels (normalizing and tempering) and consist of $MnCr_2O_4$ and $(Fe, Cr)_2O_3$ [161, 192]. This attack is generally in homogeneous due to non uniform wetting of the oxide layer with Pb-Li [163]. The dissolution of oxide layer by Pb-Li results in reduced corrosion during the ‘the incubation period’ [174]. The incubation period has been found to decrease as the temperature and the flow velocity increase [124,163]. After the incubation stage, the corrosion attack proceeds distinctively faster via direct dissolution of iron and chromium. The remaining porous zone consists of elements of low solubility in Pb-Li, such as W, Mo and V, and shows a low adherence to the steel matrix so that it can be easily eroded from the surface by the flowing melt [161]. The corrosion during the second stage is essentially uniform and generally demonstrates mass loss of almost linear in time [167]. Penetration of Pb-Li in the matrix is observed in many cases though the mode of penetration is not established [164]. The corrosion rate in the uniform dissolution phase is significantly affected by the temperature and the flow velocity [124,181]. It is thus evident that the qualification of IN RAFMS as a suitable structural material for fusion technology will only be successful when its corrosion behavior in Pb-Li is analyzed under the temperature, flow conditions and magnetic field relevant to breeding blanket applications. Such data is not available in open literature and thus is of prime importance. Moreover, the understanding of the corrosion mechanism and the specific role of oxide layer over it (if any) will help in predicting a suitable lifetime of the structures fabricated out of IN RAFMS when used in TBM applications. The corrosion rates of some of the ferritic-martensitic steels (Table 2.12) in flowing Pb-Li under different experimental conditions as shown in Table 2.13. The data for SS 316 has been included for comparison.

Table 2.11: Composition of various steels exposed to Pb-Li.

Material (Reference)	**SS 316** *(151)*	**Fe–12Cr1-MoVW** *(151)*	**MANET** *(731)*	**1.4914** *(175)*	**F82H** *(161)*	**EUROFER** 97 *(193)*	**CLAM** *(164)*
Cr	17	12	10.6	10.6	87.7	8.82	9.38
C	0.08	0.2	0.13	0.13	0.09	0.11	0.097
Mo	2.0	1.0	0.77	0.77	-	-	-
Mn	2.0	0.6	0.82	0.82	0.16	0.47	0.45
W	-	0.4	-	-	1.95	1.09	1.48
Ta	-	-	-	-	-	0.13	0.15
V		0.3	0.22	0.22	0.16	0.20	0.21
Ni	12	0.5	0.87	0.87	-	-	0.005
Nb	-	-	-	0.16	-	-	-

Table 2.12: Corrosion rates of different steels under flowing Pb-Li.

Material	Maximum Temperature (K)	Velocity (m/s)	Corrosion rate (µm/year)	Duration (hours)	Reference
SS316	773	0.01	85	6000	*151*
Fe–12Cr1MoVW	773	0.01	23	6000	*151*
MANET	773	0.30	128	6000	*173*
MANET	823	0.30	911	4000	*173*
1.4914	823	0.30	370	3700	*171*
MANET I, F82H	753	0.30	100	8000	*161*
EUROFER 97	753	0.30	90	12000	*163*
EUROFER 97	823	0.30	700	1025	*179*
EUROFER 97	823	0.22	400	12000	*167*

Material	Maximum Temperature (K)	Velocity (m/s)	Corrosion rate (µm/year)	Duration (hours)	Reference
EUROFER 97	753	0.01	40	4500	*53*
CLAM 97	753	0.08	17	8000	*164*
CLAM, EUROFER 97	823	0.10	220	12000	*194*
EUROFER 97	823	0.05	237-550	2000	*182*
EUROFER (B=1.7 T)	823	0.05	550-900	2000	*182*

CHAPTER 3

DESIGN OF EXPERIMENTS

3.1 Basis of selection of Experimental Techniques

As pointed out in Chapter 2 (Section 2.10, Table 2.10), liquid metal corrosion can be evaluated through three main techniques viz.: static pot, stirred pot and liquid metal loop (thermal or forced convection) [149, 186]. A preliminary understanding of the corrosion mechanism can be obtained under isothermal conditions through static experiments where the main driving factors are the concentration gradient of individual alloying elements between the steel and the liquid, as well as the solubility of that particular element in the liquid at the test temperature. In isothermal stirring experiments, a third factor of flow velocity is introduced which causes faster material take off from the exposed surface and thereby enhances corrosion. However, inside the TBM, the coolant flows at a particular velocity in a closed circuit having variation in temperature at different locations. This introduces another factor i.e. the temperature gradient. Such conditions can be experimentally simulated in non-isothermal liquid metal loops, where the corrosion products generated near the high temperature locations get transported along with the flow to the cooler regions where they get deposited on the available surfaces. The transport of elements prevents the liquid in the vicinity of steel surface from getting saturated with the corrosion products and thereby enhances its corrosive capability as compared to that in a static or a stirring system.

Keeping the above in mind, a series of experiments have been done at Bhabha Atomic Research Centre (BARC) in order to study the compatibility of Indian RAFMS (IN RAFMS) and modified 9Cr-1Mo steel (P91) in Pb-Li and compare the results obtained for these two materials under various operating conditions. Such experiments have been carried out in three different stages: - (i) Static experiments, (ii) Experiments under a rotational flow and (iii) Experiments in a Loop under flowing condition. The different experimental facilities that have been developed for compatibility studies under the above three conditions have been described in the following paragraphs.

3.2 Design and Development of Static Corrosion Test facility

In order to initiate corrosion testing of fusion reactor relevant materials in liquid Pb-Li, a few static corrosion test set-ups were designed and fabricated at BARC. These set-ups provided the facility of exposing corrosion coupons in liquid Pb-Li kept under isothermal and stagnant conditions. Figure 3.1 shows the schematic of the static corrosion test capsule while Figure 3.2 shows the actual photograph of two such capsules mounted on a common support. Each capsule consists of a one end closed SS316L pipe having 12 mm I.D. for containing the liquid Pb-Li. The pipe is 150 mm long and 2 mm thick. Small rectangular shaped corrosion coupons of maximum size 12 mm x 20 mm x 3 mm are used for corrosion testing in these set-ups. The samples have a hole of 4 mm diameter drilled on one side which is used for fixing them to the sample holding rod. These rods (3 mm diameter) are made up of molybdenum material since they have a minimum solubility in Pb-Li [195].

The samples are tied to the molybdenum rod with the help of molybdenum wires and the rod is fixed to the top cover of the capsule which is also made of SS316L. The sample assembly is then inserted into the test capsule and afterwards, the capsule is filled with solid Pb-Li (approx. size 5 mm x 5 mm x 3 mm) of required quantity (0.12 kg) which will allow complete dipping of the samples in molten condition. Later the top cover is welded to the capsule and a positive pressure (1.2 bar) of high purity argon gas is maintained inside it. The set-up is heated by coil heaters

(Nichrome) of 2 mm thickness and 3 kW power rating while temperature of the capsule is monitored by K- type thermocouples. Temperature of the heating zone are monitored by Proportional–Integral–Derivative Controllers (PID) and short term corrosion testing (up to 500 h) was possible at a maximum temperature of 873K (600˚C). The accuracy of temperature measurement is between ±3 K. This temperature limit is decided by the mechanical strength (150 MPa at 873 K) and the maximum allowable corrosion limit (20 µm/y for flowing Pb-Li) of the SS 316L tube material [155,196].The entire set-up is insulated with the help of zirconia mineral wool blanket having thickness of 20 mm.

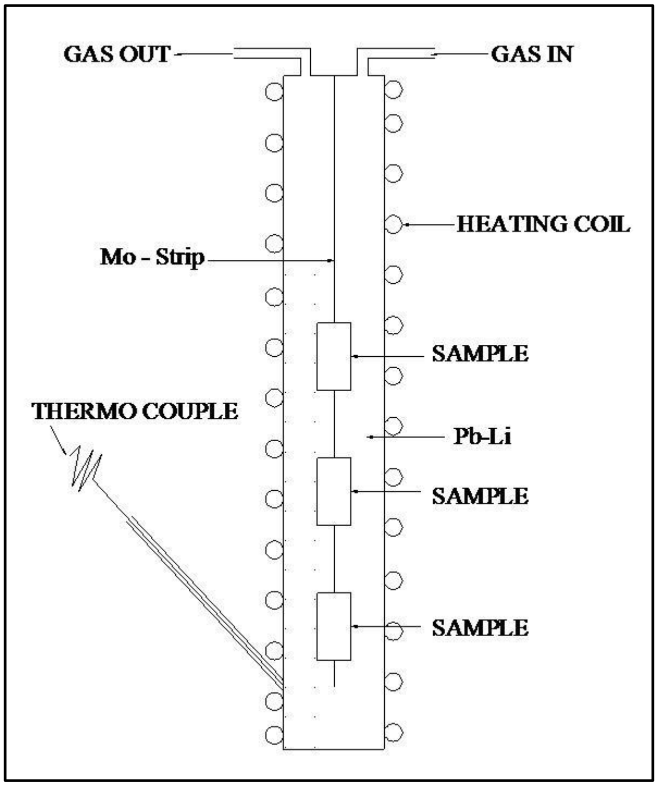

Fig 3.1: Schematic of the first static corrosion test facility.

3.2.1. The Geometric factor

The geometric factor is an important design parameter in the case of liquid metal corrosion experiments and it was introduced by M. Kondo while reporting the corrosion tests with different ferritic-martensitic steel specimens exposed to Li and Pb-17Li [125]. The geometric factor is expressed by Equation 3.1.

$$\text{Geometric Factor} = V / A \quad \ldots\ldots \quad 3.1$$

Where ‘V’ is the volume of liquid and ‘A’ is the total surface area available for corrosion in the experimental device.

As already pointed out in Chapter 2 (Section 2.9.2); corrosion under isothermal conditions is limited by the point of time when the dissolved species coming from the corrosion coupons fully saturates the corrosive liquid. In this regard, the value of geometric factor gives an idea about the corrosive capability of the liquid metal/ alloy before getting saturated with the corrosion products.

Fig. 3.2: Photograph of the first static corrosion capsules.

This means, that a higher value of geometric factor would be favorable for long term corrosion experiments such that the corrosive liquid is not saturated by the metallic impurities generated during corrosion, till the end of the experiment. Considering the total surface area of the corrosion coupons and the inner surface of the SS 316L tube available for corrosion for the above mentioned static test facility; the geometric factor comes out to be 0.2 x 10^{-2} m. This value may be considered as sufficiently safe to conduct the present experiment for 355 h since results from similar kind of experiments have been reported in literature with geometric factors lesser (0.33 x 10^{-3} m to 3.3 10^{-2} m) than the present one [125].

3.2.2. Experimental Challenges

The following are the key challenges faced in these experiments:

1. The above facility was used to conduct short term static corrosion tests upto 350 h and allowed preliminary comparison of corrosion characteristic of IN RAFMS and P91 material under isothermal conditions. There was an initial apprehension that the corrosion of the SS 316L capsule in Pb-Li may affect the overall corrosion process of the test coupons. However, after consideration of the geometric factor the validity of the results obtained were confirmed.

2. Successful sample removal from molten Pb-Li is a major challenge in conducting compatibility experiments since Pb-Li is extremely prone to oxidation above its melting point i.e. 235 °C and thus cannot be exposed to atmosphere. Moreover, at lower temperatures the Pb-Li solidifies in a cast thereby completely enveloping the samples inside it. In the above static test capsule; there was no provision of online sample removal or replacement. Thus multiple samples could be exposed for only one single time duration in Pb-Li. After the completion of an experiment, the top SS cover had to be cut off and the Pb-Li alloy had to be melted under inert gas atmosphere. This was a cumbersome process. Moreover, there was no possibility of using the same test capsule again or exposing multiple samples for different time intervals in the same test capsule.

3.3. Design and Development of Static Corrosion Test facility with online sample replacement mechanism

In order to overcome the above problems and to facilitate long term corrosion testing of structural and functional materials in heavy liquid metals and alloys like lead-lithium eutectic at elevated temperatures up to 1000˚C; a fully automated experimental facility was developed and installed at BARC. The set-up facilitates static corrosion testing under inert gas atmosphere as well as in vacuum. It also incorporates the feature of automatic sample immersion with the help of a pneumatically operated shaft. Figure 3.3 shows the schematic of this facility and the actual photograph is given in Figure 3.4

The set-up consists of a double chamber retort (80 mm inner diameter, 250 mm long) made out of Inconel 625 to withstand high temperatures. A liquid metal bath (60 mm I D, 2 mm thick, 100 mm long) is kept in the lower half (chamber) of this retort which could be heated up to 1273 K (1000 ˚C) by PLC controlled heaters. Corrosion coupons held in dedicated sample holders could be inserted into the liquid metal bath under inert gas atmosphere. A special feature of the system is a high vacuum gate valve which can separate the Inconel retort into two halves when the samples are held in the upper chamber. The upper half of the retort is generally maintained at a lower temperature through water cooled flanges at the valve junction. When the valve is in closed condition, the top cover flange of the retort could be opened and the samples can be removed or fresh samples could be loaded without the need of cooling the liquid metal till solidification or exposing the same to outside atmosphere. This helps to make the sample removal and exchange process fast, simple and efficient. This also allows repeated use of the set-up for conducting multiple experiments.

All wetted parts of the system including the sample holder, sample holding rod and the liquid metal bath are made up of molybdenum. Various type of sample holders made up to molybdenum could be used for holding different type of sample geometries. Figure 3.5 shows one such holder (including cover) having 20 mm dia and three inner holes of 8 mm diameter each of which can be used for exposing three different types of sample at a time.

The choice of Molybdenum as the container material had been made mainly because of its low solubility in Pb-Li [189,195]. Some researchers have reported that Mo interacts with the dissolved C of liquid lithium leading to formation of Molybdenum carbides ($MoC_{0.5}$) and it's precipitation on the crucible walls [125,187]. This fixing of C as carbides will also lead to lowering of the carbon potential in lithium therefore inducing further dissolution of C from the corrosion coupons [125,187]. Such C depletion from RAFM steel coupons exposed to pure Lithium may lead to the formation of ferrite on the exposed surface [187]. However, no such results as above have been reported earlier for interaction of Pb-Li with Molybdenum and further investigation are needed to extend this hypothesis to Pb-Li. On the other hand, molybdenum have been successfully used for exposing RAFM steels like F82H in Pb-Li at 823 K [189]

After completeion of the corrosion experiment, the samples are taken out of the liquid and held for cooling in the upper half of the retort under inert atmosphere. Special kind of seals have been designed and fabricated for this system; which allows movement of the sample holders through the top flange covering the retort without breaking the controlled atmosphere. Sufficient water cooling through a controlled chiller restricts the temperature at the location of the seals to ambient such that they are not damaged.

3.3.1 Geometric Factor

As given in Equation 3.1; the geometric factor for the new static corrosion test facility would be equal to the (volume of liquid) / (total surface area of the corrosion samples). Since all wetted parts including the crucible and the sample holder; are made up to molybdenum; they have not been considered in the calculation. The geometric factor with respect to the first experiment conducted in this facility (Chapter 4, Section 4.3.3) with the type of holder shown in Figure 3.5; comes out to be 3.08. This is much higher than other corrosion experiments reported in literature (0.33×10^{-3} m to 3.3 10^{-2} m) as well as those conducted in our laboratory which indicates the corrosion experiment could be safely conducted without any possibility of saturation [125].

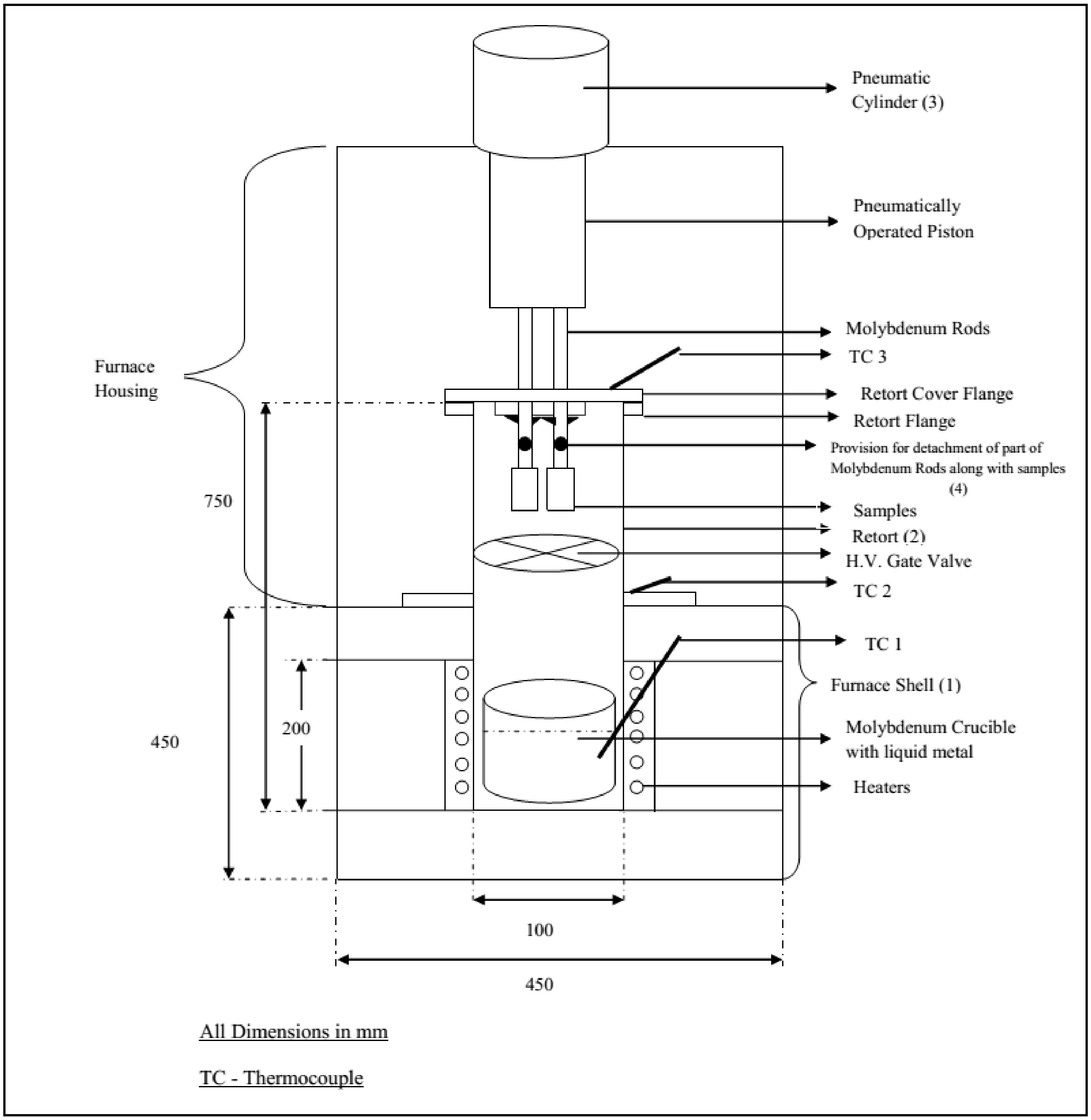

Fig 3.3: Schematic of the new static corrosion test facility with automatic sample removal.

Fig. 3.4: Experimental set-up to study the corrosion in static Pb-Li up to 1273 K.

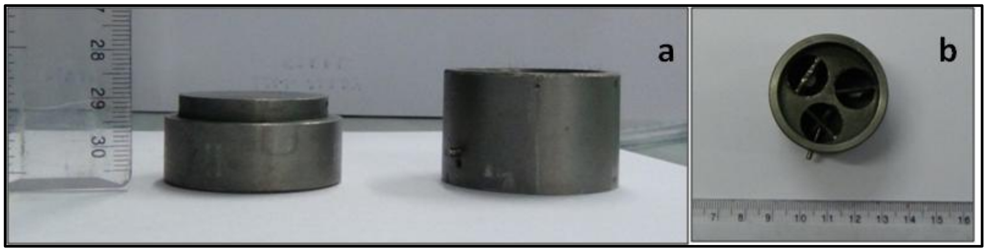

Fig. 3.5: (a) Side view of the molybdenum holder; (b) Top view of the molybdenum holder.

With the new static system in hand, the challenges regarding compatibility of containment material and sample removal were successfully overcome. Corrosion of IN RAFMS, P91 and many other structural and functional materials were studied in lead-lithium eutectic (Pb-Li) in this set-up under static conditions for durations up to 2, 000 h. Moreover, pure metals like chromium (Cr) and Iron (Fe) were also exposed to molten Pb-Li in this set-up for different time duration upto a maximum of 1, 000 h. The idea was to correlate the time dependence of the dissolution behavior of constituent elements with that of IN RAFMS and thus understand their role in the corrosion mechanism. In order to move over to the next phase of corrosion experiments where the effect of Pb-Li flow velocity over the corrosion behavior of materials could be studied; the Rotating Disc Corrosion Test Facility was developed.

3.4. Design and Development of the Rotating Disc Corrosion Test Facility

A Rotating Disc type Corrosion Test Facility (RDCTF) has been designed, fabricated, installed and commissioned to study the compatibility of structural steels in lead-lithium eutectic in a flowing condition. The facility can be used for screening of various structural materials based on their corrosion behavior in flowing Pb-Li under isothermal conditions.

The schematic of the experimental facility used for the present study is shown in Fig. 3.6 This test system consists of four major components i.e. motor, sample chamber, magnetic coupling and the lifting mechanism. A vertically mounted flange type induction motor (1/2 HP) is used to rotate a motor shaft at a frequency up to a maximum of 1400 RPM. The speed of rotation is controlled by a variable frequency drive (VFD). Although this shaft is physically isolated from the remaining parts of the system by a metallic diaphragm, it induces rotation in another shaft placed vertically below it on the opposite side of the diaphragm with the help of a hermetically sealed magnetic coupling.

The 2^{nd} shaft is attached to a screw based molybdenum rod (20 mm diameter) which carries the corrosion sample.

The sample is in the form of a metallic disc having a provision of screwing the above mentioned molybdenum rod to a hole drilled axially along its centre. The disc is immersed and rotated in a pool of molten Pb-Li contained in a molybdenum crucible which is placed inside a stainless steel 316L (SS 316L) sample chamber. The Mo crucible has a diameter of 75 mm and a height of 120 mm out of which molten Pb-Li was filled up to a maximum height of 100 mm only, to avoid spillage during rotation of the disc. This means that a maximum volume of liquid metal/ alloy that can be filled in the crucible is ~ 450 cc which amounts to ~ 4.7 Kg of Pb-Li. The sample chamber with Mo crucible and the disc specimen are heated up to the desired temperature by split heaters placed around the stainless steel container. To ensure that the sample is completely immersed into the liquid, a screw based lifting mechanism and temperature based level sensors are incorporated at the bottom of the SS 316L sample chamber. The lifting mechanism allows vertical movement of the molybdenum cylinder during operation and level sensors indicate the exact level to which the crucible needs to be lifted such that the disc remains completely immersed. Figure 3.7 shows the actual photograph of the RDCTF. The photograph of the disc type sample fixed to the rotating shaft is shown in Figure 3.8 (a) while Figure 3.8 (b) shows the lead lithium solidified in the molybdenum crucible.

3.4.1. Sample Geometry for RDCTF

In the process of developing and improvising the above test facility, a number of different sample geometries have been developed and tested.

a. Single Disc Type Sample: - Initially a disc type of sample having a maximum diameter of 60 mm and a thickness of 8 mm was used for exposing into the liquid Pb-Li. The samples had a hole drilled axially in the centre, having an internal thread to screw a molybdenum rod (sample holder) having 20 mm diameter held axially along the centre. Some of the samples had the hole drilled only upto a certain depth (for e.g. upto 4 mm) such that bottom face of the sample did not have the central hole.

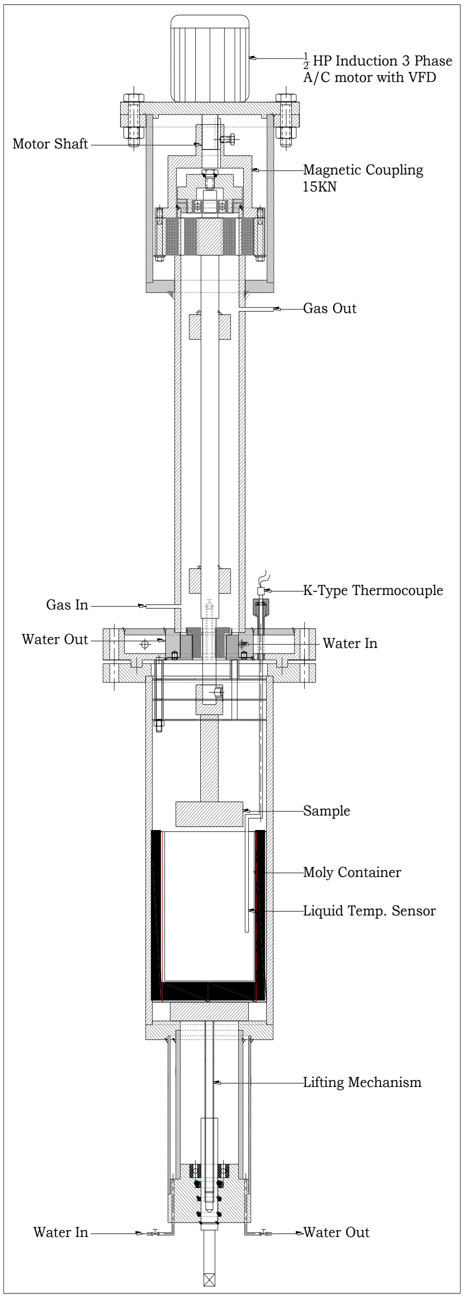

Fig.3.6: Schematic of the Rotating Disc Corrosion Test facility.

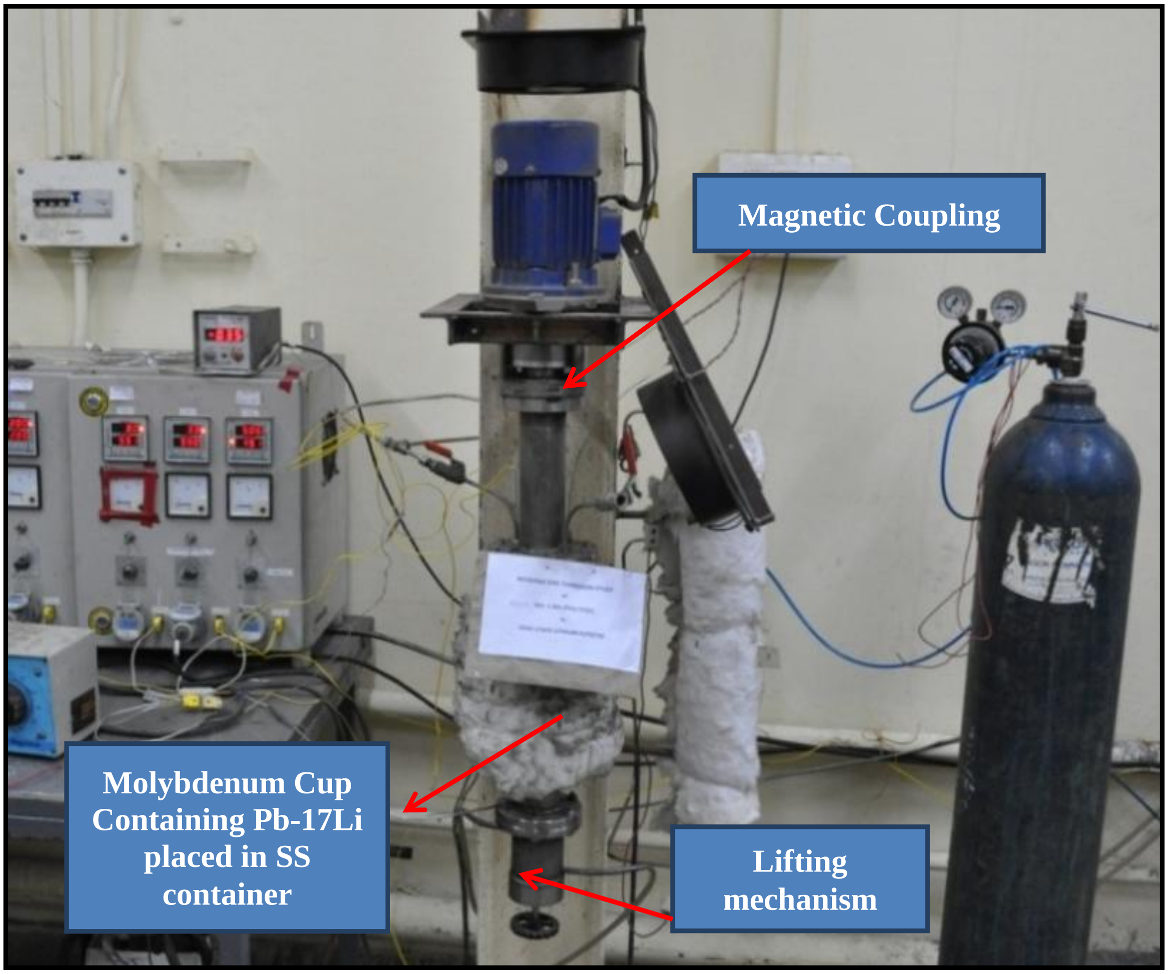

Fig 3.7: Actual photograph of the Rotating Disc Corrosion Test Facility.

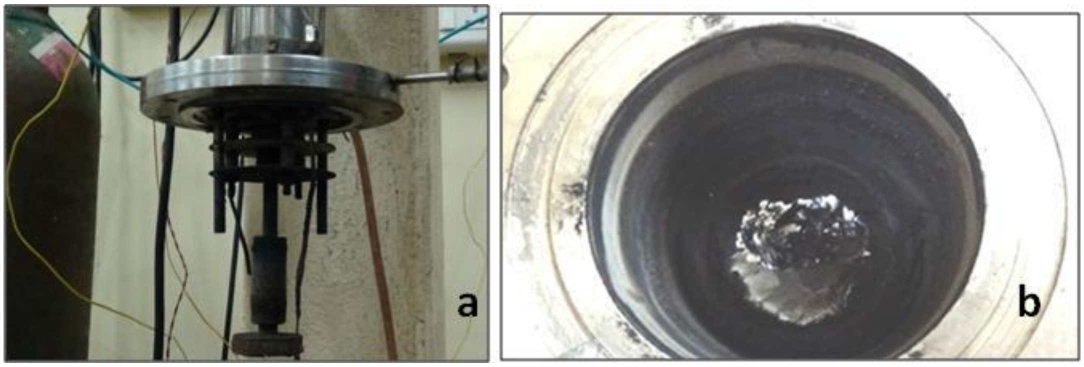

Fig 3.8 (a) Disc type sample fixed to the rotating shaft (b) Exposed Pb-Li solidified in the molybdenum crucible.

On the other hand, some had the axial hole drilled throughout its thickness. The schematic of both the samples are shown in Figure 3.9 (a) and (b) respectively. Although the former had an advantage of undisturbed sample surface which prevents any minor disturbance to the velocity profile; there was a practical challenge associated with the same.

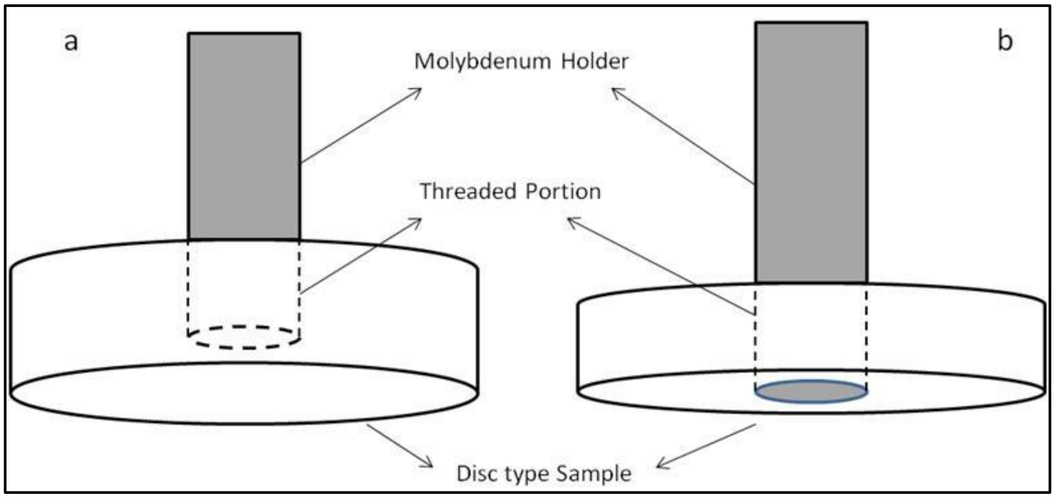

Fig. 3.9: Single disc type sample for RDCTF with (a) partial hole and (b) through hole along the centre.

The highly dense liquid (Pb-Li) always exerts a back force on the rotating disc when it is being stirred inside the molten pool. This demands enough screw length such that the disc is not accidentally isolated from the screw while rotation. Otherwise the thickness of the disc needs to be increased sufficiently which again makes the disc heavier in weight and exerts additional force on the sample holder. Therefore, the design of the disc where the screwing hole is drilled through the sample is more reliable while conducting long term corrosion experiments. Both the above sample geometries were used to conduct corrosion experiments with P91 and IN RAFMS material with Pb-Li. However, there was no possibility to expose multiple samples at a time so that time dependence of corrosion behavior under flowing conditions could be studied.

b. Segmented Disc Type Sample: In order to allow exposure of multiple samples and interim sample exchange in the RDCTF; a unique six segmented disc type sample was designed. The schematic of a segmented disc type sample fixed inside its Molybdenum sample holder; is shown in Figure 3.10. This type of samples allowed taking out of individual segments after regular intervals of time and analyzing them so as to understand the variation in corrosion rate or mechanism; if any. For fabrication of this segmented sample; initially a disc type sample having a maximum diameter of 60 mm is cut off from the plates (of P91 or IN RAFMS) with the help of Electric Discharge Machining (EDM). The disc had a central hole drilled through it having a diameter of 6 mm. The sample holder is fabricated out of a molybdenum rod (maximum diameter 65 mm) with the help of EDM and is machined in such a away so as to create a peripheral slot for accommodating the sample. Later the sample is machined at both the outer and the inner periphery in order to create specific grooves such that the disc can be accommodated in the sample holder. Afterwards, the entire top surface of the disc is ground and then polished using 1μm sized diamond paste. Finally the disk is cut into six equal segments with an included angle of 60°; with the help of EDM. Once the all the samples are fixed into the holder, a molybdenum screw having a head diameter of 6 mm fits into the central hole of the holder in such a way that the bottom surface of the integrated sample including the screw head and the holder are at level. This arrangement keeps the samples intact under flowing conditions while generates minimum flow disturbance. For the present work a 45 mm disc segmented disc type IN RAFMS sample was used. The schematic of the top surface and cross-section of one segment of this sample is shown in Figure 3.11 (a) and (b) respectively.

3.4.2. Geometric factor

Considering the total surface area of the disc type sample (60 mm dia) as that available for corrosion in the present case; the geometric factor comes out to be 6.4×10^{-2} m. On the other hand, the geometric factor of a segmented disc type sample having similar dimensions would be much lower since only the top surface is actually exposed to Pb-Li. However considering that some minimal amount of Pb-Li may also enter into the sides of the sample; the geometric factor for a 45 mm segmented disc type sample comes out to be 5.1 x 10^{-1} m. These values may be considered sufficiently safe to conduct long term corrosion experiment since results from similar kind of experiments have been reported in literature with geometric factors much lesser than the present one [125].

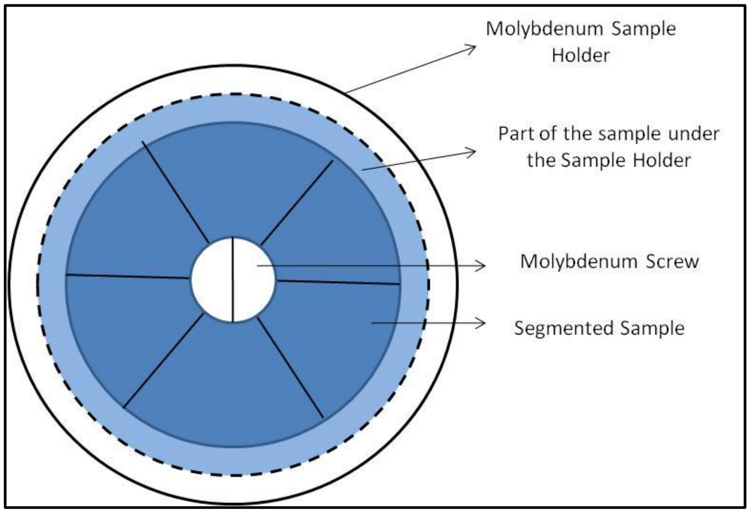

Fig. 3.10: Schematic of the six segmented sample fitted within the sample holder.

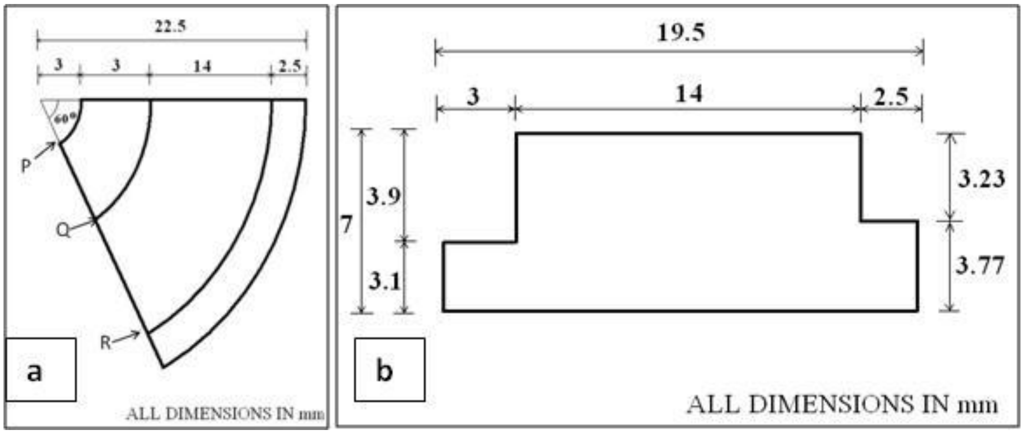

Fig. 3.11: (a) Top view and (b) Side view of one segment of the six segmented sample having 45 mm diameter.

3.4.3. Velocity Profile

The rotation of the disc specimen at a certain frequency (RPM) creates a variation of linear velocity along its radius starting from a zero value at the central axis. The linear velocity (v) corresponding to a radial distance (R) was given by Equation (1).

$v = 2 \Pi R N/60$ ……………………………………………………………….......... 3.2

Thus, there will be a variation of linear velocity along the radial direction of the disc which is illustrated in Figure 3.12. Since velocity is an important factor affecting the corrosiveness of liquid metals and alloys, the variation of linear velocity along the radius is expected to affect the extent of corrosion at different locations on the disc.

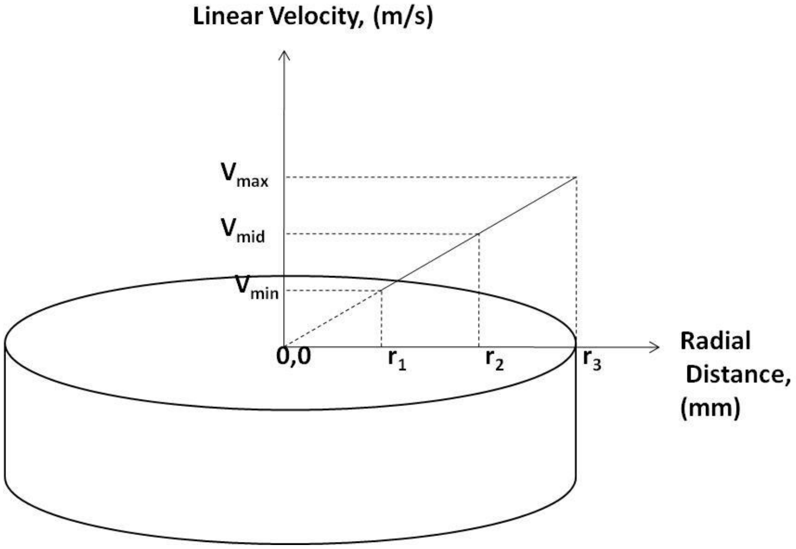

Fig. 3.12: Schematic of the disc sample showing increase in linear velocity (V) along the radial direction (R).

It may be noted that there is a possibility that the liquid may co-rotate with the disc but even in that case the co-rotation, velocity will be quite small and has been considered negligible in the present case. However, if the co-rotation of liquid is taken into consideration, then the measured corrosion rate will actually be valid for a lower value of liquid flow velocity than that calculated from rotation frequency of the disc in the present case.

The analytical solution of Equation 3.2 can give the distribution effective flow velocity of liquid along the radial direction of the disc. However, the distribution of fluid velocity in the entire fluid domain is also important in order to understand the transportation of corrosion products from the sample surface into the bulk of the liquid. For this purpose, a theoretical modeling of velocity was carried out with the help of Computational Fluid Dynamics (CFD) where three components of fluid velocity below the bottom surface of the disc have been considered i.e. radial, tangential and axial [176]. The details of the equations used to calculate these profiles and the parameters considered for CFD modeling along with the relevant references have been reported in Appendix 1.

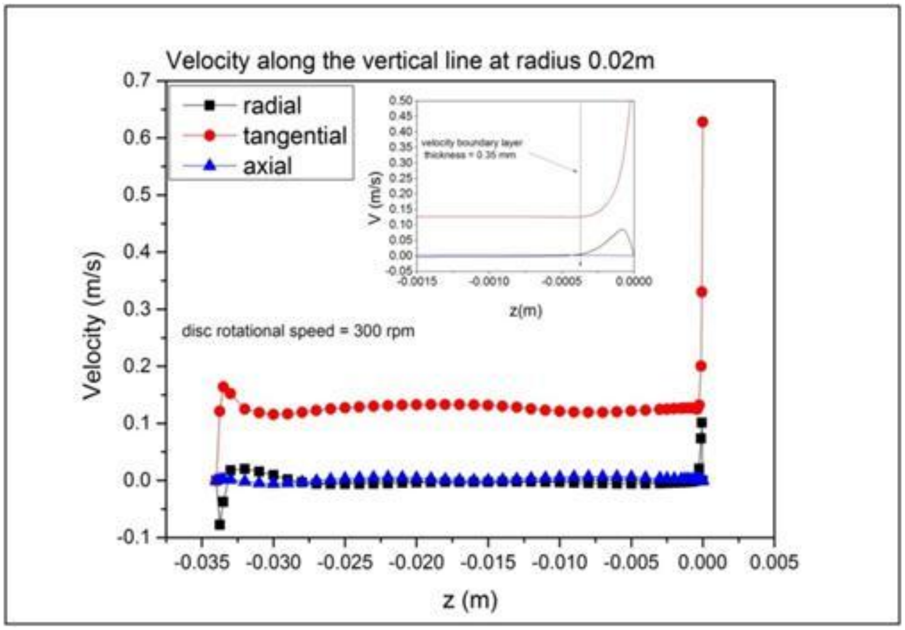

Fig. 3.13 Velocity profiles along the axial direction at radial distance of 20 mm from central axis obtained theoretically through CFD modeling.

Figure 3.13 shows the velocity profiles along the axial direction in the Pb-Li melt beneath the disc at a radial distance of 20 mm away from central axis; as obtained from CFD. The insert in Figure 3.13 shows the close up view of velocity variation near the disc bottom surface. From the variation of radial velocity coordinate, it can be said that the velocity boundary layer thickness at a radial distance of 20 mm from central axis is about 0.5 microns. Although there is no variation in the axial component upto a measurable depth below the disc surface; both the radial and the tangential component of velocity varies significantly within the above mentioned velocity boundary layer. The variation of the velocity in this layer points to the fact that any particle which gets dislodged from the disc surface due to corrosion will face a sufficiently high velocity towards the radial and tangential direction and would be easily taken away from the disc surface. The initial tendency would be to move away in the tangential direction since the tangential component is very high just below the surface. For eg ; for a disc of 50 mm diameter; the tangential velocity is ~ 0.5 m/s while the radial velocity is ~ 0.01 m/s just below the surface. However, as the particle reaches slightly downwards, the both the radial and tangential components starts decreasing and reaches a constant value. Nevertheless at all points below the disc, the tangential component always remains higher and creates a tendency to push any particle coming towards the centre of the Pb-Li melt towards the tangential direction.

Figure 3.14 shows the Radial, Tangential and Axial velocity contour at a plane parallel to disc bottom surface at a distance of 0.1 mm for a 50 mm disc rotating at 360 rpm in liquid Pb-Li obtained theoretically through CFD modeling. The disc has been indicated by an inner black circle in all the profiles. It could be clearly observed that the radial and tangential velocities are highest at the periphery of the disc which may result in maximum corrosion at this location. Once the corrosion products move away from the disc edge; they will move in the resultant radial /tangential direction untill they reach the inner edge of the molybdenum crucible. At this location; the axial velocity is maximum and thus the corrosion products will move up/down in the axial direction near the walls of the molybdenum crucible. Figure 3.15 (a) shows the axial velocity contour at a vertical plane passing through central axis of the fluid domain. It could be seen that the axial velocity beyond the disc edge is maximum near the edge of the molybdenum crucible and minimum near the disc edge. Both above and below the level of the disc, the axial velocity gradually decreases. Thus the corrosion products travelling to the edge of the molybdenum crucible will travel either up and down axially and will take a return path back to the level of the disc keeping close to the disc edge. This motion of corrosion product has been indicated by dotted line in Figure 3.15 (b).

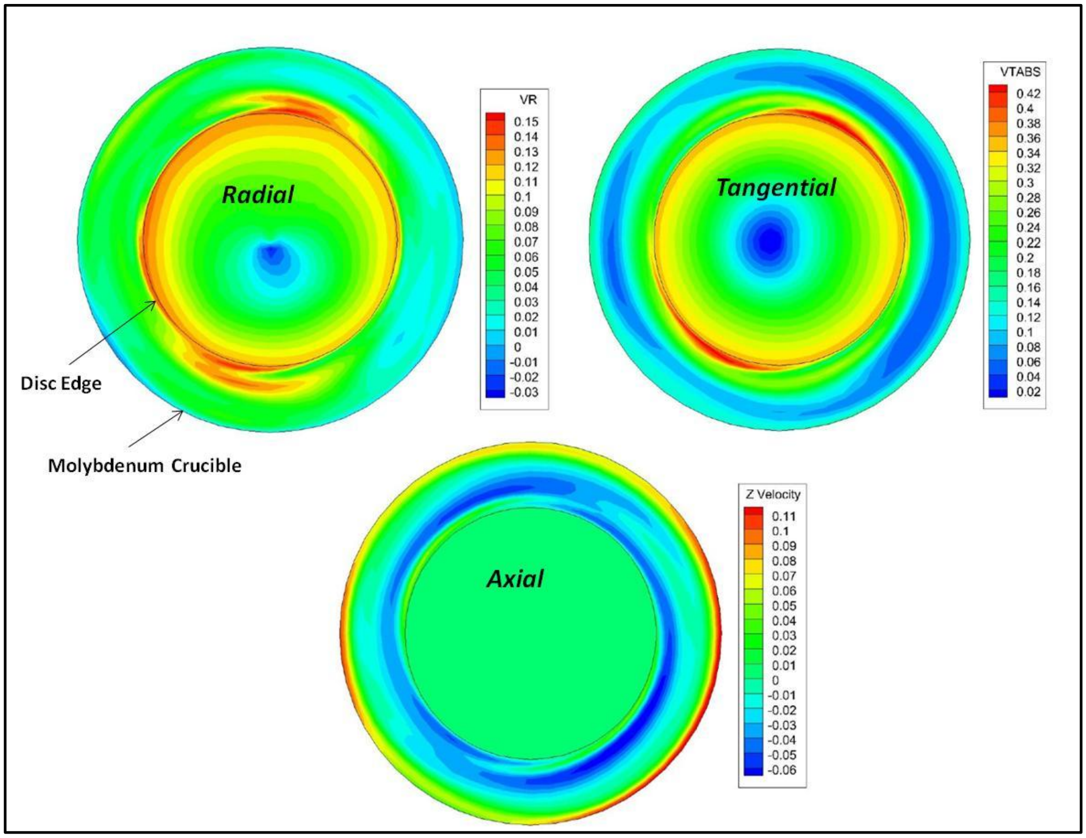

Fig. 3.14: Radial, Tangential and Axial velocity (absolute) contour at a plane parallel to disc bottom surface at a distance of 0.1 mm for a 50 mm disc rotating at 360 rpm in liquid Pb-Li obtained theoretically through CFD modeling.

The travel path of the corroded species indicates that there would be very less chance of erosion corrosion of the disc surface due to the corrosion products in liquid Pb-Li and precipitation; if any would preferably occur over the walls of the molybdenum crucible. It has been already discussed in Chapter 2 (Section 2.9.2. c; Equation 2.10) that the **wall shear stress ‘τ’** is a parameter which could be directly related to the intensity of turbulence in the fluid acting on the disc surface. This means, the higher the wall shear stress, the higher the turbulence and therefore the higher corrosive effect. The higher corrosive effect may be either due to faster removal of corroded species from the Pb-Li boundary layer adjacent to the disc surface or due to the easier detachment of the corroded layers. [140].

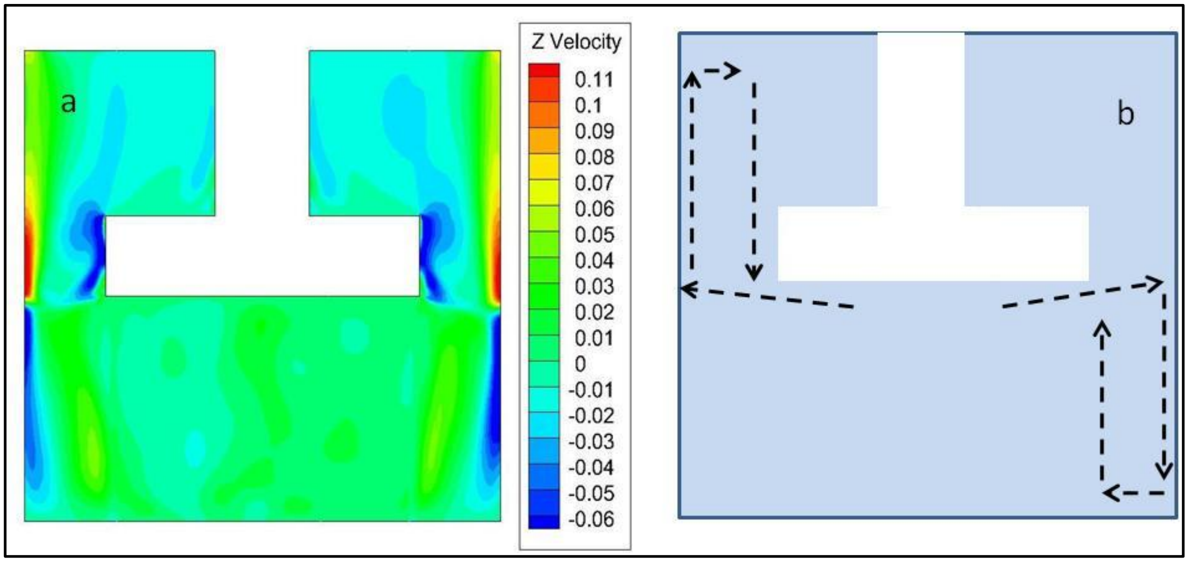

Fig 3.15: Axial velocity contour at a vertical plane passing through central axis of fluid domain.

The shear stress on the bottom surface of the disc in the radial (τ_{zr}) and tangential direction ($\tau_{z\varphi}$) have been calculated through CFD and have been plotted along the radial coordinate as shown in Figure 3.16. The details of the calculation have been given in Appendix A. It could be clearly seen that the shear stresses in both radial (τ_{zr}) and tangential direction ($\tau_{z\varphi}$) increases with increasing radial distance. This may lead to increased corrosion (dislodgement of weak corroded layer and corroded species) with increasing radial distance. Moreover, the increase in the tangential component of shear stress towards the disc edge is much greater than the radial component. This confirms the fact that any corroded species will try to travel towards the tangential direction away from the centre of the disc.

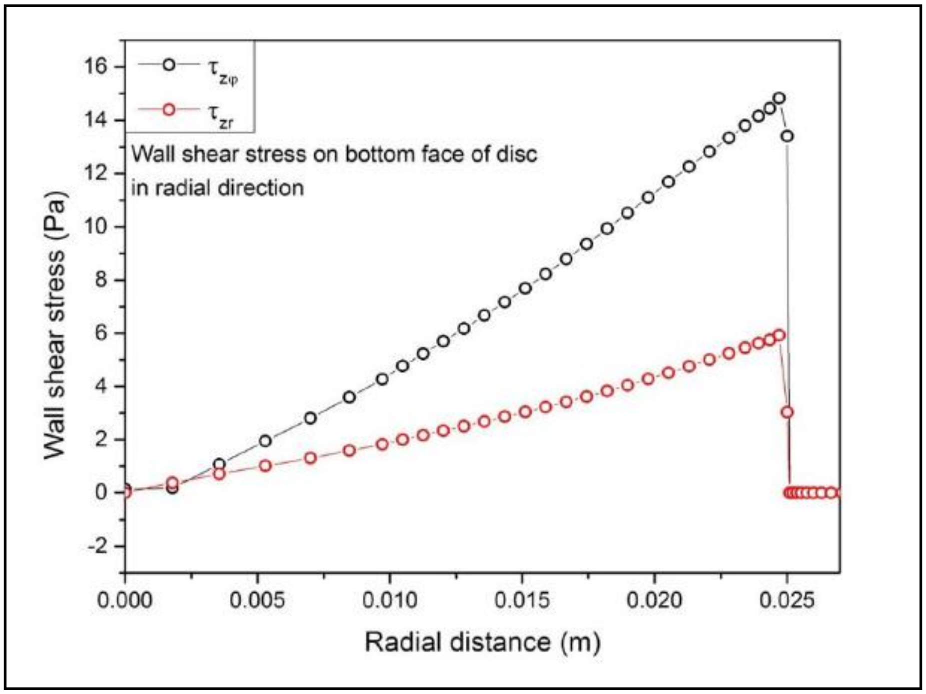

Fig 3.16: Shear stress generated for a 50 mm disc rotating at 360 rpm in liquid lead lithium obtained theoretically through CFD modeling.

With such theoretical information in hand; a number of experiments were carried out in the RDCTF with P91 and IN RAFMS material and the effect of flow velocity over the corrosion characteristics of these material under isothermal conditions within a temperature range of 773 K – 823 K (500 to 550˚C) was studied. Afterwards; the focus was shifted towards experiments under a more realistic situation simulating actual reactor conditions which led to the design of liquid metal loops.

3.5. The Electro-Magnetic Pump driven Pb-Li Loop (EMPPIL) at BARC, Mumbai

In order to study the corrosion behaviour of various structural materials in flowing lead-lithium eutectic; a forced circulation loop named as the Electro-Magnetic Pump driven Pb-Li Loop (EMPPIL) has been designed and developed at BARC. The loop allows conduction of corrosion experiments under non-isothermal flowing conditions at maximum temperatures of 823 K (550˚C) and flow velocities up to 1.5 m/s. The schematic diagram of EMPPIL indicating the major components and temperature zones is shown in Figure 3.17. It is *a "triangular"* type of loop fabricated out of SS316L tubes having 12 mm inner diameter and has a total holding capacity of 2 L of Pb-Li. The major components of this loop include an electromagnetic pump, an electromagnetic flow meter, a heater section, a sample holder and a finned tube heat exchanger with provision for forced air cooling.

The electromagnetic pump is a permanent magnet based rotating type induction pump and has been specifically developed for liquid metal loops running on liquid lead, lead bismuth of lead lithium eutectic. It consists of two parallel rotating discs having permanent magnets (Samarium Cobalt embedded over their periphery on the sides facing each other. The discs are centrally mounted on a rotating shaft which is connected to a VFD controlled DC motor. A flat channel of liquid metal (part of the loop piping) having rectangular cross-section is allowed to flow in between these rotating magnetic disc which in turn circulates the metal due to Lorentz force generated by the changing magnetic field by the principle of induction. The purpose of having a rectangular cross-section is to allow minimum gap between the magnetic poles and the liquid metal and maximum interaction with the magnetic field. The photographs of the liquid metal channel placed inside the rotating shafts are shown in Figure 3.18 (a) and (b) while a photograph of the electromagnetic pump connected to a loop is shown in Figure 3.18 (c).

A cylindrical expansion tank having 40 mm inner diameter is provided at the highest level of the loop (above the test section) for accommodating volumetric changes in Pb-Li due to thermal expansion and contraction during operation. A cylindrical melting tank having 100 mm inner diameter is connected to the loop at the bottom and was used for melting the solid Pb-Li before filling of the loop as well as for draining the liquid after the experiment. An inert atmosphere of high purity argon gas is always maintained over the molten Pb-Li in the melting tank and expansion tank. The entire loop is heated by a combination of programmable logic controlled

(PLC) trace heaters (capacity1 KW or 3 KW each) and insulated by mineral wool of sufficient thickness. K type thermocouples welded to the SS316L tubes measures the temperature at different locations.

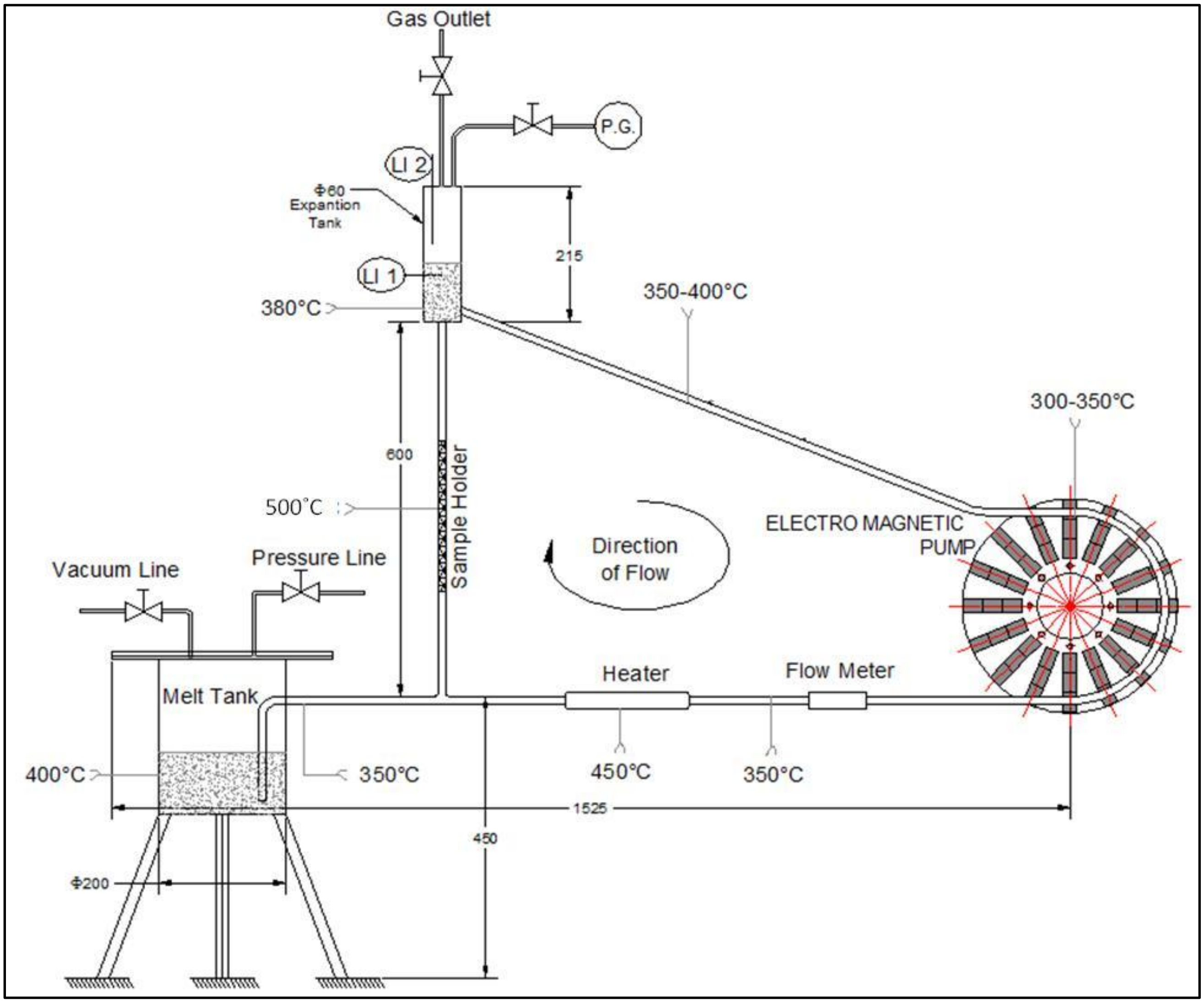

Fig. 3.17: Schematic diagram of the Electromagnetic Pump driven Pb-Li Loop (EMPPIL).

A temperature of 573 ± 5K (300 ± 5°C) is generally maintained near the electromagnetic pump in order to avoid overheating of the permanent magnets used in it. The pump helps in driving the liquid towards the electromagnetic flow-meter where the temperature is maintained within 623 ± 5K (350 ± 5°C) with the help of 1 KW capacity trace heaters. Afterwards, the liquid moves to the heater section which is traced with 3 KW heaters and carries a greater bulk of liquid (due to larger volume). This helps in increasing the liquid temperature up to 723 ± 5K (450 ± 5°C).

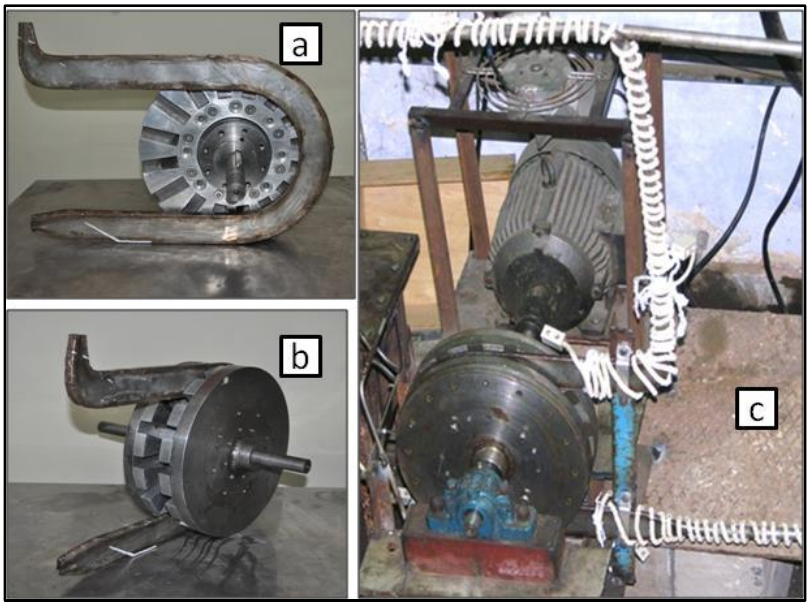

Fig. 3.18: (a) and (b) Liquid metal channel placed inside the rotating shafts and (c) the electromagnetic pump connected to a loop.

The rest of the length of loop piping between the heater section and the sample holder is heated with 3 KW trace heaters in order to finally attain a temperature of 773 ± 5 K (500 ± 5˚C) at the sample holder. The remaining part of the loop after the sample holder including the expansion tank is once again traced by 1 KW capacity heaters and the temperature distribution of these locations have been already indicated in Figure 3.15. Since the part of the loop which passed through electromagnetic pump can not traced with heaters in order to have maximum interaction of the flowing liquid with the magnetic field provided by the pump; a temperature of 573 ± 10 K (300 ± 5˚C) is automatically attained at that location. Two sets of liquid metal level indicators are provided at the melting tank and expansion tank while the cover gas pressure in both the tanks is monitored by dial gauges. The actual photograph of EMPPIL is shown in Figure 3.19.

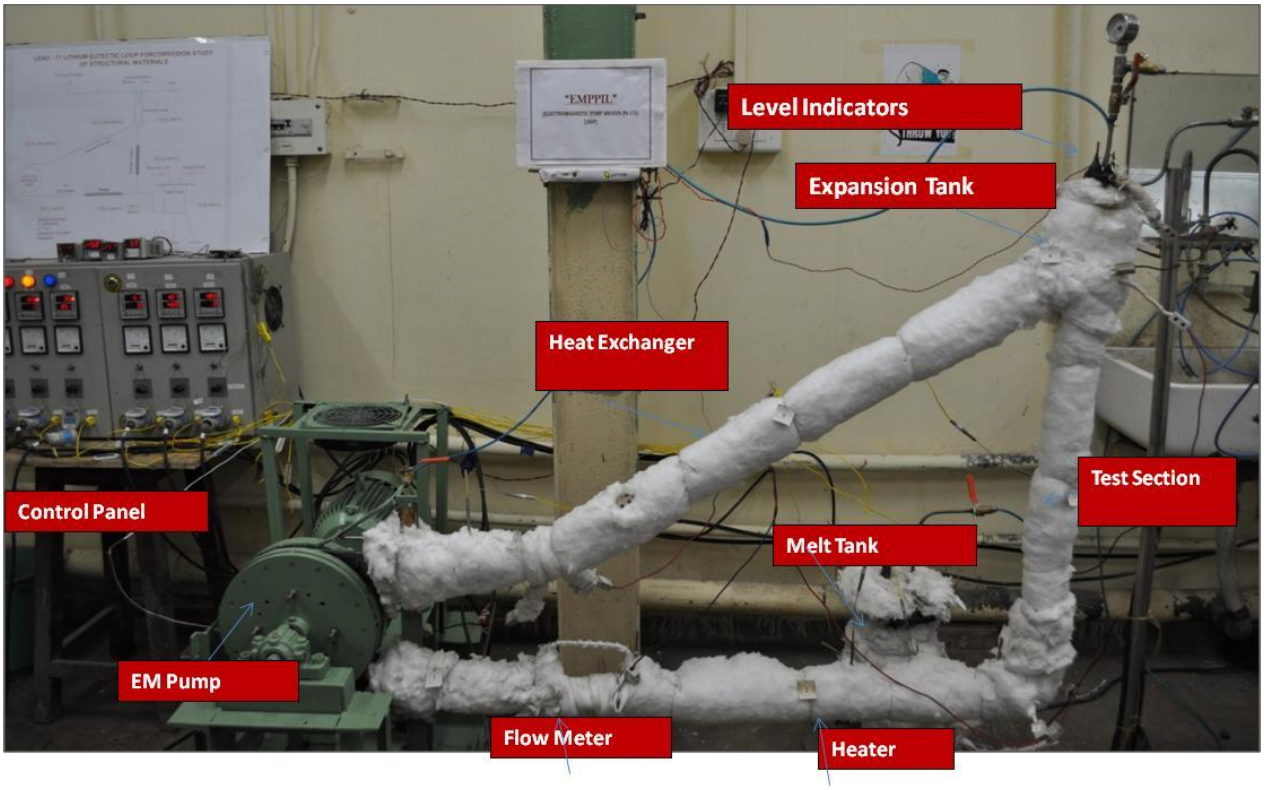

Fig. 3.19: Photograph of the Electromagnetic Pump driven Pb-Li Loop (EMPPIL).

3.5.1. Sample Geometry and Sample Holder

The sample holder of EMPPIL is 200 mm in length made of SS316L material and has an inner diameter of 15.7 mm. The sample holder made out of SS316L material was 200 mm in length and had an inner diameter of 15.7 mm. Rectangular test samples are fixed in a vertical stack inside the sample holder with the help of molybdenum screws and attachments. The greater diameter for sample holder compensates for the reduction of flow area due to placement of samples. A schematic of the sample holder having four rectangular samples of size 25 mm x 8 mm x 3 mm is shown in Figure 3.20. The samples are located one above the other, axially along the sample holder, in such a way that the centre line of the test section and the sample stack coincides. The sample holder is welded to the loop piping after fixing the samples and therefore flange joints are completely avoided in the loop in order to prevent unnecessary leakage.

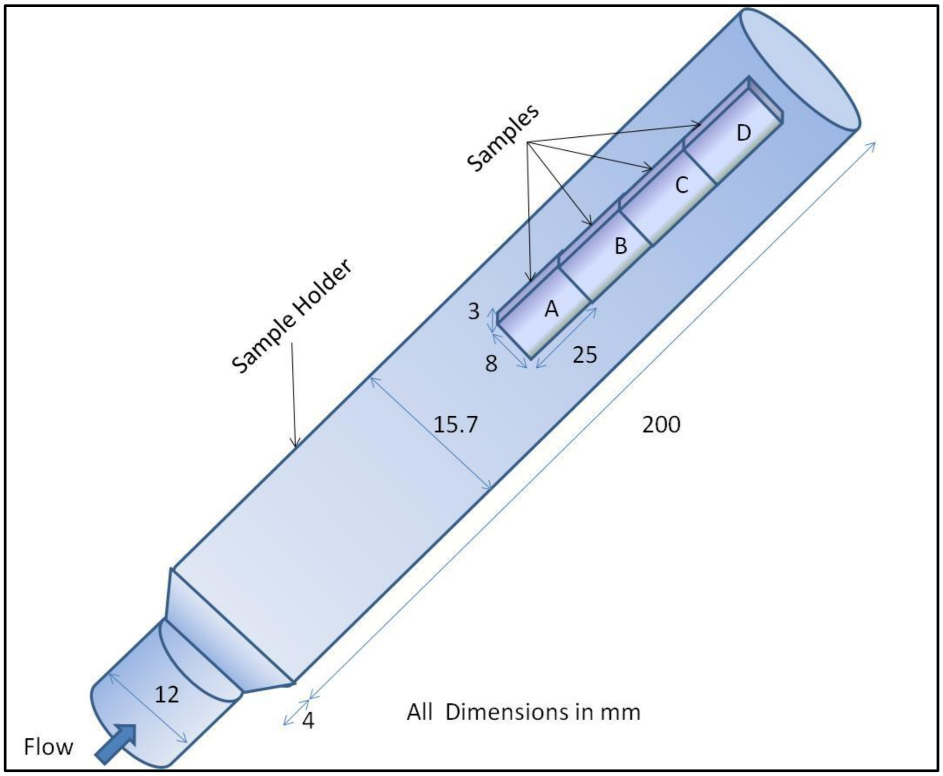

Fig. 3.20: Schematic diagram of sample holder in EMPPIL indicating the location of the samples.

3.5.2. Velocity Measurement and Distribution

The velocity of the flowing Pb-Li is measured with the help of an electromagnetic flow meter which has been also developed as a part of this study. The flow meter basically consists of C-shaped holder having two permanent magnets fixed to its inner sides. The holder is placed over the loop in such a way that a part of the loop which is flattened enough to have a rectangular cross-section (i.e. flow meter section) comes in between the magnetic poles. The flowmeter section has two metallic electrodes welded to the opposite sides of its shorter edges such that the electrodes are located normally a line which can connect the magnetic poles. A schematic drawing of the flow meter and the flowmeter section is shown in Figure 3.21.

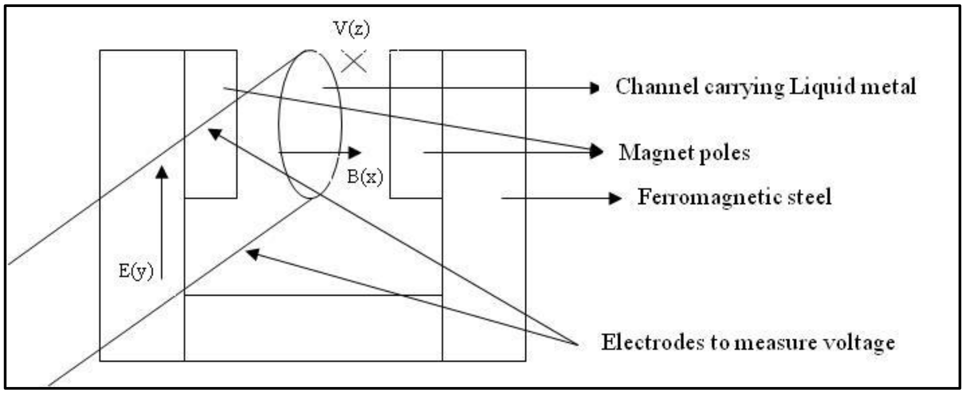

Fig 3.21: Schematic diagram of the electromagnetic flow meter.

Although an average velocity is maintained in the overall loop piping which is monitored by the electromagnetic flow meter; a variation in this value is expected to occur inside the sample holder due to the change in cross-sectional area and the presence of samples which may also create disturbance to the flow. The detailed distribution of flow velocity inside the sample holder has been simulated using CFD) technique and is shown in Figure 3.22 while the methodology adopted for CFD simulation is given Appendix 1. For this purpose; an inlet velocity of 1.5 m/s and a uniform temperature of 773 K (500°C) over the sample holder, were considered as the initial conditions.

The initial flow velocity of 1.5 m/s present at the entrance was found to decrease on entering the sample holder (1 m/s) due to increase in flow area with the minimum velocity along the walls of the holder (0.07 m/s). This indicates that the walls of the holder actually face a less aggressive condition and are protected as compared to the samples. This is because a reduction in flow velocity is directly related to reduction in corrosion rate [186]. The sample stack acts as a disturbance to the flow and therefore a high velocity almost equivalent to 1.5 m/s is regained at the beginning of the sample stack (near sample A) and along the vertical edges of the samples. Nevertheless, the center-line velocity over surfaces of all the samples remained much lesser (0.6-

1.0 m/s). The comparatively lower flow velocity along the walls of the sample holder (0.07 m/s) as shown in Figure 3.22 is one of the factors that may protect them from higher corrosion attack by lead –lithium eutectic as compared to the samples. However; as discussed in the previous sections; the geometric factor will give a better indication whether; the corrosion of SS316 L tube material may interfere with the corrosion of the actual test coupons.

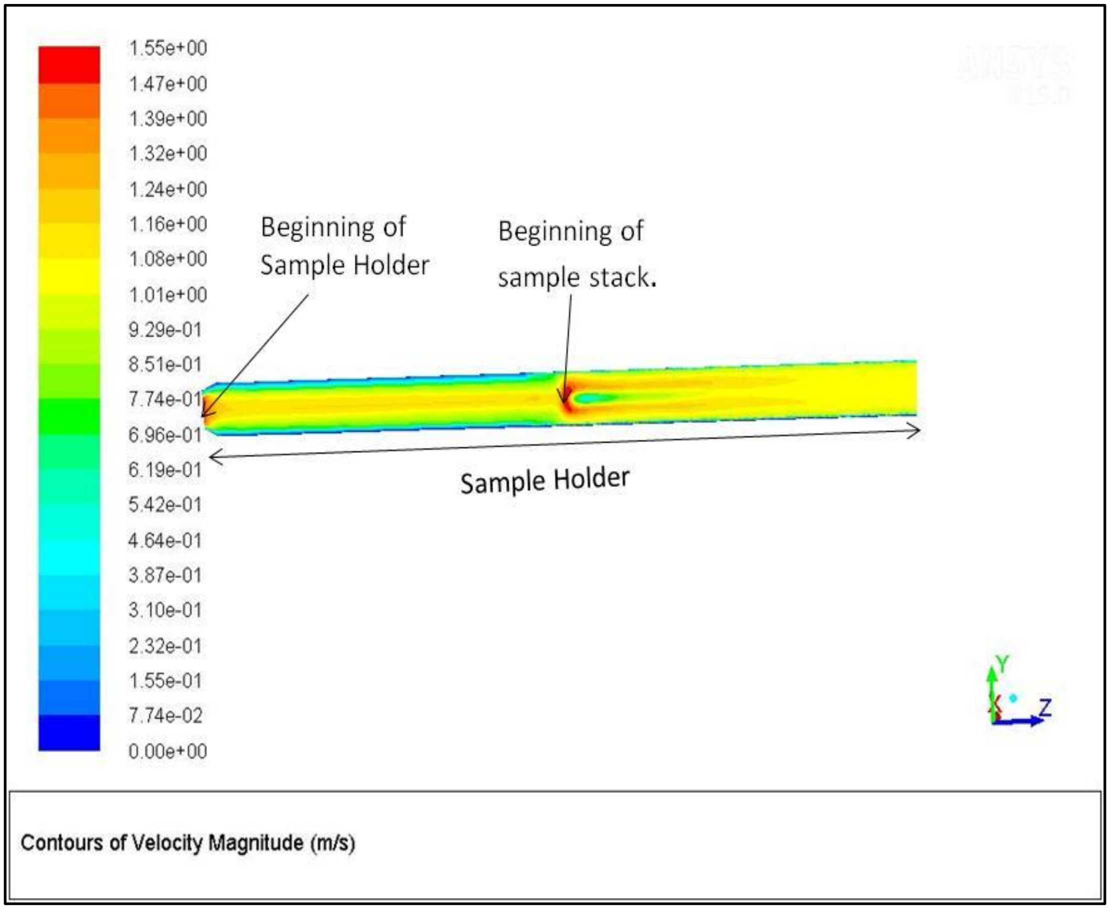

Fig 3.22: Distribution of flow velocity inside the sample holder simulated through computational fluid dynamics (CFD) technique.

3.5.2. Geometric factor

The ratio of surface area of SS316L piping to that of the corrosion coupons for those parts of the loop exposed to Pb-Li at or above 673K (400˚C) comes out to be 64. This indicates that a greater area is available for corrosion from the SS 316 L tube surfaces as compared to that from the corrosion coupons. However, considering the total surface area of the SS316L tube walls and the corrosion samples and the volume of Pb-Li causing their corrosion, the geometric factor comes out to be 1.7 x 10^{-2} m which is one order of magnitude higher than other liquid metal corrosion experiments reported in literature e.g. 0.33 x 10^{-3} m [38]. It may be noted that in the calculation of geometric factor; we have only considered those parts of the loop which are exposed to Pb-Li at or above 673K (400˚C) since measurable corrosion of SS 316 L in Pb-Li starts only above 673 K [155].

3.6. The electromagnetic pump driven loop PICOLO at KIT, Germany

The EMPILL loop at BARC was used to conduct corrosion test on P91 and IN RAFMS material in lead lithium eutectic at 773-823 K (500 -550˚C). In order to generate compare the corrosion characteristics of IN RAFMS with the European standard material EUROFER, some samples of IN RAFMS were tested in the internationally renowned forced circulation PICOLO loop at Karlsruhe Institute of Technology, Germany [161]. The isometric view of PICOLO loop is shown in Figure 3.23 [181]. It consists of a Figure-of-eight type loop with a central recuperative heat-exchanger, a test section (hot leg) and a cold leg for corrosion product deposition and impurity removal with a pump, flow meter, cooler and magnetic trap. Heat exchanger, main heater, test section (hot leg) and the tubes of the hot section were fabricated of ferritic steel (DIN 1.4922) whereas in the cold section austenitic steel (DIN 1.4571) was used. The whole circuit was connected to a dry Argon glove box on top of the expansion vessel.

The glove box has a gas purification unit, which is capable to keep the oxygen concentration below 1 ppm. The Pb-Li alloy is melted in the glove box and filled into the loop through the expansion vessel. The dump tank is used for draining the liquid metal. The test section comprises of a tube of 16 mm inner diameter and 440 mm length. The temperature in the test section is maintained at a maximum of (823K) 550 °C, the coldest temperature is maintained before the magnetic trap which is 623 K (350 °C).

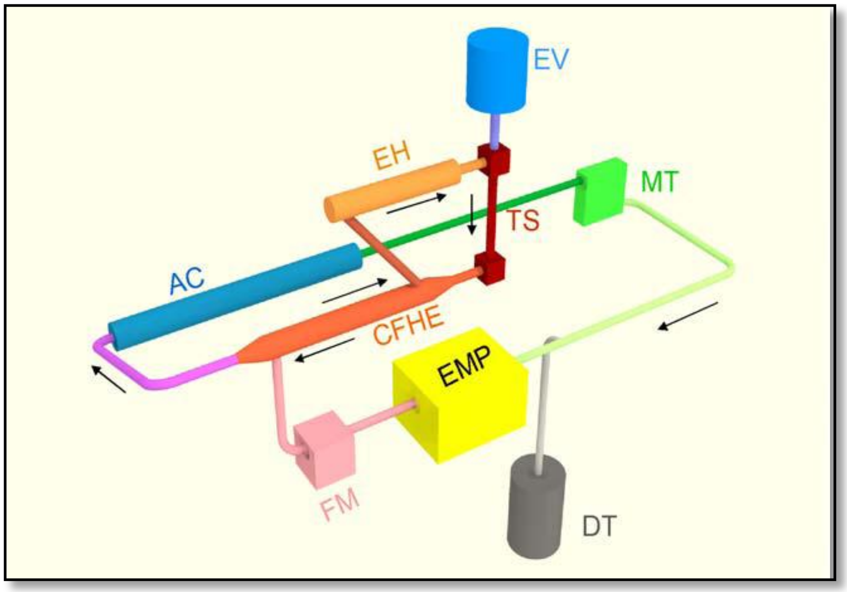

DT = Dump Tank, EMP = Electro-Magnetic Pump, FM = Flow Meter, CFHE = Counter Flow Heat Exchanger, AC = Air Cooler, EH = Electrical Heater, EV = Expansion Vessel, TS = Test Section, MT = Magnetic Trap

Fig. 3.23: Isometric view of the PICOLO loop at KIT, Germany [181].

3.6.1. Sample Geometry

The samples used for PICOLO loop a cylindrical in shape (8 mm in diameter and 35 mm length) as shown in Figure 3.24. The samples could be stacked onto one another with the help of male and female thread (screws) made on either side of the samples. Such samples have the advantage of posing minimum disturbance to flow and corrosion is expected to be uniform over its entire circumference. This facilitates the determination of corrosion rate from the reduction in thickness at any point on its surface. Many research groups are under the opinion that this method eliminates the doubts of removal of parts of corroded layer during sample cleaning which is a major requirement for determination of corrosion rate through weight loss method. However, this method depends on averaging out the measured data and thus its efficiency depends on the number of iterations conducted and does not take account of the actual loss of material.

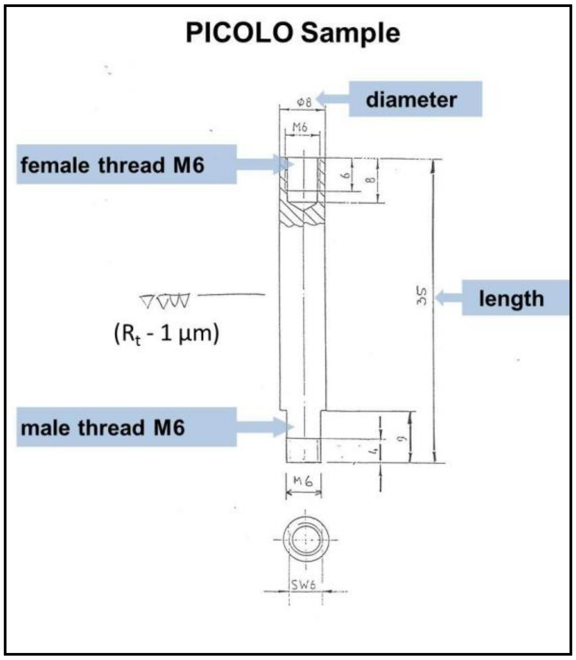

Fig. 3.24: Cylindrical corrosion test samples used in PICOLO loop.

3.7. Forced Circulation Loop with magnetic field at IPUL, Latvia

The effect of magnetic field on enhancing the corrosion attack by Pb-Li has been already witnessed for EUROFER samples [182,184] and discussed in Chapter 2 (Section 2.10). In order to study the effect of magnetic field on the corrosion of P91 and In RAFMS some experiments in flowing Pb-Li in forced circulation loops have been carried out at IPUL, Latvia and BARC, Mumbai

For conducting corrosion experiments on P91 with Pb-Li in the presence of magnetic field, a pump driven loop was set-up at Institute of Physics, University of Latvia. A schematic diagram of the loop made out of SS316 L is shown in Figure 3.25. The principle components of the loop are the electromagnetic pump; the circular liquid metal heat exchanger, the cross flow heat exchanger, the electromagnet (of 1.8 T), the MHD flowmeter and the test section. These are shown in Figure 3.26. Heater coils are wound on different parts of the loop and the temperature was maintained and controlled using PID controllers. In this loop, samples can be exposed to Pb-

Li in the test section both in the presence as well as in the absence of magnetic field, at a temperature of 773 K – 823 K (500 – 550˚C). The liquid metal flow path is as follows: - *Electromagnetic pump; Flow meter; Cross flow heat exchanger (cooler side); Test section; Cross flow heat exchanger (hotter side); Circular heat exchanger; back to the Pump.* In the cross flow heat exchanger, hot liquid metal, coming from the test section loses its heat to relatively cold liquid metal coming from the electromagnetic pump. On the other hand, in circular heat exchanger, liquid metal loses its heat to oil and oil in turn passes the heat to water. The dump tank is used to melt Pb-Li and drain back when necessary while the expansion tank is used to accommodate the change in liquid level during temperature fluctuations.

3.7.1. Geometry of the Samples and the Test section

The test section used for containing the samples has a rectangular cross-section of 36 mm x 18 mm and a thickness of 3.2 mm while the corrosion coupons have dimensions of 35 mm x 9.5 mm x1.6 mm. The parts of the test section carrying samples outside magnetic field are covered by a ferromagnetic choke in order to avoid stray magnetic fields. For the ease of placement of samples inside the test section, it had been fabricated in 3 parts and later on welded together. Inside the rectangular test section two C- shaped Niobium (Nb) plates have been fitted with the samples placed in between them. The Nb plates serves as a suitable sample holder since they have very low solubility in Pb-Li [195] and also provided better corrosion resistance to the stainless steel tubes.

Inside the sample holder, the samples are placed in the 3 regions such that some samples are placed before and after the magnetic field while some are placed in between the magnetic field. A 33 mm wide Nb plate is kept before placement of samples in of the three regions in order to stabilize the flow. A 90 mm gap is also kept on both sides of the samples placed inside the magnetic field to avoid interference with the outer samples. Figure 3.27 (a) and (b) shows different components of the test section.

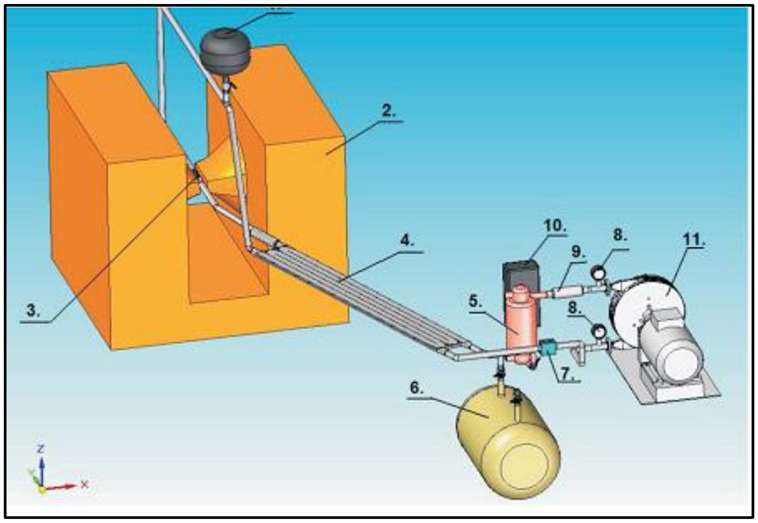

1 – expansion vessel; 2 – electromagnet; 3 – test section; 4 – counter flow heat exchanger; 5 – heat exchanger; 6 – supply tank; 7 – valve; 8 – pressure meter; 9 – flow meter; 10 – frequency converter;11 – electromagnetic pump.

Fig 3.25: Principle layout of the Pb-Li corrosion test loop at IPUL, Latvia [182].

Fig 3.26: Important Components of the loop (a) Electromagnetic Pump, (b) Circular Heat exchanger (c) Cross Flow Heat exchanger (d) Electromagnet (e) Test Section.

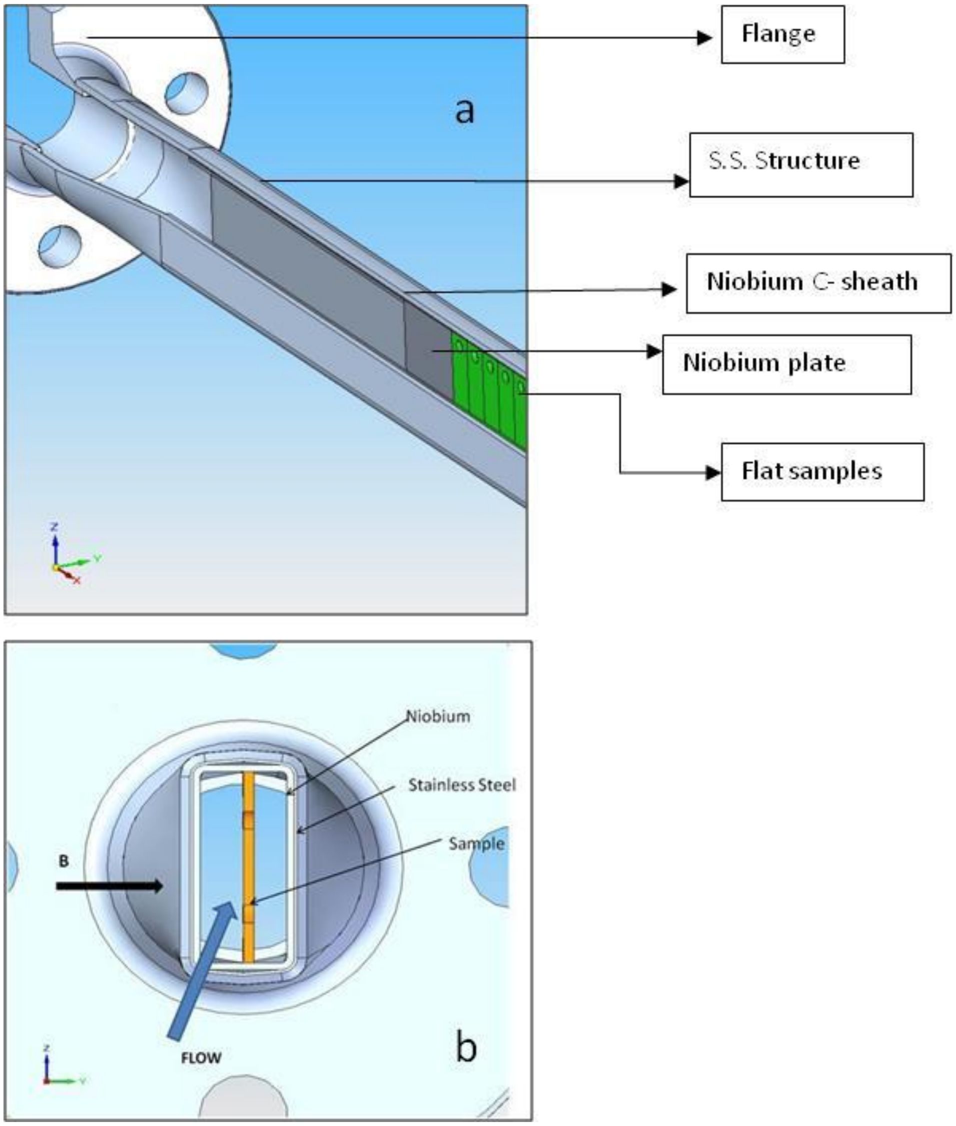

Fig. 3.27 (a): Different components in the first half of the test section before magnetic field and (b) Direction of flow and magnetic field.

3.7.2. Magnetic Field mapping in test section

The magnetic field distribution in between the pole gap of electromagnet at the region (where the samples are placed) has been measured using a Hall probe. Since the magnetic field in between the pole gap is symmetric with respect to the centre in all the directions, field mapping has been performed in only one eighth of the total pole gap volume. From the above measurements, it is observed that magnetic field is almost uniform (only 3-5% variation) from z = -25 mm to +25 mm, y= -7 to +7 mm and x= -70 mm to +70 mm as shown in Figure 3.28. Since the cross-sectional area of the test section is 39.2 mm x 22.2 mm and its length is 912 mm, it has been confirmed that the test section would be located in the uniform magnetic field region.

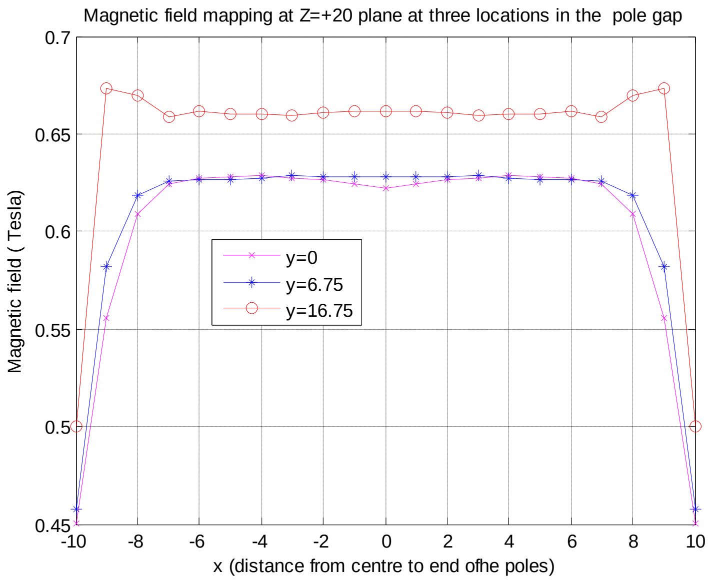

Fig 3.28: Magnetic field mapping at z= +20 mm in the IPUL loop with 1.8 T magnetic field.

3.8. Modified Electromagnetic Pump Driven Pb-Li Loop (EMPPIL-M) at BARC, Mumbai

In order to conduct preliminary corrosion experiments with IN RAFMS samples in Pb-Li in the presence of magnetic field, the EMPPIL facility existing at BARC has been slightly modified and coupled with a 0.5 T Dipole (permanent) magnet. For this, the dipole magnet has been installed over a support base such that a part of the test section comes in between the pole of the magnetic field. The samples are loaded in the test section in such a way that one/two samples are placed inside the magnetic field while others outside the field. The sample holder geometry for this loop is similar to the earlier configuration as shown in Figure 3.20. The coil type heaters are by-passed around the part of the test section within the magnetic poles and temperature is maintained at 773 K (500˚C) with the help of insulation. This ensures maximum interaction of the magnetic field with the test samples. Flat rectangular sample are specifically chosen for this loop in order to have a uniform magnetic field over the sample surface. The samples are placed in such a way so as to have the edge having the largest surface area located in a direction perpendicular to the magnetic field. A schematic of the modified EMPPIL loop is shown in Figure 3.29 while the actual photograph of EMPPIL-M is shown in Figure 3.30.

3.8.1. Magnetic Field Mapping

The uniformity of magnetic field in the space between the magnetic poles has been measured with the help of a Guassmeter. A field uniformity of 95 % has been observed over the active volume of of 35mm x 50mm x 50mm and the results are shown in Figure 3.31. The field of 0.5 T provided by the dipole magnet is comparatively lesser as compared to the field used in IPUL Loop (Section 3.7.2). However, even the results obtained from a single sample placed under uniform field can give a first had information of their corrosion behavior in the presence of magnetic field.

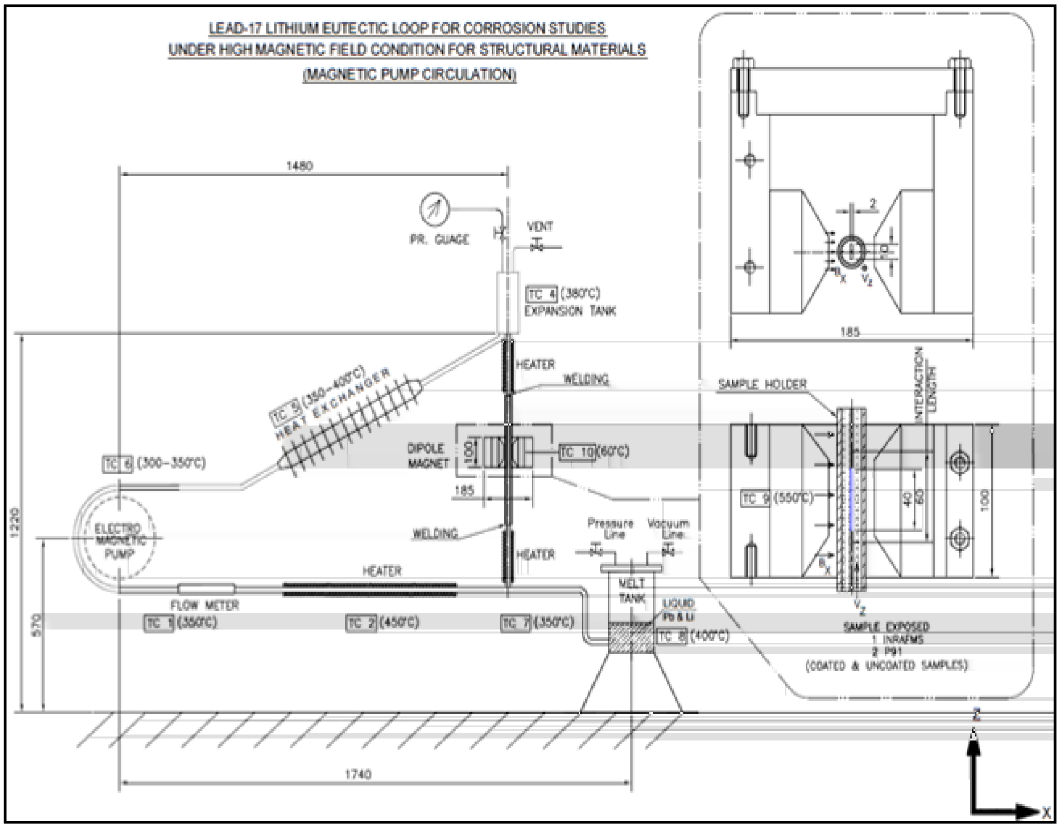

Fig 3.29: Schematic of modified EMPPILloop (EMPPIL-M) with magnetic field.

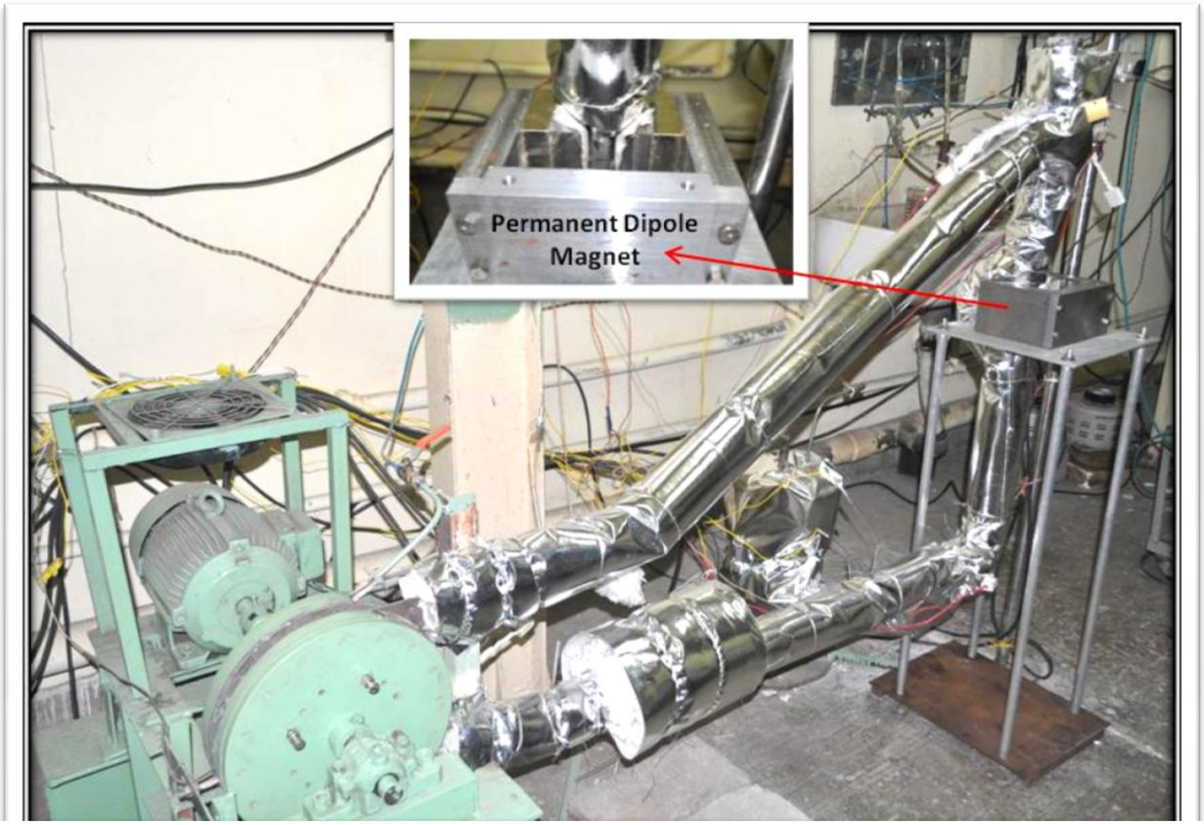

Fig. 3.30:Actual photograph of modified EMPPIL (EMPPIL-M) with permanent magnet.

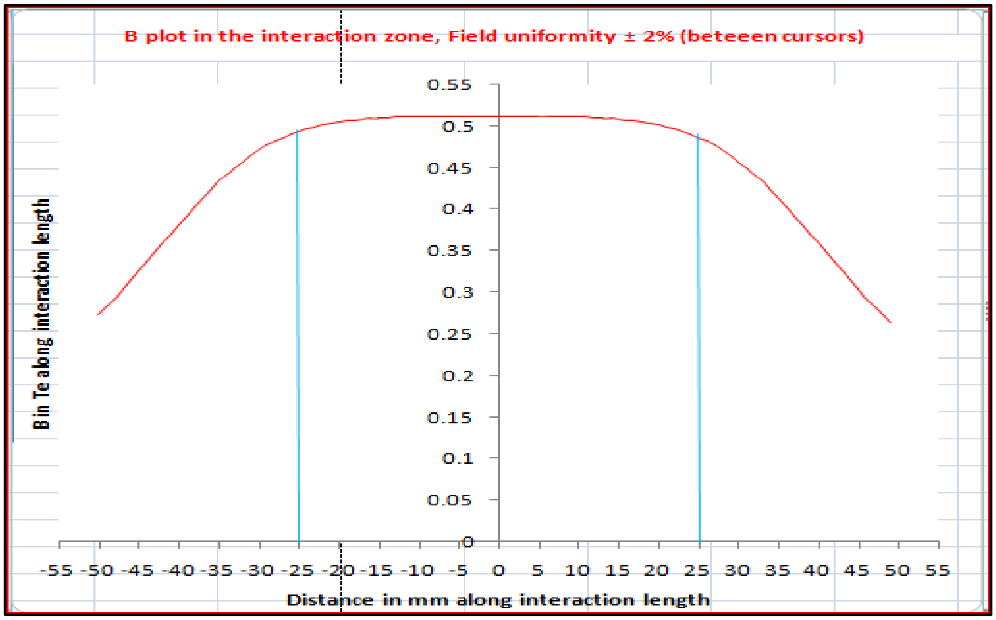

Fig. 3.31: Magnetic field mapping at z= 0 (55 mm from edge) in EMPPIL-M with 0.5T magnetic field.

3.9. Basis of selection of operating parameters

3.9.1. Selection of Temperature of Exposure

A principal mission of the ITER Test Blanket Module (TBM) program is to develop, deploy, and operate DEMO-relevant test blanket modules that can provide integrated experimental data and operational experience in a true fusion environment [12]. As discussed in Chapter 2 (Section 2.2.1; Table 2.1) the operating temperature range for Pb-Li eutectic for ITER Test Blanket module is 593 K -763 K (320–490˚C) while the maximum temperature of RAFMS material in contact with ceramic breeder zones at a heat flux of 0.5 MW/m^2 is ~ 773 K (500˚C) [14]. In this regard, the schematic diagram of the Indian LLCB TBM showing various ceramic breeder zones and the Pb-Li flow channels is shown in Figure 3.32 while the linear temperature distribution profile along various locations along this TBM at different Pb-Li flow velocities is shown in Figure 3.33. However, for a DEMO relevant Test Blanket Module the Pb-Li loop will operate within 593 K -763 K (320–490˚C) while the maximum first wall temperature may shoot upto 520˚C [14].

Initially, most compatibility testing especially with EUROFER was performed at temperatures below or at 773 K (500˚C) [161-163]. In the last 10 years, test conditions for the European TBM were modified and corrosion behavior was analyzed at a higher test temperature (823 K or 550˚C i.e. new TBM operation temperature) [167,194]. In order to study the compatibility between fusion materials and liquid Pb-Li in China, the thermal and forced convection loops of the DRAGON series (DRAGON-I, II, III and IV) have been built since 2005 for operating at 753 K-973 K (480 - 700°C) and a static isothermal capsule DRAGON-ST has been built in 2008 for operation at ∼973 K (700 °C) [165,191]. In Japan, the temperature for corrosion test of JLF 1 steel in Pb-Li eutectic under static conditions was 773 K. According to the authors, this temperature corresponds to the outlet temperature of a liquid Pb-Li in fusion blanket systems. [144].

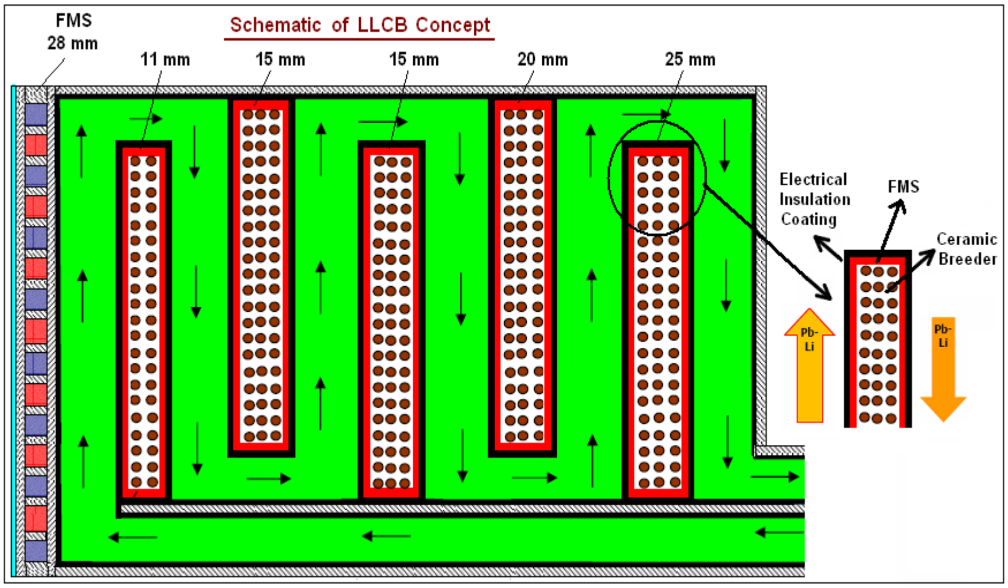

Fig 3.32: Schematic of LLCB TBM Concept. Arrows show the path of Pb-Li flow [46].

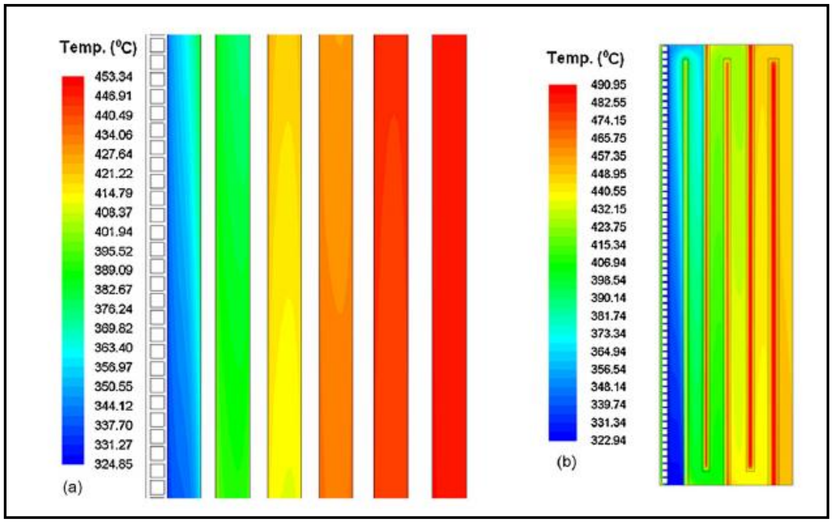

Fig 3.33: (a) Temperature contour in LLCB TBM, (b) temperature contour in Pb-Li loop only [46].

Thus, in order to choose an optimum temperature of exposure for the first set of Pb-Li compatibility experiments on IN RAFMS and for sake of comparison with the vast database of corrosion rates of F/M steels available in literature, the temperature of 773 K (500˚C) was chosen for most of our experiments. This temperature gives a reliable upper limit of the corrosion attack possible in an ITER/DEMO relevant TBM system. However, some experiments in static and flowing conditions have also been carried out at 823 K (550 °C) to assess the effect of temperature on corrosion rate. This range of temperature (773 K to 823 K) covers the best operating window for ferritic –martensitic steels in terms of mechanical properties [56].

3.9.2. Selection of Flow velocity for exposure

Examination of the variation in corrosion rates of a material exposed to Pb-Li at the same temperature in static and dynamic conditions has given the first hand indication of the effect of flow. Moreover the variation of linear velocity along the radial direction of a disc sample exposed to stirring system can also be correlated to the extent of Pb-Li attack at respective locations. On the other hand the variation of local flow velocity over individual samples exposed to a non-isothermal Pb-Li loop is also expected to cause a variation in corrosion rate. The corrosion behaviour of JLF 1 steel was also studied at flowing conditions at a Pb-Li velocity of 0.08 m/s and yielded a corrosion rate of 17 µm/y [164]. The corrosion of JLF 1 steel was studied under the above discussed i.e. static; isothermal stirring and non-isothermal stirring/flowing; and a clear effect of flow velocity on the corrosion rate was observed as given in Table 3.1 [186].

Table 3.1: Corrosion rate of JLF1 steel under various experimental conditions at 773 K [186].

	Weight loss of specimens per unit area [g/m^2]
Static test	0.294
Isothermal Flowing Test	0.382
Non Isothermal Flowing Test	0.569

EUROFER samples have been exposed in the PICOLO loop at lead lithium flow velocities within the range of 0.1 to 0.3 m/s and the direct dependence of corrosion rate with flow velocity has been already pointed out in Chapter 2 (Section 2.9.2.c) [124]. The Pb-Li flow velocity in the TBM box is expected to lie within few tens of a cm/s (0.05-0.1 m/s) [44]. Nevertheless, the flow velocity may be even higher near the TBM manifold pipes (~1 m/s) which necessitate corrosion experiments at higher flow velocities [46]. Moreover, the formation of high velocity jets (~ 1.5 m/s) is also expected in the return Pb-Li path near the common partition wall of LLCB TBM [197]. On the other hand flow of Pb-Li across the magnetic field (which is required to confine the fusion plasma) induces a current (J) in the fluid volume [P A Davidson, 2001]. This current interacts with the magnetic field (B) to produce opposing Lorentz force (J x B). The current also produces an induced magnetic field along the opposite direction [198]. Due to these factors, the flow velocity profile is completely modified where the general parabolic profile transforms to an M type profile with very high velocity near the side walls of the RAFM channels [198-199]. This also introduces additional pressure drop and joule heating [199-200]. The effect of magnetic field is quantified by Hartmann number [198]. For Indian TBM, the Hartmann number is expected to lay between18, 000-19,500 [201-202]. This also predicts that the velocity along the side walls will be around of 1- 2 m/s although the average velocity may be within 0.1 -0.2 m/s [201, 203]. Since corrosion rate is directly dependent on the flow velocity [186], the above discussed velocity distribution in the Pb-Li flow circuit Indian TBM will definitely create corresponding variation in local corrosion rates. Therefore, in order to characterize the corrosion behavior of IN RAFMS in Pb-Li eutectic under a complete range of operating flow velocities possible inside the TBM, a flow velocity range of 0.1 to 1.5 m/s has been chosen for the present study.

3.9.3. Selection of Magnetic Field

The Test Blanket Modules (TBM) will come under the influence of the intense magnetic field present in ITER [9, 13]. As shown in Figure 3.32, The Indian LLCB TBM consists of five ceramic breeder zones of different thickness and there are six Pb–Li flow channels surrounding these breeder zones as shown in Figure 3.32 [46]. The channel walls are made of ferritic martensitic steel (FMS) material of 5.0 mm thickness [46]. The channel walls parallel to the toroidal magnetic field are called “side wall” and the walls perpendicular to the toroidal magnetic field are called “Hartmann wall” [204]. The torroidal magnetic field at the location of channel walls generally lies within 1 to 4 T with the maximum of 4 T near the first walls [200]. The motion of Pb-Li in this strong toroidal magnetic field induces MHD effects which can cause change in the velocity distribution as discussed in the earlier Section (Section 3.9.2) and thereby affect the corrosion behavior of the channel walls.

Such high magnetic field of 4 T can only be provided a superconducting magnet and that needs to be integrated to a Pb-Li loop in order to conduct corrosion experiments. Since such a superconducting magnet was not available initially; the present corrosion experiments on IN RAFMS and P91 (Magnetic field range: 0.5 to 1.8 T) were carried out with the help of electromagnets and permanent dipole type magnets. A 1.8 T magnetic field of 1.8 T was provided by an electromagnet with an iron core at IPUL, Latvia. It was not possible to increase the magnetic field beyond this value since that would have led to saturation of the iron core causing non uniformity in field. in- house experiments with magnetic field were initiated with IN RAFMS material at BARC and the first experiment was carried out in a forced circular loop (EMPPIL-M) under a magnetic field of 0.5 T provided by a dipole magnet. An electromagnet with 1.8 T field have also been procured and further experiments are in progress with IN

RAFMS material at this higher field. A helium cooled superconducting magnet having 300 mm bore diameter and providing 4 T field is also under development.

The design and construction of all the experimental facilities used for evaluation of corrosion behavior of IN RAFMS and P91 under different operating conditions have been described in this chapter. The basis for choosing the operating parameters for conducting corrosion studies i.e. temperature, flow and magnetic field; have also been discussed. The next chapter deals with the details of the actual experiments conducted in these facilities, the materials used and the characterization procedure followed for analysis of the corroded samples.

CHAPTER 4

EXPERIMENTAL

4.1. Plan of experiments

With the static and dynamic corrosion test facilities in hand; a number of experiments were carried out with IN RAFMS and P91 material under different temperature and velocity conditions as mentioned in Chapter 3 (Section 3.9.1. and 3.9.2. respectively). Some experiments were also carried out in the presence of magnetic field (Chapter 3; Section 3.9.3). A brief plan of these experiments has been indicated in Figure 4.1.

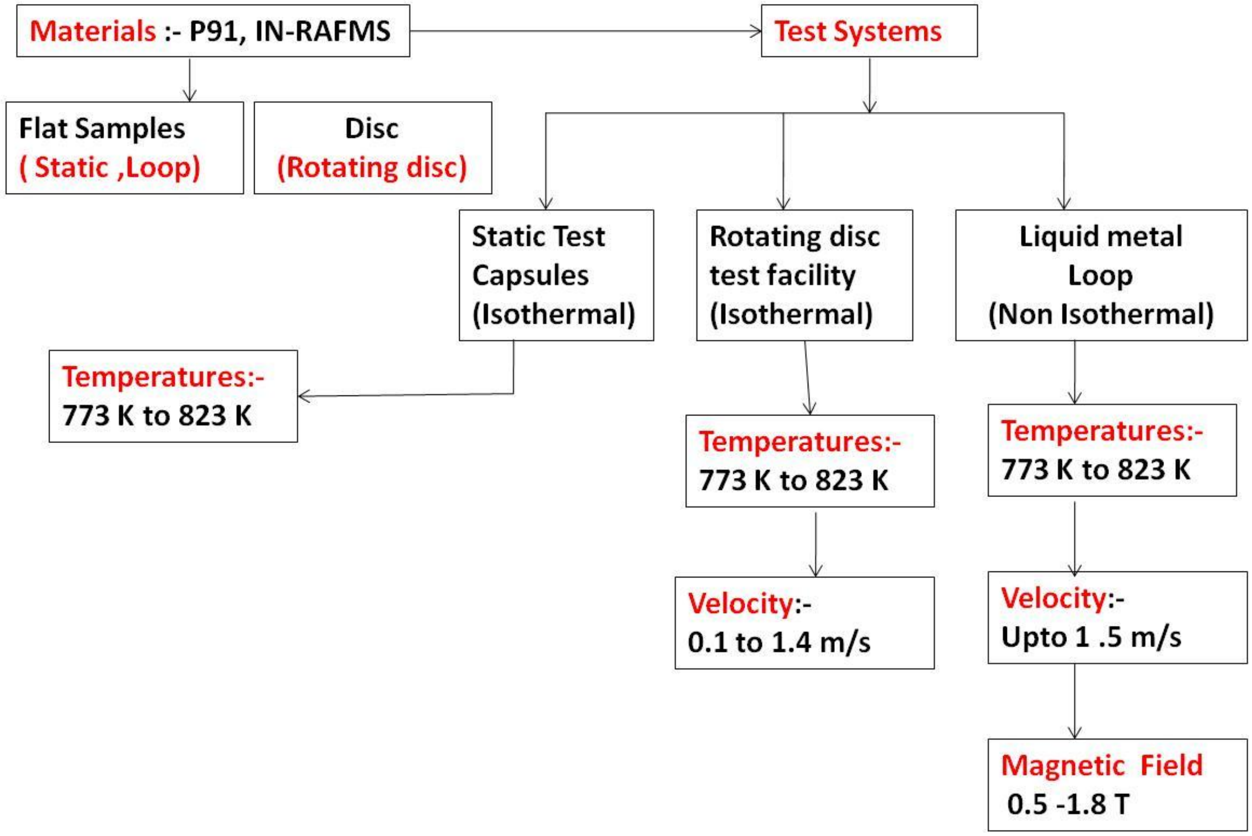

Fig. 4.1: Plan of corrosion experiments under different operating conditions.

The initial corrosion results were obtained by exposing samples to molten Pb-Li in static capsules maintained at 773-823 K (500 – 550˚C). In the next stage, dynamic corrosion testing under isothermal conditions were carried out by exposing corrosion coupons to flowing Pb-Li in the Rotating Disc Type Corrosion Facility (RDCTF) at a particular temperature. In this experiment, the effect of variation of flow velocities under isothermal conditions was studied in the temperature range of 773-823 K (500 – 550˚C). Moreover, the effect of duration of exposure was also studied in these experiments by exposing a number of samples for different time intervals in the same experimental conditions. The data collected from this facility helped in designing the basis for the third and final stage of experiments i.e. exposure of corrosion coupons in a liquid metal loop. IN RAFMS and P91 samples were exposed in forced circulation loops with Pb-Li eutectic flowing at 0.6 – 1.5 m/s and at a temperature range of 773-823 K (500 – 550 ˚C). It may be noted that for isothermal stirring experiments, the velocity varied from 0.3 to 1.4 m/s. Thus, within experimental limitations, the maximum velocities in both systems were kept nearly similar in order to allow comparison of experimental data. Finally, some experiments on IN RAFMS and P91 have also been carried out to study the effect of magnetic field when exposed to a forced circulation Pb-Li loop. Some of the above experiments in Pb-Li loop (with and without magnetic field) have been carried out at University of Latvia and Karlsruhe Institute of Technology.

4.2. Materials used

The study of the corrosion behavior of fusion reactor structural materials like IN RAFMS and P91 in lead lithium eutectic has been the major objective of this research work. The samples from these materials for corrosion study had been cut to required dimensions by Electric Discharge Machining (EDM). All samples were metallographically prepared up to diamond finish before exposure to Pb-Li. The results from pre-test characteristics of these materials, the SS316 L tubes (for Pb-Li loop) and the lead-lithium alloy have been given in the following paragraphs.

4.2.1. The Indian RAFMS and P91 steel

Plates of Indian Reduced Activation Ferritic Martensitic Steel (IN RAFMS) having thicknesses of 6 mm and 8 mm were initially was obtained from MIDHANI, India through IPR while 30 mm thick plates of P91 were procured separately from M/S D. G. Consultants, Mumbai. The chemical composition of the IN RAFMS and P91 materials were analysed through Inductively Coupled Plasma- Atomic Emission Spectroscopy (ICP- AES) and are listed in Table 4.1. It may be noted that the tungsten (W) content in both the plates of IN RAFMS was slightly different since they were from two different heats of RAFMS initially produced at MIDHANI as discussed in Chapter 2 (Section 2.8; Table2.8). However, due to the very low solubility of W in lead-lithium eutectic [195]; this slight difference in its content was not expected to have a great effect on the corrosion behavior of RAFMS and the results of corrosion tests on samples from both these plates could be thus compared safely. For the sake of simplicity in this thesis, the samples fabricated from both these plates have been denoted to be of IN RAFMS material. However, the composition have clearly specified, wherever necessary

The plates of IN RAFMS and P91 had been initially produced through Vacuum Induction Melting/ Vacuum Arc Refining (VIM/VAR) route and subsequent hot rolling. Both these plates were obtained under normalised and tempered conditions at temperatures reported in Table 4.2. Both normalizing and tempering was followed by air cooling to get the tempered martensite microstructure in these materials.

Sample Preparation: -Corrosion coupons for static and flowing tests (both rectangular and disc type) were fabricated through *wire cut EDM* machine as per dimensions already mentioned in Chapter 3 (Sections 3.3 – 3.8). Then they were were prepared for Pb-Li exposure by grinding them on SiC abrasive papers on successively finer grit up to 1200 grit and polishing them up-to diamond finish. This was to avoid any surface non uniformity of each sample which may lead to enhanced localized corrosion. Finally, each sample was marked for identification and weighed before exposure to lead-lithium eutectic in different test systems.

Table 4.1: Composition of the P91 and IN RAFM steel used (all in wt %).

Elements	P-91	INRAFMS (8 mm thick plate)	IN RAFMS (6 mm thick plate)
Chromium	9.4	9.04	9.04
Carbon	0.1	0.08	0.08
Manganese	0.5	0.55	0.55
Vanadium	0.2	0.22	0.22
Tungsten	-	1.4	1.0
Tantalum	-	0.06	0.06
Nitrogen	0.05	0.0226	0.0226
Oxygen	-	0.0057	0.0057
Phosphorus	0.019	0.002	0.002
Sulphur	0.002	0.002	0.002
Molybdenum	1	-	-
Nickel	0.05	-	-
Niobium	0.06	-	-
Aluminium	0.004	-	-
Silicon	0.45	-	-

Table 4.2: Normalizing and Tempering temperatures of IN RAFMS and P91.

	IN RAFMS	P91
Normalizing	1323 K (1050 ˚C) for 15 min	1353 K (1080 ˚C) for 1 hr
Tempering	1033 K (760 ˚C) for 5 min	1033 K (760 ˚C) for 2 hr

4.2.2. The SS316L tubes

SS316 L material (in the form of pipes) were used for fabrication of some of the initial static test capsules and the forced circulation lead lithium loop (EMPPIL) as described in Section 3.3, 3.5 and 3.9) . The composition of the same is shown in Table 4.3.

Table 4.3: Composition of SS316 L used for fabricating static corrosion test set-up and forced circulation loop (EMPPIL).

Elements	Cr	Mo	Mn	Ni	C	Fe
wt%	17.19	2.25	1.55	13.16	0.02	balance

4.2.3. The lead – lithium eutectic

In view of the extensive corrosion database available with lead- 17 atom % lithium eutectic (Pb-17Li) [151, 161 -164]; the initial corrosion experiments under static/stirring conditions had been conducted with Pb-17Li alloy. However, as pointed out in the Chapter 2 (Section 2.4); the internationally accepted eutectic point has now shifted to Pb - 15.7 (~16 atom %) Li [70]. In view of this; the composition of lead-lithium alloy used in the later stage for the loop type experiments was chosen to be Pb-16atom % Li or Pb-16Li. Although the atomic percentages of both these alloys are slightly different (~7.5% difference); their composition in weight percentages fall in the range of Pb-0.6 ±0.02 wt % Li. All batches of Pb-Li alloy used for the present study were procured from IPUL, Latvia and have been prepared by MHD induction stirring route [205]. The lead lithium eutectic was obtained as solid chunks (1 kg each). The composition of the alloy was analyzed by ICP-AES and is indicated in Table 4.4. High purity argon (< 1 ppm of O_2 and H_2O) was used as a cover gas for Pb-Li and for filling in the liquid Pb-Li in the loop.

4.2.4. Heaters, Insulation and Thermocouples

Heating coil (Nichrome) of 2 mm thickness covered with white colored ceramic beads was used for heating all parts of the loop as shown in Figure 4.2(a). All the heaters are connected through PID controllers. Mineral wool was used as heat insulation in all experimental facilities except the modified pump driven loop with magnetic field (EMPPIL-M), where aluminium and glass fibre tissue faced slab was used as shown in Figure 4.2 (b). K –type thermocouples were used for temperature measurement. They were coordinated with the heaters and PID controller for feedback temperature control in the loop.

Table 4.4: Composition of lead-lithium eutectic used for different corrosion experiments.

Elements	Pb-17Li	Pb-15.7 or Pb-16 Li
Li (wt %)	0.61	0.58
Bi(ppm)	164	149
Fe(ppm)	10	16
Cr(ppm)	<0.1	<0.1
Ni (ppm)	5.7	4.9
O (ppm)	20	27

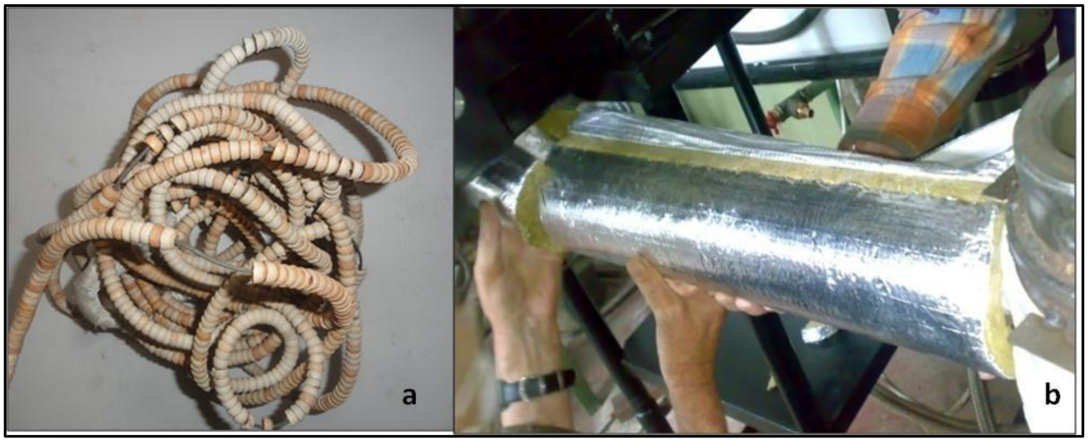

Fig. 4.2: (a) Alumina beads insulated Nichrome Heating Coil and (b) Aluminium and glass fiber insulation.

4.3. Corrosion Study of P91 and IN RAFMS in isothermal and static Pb-Li

4.3.1. Characterization of as-received material

For characterization of the as-received IN RAFMS and P91 materials; small samples of size 10 mm x 10 mm x 5 mm were cut with the help of EDM. These samples were metallographically prepared by grinding them at SiC abrasive papers of up to 1200 grit and polishing them up-to diamond finish.

The as-received surfaces of IN RAFMS and P91 were initially characterized by X Ray Photo electron Spectroscopy (XPS) in order to identify the native oxides present over it (i. e. before exposure to Pb-Li). It may be noted that diamond polished surfaces of both the materials were used to this analysis in order to replicate the exact conditions before exposure to Pb-Li in all experiments. The XPS measurements were performed using a PHI 5000 VersaProbeII , Focus X-ray Photo-electron Spectroscopy equipped with a monochromatic Al Kα (1486.7 eV) X-ray source. To determine the chemistry of the oxide layer formed, the XPS survey scan and high-energy resolution spectra of characteristic peaks of the elements like Fe 2p, Cr 2p, Mn 2p, Mo 2p, W 2p, C 1s, and O 1s were acquired using a Hemispherical Spherical Analyzer (HSA) equip with a 16-channel Multi-Channel Detector (MCD) with pass energy of 46.950 eV.

The choice of elements for high resolution scans were based on the literature evidence of the oxides generally formed over ferritic-martensitic steels. [161, 192, 206]. In order to get an idea about the thickness of the oxide scale and the oxide chemistry at the sub-surface zones, XPS depth profiling was done by sputtering with Ar+ ions of energy 2kV .The sputter etching rate calibrated using pure silicon oxide (with 100 nm thickness) was about 0.5nm/min. The sputtering was done at every 2 nm upto a total depth of 24 nm. The high resolution elemental spectra were de-convoluted and fitted using Origin 8.5 software, with Gaussian–Lorentzian lines and Shirley background type. The variation of concentrations of constituent elements upto a depth of 24 nm for both P91 and RAFMS were also plotted from the data obtained through XPS.

The micrographs of the as-received surface of IN RAFMS and P91 were recorded through optical microscope and Secondary Electron Microscope (SEM) after etching with the help of Villela’s reagent (5 ml picric acid; 1 ml HCL, 100 ml ethanol). An etching time of 5 – 7 seconds was generally found sufficient for a good microstructure. The composition at various locations of the as-received surface was recorded through Energy Dispersive Spectroscopy (EDS). Electron Back Scattered Diffraction (EBSD) examination of IN RAFMS and P91 surfaces was also done for phase fraction analysis after electro-polishing the samples in a 90:10 solution of perchloric acid and acetone. The electrolyte was maintained at -35˚C and electro polishing was carried out at 20 V for 20 s at 20% coolant flow.

4.3.2. Corrosion of IN RAFMS and P91 in static Pb-Li at 773 K and 823 K

In the first static experiment flat samples of IN RAFMS and P91 were exposed in separate test capsules which have been shown in Figure 3.1 in Section 3.2 (Chapter 3). The Pb-Li had a composition of 17 at%Li in this case. The P91 samples were of size 12mm x10 mm x 2mm whereas the IN RAFMS samples had a size of 12 mm x 20 mm x 3 mm. The samples were diamond polished on all sides and the weight of the samples was recorded before exposure. They had a hole of 4 mm diameter drilled on one side which was used for fixing them to a molybdenum rod. Two samples each of IN RAFMS and P91 were exposed in every test capsule and likewise, two capsules were prepared. One of the capsules was maintained at 773 K while the other was maintained at 823 K and both were kept in this condition for 355 h continuously. On completion of the experiment, both the set-ups were cooled to room temperature. Afterwards, the top cover was cut off and liquid Pb-Li was drained out by heating the set-up in a upside down manner inside a controlled atmosphere furnace. Later the samples were removed from their molybdenum fixtures and the adherent Pb-Li cleaned off by repeatedly exposing them in a mixture of acetic acid, acetone and hydrogen peroxide in the ratio 1:1:1. In the solution, the Pb was dissolved according to the following chemical reaction [125]:

$$2Pb + O_2 + 4CH_3COOH \rightarrow 2Pb\ (CH_3COO)_2 + 2H_2O \ \ldots\ldots\ldots\ldots\ldots\ldots\ldots\ldots\ldots\ldots\ldots\ldots\ldots.....\quad 4.1$$

It may be noted that, M. Kondo et al. had reported earlier that a cleaning mixture of acetic acid, H_2O_2 and ethanol in the ratio 1:1:1 was used for removing the adhered lead-lithium alloy [125]. It was shown to cause dissolution of pure metals like Fe and Cr as well as FM steel samples [125]. Keeping this in mind, a blank cleaning run was conducted on a fresh (unexposed) piece of IN RAFMS material to measure the weight loss on exposure to the mixture of acetic acid, acetone and hydrogen peroxide which was used for cleaning in the present experiment. It was observed that weight loss took place at a rate of 2.5 µg/ mm^2 after four iterative cleaning treatments causing a weight reduction of 0.019%. Although this loss was negligible, it was still considered during calculation of weight losses of all IN RAFMS and P91 specimens due to corrosion.

After cleaning of the samples of IN RAFMS and P91 exposed to Pb-Li for 350 h in the present experiment, the weights of the samples were recorded upto an accuracy of four decimal places and compared with the initial weight. Thereafter, the cross-section of the samples were mounted in conducing resin and polished to obtain diamond finish. Etching of these samples was carried out in Villela's reagent. The mounted samples were analyzed through optical microscopy and SEM – EDS.

4.3.3. Corrosion of IN RAFMS and constituent elements in static Pb-Li at 773 K for 1, 000 h

The first experiment under static conditions allowed a preliminary comparison of the two materials: IN RAFMS and P91 based on their corrosion behavior in Pb-Li. Later, the dissolution behavior of IN RAFMS, Iron and Chromium was investigated under similar experimental conditions in a new experimental set-up described in Section3.3 (Figure 3.3. and 3.4). Low alloy steel was used as a substitute for pure iron in the absence of the later. The lead-lithium alloy (Pb-Li) used in this case was from the new batch and had the eutectic composition of Pb-15.7 at% Li.

Three samples each of IN RAFMS, Low alloy steel (99.7 % Fe, 0.3 % Mn) and pure Chromium were exposed to Pb-Li at 773 K for a total duration of 1000 h in the new experimental facility. All corrosion samples were prepared by grinding and polishing upto diamond finish.The samples were then indentified my marking with an alphabet punch as shown in Figure 4.3. Later the dimensions and weights of the samples were carefully recorded with the help of Vernier calipers and electronic weighing balance respectively. These are listed in Table 4.5. Both the samples were later placed in separate pockets of the molybdenum holder and later the holder was fixed to the immersing rod. Then the H V Gate valve was kept under OPEN condition during this time.

Fig. 4.3: Samples of IN RAFMS, Low-Alloy Steel and Pure Cr.

On the other hand, solid Pb-Li chunks (weighing ~0.45 kg) were filled into the molybdenum liquid metal bath and placed inside the lower chamber of the Inconel retort. The amount of Pb-Li to be filled in the liquid metal bath was decided on the basis of volume of the sample holder so that there was no overflow of liquid when the holder containing the samples is immersed.

Once the Pb-Li was in place, the sample holder was lowered into the middle level of the retort and the top cover flange of the retort was closed. A vacuum of 10^{-2} mbar was generated inside the retort in order to remove all the gases. Thereafter, argon gas was filled in the chamber and maintained at a pressure of 1.5 bars. Later the temperature of the lower part of the retort was raised upto 773 K (500°C). Sufficient holding time (upto 24 h) was allowed at this temperature in order allow the complete melting of Pb-Li. Afterwards, sample holder was further lowered and immersed into the molten Pb-Li. The final position of the holder was fixed based on indications obtained from the level sensor which had been calibrated previously. The set-up was maintained in this condition for 250 h continuously.

Table 4.5: Dimensions of pure Cr, low alloy steel and IN RAFMS samples before exposure to Pb-Li.

Material	Duration	Length	Breadth/Base	Thickness	Surface Area (mm^2)
Pure Cr	250 h	6.20	5.75	2.34	127.226
	500 h	6.35	5.91	0.98	102.64
	1000 h	8.18	7.35	2.33	160.91
Low Alloy Steel	250 h	10.02	10.05	0.8	233.51
	500 h	10.2	10.1	2.2	295.36
	1000 h	10.27	9.94	2.99	325.02
IN-RAFMS	250 h	9.86	8.15	1.66	220.00
	500 h	10.81	10.0	1.89	293.78
	1000 h	9.87	7.93	1.85	220.51

After 250 h, the sample holder was taken upto the middle position (above the H V gate valve) and later the valve was closed. The holder was cooled by purging argon in the top half of the retort for 3-4 h. The liquid metal on the bottom half however was left undisturbed at 773 K. After temperature of the top half of the retort reached to room temperature the cover flange was opened and the sample was taken out of the set-up to its top most position. Then the sample holder was detached from the immersing rod and it was opened. One of the RAFM samples was taken out of the holder and the other one remained inside it. The holder was closed again and once again lowered to the middle portion of the retort. The cover flange was closed and the top position of the retort was allowed to obtain vacuum upto10^{-2} mbar. Later inert gas purged into the chamber and a pressure of 1.5bar was maintained. After this the H V Gate valve was opened and the same holder was lowered into the molten Pb-Li kept at 773 K. The second set of samples (Low Alloy Steel, Cr and IN RAFMS) were exposed to Pb-Li for another 250 h (total 500 h) and later taken out by the procedure described above. The last set of samples (Low Alloy Steel, Cr and IN RAFMS) was taken out after a total duration of 1, 000 h. All samples were cleaned off the adherent Pb-Li by repeatedly exposing them in a mixture of acetic acid acetone and hydrogen peroxide in the ratio 1:1:1. Afterwards, the weights of the samples were recorded and compared with the initial weight. Thereafter, the surface and cross-section of the samples were analyzed through SEM –EDS.

4.4. Corrosion Study of P91 and IN RAFMS in isothermal and rotating Pb-Li

4.4.1. Corrosion of P91 (disc) in Pb-Li at 773 K in the RDCTF

The first experiment in the Rotating Disc Corrosion Test Facility (RDCTF) was conducted with a disc type P91 sample in normalized and tempered condition for studying the material's compatibility in flowing Pb-Li at 773 K. The facility has been already described in Section 3.4 (Figs. 3.6, 3.7and 3.8). The lead-lithium alloy had 17 atom % Li in the present experiment i.e. Pb-17Li. The velocity profile of Pb-Li in the molybdenum crucible of this facility for a reference disc type sample had been obtained by CFD modeling and described Section 3.4.3. The methodology adopted for CFD simulation is given Appendix 1.

The P91 sample having 40 mm diameter and 6 mm thickness was initially fabricated by wire EDM cutting and later metallographically polished up to diamond finish as shown in Figure 4.4. Afterwards, the sample was weighed before coupling the same to the sample holder. Solid Pb-Li chunks weighing a total of 4.75Kg (0.45 L) were initially placed in the Mo crucible when it was at its bottommost position. This amount of Pb-Li could fill the Mo crucible up to a height of 95 mm.

Fig 4.4: The disc shaped P91sample (40 mm dia; 6 mm thick).

After fixing of the P91 disc to its molybdenum holder, the outer chamber of the RDCTF was sealed through water cooled flanges and inert atmosphere was maintained at 1.5 bar by purging high purity argon gas inside. Afterwards, the chamber was heated upto 773 K and the Mo crucible was slowly taken up with the help of the lifting mechanism. Once the desired height had been attained for ensuring complete dipping of the disc in molten Pb-Li, the motor was switched on and maintained at 700 RPM for the entire duration of experiment i.e. 2000 h. An important objective of this study was to investigate the effect of this linear velocity gradient on the corrosion behavior of molten lead-lithium along the radial direction of the P91 disc. It was calculated that the rotational speed of the P91 disc corresponded to a range of linear velocities from zero at the centre to 1.4 m/s along the disc edge.

On completion of 2, 000 h, the Mo crucible was brought down from its original position while at the operating temperature and the set-up was then cooled for removal of the sample. Afterwards, the sample was cleaned off the adhering lead-lithium by repeatedly exposing it to a mixture of acetic acid, acetone and hydrogen peroxide in the ratio 1:1:1. Later the weight of the specimen was measured upto an accuracy of four decimal places in order to deduce weight loss due to corrosion. The macrographs of the sample were recorded through a stereo microscope and various compounds formed on the surface were investigated through micro – Raman spectroscopy. Later, the intrusive effect of corrosion was investigated at different positions along the radius of the disc using SEM-EDS. The effect of Pb-Li exposure on the mechanical strength of P91 was analyzed through micro hardness analysis. The results obtained from the above characterizations are discussed in the following sections.

4.4.2 Corrosion of IN RAFMS (disc) in Pb-Li at 773 K in RDCTF

After P91, the compatibility of IN RAFMS material in molten Pb-Li was studied under isothermal stirring conditions in the RDCTF at 773 K. For this purpose, a disc type IN RAFMS sample (in normalized and tempered condition) with a diameter of 60 mm and thickness of 6 mm was used. The disc type sample had an internal thread to screw a molybdenum rod (sample holder) having 20 mm diameter, axially along the centre. It was polished up to diamond finish and later weighed before coupling the same into the sample holder. Similar to the earlier experiment with P91, the lead lithium alloy used in this study had 17 atom % Li i.e. Pb-17Li. It may be noted that fresh Pb-17Li (4.75 Kg) was filled in the molybdenum crucible before starting this experiment. The IN RAFMS disc was dipped in Pb-Li under inert atmosphere by the procedure described earlier for P91 (Section 4.4.1). The temperature of exposure and motor rotation speed were maintained at 773 K and 360 RPM respectively for a total duration of experiment i.e. 3000 h.

It was calculated that the rotational speed of the IN RAFMS disc corresponded to a minimum velocity (V_{min}) of 0.38 m/s at the beginning of solid radius (R=10 mm) to a maximum velocity (V_{max}) of 1.13 m/s at the periphery of the disc (R=30 mm) . V_{mid} denotes a mid range velocity of 0.75m/s at R=22 mm. This variation of linear velocity along the radial direction of the disc has been illustrated in Figure. 4.5. Since velocity is known to be an important factor affecting the corrosiveness of liquid metals and alloys [124], the variation of linear velocity along the radius was expected to affect the extent of corrosion at different locations on the disc. On completion of 3000 h, the IN RAFMS disc was removed from the set-up and cleaned off the adherent Pb-Li in a similar manner as described for P91 (Section 4.4.1) Later the weight loss due to corrosion was recorded up to an accuracy of four decimal places.

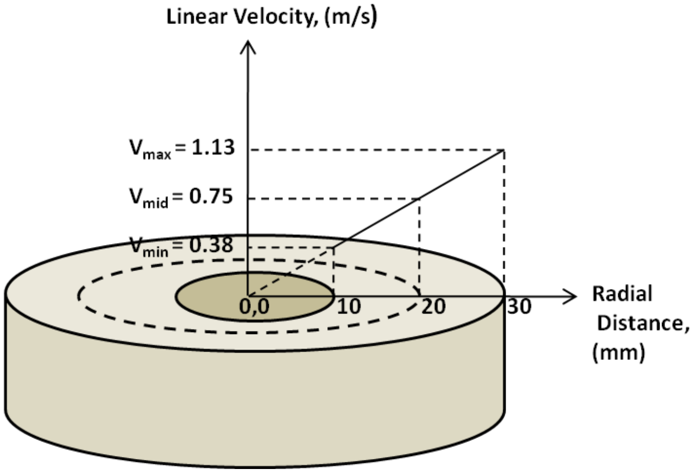

Fig. 4.5: Schematic of the IN RAFMS disc sample showing increase in linear velocity (V) along the radial direction (R).

The content of metallic impurities in the solidified lead-lithium before and after the experiment was analyzed by Inductively Coupled Plasma - Atomic Emission Spectroscopy (ICP-AES). The photograph of the IN RAFMS disc exposed to Pb-Li was recorded initially and then the intrusive effect of corrosion was investigated at different positions along the radius of the disc using Optical Microscopy, SEM-EDS and Glow Discharge Optical Emission Spectroscopy (GD-OES). Later, the micro-structural changes caused by Pb-Li attack were further analyzed with the help of EBSD technique. The effect of Pb-Li exposure on the mechanical strength of IN RAFMS was analyzed through micro hardness analysis.

4.4.3. Corrosion of IN RAFMS (segmented sample) in Pb-Li at 823 K in RDCTF

In order to study the dependence of the corrosion process with the duration of exposure, a six segmented disc type sample made of IN RAFMS was designed and fabricated as described in Section 3.4.1. The segmented disc was fabricated out of an IN RAFMS disc of 45 mm diameter and 7 mm thickness. The sample along with its dedicated sample holder made out of molybdenum is shown in Figure 4.6.

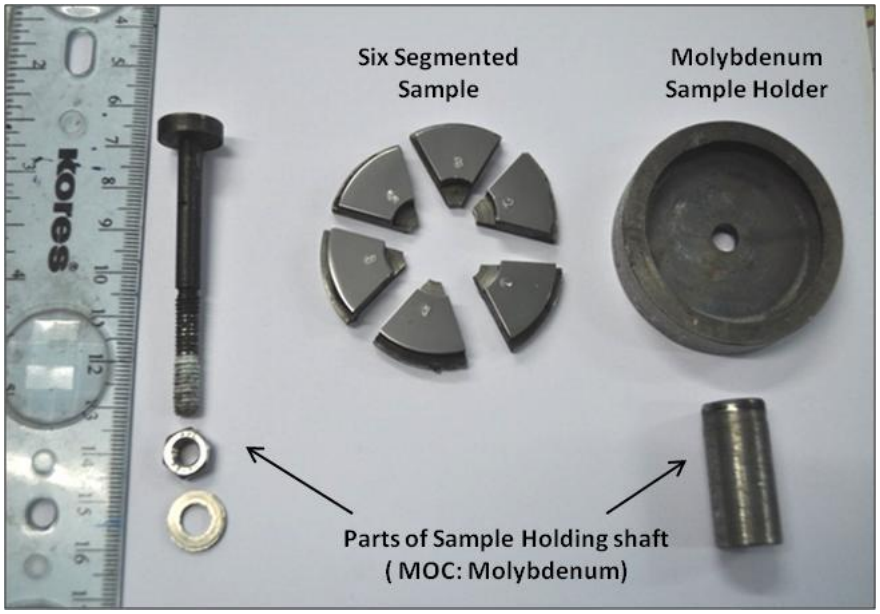

Fig.4.6: The six segmented IN RAFMS sample along with the parts of molybdenum sample holder.

The procedure for calculation of the total wetted area of the sample (which will be exposed to Pb-Li) is depicted in Figure 4.7. After adding the areas of all the sections on the top and sides of the sample, the total wetted area comes out to be 683.54 mm^2. It may be noted that the area of the bottom face of the samples are not taken into account considering minimum exposure to liquid metal at this locations. The 6 segments were labeled from 1 to 6 by punching method and arranged serially while fixing inside the sample holder. Figure 4.8 (a) shows the six segments after fixing into the molybdenum holder.

After filling fresh Pb-Li (4.75 Kg) in the molybdenum crucible, the sample holder with six segmented sample was attached to the main shaft RDCTF as shown in Figure 4.8(b). It was later dipped in molten Pb-Li at 823 K in the procedure described for P91 samples in Section 4.4.2 and rotated at 360 RPM with the help of the induction motor. As per equation 3.2 (Chapter 3; Section 3.4.1), the above angular velocity resulted in a maximum liner velocity of 0.75 m/s at the outer periphery of the disc (i.e. point P in Fig 4.7), and 0.1 m/s at the inner periphery (i.e. point Q in Fig 10).

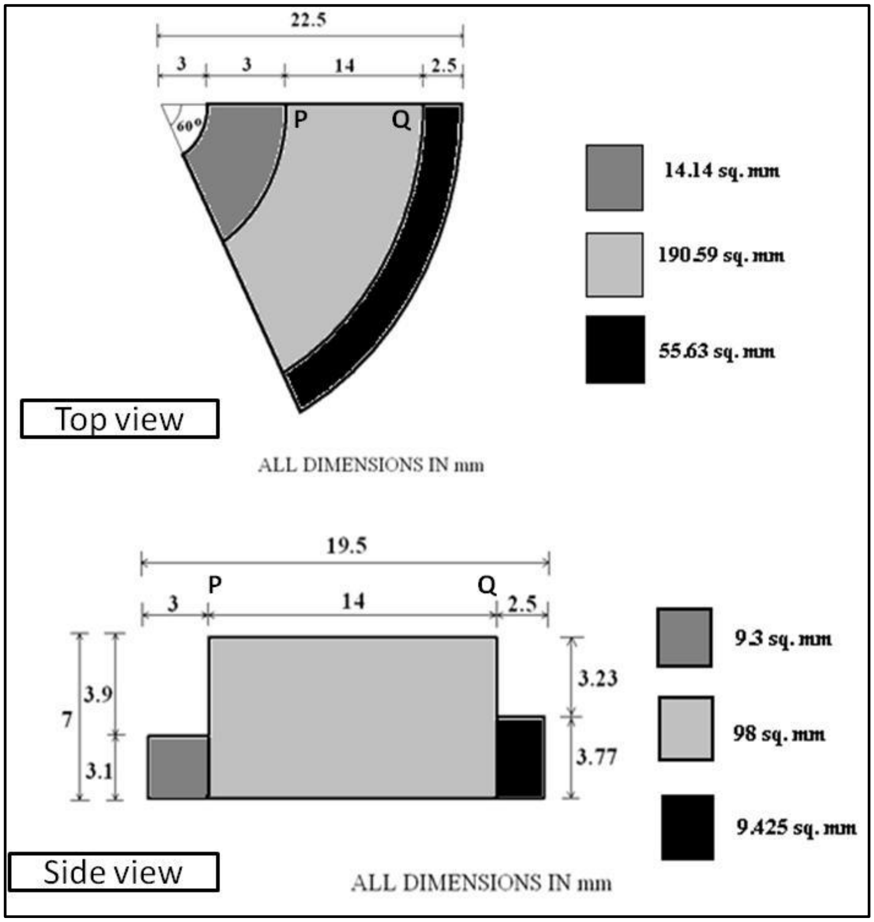

Fig. 4.7: Calculation of wetted area of a single segment.

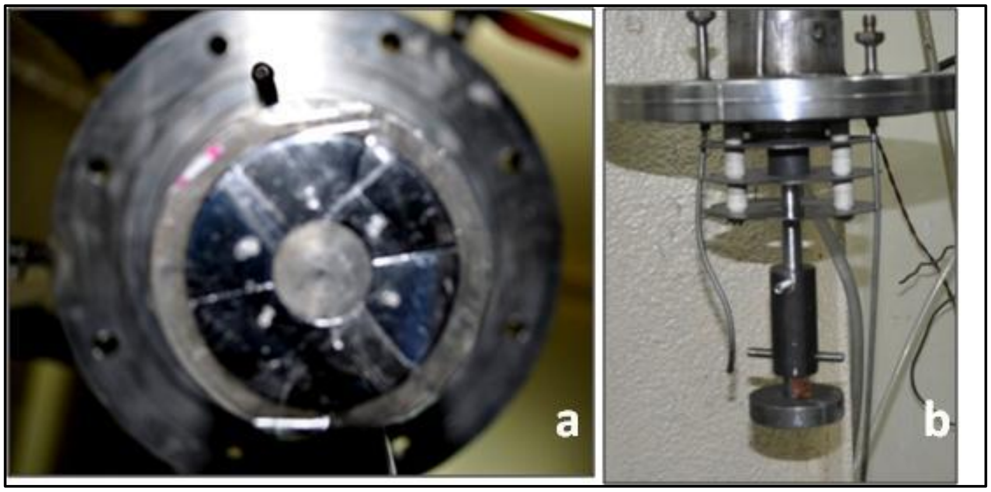

Fig 4.8: (a) Assembly of segmented IN RAFMS sample; (b) Sample holder fixed to RDCTF.

The experiment was carried out for a total lead lithium exposure of 10, 000 h with sample removal being carried out after every 2, 000 h. Sample nos. 1 and 2 were taken out of the set-up after the first 2000 h of exposure to Pb-Li. Sample 2 was subjected to cleaning procedure and was again exposed in the set-up for another 2000 h. Sample 3 was taken out straight after 4000 h of exposure. The corrosion of Sample 2 and 3; both of which were exposed for a total duration of 4, 000 h was later compared in order to study the effect of cleaning. Figure 4.9 shows the exposed IN RAFMS sample nos. 1, 2 and 3 respectively. Sample nos. 4, 5 and 6 were taken out after 6000 h, 8000 and 10, 000 h respectively. The total run time of the experiment including repairs and power shut downs was approximately 2 years.

It may be noted that that after taking out every sample from the holder; the vacant space was always filled by dummy molybdenum segments having exactly similar dimensions as the IN RAFMS samples. These segments were earlier fabricated from a 45 mm Molybdenum disc in a procedure described for the IN RAFMS material. This was done in order to complete the circular disc in every stage so that it could be held properly inside the molybdenum holder and minimum flow disturbance was ensured.

Fig. 4.9: IN RAFMS segments after exposure to Pb-Li in the rotating disc test set-up.

Every sample was cleaned in a mixture of acetic acid, acetone and hydrogen peroxide (1: 1: 1) in order to remove the adherent Pb-Li and measure the weight loss due to corrosion. Later, all the samples were cut radially into two halves with each half having an included angle of 30˚. One of the halves was mounted on its cross-section and the other was investigated on the top surface only. Both the surface and cross-sections of the samples were analyzed through SEM-EDS. In order to study the effect of velocity on the corrosion behavior of IN RAFMS; the samples were mainly studied at two major locations i.e. at the outer periphery of the disc (point P in Fig 4.10; which was exposed at 0.75 m/s) and at the inner periphery (Point Q in Fig 4.10; which was exposed at 0.5 m/s). The velocity profile of Pb-Li had been already obtained theoretically through CFD analyses as given in Figure 3.14 (Section 3.14, Chapter 3). However, the effect of temperature gradient could not be studied in the RDCTF since it was an isothermal system. For this purpose, further experiments were carried out in a non isothermal liquid metal loop which can circulate Pb-Li through different temperature zones as expected in an actual reactor

4.5. Corrosion of IN RAFMS and P91 in non-isothermally flowing Pb-Li

4.5.1. Corrosion of IN RAFMS in Pb-Li at 773 K in the EMPPIL at BARC

The design of Electro-Magnetic Pump driven Pb-Li Loop (EMPPIL) at BARC has been already described in Chapter 3 (Section 3.5) and the schematic of this loop is shown in Figure 3.15. The composition of lead-lithium alloy used for corrosion studies in this loop was 15.7 atom % Li or

Pb-16Li. The first experiment in EMPPIL was carried out with samples of an India produced RAFM steel (RAFMS) which were exposed to Pb-Li at 773 K for 5, 000 h. This material (Fe-9Cr-1W-0.06Ta) belonged to one of the heats of RAFM steel produced during the initial phase of development of IN RAFMS (Table 2.8).

For the present experiment, four IN RAFMS samples of size 25 mm x 8 mm x 3 mm were initially prepared by metallographic grinding and diamond polishing and later weighed before placing them inside the sample holder of EMPPIL. The geometry of the sample holder (SS316 L pipe with inner diameter of 15.7 mm) has been already shown in Figure 3.20 and discussed in Section 3.5.1 (Chapter 3). The four samples of IN RAFMS (A, B, C and D) having dimensions of 25 x 8 x 3 mm were held inside the sample holder with the help of molybdenum fittings. The velocity profile of Pb-Li in the sample holder of EMPPIL (Figure 3.22) had been obtained by CFD modeling and the methodology adopted for CFD simulation is given Appendix 1. As shown in Figure 3.22, the sample A faced the maximum velocity while Sample D faced the minimum velocity. The sample holder was welded to the loop piping after fixing the samples and therefore flange joints were completely avoided in the loop in order to prevent unnecessary leakage.

Pb-Li alloy chunks weighing 40 Kg were initially filled inside the melting tank. The entire loop including melting tank was first evacuated and later purged with high purity argon gas to remove any adherent gasses on the tube walls. Later the melt tank was slowly heated to 623 K to allow melting of Pb-Li (melting point = 508 K). Afterwards, the rest of the loop was heated to 623 K and sufficient holding time was allowed so that the temperature of the entire loop was stabilized at that temperature. Thereafter, the molten Pb-Li was lifted up into the main loop through argon gas pressurization in the melt tank. When the liquid metal reached sufficient height in the expansion tank as indicated by the level indicators, the melting tank was disconnected from the main loop through freeze valve operation in the connecting line. Afterwards, liquid was allowed to rotate inside the loop with the help of the electromagnetic pump. The average velocity of Pb-Li flow was fixed at 1.5 m/s as measured by the electromagnetic flow meter. Finally the temperature of heater and test section was increased and a constant temperature of 773 K was maintained along the entire length of test section.

The loop was operated with the IN RAFMS samples for 5, 000 h continuously. Afterwards, the molten Pb-Li was drained back into the melt tank and the loop was allowed to cool down to room temperature. Later the IN RAFMS samples were taken out of the loop and two out of the four samples from upstream (Sample A in Figure 3.19) and downstream locations (Sample D in Figure 3.19) were cleaned off the adherent Pb-Li by repeatedly exposing to a mixture of acetic acid, acetone and hydrogen peroxide in the ratio 1:1:1. The weight of the samples after cleaning was noted in order to measure the weight loss due to Pb-Li exposure and corrosion rate. Afterwards, the cross-section of the cleaned and unlearned samples was analyzed with the help of Optical Microscopy and SEM-EDS. The composition of the exposed Pb-Li was analyzed with the help of ICP-AES.

4.5.2. Corrosion experiments in the forced circulation loop PICOLO at KIT

The data generated from EMPPIL was sufficient to give an indication of the corrosion behaviour of IN RAFMS under flowing conditions and compare it with the static and rotating disc corrosion results. However, it was also necessary to compare the corrosion behavior of IN RAFMS with the European standard material EUROFER under similar experimental conditions. For this purpose, ten samples of IN RAFMS were exposed to Pb-Li eutectic (Pb-15.7 at % Li) in the PICOLO loop at KIT, Germany.

a. Samples for Corrosion Study

For fabrication of test samples; a 12 mm thick RAFMS plate (0.02 m x 0.02 m) in its standard heat treated condition (as mentioned in Table 4.2) was sent to KIT. The test samples were fabricated by cutting and turning of the plate to required sample dimensions as already indicated in Fig 3.24 (Chapter 3, Section 3.6). The samples were subsequently cleaned in an ultrasonic bath (acetone) and dried before exposure to Pb-Li. The test samples (8 mm diameter) were screwed together to a stack of 12 pieces for loading into PICOLO loop. The total length of the test rod was about 400 mm. Fig 4.10 shows the actual photograph of the IN RAFMS sample fabricated for corrosion testing in PICOLO loop.

Fig. 4.10: Sample of IN RAFMS fabricated at KIT.

b. Corrosion Experiment

For the present experiment, five corrosion samples of IN RAFMS were fabricated and diamond polished before exposure in the PICOLO loop. The details of the sample design are given in Section 3.6. The diameter of all the samples was measured before exposure by LASER scanning. The measurement was carried out at 9 to 10 points at regular intervals along the length of the sample such that the entire lengthwascovered. Moreover, at every point along the length, the diameterwasmeasured at a 12 number of turning angles (at a difference of 30˚ each); the average of which gave the final data of diameter at that point of length. It may be noted at a measurement deviation/error upto eight (8) decimal places were also considered in these readings.

Afterwards, the five IN RAFMS samples were loaded into the PICOLO loop and the loop was filled with Pb-Li. The sample holder temperature was raised to 823 K (550˚C) and Pb-Li was made to flow at a velocity of 10 cm/s with the help of electromagnetic pump. The loop was operated in this condition for 8, 000 h in this condition. The first IN RAFM sample was taken out after 550 h and then after every 2, 000 h starting from around 2015 h to 8, 059 h. Sample removal and exchange was carried out in the glove box above the expansion tank which eliminates the necessity to drain the Pb-Li. The experiment was carried out.

c. Measurement of Corrosion rate

After exposure, the samples IN RAFMS were cleaned off the adherent Pb-Li and then diameter of all samples after exposure was also measured by LASER scanning in the procedure described before. For each sample, the diameter after exposure was recorded at the same points along the length and at similar turning angles as was done before exposure. Then the difference in diameter due to Pb-Li exposure was calculated for every point along the length from the average of data obtained at various turning angles. The final average difference in diameter calculated from every point of length gave the average "radial material loss" for a particular sample i. e. for a particular time of exposure. All such data points (difference of diameter in µm) were then plotted against their corresponding duration of exposure (in h) and a linear fit of data was made. The extrapolation of this line to 8760 h (1 year) gave the radial material loss after one year which was actually the corrosion rate (µm/year). At present, the microstructural examination of the surface and cross-section of these samples through SEM-EDS is under progress and these results will not be reported in the present thesis.

4.6. Corrosion of IN RAFMS and P91 in the presence of Magnetic field

4.6.1 Corrosion of P91 in the presence and absence of magnetic field in the forced circulation Pb-Li loop at IPUL, Latvia

The first hand experience of operating a forced circulation Pb-Li loop with integrated magnetic field was obtained at Institute of Physics, University of Latvia (IPUL), where the corrosion of P91 material was studied in Pb-Li under a magnetic field of 1.7 T at a temperature of 823 K (550 ˚C) . This experiment was carried out under the aegis of a joint collaboration between DAE, India and IPUL. The design of the loop and its components has been already described in Section 3.6 (Chapter 3). The dimensions of the flat samples were 35 mm (length) × 9.5 mm (width) × 1.6 mm (thickness). Samples were made of P-91 whose material composition is given in Table 4.1. The test section has been earlier described in Figure 3.26 (a) and (b). As shown in Figure 4.11; it consisted of three regions viz Region 1, 2 and 3 with Region 1 and Region 3 present before and after the magnetic field respectively. The samples placed in different regions have been identified as A, B, C, E, O and T. The Region 2 was located in the gap between the magnetic poles and experienced 1.7 T magnetic field; the uniformity of which has been already shown in Figure 3.27. To eliminate the influence of scattered field on the samples placed outside magnetic field; ferromagnetic yokes were placed over Region 1 and 3. Each of the region had six flat samples marked A, B, C, E, O and T and arranged alphabetically; with the sample A being the first one to face the flow in all cases.

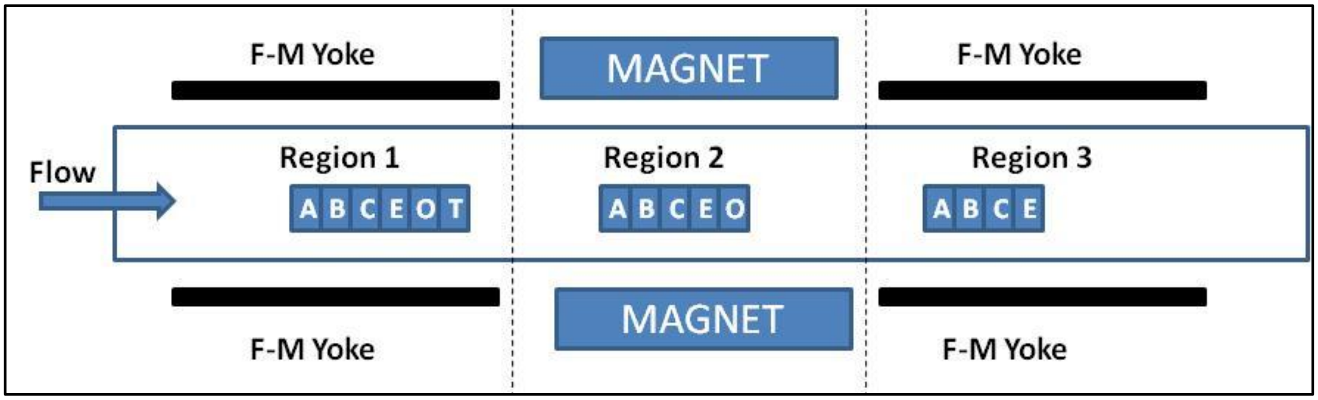

Fig 4.11: Different regions of the test section (inside and outside magnetic field) in the forced circulation Pb-Li loop at IPUL, Latvia.

The experimental run was carried out on P91 material with the above configuration in the IPUL Pb-Li loop for duration of 1000 h.The temperature of the test section was maintained at 823 K and the Pb–Li flow velocity as measured by the electromagnetic flow meter was15 cm s^{-1}. After exposure to the liquid metal, the samples were removed from the test section. They were dipped in lithium at 400°C for 4 h, to remove the adherent Pb–Li. After measuring the weight, the macrographs of the samples were recorded by stereo microscopy while micrographs were recorded with the help of SEM EDS. Later samples were cut and prepared for metallographic studies. The samples were analyzed using analytical methods such as optical microscopy, SEM-EDS and Electron Probe Micro Analysis (EPMA)

4.6.2. Corrosion of IN RAFMS in the presence and absence of magnetic field in EMPPIL-M at BARC, India

After the first corrosion experiment with IN RAFMS under flowing Pb-Li in the electromagnetic pump driven Pb-Li Loop (EMPPIL) at BARC; the next step was to study the effect of magnetic field over its corrosion behavior. This study was conducted in the modified EMPPIL (EMPPIL-M) which have been already described in Section 3.7.2 (Chapter 3). The vertically mounted SS316L sample holder was similar to the one used in EMPPIL (Figure 3.19) except that it had a length of 300 mm. The sample holder had an inner diameter of 15.7 mm and contained a total of six RAFM samples (A, B, C, D, E and F). The schematic of the present sample holder with the samples and integrated magnet has been shown in Figure 4.12. Each sample had the size 40 mm x10 mm x 2mm making the total length of sample stack to be 240 mm.

All these samples were metallographically polished upto diamond finish and weighed before loading into sample holder. Moreover, the roughness profile and roughness parameters over the surface of these samples were recorded with the help of an optical profilometer. Since the vertical length of the magnetic pole was 50 mm, it was possible to place only one sample completely under the influence of uniform magnetic field. The 0.5 T magnetic field was integrated at with the sample holder in such a manner that the last sample starting from the direction of flow (Sample F) faced the magnetic field. It had been earlier observed in the CFD generated velocity profile of EMPPIL (Figure 3.22) that, local rise (fluctuations) in velocities are created when the flowing liquid first impinges on the sample stack and it takes a certain distance (~100mm) to reduce this fluctuations to minimum. This allowed the flow to stabilize before entering the magnetic field region. As observed in Figure 4.12; sample A to D was present completely outside the magnetic field while sample F was located completely inside the magnetic field. On the other hand, Sample E was located partially inside the magnetic field.

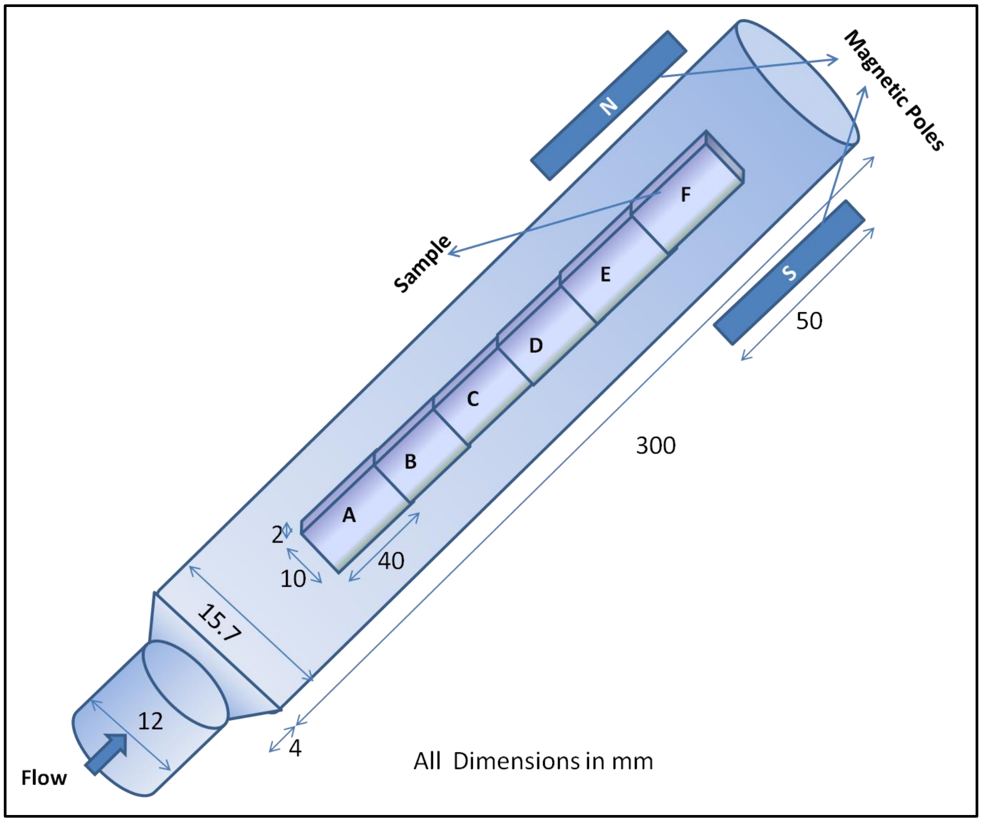

Fig. 4.12: Schematic diagram of sample holder in EMPPIL-M indicating the location of the samples and magnetic field.

Once the sample holder along with the RAFM samples were integrated with the main loop; the loop was evacuated through the expansion tank and then flushed with argon to remove any adhered gasses. Afterwards the entire loop was heated to 623 K (350 ˚C) and molten Pb-Li through from dump tank was filled into the loop through argon gas pressurization. The loop was commissioned in a similar procedure as used in EMPPIL (Section 4.5.1) and the temperature of the test section was maintained at 773 K (500˚C). By adjusting the rotation speed of electromagnetic pump, the average velocity of Pb-Li flow was fixed at 1.5 m/s as measured by the electromagnetic flow meter. This condition matched with that of the earlier experiment with IN RAFMS in EMPPIL.

The loop (EMPPIL-M) was operated with magnetic field for 2, 800 h continuously. Afterwards, the molten Pb-Li was drained back into the melt tank and the loop was allowed to cool down to room temperature. Later the IN RAFMS samples were taken out of the loop and for the preliminary investigation of the effect of magnetic field on the corrosion behaviour, two main representative samples were chosen. These were "Sample D" which was completely outside the magnetic field and "Sample F" which was completely inside the magnetic field (Figure 4.15). Out of the four samples; sample D was chosen to represent the location outside magnetic field because it was expected that some disturbance of flow would occur at the beginning of the sample stack (i.e near sample A) as shown in Fig 3.22. However, the disturbancewassupposed to be stabilized as the flow reaches the fourth sample D. Thus both sample D (outside magnetic field) and sample F (inside magnetic field) would have similar flow conditions except that of the effect on flow created by magnetic field. These samples were cleaned off the adherent Pb-Li by repeatedly exposing to a mixture of acetic acid, acetone and hydrogen peroxide in the ratio 1:1:1. The weight of the samples after cleaning was noted in order to measure the weight loss due to Pb-Li exposure and corrosion rate. Thereafter the surface roughness profile and parameters of these exposed samples were measured with the help of optical profilometer and the surface macrographs were recorded with stereo-microscope. Afterwards, the surface and the cross-section of these samples examined with the help of Optical Microscopy (OM) and Secondary Electron Microscopy-Energy Dispersive Spectroscopy (SEM-EDS). The composition of the exposed Pb-Li was analyzed with the help of Inductively Coupled Plasma - Atomic Emission Spectroscopy (ICP-AES).

4.7. Characterization Instruments and Techniques

Characterization of the exposed samples at BARC has been initially carried out through weight loss measurement in order to generate the corrosion rate under various conditions. For these purpose electronic weighing balance (measuring weights upto six decimal places) has been used. Afterwards the gross effects of Pb-Li attack on some of the sample surfaces have been recorded by taking the photographs of the samples have been recorded through Digital Camera and Stereo Microscope. The surface of the unexposed specimen has been characterized by Optical Microscopy, SEM-EDS, EBSD and XPS.

Later microstructural examination of the surface and the cross-section of exposed specimen have been carried out through Optical Microscope (OM) and SEM-EDS, EBSD, EPMA and GD OES. The effect of Pb-Li exposure on the mechanical strength of samples has been investigated through Micro Hardness testing. In order to find the effect of magnetic field on the surface roughness of corroded samples, an Optical profilometer have been used while the analysis of exposed Pb-Li alloy has been carried out through ICP-AES. The technical specifications of all the above mentioned techniques are listed below in Table 4.6. The following Chapters 5 to 8 discusses the results obtained from all the above experiments carried out under various operating conditions.

Table 4.6: Technical Specifications of the Instruments used for characterization.

Sl. No.	Instruments	Make	Technical Specifications
1.	Digital Electronic Weighing Balance	Citizen	Model No :Cx 265 N; Capcity = 80/220 gm; Readability= 0.01/0.1 mg; Repeatability(+/-) = 0.02/ 0.1 mg.
2.	Digital Camera	Sony	HDR-CX280 E Handycam
3.	Stereo Microscope	Olympus	Model No :RX 20; Resolution up to 600 line pairs per mm; 7:1 zoom ratio with 0.8 x to 5.6 x range.
4.	Optical Microscope	Carl Zeiss	Axio Vert A1 inverted optical microscope with bright field, dark field, polarized light and DIC modes. Magnification range: 50 x to 1000 x
5.	Secondary Electron Microscope – Energy	Carl Zeiss	Carl Zeiss Auriga FEG dual beam Scanning electron microscope with Oxford EDS

	Dispersive Spectrometry (SEM-EDS) and		(X Max EDS Detector with Aztech Software) Voltage range upto 30 kV
6.	Electron Back Scattered Diffraction Technique (EBSD),	OXFORD	Nordlys Max 2 EBSD Detector attached to Carl Zeiss SEM
7.	3-D Optical Profilometer	Taylor Hobson	Model No CCI MP-HS non-contact optical profiler. High speed 1 MP camera combined with 1/10 Å vertical resolution. <0.2 Å RMS repeatability.
8.	X Ray Photo Electron Spectroscopy	ULVAC-PHI, INC	PHI 5000 Versa Probe II, Focus x-ray Photo Electron Spectroscopy, Monochromator X Ray Source of Al – K α, X Ray setting at 25 W, 15 KV; Argon ion sputtering at 2 KV. Energy Resolution – 0.67 eV
9.	Glow Discharge Optical Emission Spectroscopy (GD OES)	HORIBA	JY 500 RF; spectral coverage from 110 to 800nm
10.	Electron Probe Micro Analysis (EPMA)	CAMECA	SX 100; Acc.Voltage:0.2 to 40 kV Beam Current:10-to 10-12A; Beam Diameter:0.6µm at 15kV and 100nA; SEM Image Magnification: 150X to 400,000X
11.	Inductively Coupled Plasma-Atomic Emission Spectroscopy	HORIBA	JY 2000, Wavelength range from 190-800 nm Resolution: up to 19 pm Detector: PMT
12.	Microhardness Tester	Future Tech-Corporation	Model No FM-7, Load = 98.07 – 9807 mN, 10 – 1000 G; Indenters : Diamond Vickers (HV), Diamond Knoop (HK); Magnification = x400 (lens 40 x ocular 10) Accuracy :According to JIS B-7734 and ASTM E-384

CHAPTER 5

CORROSION BEHAVIOR OF FERRITIC/MARTENSITIC STEELS IN ISOTHERMAL Pb-Li

---

Before initiation of corrosion experiments, the as-received samples of IN RAFMS and P91 were analyzed for their microstructure and surface oxides. The results of these studies have been reported in the first part of this chapter. The later part discusses the results from experiments carried out under isothermal and static conditions to understand the effect of alloying elements and temperature of exposure on the corrosion behavior of IN RAFMS and P91. The final part of this chapter reports the results from dynamic experiments carried out in the Rotating Disc Corrosion Test Facility (RDCTF) to establish the effect of flow velocity on Pb-Li attack.

5.1. Characterization of as-received IN RAFMS and P91

5.1.1. Microstructure Characterization

Figure 5.1 (a) and (b) shows the optical micrograph of IN RAFMS and P91 material used in this study, respectively. Both the materials showed tempered martensite structure with prior austenite grain boundaries containing the martensitic laths [23, 207]. The SEM micrographs of P91 and IN RAFMS are respectively shown in Figure 5.2 (a) and (b). In the tempered martensitic structure, the grain boundaries of prior austenite grains and martensitic laths were found to be decorated with light colored precipitates. The precipitates were discontinuous and seemed to be finer in P91 than in IN RAFMS. EDS spot analysis was carried out on the IN RAFMS material over the grain boundary precipitates and matrix. As shown in Table 5, the precipitates contained higher amounts of chromium and tungsten indicating them to be tungsten rich $Cr_{23}C_6$ as discussed in Section 2.8 [23-24].

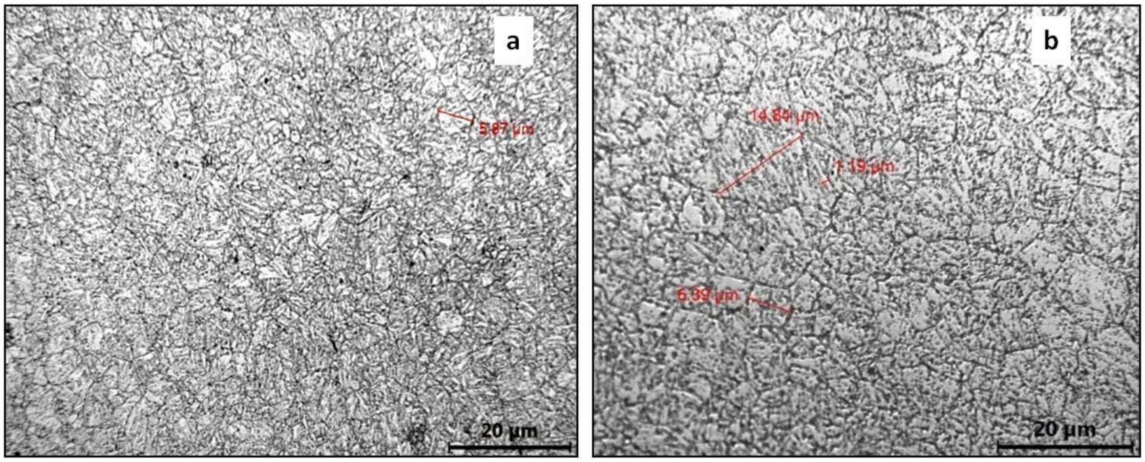

Fig. 5.1: Optical micrographs of the as-received materials (a) P91 and (b) IN RAFMS.

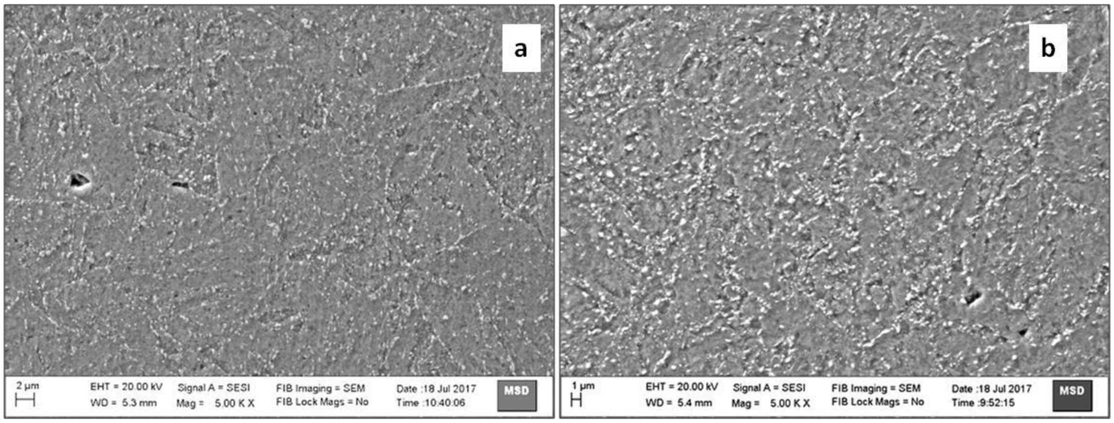

Fig. 5.2: SEM micrographs of the as-received materials (a) P91 and (b) IN RAFMS.

Table 5.1: Composition of grain boundary precipitates and matrix for IN RAFMS as obtained through EDS spot analysis (all in wt%).

	Fe	Cr	W	Mn	V
Grain Boundary Precipitates	86.5	10.6	1.7	0.6	0.6
Matrix	88.0	9.6	1.3	0.9	0.3

The EBSD maps of the surface of IN RAFMS and P91 are shown in Figure 5.3 while the fractions of various phases are listed in Table 5.2. The prior austenite grain size (PAG) of IN RAFMS was found to be higher than P91from Figure 5.3 while Table 5.2 showed the presence of significant fraction of $Cr_{23}C_6$ was found in both the materials. From EBSD "hkl" software, the PAG size of IN RAFMS was found to be ~14 µm while it was ~ 10 µm for P91 [208]. The martensitic lath size of IN RAFMS varied between 1- 2 µm while it was below 1 µm in case of P91. The content of grain boundary precipitates ($Cr_{23}C_6$) was found to be slightly higher in P91. The other type of fine precipitates generally found in the matrix of these materials is of MX type (i.e. NbC, VC, NbN, VN in case of P91 and TaC, VC, VN, TaN in case of IN RAFMS). These however, could not be properly indexed through the present analysis owing to their small size [23]. Nevertheless, author has confirmed the same through Transmission Electron Microscopy (TEM) in the present study but has not been shown since such reports are already available in literature [23-24].

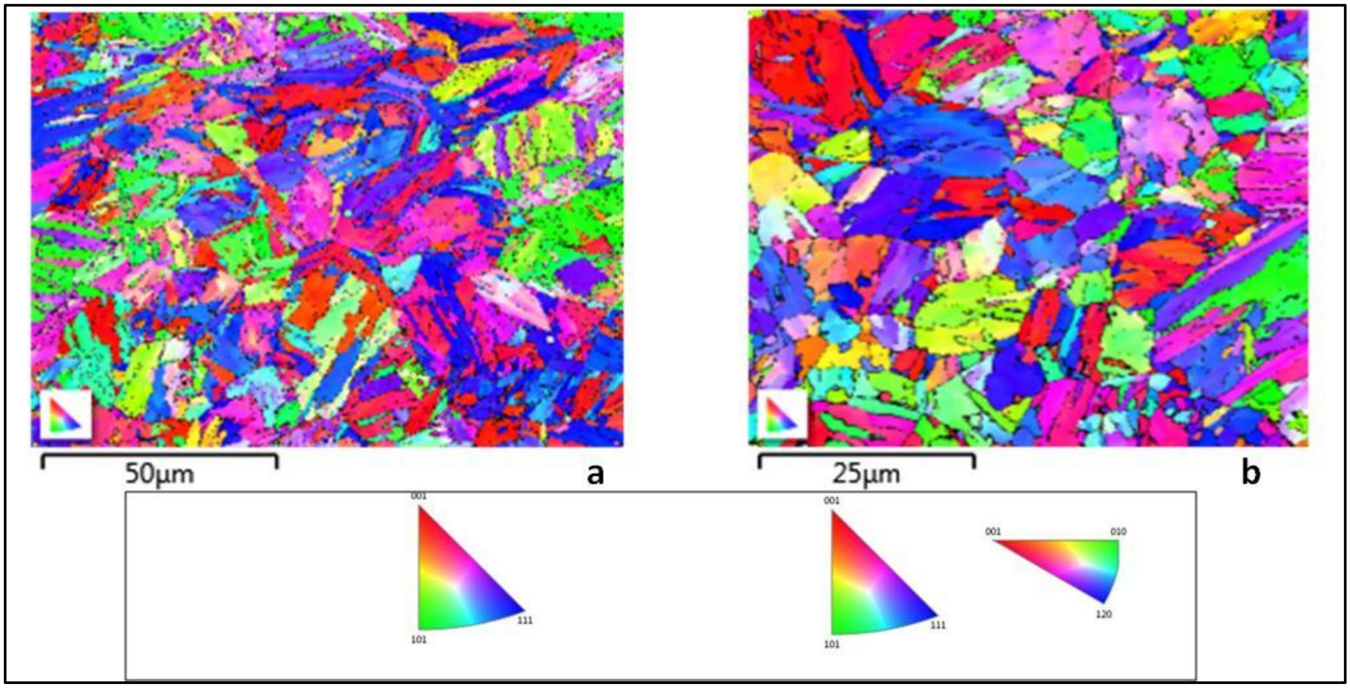

Fig 5.3: EBSD color maps of the as-received materials (a) P91 and (b) IN RAFMS.

Table 5.2: Phase fraction analysis of the as-received P91 and IN RAFMS material recorded through EBSD.

P91		**IN RAFMS**	
Phase Name	Phase Fraction (%)	Phase Name	Phase Fraction (%)
Fe	52.86	Fe	53.41
$Cr_{23}C_6$	24.44	$Cr_{23}C_6$	20.77
NbC	0.05	TaC	0.00
VC	0.02	VC	0.09
NbN	0.05	VN	0.02
VN	0.05	TaN	0.01

5.1.2. Characterization of oxide film on surface

It has been already discussed in Section 2.10 that ferritic/martensitic (F/M) steels develop a passive film on their surface on exposure to air or during vacuum heat treatment [161-162]. This film plays an important role in deciding the corrosion behavior of these steels in Pb-Li [161-164]. Keeping this in mind, the surfaces of IN RAFMS and P91 were characterized by X – ray Photo electron Spectroscopy (XPS) (in diamond polished condition) in order to know the nature of the passive oxide film, if any. The conditions and parameters of XPS analysis have been already reported in Section 4.3.1 (Chapter 4).

The survey scans of the surface of P91 and IN RAFMS in Figure 5.4 (a) and (b) showed the presence of iron (Fe 2p), chromium (Cr 2p) and oxygen (O1s). Manganese was not observed throughout both the spectra. Interestingly, the presence of tungsten (W 4f) in metallic as well as oxide form was observed on the surface of IN RAFMS although P91 surface did not show any molybdenum (Mo 3d) peak. The survey spectra on P91 at all other depths (upto 10 nm) showed molybdenum metallic peak but its oxidation state was never observed. Therefore, the high resolution spectra's of Fe 2p, Cr 2p and O1s were recorded for both the materials. Along with that, the high resolution spectra's of W 4f was also recorded for IN RAFMS.

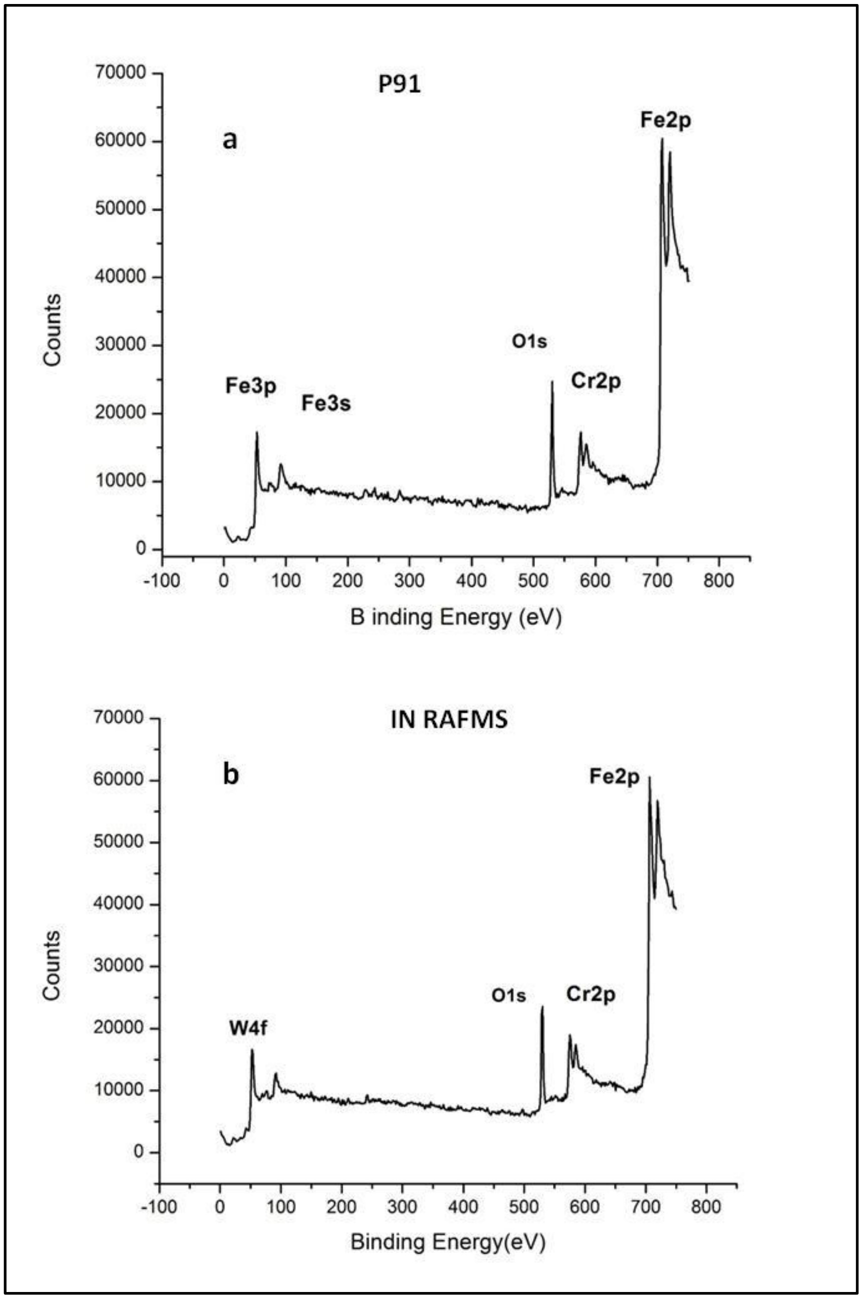

Fig 5.4: XPS Survey Spectra on the surface of as-received (a) P91 and (b) IN RAFMS.

Figure 5.5 show the high resolution spectra of iron (Fe 2p) over the surface as well as at a depth of 2 nm and 4 nm for as-received P91 and IN RAFMS. Metallic (Fe $2p_{3/2}$) and oxidation peaks of iron could be distinguished at the surface of both the materials as well as upto a depth of 4 nm.

The metallic peaks were at 706.2 eV for both P91 and RAFMS [192]. The presence of both Fe^{+2} $2p_{3/2}$ and Fe^{+3} $2p_{3/2}$ in P91 and IN RAFMS upto a depth of 2 nm possibly indicated the presence of magnetite (Fe_3O_4). The peaks of Fe^{+2} and Fe^{+3} were at 709.82 eV and 712.52 eV for P91 and 709.83 eV and 712.26 eV for IN RAFMS [206]. Figure 5.6 (a) and (b) show the depth profile of the high resolution spectra of iron for P91 and IN RAFMS respectively. The presence of iron oxides could not be observed at 6 nm depth thus indicating its presence upto ~ 4-5 nm from the surface. Fe_2O_3 was possibly present towards the outer side (2 nm) below which a layer of FeO existed (upto 5 nm).

The high resolution spectra of chromium (Cr 2p) on the surface, at 4 nm and 8 nm depth for as-received P91 and IN RAFMS is shown in Figure 5.7. The oxidation state of chromium (Cr^{+3} $2p_{3/2}$) could be noted over the surface of P91 and IN RAFMS. However, the peak intensity was not significant enough to justify its presence. This showed that very slight Cr_2O_3 might be formed on the surface of these materials. Nevertheless, the oxide peak became quite strong at 4 nm where metal (Cr $2p_{3/2}$) and oxide (Cr^{+3} $2p_{3/2}$) could be observed at 573.7 eV and 575.8 eV respectively for P91 and at 573.2 eV and 575.2 eV respectively for IN RAFMS [206]. The depth profiles of chromium spectra in P91 and IN RAFMS are shown in Figure 5.8 (a) and (b) respectively. The oxide peak (Cr^{+3} $2p_{3/2}$) was found upto 8 nm in both the materials. These results implicated that Cr_2O_3 was mainly present in the subsurface layer of both the materials. It also existed upto a greater depth (~8-9 nm) as compared to FeO / Fe_2O_3 (~4-6 nm) which implies that an inner layer of pure Cr_2O_3 might be present at 6-8 nm.

Figure 5.9 shows the high resolution spectra of oxygen (O1s) at the surface as well as at 2 nm and 4 nm depth of as-received P91 and IN RAFMS samples. Figure 5.10 (a) and (b) which gives the depth profiling on oxygen spectra for P91 and IN RAFMS respectively [192]. The sharp oxide peak (O^{-2} 1s) could be clearly observed upto 8 nm at 529.3 eV for P91 and 529.07

eV for IN RAFMS. This depth matched well with the occurrence of the oxidation states of Fe and Cr thus confirming the thickness of the passive scale to be around 8 nm.

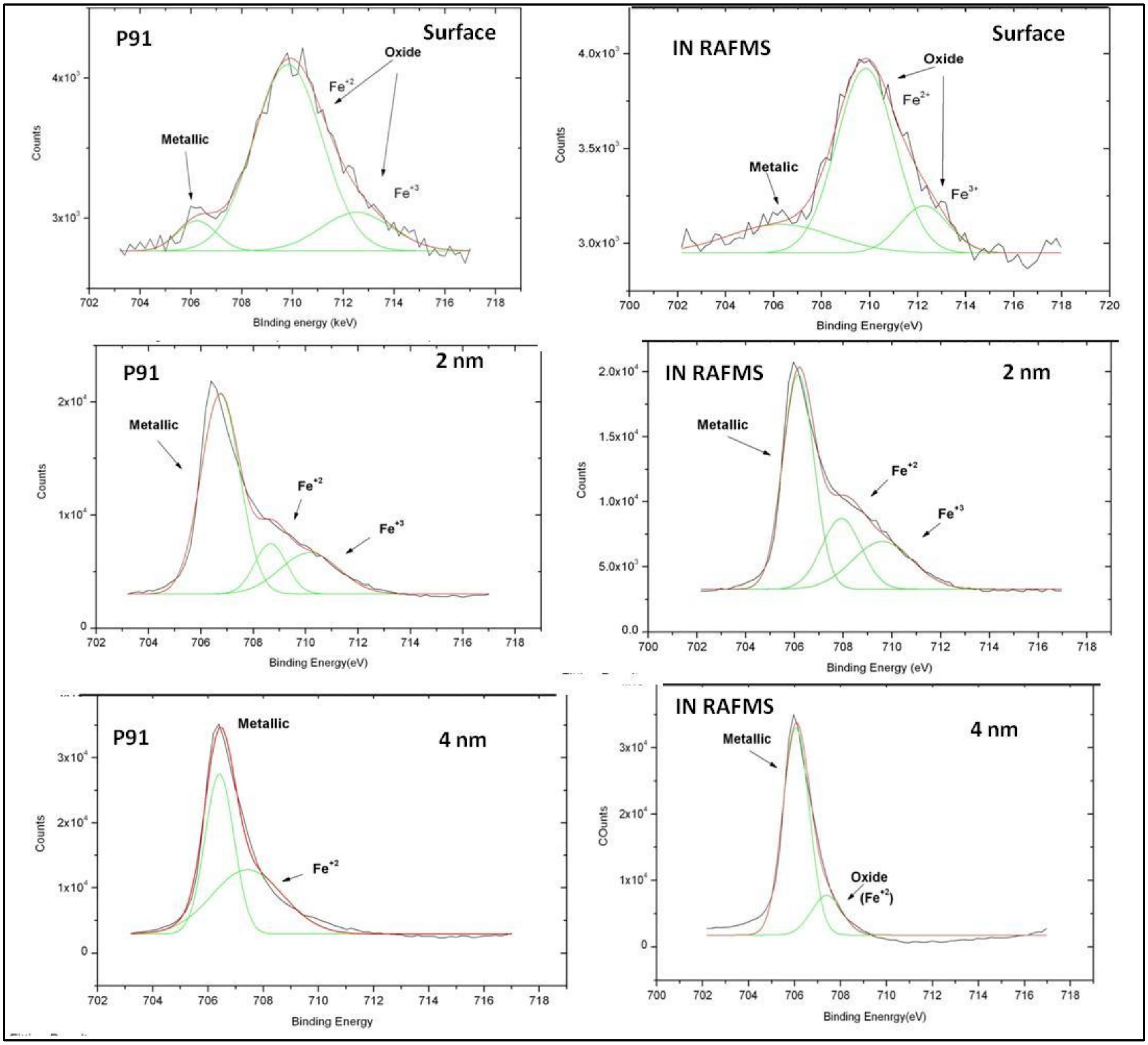

Fig. 5.5: High resolution spectra of iron (Fe 2p) taken on the as-received sample of P91 and IN RAFMS on surface, 2nm depth and 4 nm depth.

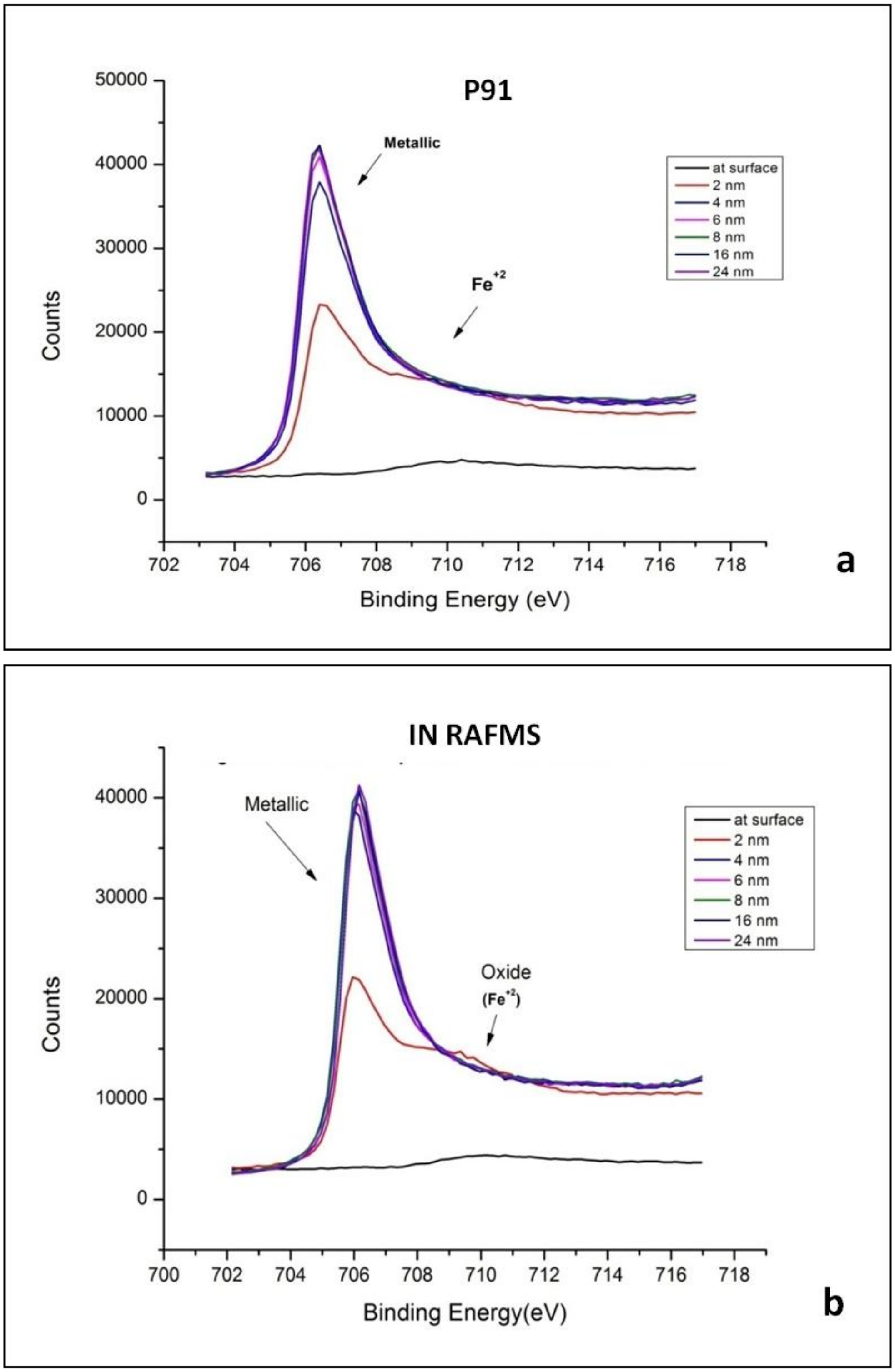

Fig. 5.6: Depth profile of XPS High Resolution spectra of iron (Fe 2p) upto 24 nm in the as-received samples of (a) P91 and (b) IN RAFMS.

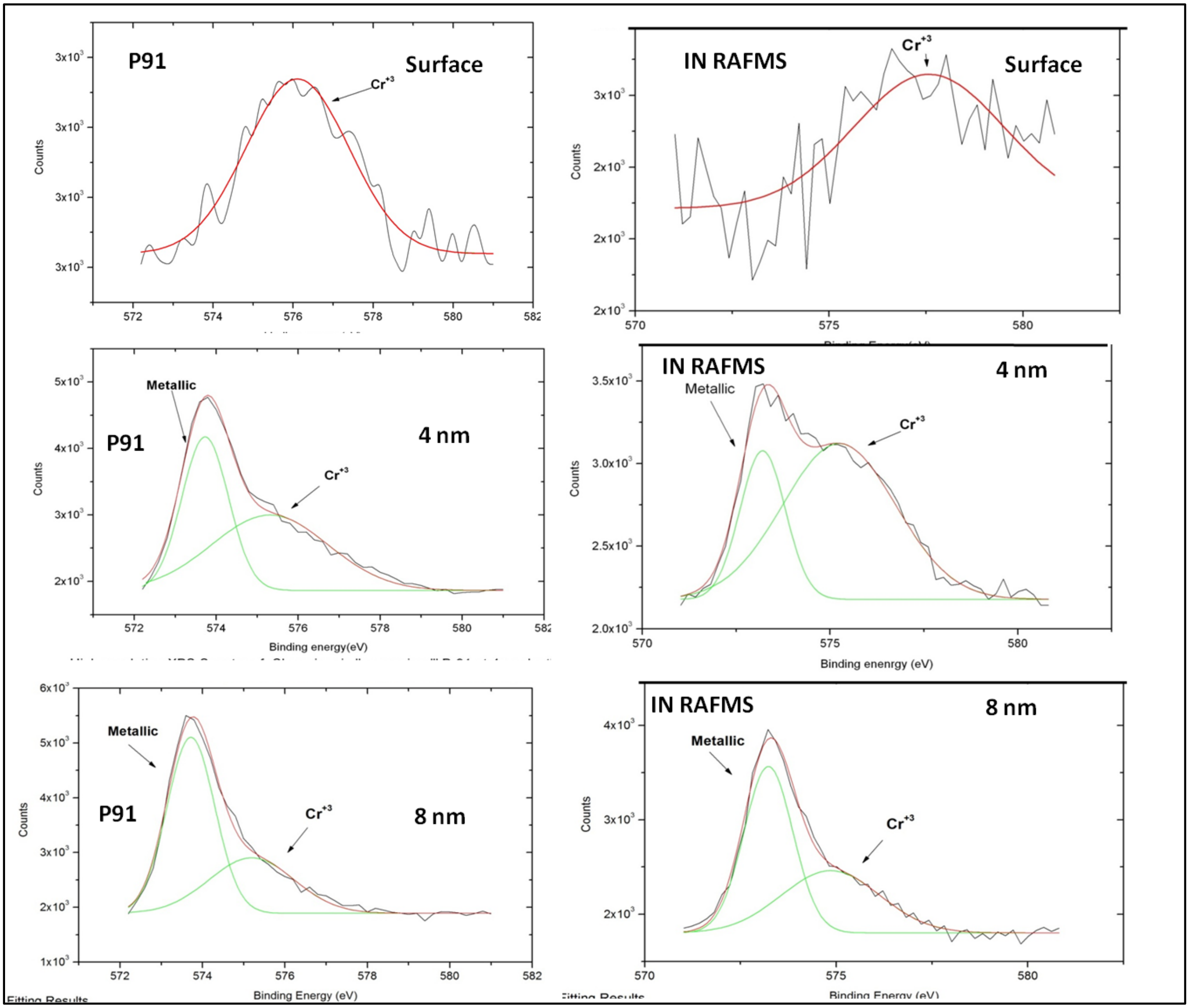

Fig.5.7: High resolution spectra of chromium (Cr 2p) taken on the as-received sample of P91 and IN RAFMS on surface, 4nm depth and 8 nm depth.

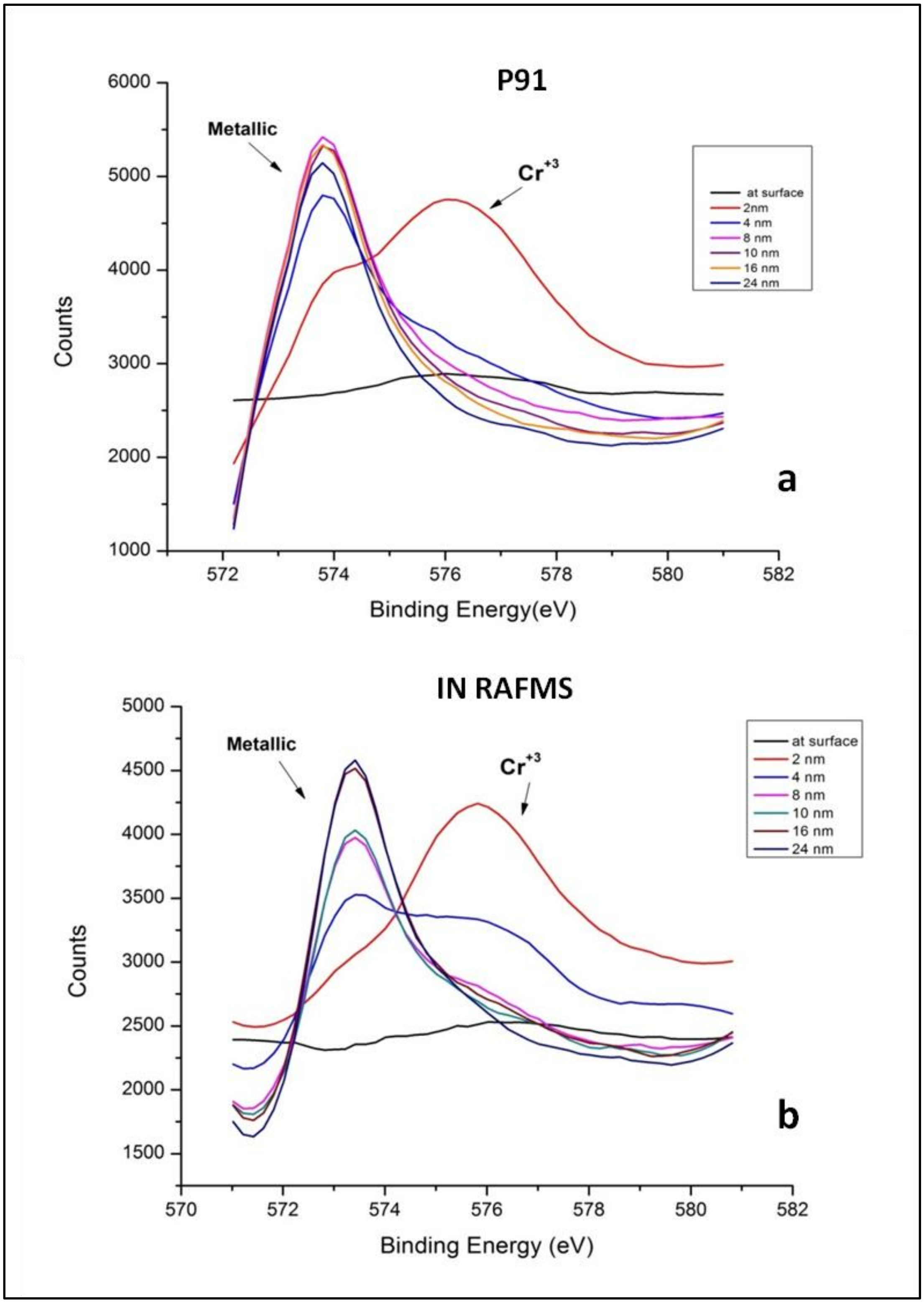

Fig. 5.8: Depth profile of XPS High resolution spectra of chromium (Cr 2p) up to 24 nm in the as-received samples of (a) P91 and (b) IN RAFMS.

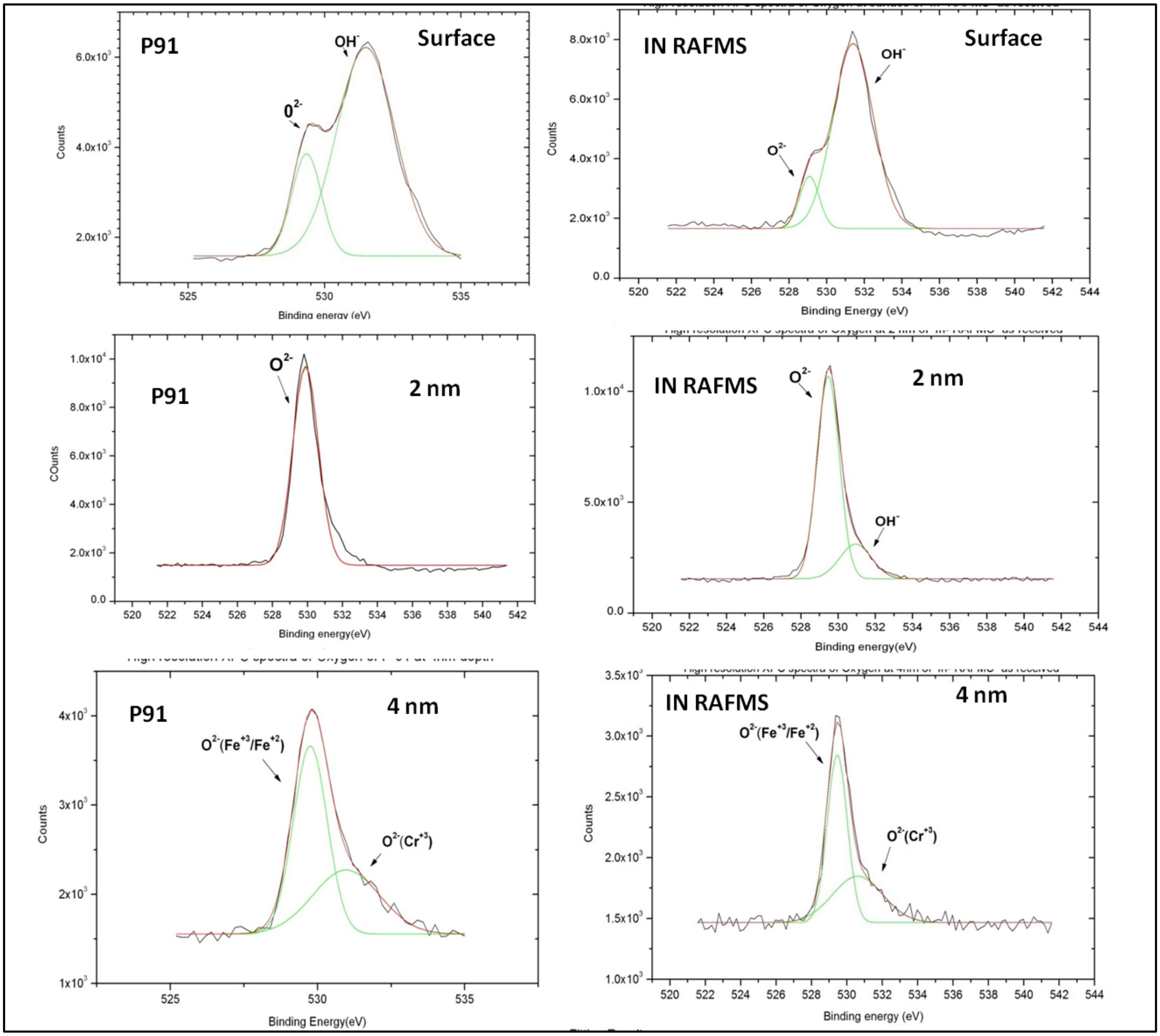

Fig. 5.9: High resolution spectra of oxygen (O 1s) taken on the as-received sample of P91 and IN RAFMS on surface, 2nm depth and 4 nm depth.

The high resolution spectra of tungsten (W 4f) on the surface of IN RAFMS and at a depth of 2nm are shown in Figure 5.11. The presence of metallic peaks were noted at 30.11 eV (W 4f $_{7/2}$) and at 32.89 eV (W 4f $_{5/2}$) [209]. Distinct peaks corresponding to the oxidation states of tungsten (WO_2 and WO_3) were noted at 34.69 eV for W $^{+4}$ 4f $_{7/2}$ and at 36.70 eV for W $^{+6}$ 4f $_{7/2}$ on the surface of IN RAFMS as well as 2nm [209].

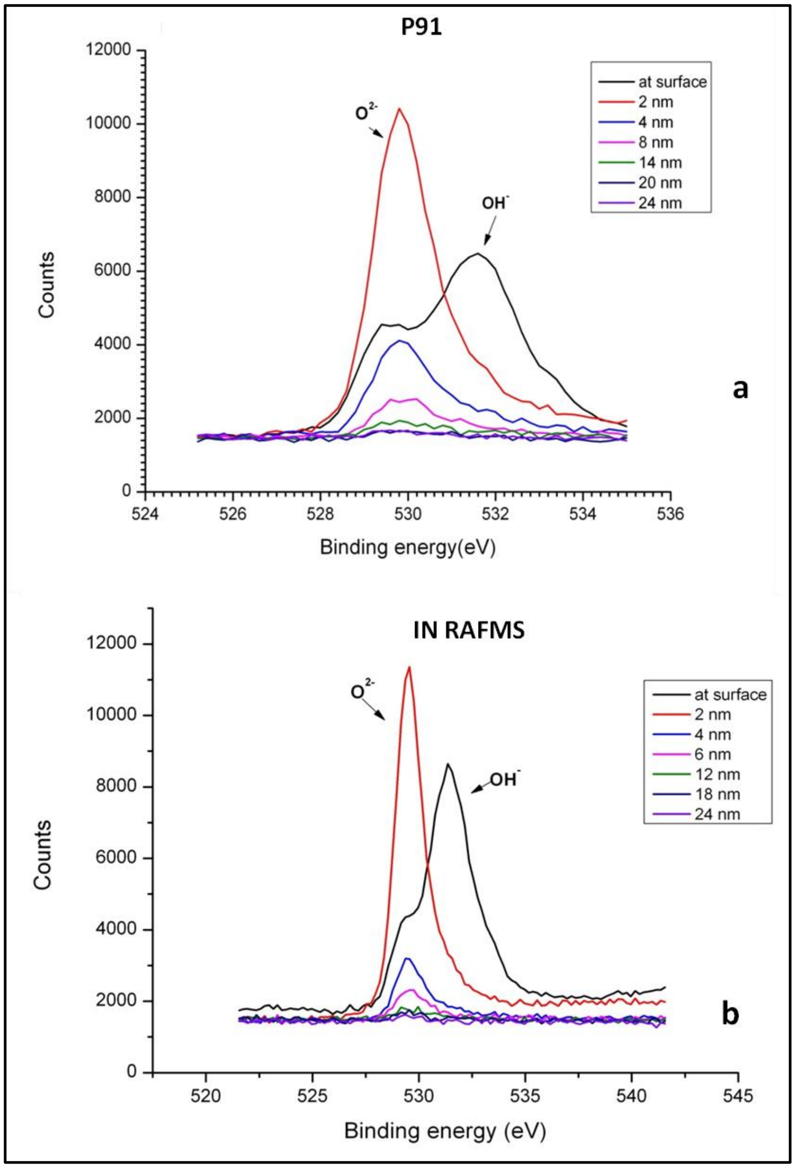

Fig. 5.10: Depth profile of XPS High resolution spectra of oxygen (O1s) up to 24 nm in the as-received samples of (a) P91 and (b) IN RAFMS.

Figure 5.12 (a) and (b) shows the depth profiles of the high resolution spectrum of molybdenum (Mo 3d) and tungsten (W 4f) and in case of P91 and IN RAFMS respectively recorded up to a depth of 24 nm. In the case of IN RAFMS, tungsten oxidation states were present up to a depth 2nm beyond which only tungsten metal was observed as shown in Figure 5.12 (b).

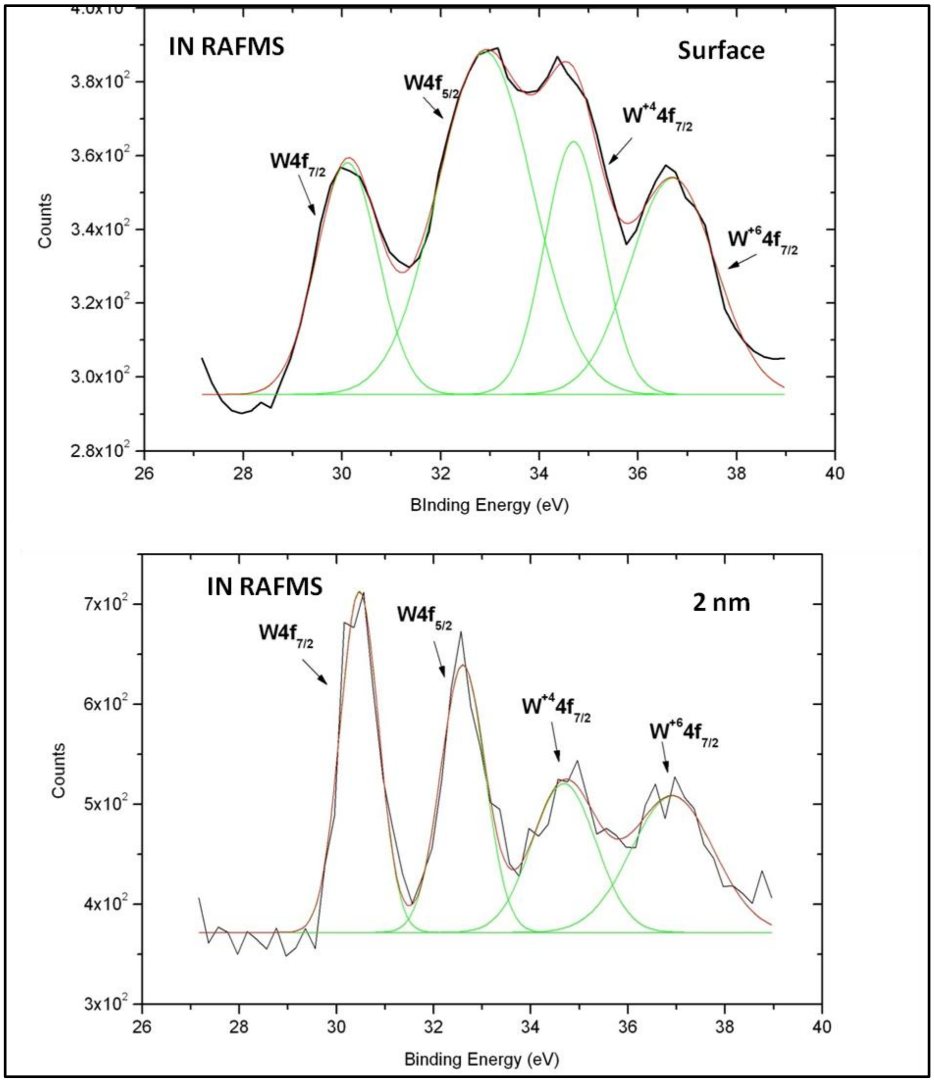

Fig. 5.11: High resolution spectra of tungsten (W 4f) taken on the as-received sample of IN RAFMS on surface and at 2 nm depth.

In comparison with tungsten, the absence of oxidation states of molybdenum in the surface layers could be clearly observed. This indicated that molybdenum oxide was not formed in P91 under similar conditions (diamond polished) as that required for formation of tungsten oxide in IN RAFMS. It may be noted that oxidation states could not be resolved even after rigorous de-convolution of the high resolution molybdenum spectra. The reason for this probably lies in the standard free energy of formation (ΔGf °) of the oxides of tungsten and molybdenum. Table 5.3

shows the ΔGf ° values for molybdenum and tungsten oxides at different temperatures as obtained from analysis carried out using the Factsage 7.2 software.

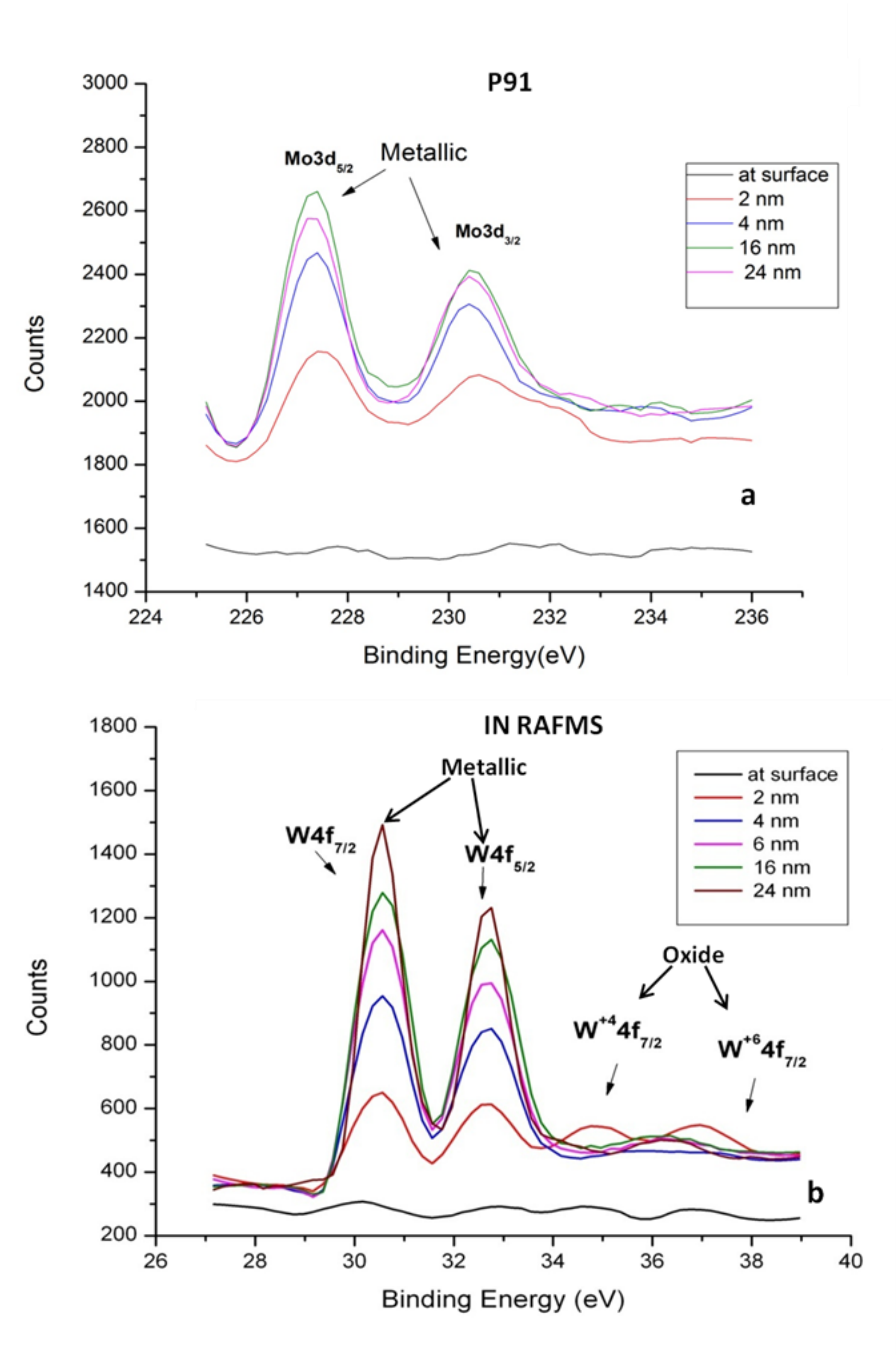

Fig 5.12: Depth profile of XPS high resolution spectra of (a) molybdenum (Mo 3d) in case of P91 and (b) tungsten (W 4f) in case of IN RAFMS up to 24 nm.

Table 5.3: Standard free energy of formation of various oxides at different temperatures.

Oxide	Temperature	ΔG_f ° (KJ)
MoO_2	313 K (40°C)	-0.571
MoO_3	313 K (40°C)	-0.718
WO_2	313 K (40°C)	-0.577
WO_3	313 K (40°C)	-0.840
MoO_2	773 K (500°C)	-0.492
MoO_3	773 K (500°C)	-0.614
WO_2	773 K (500°C)	-0.494
WO_3	773 K (500°C)	-0.708

It was observed that the ΔGf ° values of tungsten oxides (especially WO_3) were higher than corresponding molybdenum oxides at lower (313 K) as well as at higher temperature i.e. 773 K. Thus, under atmospheric conditions, the stability and tendency of formation of tungsten oxides and especially the trioxide (WO_3) will be higher than molybdenum oxides. However, since the difference in ΔGf ° is not too large, it may be possible that molybdenum oxides also form if P91 is exposed to atmosphere for a longer duration. Nevertheless, under present condition (diamond polished and preserved for 1 day before exposure to Pb-Li), the presence of WO_2 and WO_3 can create a difference in the extent of Pb-Li attack of IN RAFMS as compared to P91. One of the reasons for this might be lower solubility of tungsten in Pb-Li [195] which may keep the oxide layer intact for a longer time.

5.2. Corrosion studies in isothermal and static Pb-Li

5.2.1. Corrosion of IN RAFMS and P91 at 773 K and 823 K for 355 h

The corrosion behavior of the IN RAFMS and P91 material was initially compared through static tests in Pb-Li. The samples of IN RAFMS and P91 were exposed to Pb-Li for 355 h at 773 K and

823 K in static corrosion test capsules described in Chapter 3 (Section 3.2) and the experimental procedure has been described in Section 4.3.2 (Chapter 4).

5.2.1.1. Corrosion rate

Table 5.4 shows the weight loss results from the above experiment where P91 material was found to lose 0.9 mg after exposure to Pb-Li at 773 K. This could be extrapolated to a corrosion rate of 0.77 µg/cm^2.h for P91 in static Pb-Li. If the dimensions of an individual P91 sample are taken into account, this weight loss would lead to a thickness reduction rate of 8.64 µm/y. It is expected that this corrosion rate will be magnified in an actual fusion reactor system, due to the presence of flowing Pb-Li which would enhance its corrosive capability [149]. The corrosion rate of P91 increased to 1.71 µg/cm^2.h (19.2 µm/y) when exposed to Pb-Li at 823 K. This confirmed the direct dependence of Pb-Li corrosion attack on temperature [167]. This was related to the increase in solubility of major constituents like Fe and Cr in Pb-Li with increase in temperature as well as the increase in diffusivity of the constituent elements in the steel matrix [100,195].

Table 5.4: Weight loss of P91 and IN RAFMS after exposure to Pb-Li for 355 h.

Sample	Temperature (K)	Initial weight (g)	Final weight (g)	Weight Change (g)	Corrosion Rate (µg/cm ^{2}.h)	Corrosion rate (µm/y)
P91	773	1.434 ± 0.002	1.4331 ± 0.001	- 0.0009	0.77	8.64
IN RAFMS	773	5.62 ± 0.001	5.6360 ± 0.002	+ 0.016	-	-
P91	823	1.570 ± 0.004	1.550 ± 0.004	- 0.020	1.71	19.2
IN RAFMS	823	5.565 ± 0.002	5.579 ± 0.002	+ 0.014	-	-

Interestingly, no loss in weight was observed for the IN RAFMS material at both the temperatures although some weight gain was recorded. It has been already mentioned in Chapter 2 that thermal treatments of ferritic martensitic steels can lead to the formation of surface oxides [161, 192]. Such oxide build up can occur during sample insertion/removal from liquid Pb-Li when the sample is held under inert atmosphere at high temperature (773 K). These oxides form over and above the air formed oxide film as detected by XPS (Section 5.1.2) and can lead to slight weight gain in both P91 and IN RAFMS. However, the weight loss of P91 samples due to Pb-Li corrosion must have been significant enough such that the effect of weight gain due to oxidation has not been reflected in the final weight as observed in the case of IN RAFMS (Table 5.4). In this regard, the presence of tungsten oxide in the passive layer of IN RAFMS and its effect on the greater stability of passive layer has been already discussed in Section 5.1. This may be one of the reasons contributing greater corrosion resistance of IN RAFMS.

It is very well known that for chemical reactions; an increase in reaction temperature by 10 K may double the reaction rate [210]. In fact, the Arrhenius Equation given by Equation 5.1 has been successfully used in chemical reaction kinetics to describe the temperature dependence of the reaction rate constant.

$$k=A \exp(-E/RT) \quad \ldots\ldots\ldots\ldots\ldots\ldots \quad 5.1$$

Where k is the reaction rate constant, A is the frequency factor or the pre-exponential factor and E is the activation energy, R is the universal gas constant and T is the temperature [211].

Although a doubling in the rate of weight loss of P91 is observed in the present case of Pb-Li corrosion too; however this increase takes place over a much larger span of temperature i.e. 50 K. This may point to the fact that the kinetics of liquid metal corrosion (governed by dissolution of alloying elements and their solubility in liquid metal) is much slower than that of an electrochemical corrosion (governed by chemical reactions taking place at cathode and anode). In this regard, Tortoelli et al. have described the dissolution of ferrous alloys in Pb-Li by Equation 5.2 [157].

$J = r. (C_s - C)$…………………………………………………………………………… 5.2

Where ‘J’ is the flux of a particular element into Pb-Li ($g/m^2.s$) (i.e. dissolution rate), ‘r’ is the mass transfer coefficient ($g/m^2.s$), ‘C_s’ is the solubility (ratio) of that element in Pb-Li at the experimental temperature ‘T’ and ‘C’ is the actual concentration of that element (ratio). Now the solubility of a particular element; for e.g. iron in Pb-Li could be expressed as Equation 5.3 [195]

$\text{Log } C_{Fe} = 7.236 - 9345\ T^{-1}$……………………………………………………………… 5.3

where ‘C_{Fe}’ is the solubility of iron at temperature, ‘T’. Therefore as temperature increases, the solubility on an element in the liquid also increases and thus the value of (C_s- C) also increases (assuming a constant “C” at a time “t”).

The overall mass transfer coefficient for the dissolution type corrosion is derived from the Sherwood number which is the non-dimensional number for mass transfer in fluids. Sherwood number depends on material properties like density (in solid and liquid), diffusivity, viscosity; etc which is again functions of temperature [144, 188]. It may be noted that for dynamic systems, the mass transfer coefficient will also depend on the velocity of flow [144]. This implies that the corrosion rate in liquid metals can vary significantly with temperature of exposure. Nevertheless, the theoretical model stating the nature of such dependence is a scope of future studies. However, experimental data from RAFM steels exposed to static lithium have established that the corresponding mass transfer coefficient increases from 4.08×10^{-8} m/s at 773 K to 1.81×10^{-7} m/s at 873 K [125]. The temperature dependence of Pb-Li corrosion was also studied by Borgstedt et al. where they exposed martensitic steel X18CrMoVNb121 (1.4914, MANET) to flowing Pb-Li in PICOLO loop at 773 K and 823 K. They calculated an activation energy of 200 (kgJ/g - atom) for steady state corrosion which also reflects the significant role of temperature in liquid metal corrosion [174].

5.2.1.2. Micro-structural Investigation

The samples of P91 and IN RAFMS exposed to Pb-Li were further analyzed through optical microscopy and SEM-EDS. The samples exposed at both at 773 K and 823 K showed similar results indicating no change in the basic corrosion mechanism with temperature. For a concise representation, only the results from the samples exposed for 773 K are presented here. Figure 5.13 shows the optical micrographs of the cross-section of the P91 sample before and after exposure to Pb-Li at 773 K. As compared to the unexposed surface in Figure 5.13 (a), the exposed surface in Figure 5.13 (b) showed prominent corrosion attach which seemed preferably along grain boundaries. Some evidence of grain boundary attack has been earlier reported for EUROFER samples when exposed to Pb-Li at 753 K [163]. Figure 5.14 show the optical micrographs of the cross-section of the IN RAFMS sample before and after exposure to Pb-Li at 773 K. The unexposed surface of IN RAFMS could be observed from Figure 5.14 (a). As compared to P91, preferential grain boundary attack was not observed on the surface of exposed IN RAFMS sample as shown in Figure 5.14 (b).

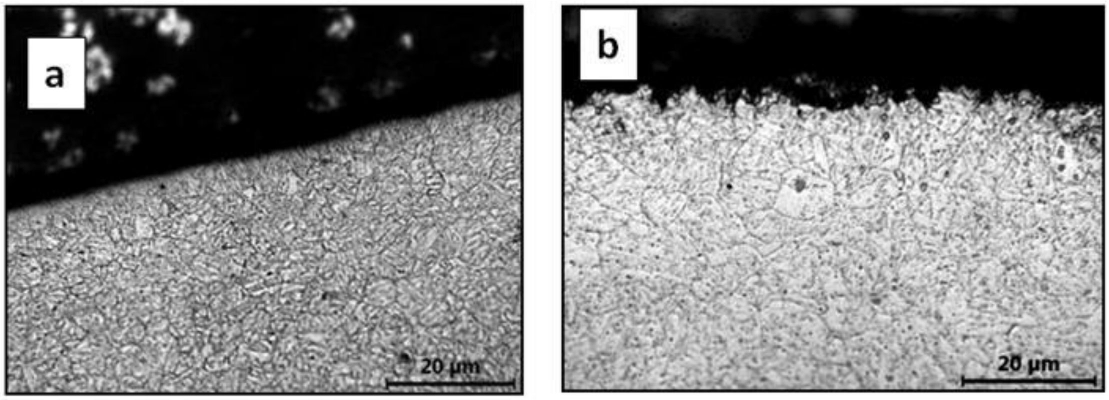

Fig. 5.13: Optical micrographs of P91 sample before and after exposure to Pb-Li at 773 K for 355 h: (a) surface before exposure; (b) surface after exposure.

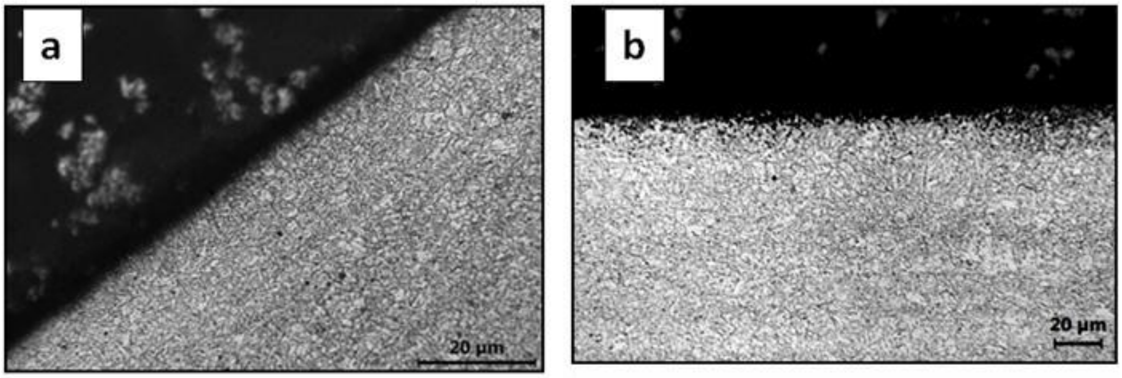

Fig. 5.14: Optical micrographs of IN RAFMS sample before and after exposure to Pb-Li at 773 K for 355 h: (a) surface before exposure; (b) surface after exposure.

Figure 5.15 (a) and (b) show the SEM images of the cross-section of the P91 and IN RAFMS samples after exposure to Pb-Li. No corroded layer was found on the Pb-Li facing surface of both the exposed samples. Figure 5.15 (a) and (b) respectively show the EDS line scans of Fe, Cr and O were taken across the exposed surfaces of P91 and IN RAFMS. It was observed that the concentrations of Fe and Cr decreased slightly at the exposed surface of both the samples within a distance of 0.5 µm. Such dissolution of alloying elements from Pb-Li exposed surface has been noted earlier for JLF 1 steel when exposed to static Pb-Li at 873 K [125].

As shown in Figure 5.15 (a) and (b), the oxygen concentration remained almost constant over the cross-sections of the P91 and IN RAFMS sample respectively. This oxygen was possibly sourced from the post exposure surface oxidation during sample preparation through grinding and polishing. However, the oxygen content at the exposed surface was found to be comparatively higher in the IN RAFMS sample (Figure 5.15 (b)) as compared to P91 (Figure 5.15 (a)). This once again indicated the presence of a stronger passive oxide over the IN RAFMS surface which may be the reason behind no weight loss.

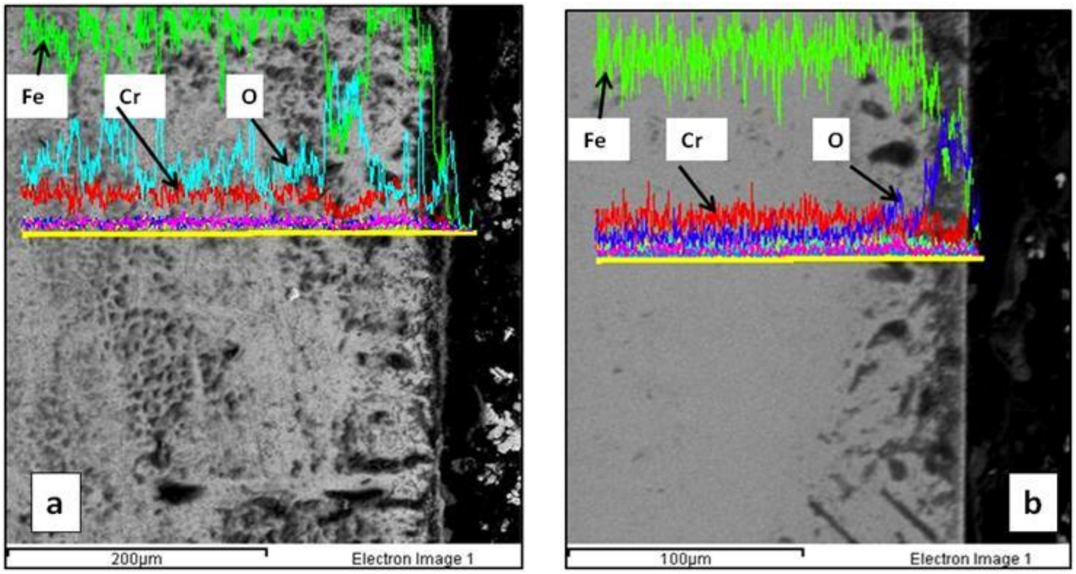

Fig. 5.15: SEM images and EDS profiles of Fe, Cr and O on the (a) P91 and (b) IN RAFMS sample exposed to Pb-Li eutectic at 773 K for 355 h.

In this regard, the atomic concentration of oxygen, chromium, iron, manganese and molybdenum (or tungsten) on the as-received materials was recorded through XPS. Figure 5.16 (a) and (b) show these concentration profiles for P91 and IN RAFMS respectively. The higher oxygen content could be clearly noted on the IN RAFMS surface which complements the results of SEM – EDS analysis shown in Figure 5.15. The depth of the oxide layer in both the material was found to 6-8 nm under as-received (diamond polished) condition. Similar results were also obtained from the high resolution XPS scans reported in Section 5.1.

Since IN RAFMS did not show any weight loss, the decrease in Fe and Cr content in its case might be due to the presence of the passive oxide layer which prevents its weight loss till 355 hrs [161]. On the other hand, the decrease of alloying elements in the case of P91 might additionally be due to their dissolution in Pb-Li since significant weight loss and Pb-Li attack along grain boundaries were noted.

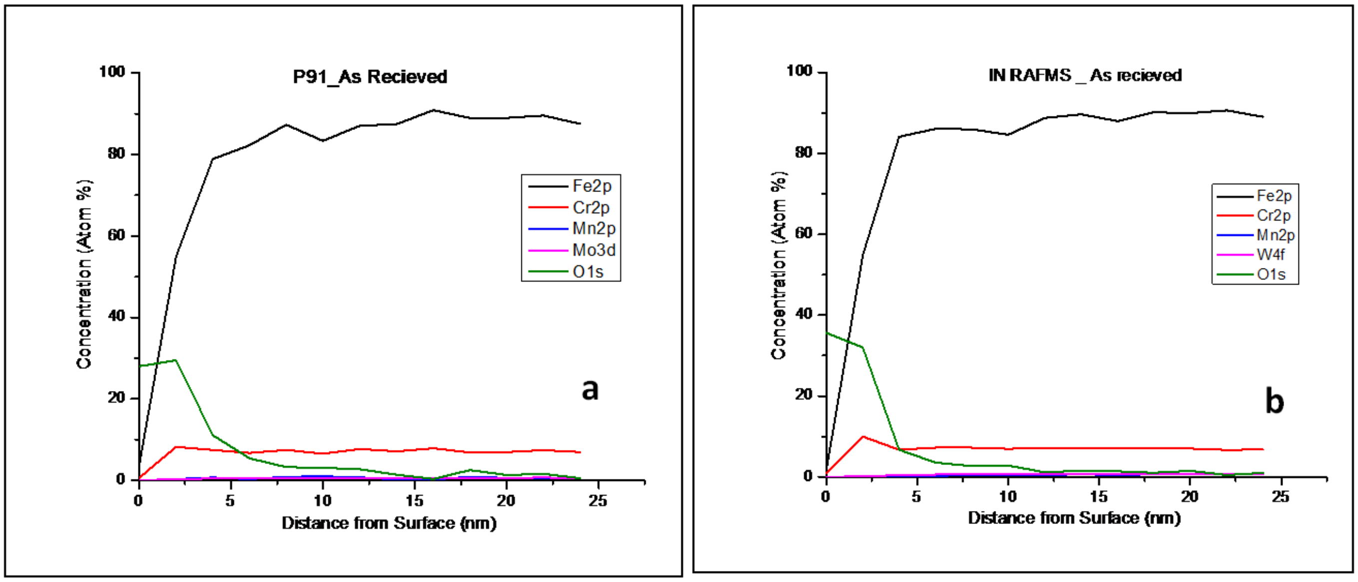

Fig 5.16: Atomic Fractions of oxygen, chromium, iron, manganese and molybdenum (or tungsten) on the as-received (a) P91 and (b) IN RAFMS as obtained through XPS.

5.2.1.3. Summary

1. The corrosion compatibility of P91 and IN-RAFMS material was tested in molten Pb-Li for 350 h at 773 K and 823 K in static condition.
2. Weight loss occurred at a rate of 2.53 µg/h for P91 material at 773 K whereas IN RAFMS showed negligible weight loss after 355 h. This was possibly due to a stronger passive layer in case of IN RAFMS.
3. The weight loss of P91 was found to be almost double after increase in test temperature from 773 K to 823 K thereby showing the direct dependence of dissolution rate with temperature.
4. Corrosion of P91 by Pb-Li was associated with the depletion of Fe and Cr from the exposed surface and preferential attack along grain boundaries.

5.2.2. Corrosion mechanism of IN RAFMS in Pb-Li at 773 K

In order to understand the effect of alloying elements on the corrosion behavior, samples of IN RAFMS, low alloy steel and pure Cr were exposed to Pb-Li at 773 K for 1, 000 h in the new static experimental set-up with automatic sample removal facility (Section 3.3). One set of samples was removed for analysis after 250 h, 500 h and 1000 h. Figure 5.17 shows the photograph of the cleaned samples after exposure to Pb-Li for 500 h. The metallic luster over the unexposed and polished surface as shown in Figure 4.3 (Section 4.3.3) could not be observed in the present case.

Fig. 5.17: Exposed samples of IN RAFMS, low alloy steel and pure chromium after exposure to Pb-Li at 773 K for 500 h.

5.2.2.1. Dissolution Rate of pure metals and IN RAFMS

The weight loss of pure Cr, Low alloy steel and IN RAFMS samples after exposure to Pb-Li for 250 h, 500 h and 1, 000 h are indicated in Table 5.5, Table 5.6 and Table 5.7 respectively. It may be noted that IN RAFMS suffered negligible weight loss in the first 250 h. The Tables 5.5 - 5.7 give the weight loss / unit area (W/A) as well as the total thickness loss for all the three materials exposed to Pb-Li. The reduction in thickness for pure chromium, low alloy steel and IN RAFMS has been plotted with the duration of exposure in Figure 5.18. The weight loss of IN RAFMS and low alloy steel have been found to increase with time while the weight loss of pure chromium increased in the first 500 h but later dropped slightly at 1, 000 h resulting in an overall decreasing trend.

Table 5.5: Weight Loss of IN RAFMS in Pb-Li at 773 K after 250 h.

Sample No.	Sample Name	Weight loss in 250 h (g)	Exposed Area (cm^2)	Weight Loss/area ($\mu g/cm^2$)	Reduction in thickness (µm)
1.	Pure Cr	0.0026	1.27226	2043.6	2.84
2.	Low Alloy Steel	0.0003	2.33514	128.47	0.16
3.	IN RAFMS	0.0001	2.2000	Negligible	Negligible

Table 5.6: Weight Loss of IN RAFMS in Pb-Li at 773 K after 500 h.

Sample No.	Sample Name	Weight loss in 500 h (g)	Exposed Area (cm^2)	Weight Loss/area ($\mu g/cm^2$)	Reduction in thickness (µm)
1.	Pure Cr	0.0029	1.0264	2825.4	3.92
2.	Low Alloy Steel	0.0005	2.9536	169.28	0.21
3.	IN RAFMS	0.0002	2.9378	68.07	0.08

Table 5.7: Weight Loss of IN RAFMS in Pb-Li at 773 K after 1, 000 h.

Sample No.	Sample Name	Weight loss in 1000 h (g)	Exposed Area (cm^2)	Weight Loss/area ($\mu g/cm^2$)	Reduction in thickness (µm)
1.	Pure Cr	0.0030	1.6091	1864.3	2.59
2.	Low Alloy Steel	0.0016	3.0719	520.8	0.66
3.	IN RAFMS	0.0008	2.2051	363.79	0.46

It could be observed from Figure 5.18, that the dissolution / corrosion rate of pure chromium was higher than pure iron (Low alloy steel) in all the exposures. However, it is also known that at 773

K, the solubility (Cs) of iron in liquid Pb-Li [212] was higher than chromium [213] as given below:-

Cs (Fe/Pb-Li) $_{500^\circ C}$ = 47 wppm

Cs (Cr/Pb-Li) $_{500^\circ C}$ = 10 wppm

Where Cs is the maximum solubility of a pure element in liquid metal.

Therefore, there must be some other factor governing the dissolution rate in Pb-Li. Moreover, the corrosion rate of IN RAFMS was found similar to that of iron which may indicate that the corrosion of IN RAFMS was mainly dependent on the dissolution of iron. As indicated in Section 2.9.2.c, Liquid metal corrosion comprises of the following main steps:-

1. Dissolution of metallic species from the solid surface into the boundary layer of liquid metal.
2. Diffusion of metallic species through the Pb-Li boundary layer and transport into the bulk liquid.

Now, the diffusion coefficient of iron in liquid Pb-Li has been found [214-215] to be much smaller than that of chromium:-

D (Fe/Pb-Li) $_{500^\circ C}$ = $4 \pm 2\text{x}10^{-14}$ m^2 s^{-1}

D (Cr/Pb-Li) $_{500^\circ C}$ = $9 \pm 2.5\text{x}10^{-11}$ m^2 s^{-1}

where D is the diffusion coefficient of the metallic species in Pb-Li.

Therefore, although the solubility of Fe in Pb-Li is much higher than chromium, the slower diffusivity of Fe through the Pb-Li might limit its dissolution. Nevertheless, the diffusion of metallic species through the liquid boundary layer becomes the rate determining step for liquid metal corrosion. Since the diffusion of iron determined the overall dissolution, the corrosion rate of IN RAFMS was found similar to pure iron after 1, 000 h. Since the diffusivity of chromium in Pb-

Li is almost three orders of magnitude higher that iron, the dissolution rate of chromium was highest after 1, 000 h. However, the slight decrease in dissolution rate of chromium after the initial 500 h was possibly a result of its lesser solubility in Pb-Li [125].

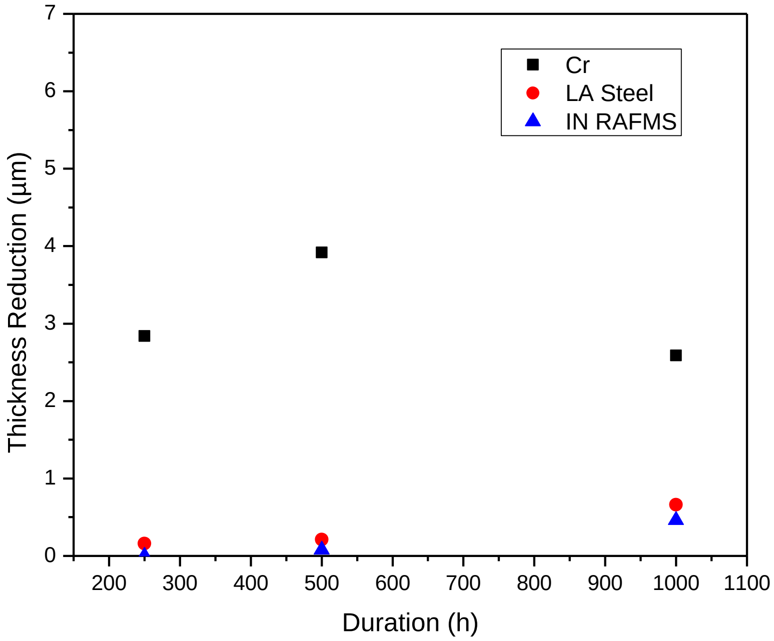

Fig. 5.18: Plot of reduction in thickness vs duration of exposure for pure Cr, Low Alloy Steel and IN RAFMS.

It has been reported that the diffusivity of Cr in 1.4941 steel matrix is 1.5 – 2 x 10^{-20} m^2s^{-1} [215]. Considering a similar diffusivity of Cr in IN RAFMS, it is evident that dissolution rate of Cr from the exposed surface into Pb-Li will be higher than its rate of replenishment from inner matrix. This may lead to the formation of a Cr depleted zone after some time when the entire Cr from surface layer has dissolved. Similar results have been reported earlier when Fe–Cr alloys DIN 1.4914 and Orion were exposed to Pb-Li along with pure chromium and iron at 773 K [215]. Formation of chromium depleted surface layers have also been reported when EUROFER 97 samples were exposed to flowing Pb-Li in LIFUS II loop at 753 K [212].

5.2.2.2 Effect of Pb-Li attack on the microstructure of IN RAFMS

The surface microstructure of the as-received IN RAFM sample after etching with Villela's Reagent has been already shown in Figure 5.2 (b). The micrographs of the IN RAFMS surface after exposure to Pb-Li at 773 K for 500 h and 1, 000 h are shown in Figure 5.19 (a) and (b) respectively. The two most distinct features that could be noted after the Pb-Li exposure were:

(a) Preferential Grain Boundary attack
(b) Absence of grain and lath boundary carbides

It was also observed that the extent of Pb-Li attack over the surface of the sample exposed for 500 h was non uniform. The attack was only along the boundaries of sub-grains / laths in some regions, while removal of the matrix inside the attacked boundaries was noted in other parts. Such kind of a surface probably shows the various steps involved in the initial stages of Pb-Li attack. The surface after 1, 000 h of exposure continued to show non uniform attack with deep penetrations across grain boundaries at some places with significant material removal while shallow grain boundary attack at other locations. The non uniform nature of lead-lithium corrosion has also been recorded by Glassbrenner et al. for various RAFM steels exposed to flowing Pb-Li [161-162]. They have attributed such attack to the non-uniform dissolution of the passive oxide scales present over the steel surface. Similar results were also noted in case of EUROFER and CLAM steel specimens when exposed to Pb-Li in PICOLO loop at 823 K for 500 h and 1, 000 h [194]. Such behavior was also attributed to greater dissolution of oxide scale at certain locations [194]. This once again depends on the initial thickness of the air formed oxide layer and density of grain boundaries over a particular region.

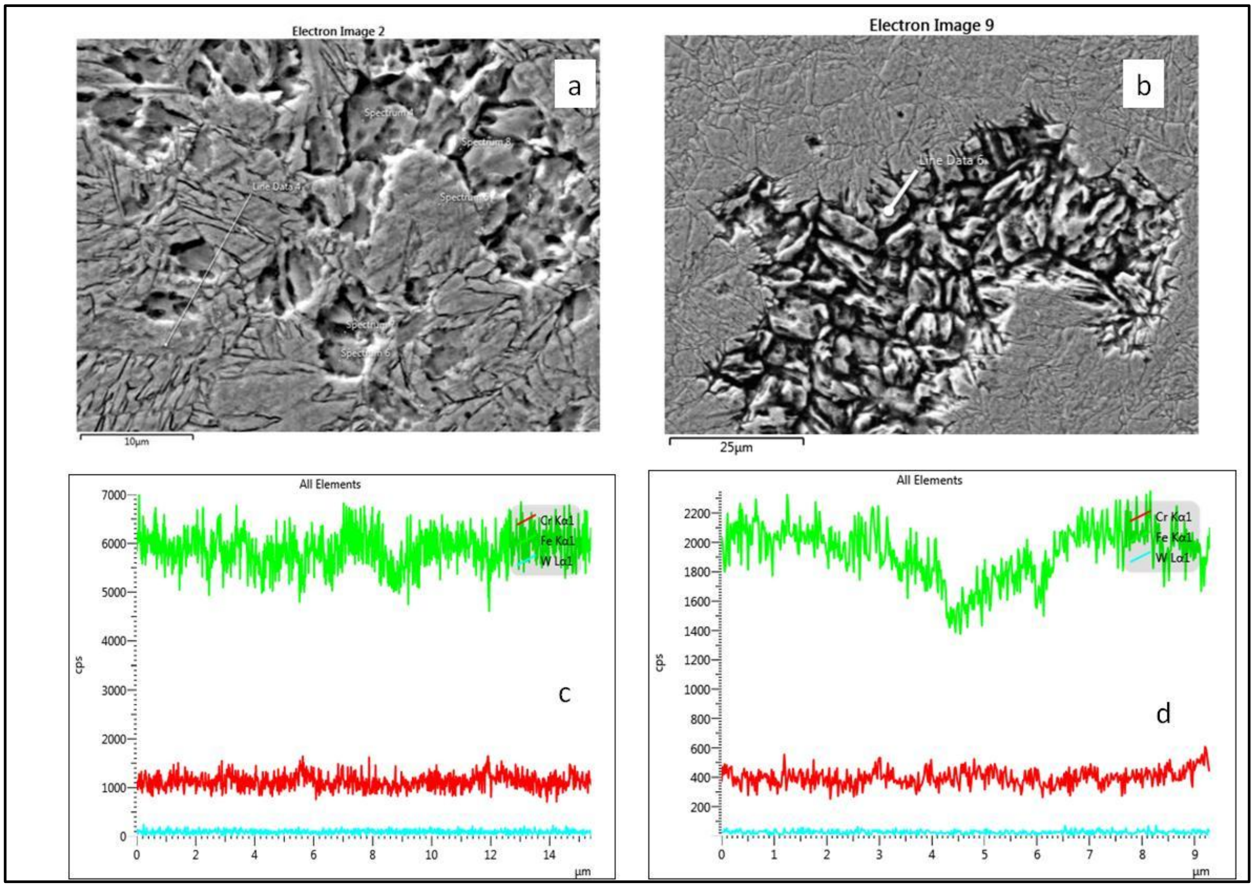

Fig. 5.19: Surface Microstructures of (a) IN RAFMS after exposure to Pb-Li for 500 h, (b) IN RAFMS after exposure to Pb-Li for 1000 h; Elemental line scans of Fe, Cr and W over IN RAFMS across grain boundaries after exposure to Pb-Li for (c) 500 h and (d) 1, 000 h.

The preferential attack along grain and lath boundaries have been reported way back in 1986 when ferritic steel HT-9 and P91 were exposed to flowing Pb-Li at 753 K [155]. The authors have reported the formation of an etched appearance on the surface due to Pb-Li attack as observed in the present case [155]. Another study with different F/M steels exposed to Pb-Li has also reported that Pb-Li preferentially attacked along martensitic lath boundaries [161]. They also observed that out of three different steels i.e. F82H, OPTIFER and MANET I, the lath boundary attack on MANET I was more pronounced than for the other steels. The explanation for this behavior was given on the basis of formation of more $M_{23}C_6$ (M=Cr, Fe, Mo, W, V) precipitates on martensitic lath boundaries of MANET I than the other steels investigated [due to higher carbon and chromium content]. The formation of these $M_{23}C_6$ precipitates can cause a depletion of Cr, Mo, W and V in the vicinity of the martensitic lath boundaries, making matrix dissolution easier in these areas [161].

For further investigation, composition profiles of Fe and Cr were mapped across the attacked grain boundaries on the exposed IN RAFMS surface through EDS line scan. Figure 5.19 (c) and (d) shows the composition profile of Fe and Cr over the attacked grain boundaries of the samples exposed to Pb-Li for 500 h and 1, 000 h respectively. The path of the line scans has been indicated in Figure 5.19 (a) and (b). Although the change in the content of chromium at the grain boundary could not be identified clearly in the line scans but depletion of iron is observed. The depleted region seemed wider for the sample exposed for 1, 000 h indicating greater material removal from the grain boundary region.

Figure 5.20 shows the high magnification image of IN RAFMS material after 500 h of exposure to Pb-Li. Other than the absence of carbides, certain grooves indicating preferential removal of material could be observed. These grooves were of varying sizes ranging from 600 nm to 1 µm and may have formed due to removal of an entire sub-grain within a prior austenite grain. Sub-grains can form during thermal ageing due to the martensitic lath recovery through a process of dislocation movement and dislocation annihilation, resulting in the migration of martensitic lath boundaries [216-217]. The loss of material from sub-grains in the initial stages of Pb-Li attack has been also reported for JLF-1 steel exposed to flowing Pb-Li. [125]. They have attributed this to the fact that the liquid Pb-Li penetrates the sub-grains boundaries causing them to be dropped or peeled off under flowing conditions.

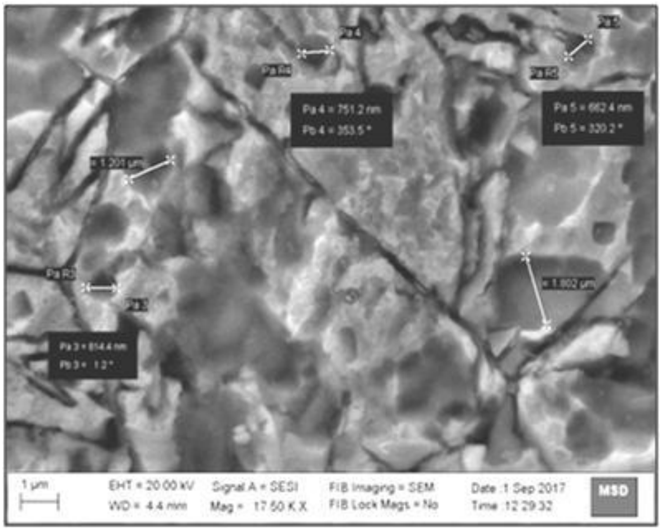

Fig. 5.20: High magnification SEM image of IN RAFMS sample exposed for 500 h in Pb-Li.

The composition at various locations on the surface of the exposed IN RAFMS samples was also recorded through spot EDS analysis. Figure 5.21 (a) and (b) shows the location of spot EDS for the IN RAFMS material after exposure to Pb-Li for 500 h and 1, 000 h respectively. The composition of the various spots is listed in Table 5.8. It could be observed that after 500 h, some of the locations (e.g. Spot 1) were slightly enriched in chromium (10.6%) where the oxygen content was also higher (4.9%). However, the other regions (e.g. Spot 2) were comparatively richer in tungsten (1.7%). Enrichment of tungsten have been reported for low activation ferritic / maretnsitic steels like MANET I, Optifer IVa and F82H-mod samples after exposure to flowing Pb-Li. This was associated with leaching of the major constituent elements like Fe and Cr due to their higher solubility as compared to W [161]. Thus the tungsten enriched areas in the present case must be the regions which experienced greater Pb-Li attack.

It has been already reported that the initial phase of Pb-Li attack over RAFM steels like EUROFER constitutes dissolution of the passive oxide layer containing oxides of Cr, Fe and Mn. [163-164]. Similar oxides have also been noted over the as-received IN RAFMS steels used the present study (Section 5.1). Difference in oxygen content over the exposed IN RAFMS surface and lesser oxygen content in the regions having W enrichment, points to the fact non that uniform dissolution of the passive oxide layer led to non uniform Pb-Li attack. Y. Chen et al. has observed that exposure of CLAM steel to flowing Pb-Li resulted in minimum attack on the specimen surface during the initial 2, 000 h of exposure since they were protected by the passive layer of Cr_2O_3 or $(Fe_xCr_{1-x})_2O_3$ [164]. However, they reported that some areas may suffer attacks due to the reaction of Fe_3O_4 and Pb to produce lead oxide and iron [164]. This observation complements our present results of non uniform attack even in the presence of oxygen rich locations on the surface.

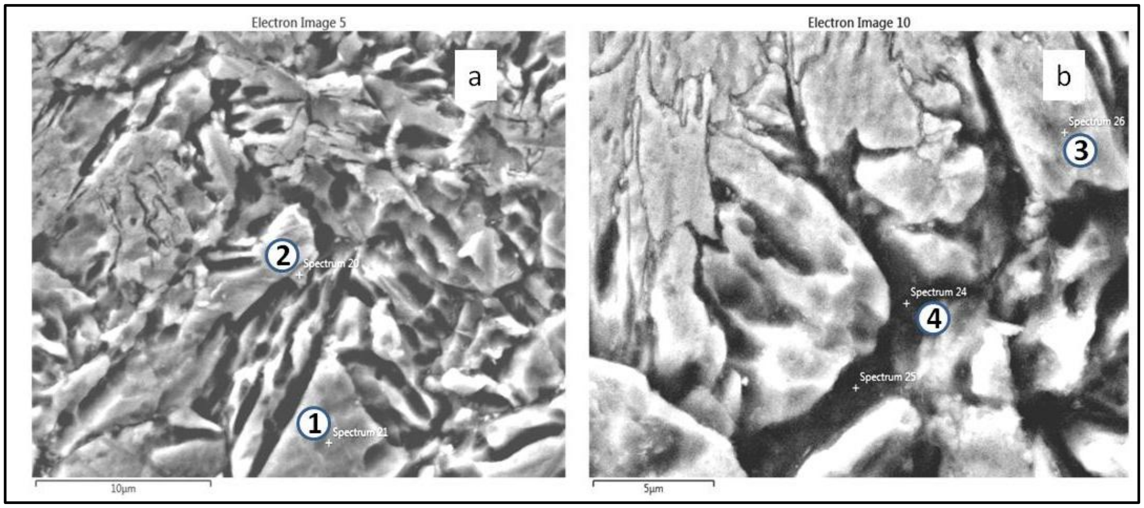

Fig. 5.21: Locations for spot EDS analysis over the surface of IN RAFMS material exposed to Pb-Li for (a) 500 h and (b) 1,000 h.

The content of Cr further decreased over some parts of the exposed surface at 1, 000 h (Spot 3) while W enrichment was sustained, showing continued Pb-Li attack. The association of chromium depletion with Pb-Li attack and formation of chromium depleted surface layer has been already discussed Section 5.2.2.1. The higher amount of chromium and oxygen at the other parts (Spot 4) indicated that passive layer was still intact at these locations even after 1, 000 h. Lead was also found over the exposed surface (probably present inside grain boundaries) in the present case. Figure 5.22 (a) and (b) shows the cross-sectional SEM images of the IN RAFMS samples exposed for 500 h and 1,000 h respectively. The undulations on the exposed boundary of both the samples gave a clear indication of Pb-Li attack. These undulations may be created by the grain boundary penetration of Pb-Li or the non uniform dissolution of oxide scales. Both these phenomenon have also been observed through microstructural (Figure 5.19) and compositional analysis (Table 5.8) of the exposed surface.

Table 5.8: Composition at various locations on the surface of IN RAFMS exposed to Pb-Li for 500 h and 1, 000 h (all values in wt %).

Duration	**Location**	**Cr**	**W**	**V**	**Mn**	**O**	**Pb**	**Fe**
After 500 h	Spot 1	10.5	1.4	0.3	0.8	4.7	-	Base
After 500 h	Spot 2	9.3	1.7	0.3	0.7	0.4	-	Base
After 1000 h	Spot 3	9.1	1.6	0.6	0.6	0.6	-	Base
After 1000 h	Spot 5	9.9	0.9	0.6	0.3	2.0	-	Base

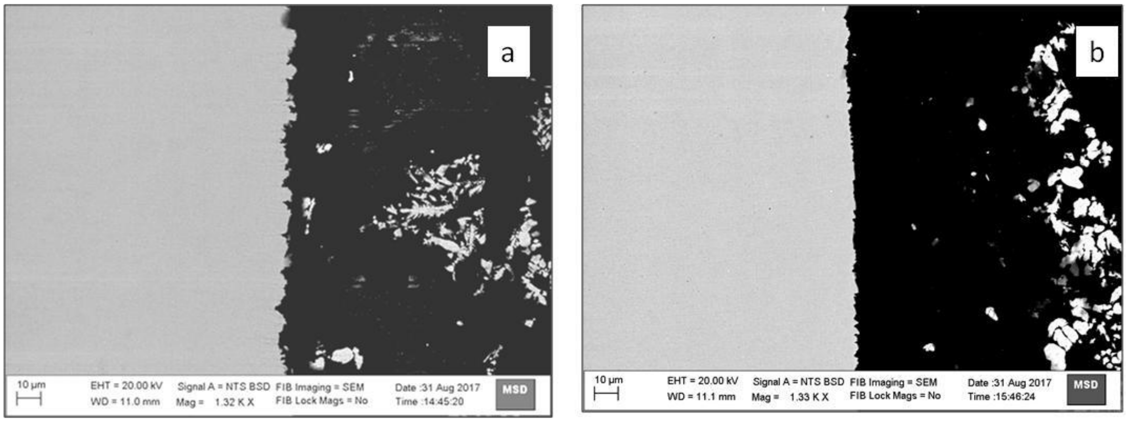

Fig. 5.22: Cross-section IN RAFMS after exposure to Pb-Li for (a) 500 h and (b) 1, 000 h.

The interaction of Pb-Li with IN RAFMS was further studied through compositional analysis over the cross-section of the exposed samples. Figure 5.23 (a) and (b) shows the path of EDS line scans while Figure 5.23 (c) and (d) shows the composition profiles of Fe, Cr, Pb and W for the samples exposed for 500 h and 1, 000 h respectively. Both the samples showed decrease in Fe and Cr content within a very short distance from the exposed surface. Raw data extracted from EDS software revealed that this depth was very small i.e. around 1 µm for both the samples. This implied that the weight loss of IN RAFMS obtained during the initial 1, 000 h (Tables 5.5 to 5.7) was predominantly due to the dissolution of oxide scales. However, the depletion of chromium at the exposed surface comes in agreement with the fact that the diffusion of Cr in IN RAFMS matrix is slower than its dissolution rate in Pb-Li. A similar chromium depleted zone of up to 0.7 µm from the exposed surface have been noted for DIN 1.414 steel when exposed to Pb-Li at 773 K for 500 h [215].

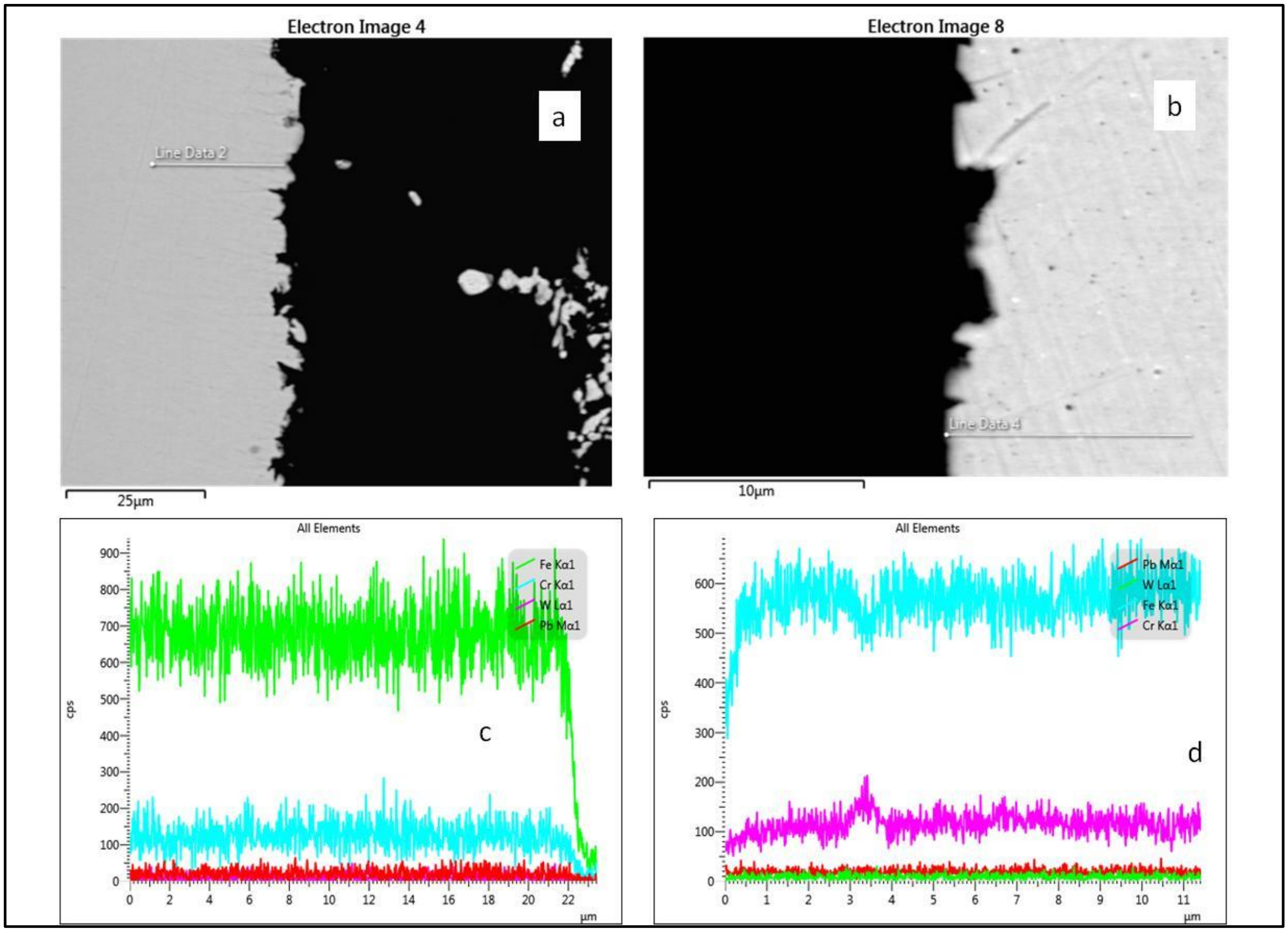

Fig. 5.23: Path of EDS line scans over the cross-section of IN RAFMS material exposed to Pb-Li for (a) 500 h and (b) 1000 h. Elemental line scans of Fe, Cr, Pb and W over IN RAFMS after exposure to Pb-Li for (c) 500 h and (d) 1, 000 h.

5.2.2.3. Corrosion Mechanism in static Pb-Li up to 1000 h.

The SEM-EDS analyses of the exposed IN RAFMS surface indicated that some regions containing higher chromium and oxygen were not affected by Pb-Li even after 1, 000 h of exposure (Table

5.8). This also confirmed that the corrosion of RAFM steels including IN RAFMS in Pb-Li was initiated by dissolution of the passive layer in a non uniform manner [164]. The constitution of oxide scales over the as-received IN RAFMS material has been already established through XPS analysis in Section 5.1 which showed chromium oxide (Cr_2O_3) mainly present in the subsurface layer up to a depth of 8 nm. The presence of some Cr and O rich areas on the 1, 000 h exposed sample thus indicates that some portion of the Cr_2O_3 layer was still present at certain parts of the sample. This has been also confirmed from XPS analysis of the exposed IN RAFMS sample where the presence of Cr_2O_3 was detected up to a depth of 2-3 nm from the exposed surface after 500 h.

The IN RAFMS samples also depicted grain boundary attack (Fig 5.19 and 5.22) as one of the preferred modes of Pb-Li attack during the above discussed period of oxide scale dissolution. As discussed earlier, the presence of grain boundary carbides in F/M steels may lead to depletion of alloying elements in their vicinity. Depletion of chromium adjacent to the grain boundaries due to the presence of Cr-rich carbide precipitates have been already observed in the case of 13 wt% Cr martensitic stainless steel [218]. Such decrease of the content of alloying elements, especially Cr, can lead to the weakening of the passive oxide layer (consisting of Cr_2O_3 and Fe_2O_3 as observed in Section 5.1) in the grain boundary region. This passive layer generally protects the steel surface from Pb-Li attack for certain time also known as Incubation Period [164,181]. Therefore, the absence/weakening of the protective passive film at the grain boundaries can make them prone to preferential Pb-Li attack as observed in the present case. A similar explanation is also valid in case of intergranular corrosion of sensitized stainless steels which happens due to the precipitation of chromium carbides leading to chromium depletion in the adjacent regions [121].

Results from Section 5.2 have shown higher corrosion attack on P91 samples as compared to IN RAFMS (Table 5.4). This might be because of the higher fraction of $Cr_{23}C_6$ precipitates present in P91 as compared to IN RAFMS (Table 5.2) which created greater chromium depletion along its grain boundaries. Nevertheless, the presence of tungsten oxide on the surface of IN RAFMS is also a major reason for its higher corrosion resistance. The absence of carbides ($Cr_{23}C_6$) over the surface of the exposed IN RAFMS sample (Figure 5.19) is also a possible consequence of grain boundary attack since the dissolution of matrix around the carbides can lead to *carbide dropping*. Such dropping of carbides can also be a reason for the formation of grooves over the exposed IN RAFMS surface as shown in Figure 5.20. With increasing time of exposure it is also possible that the Pb-Li channels formed by grain boundary attack may encircle an entire grain causing grain dislodgement/dropping. However, the entire process described above does not take place uniformly over the whole surface. This is because of the non uniform dissolution of oxide layer which results in localized attack as observed in Figure 5.19 (a) and (b). Compositional analysis through EDS (Figure 5.23 and Table 5.8) has also shown dissolution of iron and chromium also takes place from the steel matrix into the Pb-Li channels formed along grain boundaries. From these observations, the possible corrosion mechanism of Pb-Li during the initial 1000 h of exposure (when oxide layer still exists) has been summarized in Figure 5.24

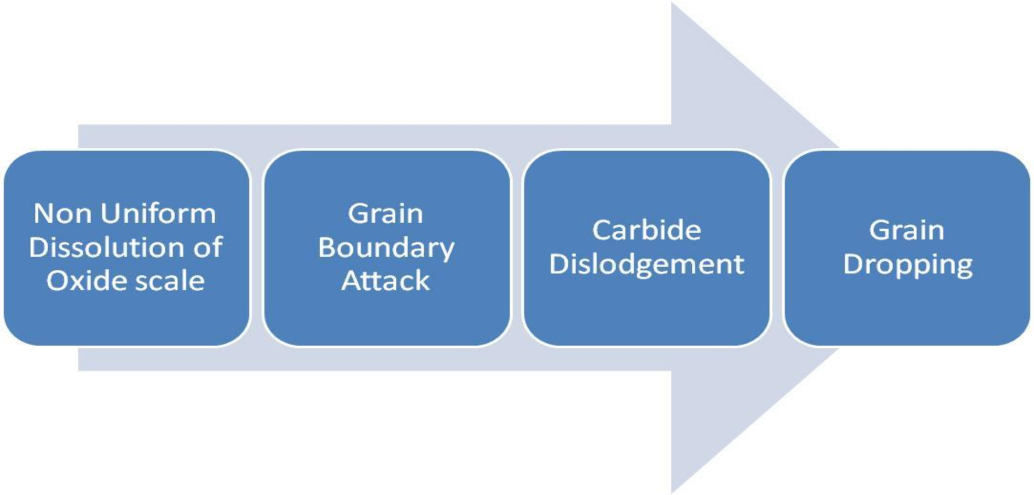

Fig. 5.24: Initial steps in corrosion of IN RAFMS in Pb-Li.

5.2.2.4. Modeling chromium depletion

The EDS line scan on IN RAFMS cross-section after 1, 000 h showed depletion of chromium up to a depth of around 1 µm (Figure 5.23). Considering that the slow diffusion in the steel matrix as a governing factor for Cr dissolution and depletion in the near surface region and that the actual steel-Pb-Li interface, actually moves inwards with time, the Fick's 2nd law can be written as per Equation 5.4.

$$dC/dt = D.\ d^2C/dx^2 + V.\ dC/dx \ \ldots\ldots\ldots\ldots\ldots\ldots\ldots\ldots\ldots\ldots\ldots\ldots 5.4$$

Where $C\ (x,\ 0) = C_0$ and $C\ (0,\ t) = 0$, for $t > 0$. *V*: dissolution rate of the interface; *D*: diffusion coefficient of chromium; *C (x, t):* Cr content as a function of depth in the matrix *x*; and time *t*; C_0: initial content of chromium in IN RAFMS; *x*= 0: interface matrix-liquid metal [215].

Here we consider the surface concentration of chromium to be zero after certain time (t) since the original surface gets dissolved gradually and the steel-Pb-Li interface moves. Equation 5.4 can be resolved with Laplace transforms into Equation 5. 5:

$$\frac{C(x,t)}{C_0} = 1 - 0.5\ \{erfc\left[\frac{x+Vt}{2\ D^{0.5}\ t^{0.5}}\right] + \exp(-VD^{-1}x)\ erfc\left[\frac{x-Vt}{2\ D^{0.5}\ t^{0.5}}\right] \ldots\ldots\ldots\ldots\ldots\ldots\ldots\ldots\ldots .\ 5.5$$

Where erfc (x) = 1 - erf (x) and erf (x) = $2\pi^{0.5}\int_0^x(-y^2)dy$

Considering IN RAFMS steel exposed for 1, 000 h ($t = 3.6 \times 10^6$ s) at 773 K in liquid Pb-Li, we have:

C_0 = 11 at. % (i.e. 9 wt %); V= 0.14×10^{-13} m/s {i.e. 5.25×10^{-5}µm/h from Table 5.7}; Diffusivity of chromium in steel = 10^{-20} m^2/s [100, 214] ;

Therefore, the Equation 5.5 reduces to the simplified form of Equation 5.6.

$$\frac{C(x,t)}{11} = 1 - 0.5\ \{erfc[2.63(x + 0.501)] + \exp(-1.4x)\ erfc[2.63(x - 0.501)]\} \ldots\ldots\ldots\ldots\ldots 5.6$$

Where ‘x’ is in µm and *C* is in at.%

Equation 5.6 can be plotted to get the chromium content profile (Figure 5.25) starting from the Pb-Li-steel interface (x = 0) and into the inner unaffected matrix. Figure 5.25 has been compared with the actual EDS line scan of chromium obtained over the IN RAFMS steel after 1000 h (Fig. 5.21 (d)). The chromium depletion zone from Equation 5.6 comes out to be around 1 µm. The experimentally obtained chromium depletion zone (Fig 5.21 (d)) is almost similar to that predicted by the model thus indicating its suitability in validation of experimental data.

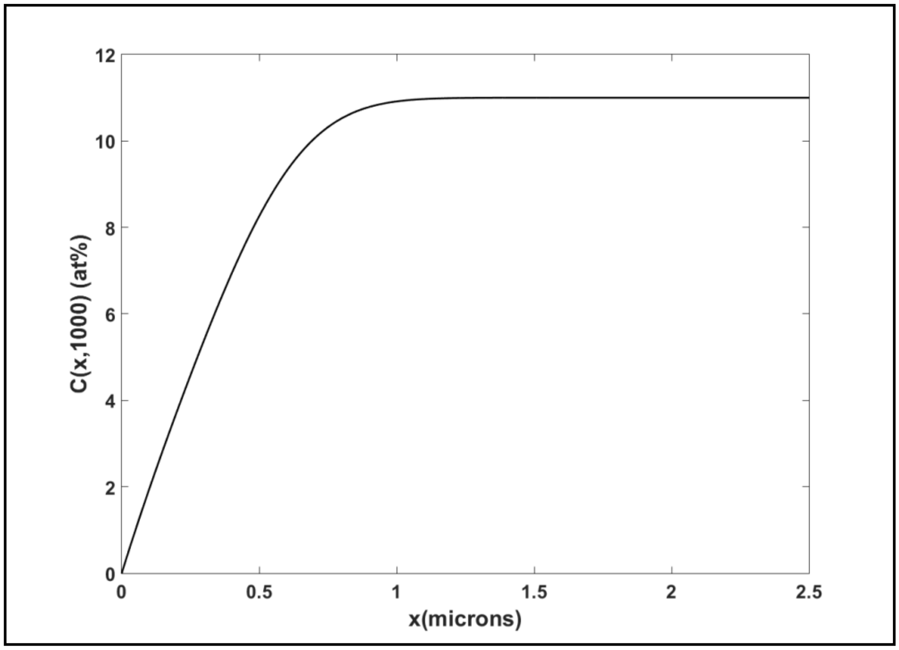

Fig. 5.25: Chromium content profile calculated from Equation 5.6.

5.2.2.5. Summary

1. The corrosion of IN RAFMS, pure chromium and low alloy steel (containing 99.7 % iron) was investigated in static Pb-Li at 773 K for exposure durations up to 1000 h.
2. The weight loss of chromium was found to be the highest during the entire experiment although its solubility in Pb-Li was lower than iron at 773 K. This was mainly because of the higher diffusivity of chromium in Pb-Li.

3. The weight loss of IN RAFMS was found to almost similar to that of pure iron indicating that dissolution iron was the rate controlling step. This was because of the fact that the diffusion rate of iron in the Pb-Li boundary layer was lesser than chromium.
4. The higher diffusion rate of chromium in Pb-Li initially leads to its faster depletion from the exposed surface. However, the slower diffusivity of chromium in IN RAFMS matrix actually controls its depletion from the steel matrix and may also result in the formation of a chromium depleted layer.
5. The Pb-Li attack is non uniform in nature and begins with dissolution of passive oxide scales. This is associated with penetration of Pb-Li along grain boundaries where the passive layer may be weaker. Corrosion proceeds by dissolution of iron and chromium into the grain boundary channels of Pb-Li. Grain boundary attack leads to dislodgement of grain boundary carbides and may finally give way to grain dropping.
6. The depletion of Cr and Fe occurred over a depth of 1 µm into the steel matrix while tungsten was enriched on the exposed surface due to its very low solubility in Pb-Li. The chromium depletion can also be theoretically calculated using modified Ficks 2nd law.

5.3. Corrosion studies in isothermal and flowing Pb-Li

The corrosion behavior of IN RAFMS and P91 in static Pb-Li showed the effect of temperature and alloying elements on the corrosion process. The next step was to incorporate the effect of flow velocity for which three major experiments were conducted in the Rotating Disc Corrosion Test Facility (RDCTF) as follows: -

a) Corrosion of disc type P91 sample in Pb-Li at 773 K

b) Corrosion of disc type IN RAFMS sample in Pb-Li at 773 K

c) Corrosion of segmented disc type IN RAFMS in Pb-Li at 823 K

The RDCTF has been already described in detail in Chapter 3 (Section 3.4) and the details of the above three experiments carried out in RDCTF have been given in Chapter 4 (Section 4.4).

5.3.1. Corrosion of P91 in Pb-Li at 773 K in RDCTF

The corrosion of P91 material under isothermal stirring conditions was studied in the RDCTF by exposing a 40 mm diameter P91 disc (6 mm thick) to molten Pb-Li at 773 K. The maximum linear velocity at the periphery of the disc was 1.4 m/s (average velocity ~0.7 m/s). The detailed experimental procedure and operating parameters for this study has been described in Chapter 4 (Section 4.4.1). As shown in Table 5.9, the exposed P91 sample underwent a weight loss of 330 mg on exposure to Pb-Li for 2, 000 h. In addition, prominent effects of Pb-Li exposure were observed on the sample surface and cross-section. Moreover, the extent of these effects was found to vary with increasing radial distance from the centre of the sample. This is expected to be related to the variation of Pb-Li flow velocity. To bring out these differences, characterization of both the sample surface and cross-section has been done at distances of 5 mm and 20 mm from the centre of the disc. In the following sections, these two locations have been referred as the centre and edge of the sample respectively.

Table 5.9: Corrosion rate of P91 disc exposed to Pb-Li at 773 K in RDCTF.

Initial Weight (g)	Final weight (g)	Weight Loss in 2, 000h (g)	Corrosion rate (mg/cm^2)	Corrosion rate (μg/cm ^{2}.hr)
198.57	198.24	0.330	8.4	4.2

5.3.1.1. Effect of Pb-Li on surface of P91

The metallic luster of the P91 disc was found to change into a dull appearance after exposure to Pb-Li as shown in Figure 5.26 (a) and (b). Moreover, the dark and light colored surface patches towards the periphery of the disc gave an evidence of non uniform attack in this region as compared to the centre (spot "C" in Figure 5.26 (b)).

Figure 5.27 (a) and (b) shows the SEM images of the exposed surface at the centre and edge of the disc respectively. A two layered structure was observed near the edge of the sample (Fig 5.27 (b)) where the appearance of the broken top layer matched with that of the central region. It is expected that this variation in appearance of the exposed surface is directly related to the higher flow velocity towards the edge of the disc (~1.4 m/s). Gross non uniform attack has been earlier observed due to erosion corrosion of F82H steel in lead- bismuth eutectic (LBE) (flowing at 2 m/s) at 823 K [220].

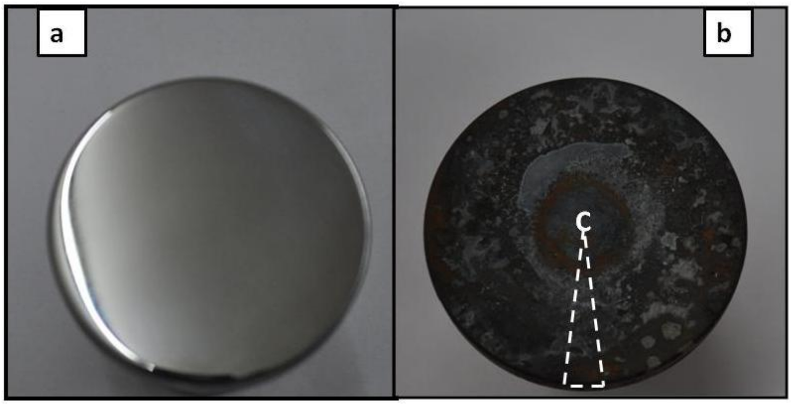

Fig. 5.26: The P91 disc (a) before and (b) after exposure to Pb-Li at 773 K for 2, 000 h.

5.3.1.2. Effect of Pb-Li into the depth of P91

To study the changes in composition and morphology for the P91 sample, a triangular slice having an included angle of 15° was cut off from the disc. The slice is indicated by dotted lines in Figure 5.26 (b). This slice was mounted on its cross-section such that the exposed material along the entire radius of the disc could be studied from a single sample. The mounted sample was etched with Villella's reagent and examined through SEM-EDS. It may be noted that, the etching was carried out to reveal any change in microstructure of the exposed surface. Figure 5.28 (a) shows the SEM image cross-section of an as–received P91 material whereas Figures

5.28 (b) and (c) shows similar images of exposed P91 disc at the centre and edge of the disc respectively.

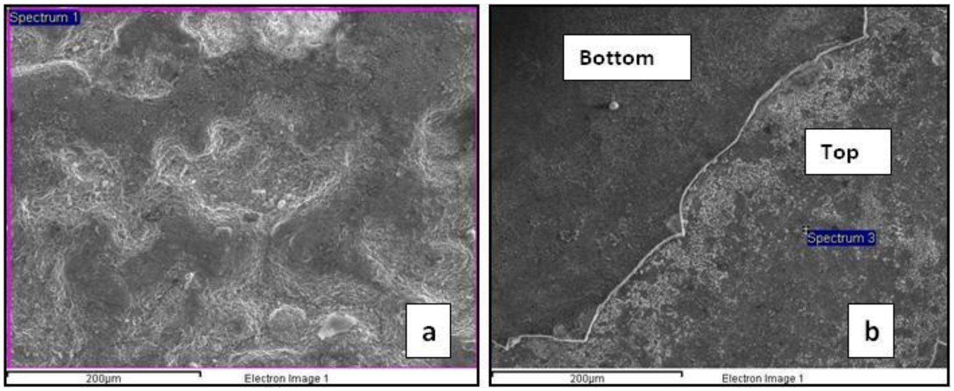

Fig. 5.27: SEM images at the (a) centre and (b) edge on the surface on the exposed P91 disc.

In comparison with the unaffected surface of the as-received material, a prominently attacked surface layer was clearly visible in the SEM images of the exposed sample. This layer had a wavy appearance near the edge of disc in comparison to its uniform nature at the centre. This may be a result of the edge effect created by non uniform attack of Pb-Li over the sample surface. Such non uniform attack can happen either due to erosion-corrosion as described earlier (Section 5.3.1.1) or due to non-uniform dissolution of the passive oxide scales as has been observed in many other F/M steels like EUROFER [163]. In the present case, the thickness of the attacked layer varied from 24 µm at the edge of the disc while it was around 16 µm at the centre. This was possibly associated with an increase in flow velocity towards the edge of the disc [186]. Moreover the sinusoidal surface profile created towards the sample edge is a typical signature of accelerated corrosion (or erosion-corrosion) at higher velocities [220]. The effect of flow velocity was also reflected in Figure 5.28 (b) where a few loose pieces of steel matrix could be seen attached to the corroded layer/edge. These pieces might not have eroded away due to the lower velocity at this region. It may also be marked that the cross-section at both the centre and edge of the sample seemed preferentially etched up to a certain depth from the exposed surface which might be a signature of preferential grain boundary attack. Grain boundary attack has also been observed in case of HT-9 steel when exposed to flowing Pb-Li at 753 K [155].

5.3.1.3. Effect of Pb-Li on composition of P91

The effect of Pb-Li interaction on the composition of the exposed samples was analyzed through EDS line scans of iron and chromium on the cross-section of the P91 disc. The paths of the line scans over the centre and edge of the sample are indicated in Figures 5.28 (b) and (c) while the actual line scans are shown in Figure 5.29. The depletion of iron and chromium could be noted near the exposed surface although iron depleted to a greater depth at both the locations (i.e. at centre and edge). The depth of the iron depleted layer was around 36 µm at the sample edge while it was around 29 µm at the centre. This trend matched with the greater thickness of the attacked surface layer at the edge. Although the chromium depletion could not be clearly distinguished from the line scans, the spot EDS analysis showed only 1.49 wt% and 0.89 wt % of chromium present at the center and edge of the exposed surface, respectively. An increase in the molybdenum content up to 1.9 % was also recorded near the edge through spot EDS on the exposed surface. On the other hand, slight amount of lead varying between 0.16-0.26 wt% was also observed at certain points over the cross-section of the sample with no specific location preference.

5.3.1.4. Effect of Pb-Li on strength of P91

Micro-hardness tests were carried out on the mounted P91 sample using a diamond indenter and applying a load of 2.94 N for a dwell time of 5 s. The overall hardness of the bulk material was found to decrease from an original of 290 HV to 250 HV after exposure to Pb-Li for 2000 h. This is possibly due to the long term tempering effect of the P91 disc at 773 K. The hardness of the affected layer varied between 240 HV near centre and 220 HV near the sample edge thus indicating the lowering of strength on Pb-Li exposure with greater decrease at regions facing higher flow velocities. Increase in porosity of the surface layer due to leaching of alloying elements may also be one of the factors responsible for its reduced strength.

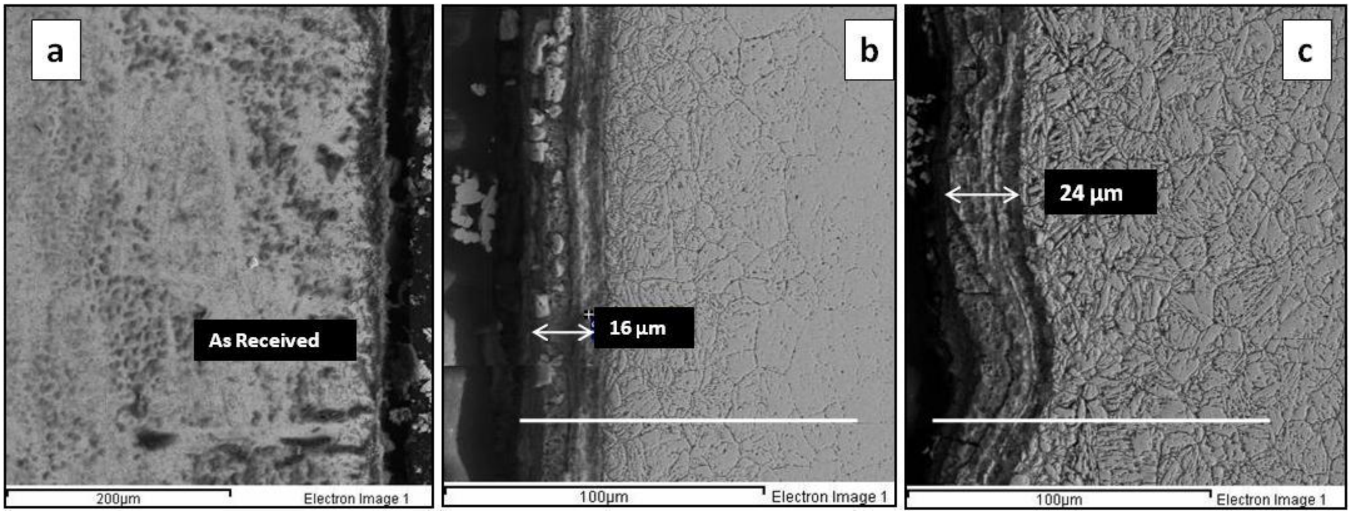

Fig.5.28: SEM images of the cross-section of (a) unexposed P91 material and at the (b) centre and (c) edge of the exposed P91 disc.

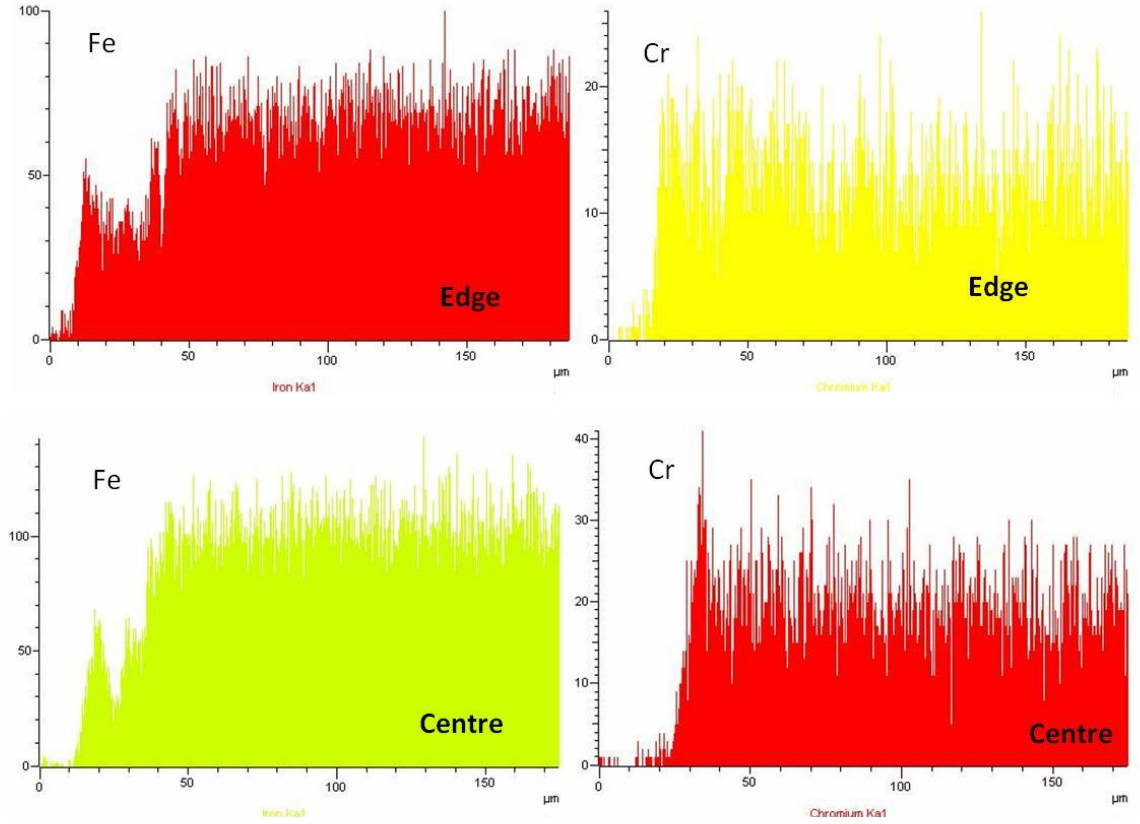

Fig.5.29: EDS line scans for iron and chromium taken across the cross-section at the centre and edge of the exposed P91 sample. Paths of line scan shown in Figure 5.28.

5.3.1.5. Discussion of results

The weight loss suffered by the P91 sample at a rate of 4.2 µg/cm^2.h in 2, 000 h was comparatively higher than previous experiments conducted with P91 and other ferritic/martiensitic steels exposed to Pb-Li flow especially in loop configurations [177-178]. In such reported work, the Pb-Li flow velocity ranged from 1 cm/s to 0.5 m/s only [155, 161-162, 182]. A corrosion rate of 0.52 µg/cm^2.h (i.e. 1.3 mg/cm^2 for 2500 h) was observed for EUROFER steel exposed to Pb-Li at 773 K in a thermal convection loop at 1 cm/s flow velocity [178]. Thus, the higher corrosion rate of P91 in the present study could be explained by the substantially higher liquid velocity i.e. maximum of 1.4 m/s.

The variation in the morphology of the exposed surface P91 specimen with respect to increasing radial distance from the centre ((Figure 5.27 (a)) was governed by the difference in linear velocity. The depth of the iron depleted surface layer has also been found to vary with change of Pb-Li flow velocity. As shown in Figure 5.28, the layer had a maximum depth of 24 µm at the edge which decreased to 16 µm near the centre. The reason for the variation in depth, structure and composition of the Fe- depleted layer could be explained on the basis of relative solubility of Fe and Cr in Pb-Li and increase in flow velocity towards the sample edge.

The outer surface of the exposed sample was depleted of chromium and the percentage of depletion was found to be quite high (97%) with respect to their original composition. Similar Cr depletion was also recorded for JLF 1 steel exposed to molten Pb-Li at 873 K [221]. They attributed the formation of this layer to the higher solubility of chromium in Pb-Li than iron at this temperature. As discussed in the case of static experiments in Section 5.2.2, a chromium depletion zone is generally formed below the exposed surface of the ferritic/martensitic steels. However, the present results indicated that an iron - chromium depleted layer may have formed initially on the exposed P91 surface due to dissolution of both these elements in Pb-Li.

However, it was not possible to find the exact depth of this layer since, the initial steel- Pb-Li interface may not be left at any place after 2, 000 h of Pb-Li exposure. In this regards, the detachment of large chunks of F82H steel surface into flowing lithium has been reported earlier [222]. The authors have attributed this to the creation of defects during lithium penetration and detachment of the associated weak surfaces due to shear stress associated with flow. Therefore, it is difficult to predict the exact location of the originally exposed surface in such flowing systems. In the present case, it was highly possible that some portion the Fe-Cr depleted layer formed into the initially exposed surface of P91 had already dissolved away into Pb-Li. However, the present trend of higher iron depletion towards the edge indicates greater Pb-Li attack at higher velocities. The greater depth of iron depletion as compared to chromium might be because of its higher solubility (40 wppm) in Pb-Li than chromium (10 wppm) at 773 K [212-213]. It may also be associated with the slower diffusivity of chromium in steel matrix as discussed in Section 5.1.2 [215]. On the other hand, the enrichment of molybdenum over the exposed surface towards the sample edge was possibly due to its very low solubility in Pb-Li and higher Fe-Cr depletion in this area. [221. However, the presence of lead (up to 0.26 %) at certain locations over the exposed surface as well as the preferential etching up to a certain depth from the exposed surface (Figure 5.28 (b) and (c)) must be associated grain boundary attack of Pb-Li.

It is certain that the Pb-Li boundary layer would be much thinner in a flowing system like rotating disc than a static system [223]. Therefore the transport of dissolved elements like iron and chromium through the boundary layer in a flowing system would be much faster. Moreover, the depleted elements would be immediately taken away from the liquid near the exposed surface by flowing Pb-Li and thus the surface would be exposed to fresh Pb-Li. Thus the Pb-Li attack would be much more pronounced in a flowing system like the RDCTF as compared to the static systems. This is confirmed by the greater corrosion rate of P91 (4.2 μg/cm ^{2}.h) as compared to the static experiments (0.77 µg/cm ^{2}.hr) described in Section 5.2.1. Since the flow velocities were quite low near the centre of the disc (~0.3 m/s) the elemental dissolution was less pronounced which was revealed through the lesser chromium depletion at this location. On the other hand, higher flow velocities at the edge (~1.4 m/s) must have accelerated the elemental depletion resulting in a lesser surface chromium content.

5.3.1.6. Summary

1. Corrosion compatibility of P91 with molten Pb-Li was analyzed in a rotating disc corrosion set-up for 2, 000 h at 773 K and a corrosion rate of 4.2 µg/cm^2.h was observed for the P91 disc sample.

2. The Pb-Li attack was non uniform in nature especially towards the edge of the disc due to higher flow velocity at that location. The Pb-Li exposure was also associated with preferential attack along grain boundaries similar to that in static experiments described in Section 5.2.1.

3. The corrosion of P91 material was mainly governed by dissolution of iron and chromium into molten Pb-Li. This resulted in formation of a Fe-Cr- depleted layer near the exposed surface where the extent of depletion increases with increasing velocities towards the edge of the disc. The relative solubility and diffusivity of individual elements in Pb-Li may also affect the extent of elemental depletion.

5.3.2. Corrosion of IN RAFMS in Pb-Li at 773 K in RDCTF

After P91; the corrosion behavior of IN RAFMS material under isothermal stirring conditions was studied in the RDCTF by exposing a 60 mm diameter disc (8 mm thick) to molten Pb-Li at 773 K and at a maximum flow velocity of 1.12 m/s at the periphery of the disc (average velocity

~0.7 m/s). The detailed experimental procedure and operating parameters have been described in Chapter 4 (Section 4.4.2).

5.3.2.1. Corrosion rate and microscopic investigation of IN RAFMS

The exposed IN RAFMS disc suffered a weight loss of 200 mg on exposure to Pb-Li at 773 K over 3000 h as represented in Table 5.10. Similar to P91, the IN RAFMS surface was found to have lost its metallic/ diamond finished appearance after exposure to Pb-Li as shown in Figure 5.30. The color differences observed on the specimen surface may be attributed to the formation of various surface oxides post exposure as has also been noted previously for other ferritic-martensitic steels [164].

Table 5.10: Corrosion rate of IN RAFMS disc exposed to Pb-Li at 773 K in RDCTF.

Initial Weight (g)	Final weight (g)	Weight Loss in 3000 h (g)	Exposed area (cm^2)	Corrosion rate ($\mu g/cm^2.h$)	Corrosion rate (µm/y)
155.65	155.45	0.200	65.31	1.02	11.45

In order to study the effect of Pb-Li exposure into the depth of IN RAFMS material, a slice of the disc was cut off along the dotted lines shown in Fig. 5.30. The dotted lines met at the center of the disc forming a 20° angle. This slice was then mounted on its cross-section and was studied in unetched and etched (using Villella's reagent) condition through optical microscopy and SEM-EDS. To understand the dependence of corrosion intensity on increasing linear flow velocity of Pb-Li along the radial direction, optical images of the mounted cross-section were recorded at distances of 12 mm, 22 mm and 30 mm from the centre of the disc. These three locations have been referred as the centre, middle and edge of the sample. The optical image of the unexposed sample is shown in Figure 5.31 (a) while and those for the centre, middle and edge locations are shown in Figure 5.31 (b), (c) and (d) respectively.

Fig. 5.30: Appearance of the IN RAFMS disc after exposure to Pb-Li at 773 K for 3, 000 h.

In comparison with the unaffected surface of the unexposed material (Figure 5.31 (a)), a preferentially etched surface layer was clearly visible in the optical images of the exposed sample. The depth of the preferentially etched layer increased gradually from 30 μm at the centre of the disc to 66 μm at the middle and 114 μm at the edge. As discussed in the case of P91 (Section 5.3.1), this layer was possibly a result of Pb-Li attack along grain and the variation in depth was related to the increase in Pb-Li flow velocity towards the edge of the IN RAFMS disc as shown in Figure 4.5 (Section 4.4.2).

Figure 5.32 gives a magnified optical image of the interface between the unaffected IN RAFMS matrix and the heavily etched layer at the region shown by the box in Figure 5.31 (c). The preferential attack could be clearly observed along the grain boundaries and martensite lath boundaries in the above discussed layer. To understand these effects in detail, SEM images were recorded for the mounted sample both in the polished (un-etched) condition as well as after etching.

Figure 5.33 shows the SEM image of the un-etched cross-section of the exposed IN RAFMS disc near its edge. A light colored (attacked) layer could be clearly observed up to a depth of 30 μm from the Pb-Li exposed surface. The entire layer had channels penetrating into it from the surface which later joined below the surface creating a fragmented appearance. On the other hand, the IN RAFMS matrix below the aforesaid corroded layer contained prominent pits having light colored traces in the adjacent regions (Figure 5.33). These pits could be observed up to a depth of 100 µm from the exposed surface and could be associated with preferential attack at certain locations on the steel matrix. Similar pit like features have also been observed later as dark spots in the EBSD map of the IN RAFMS sample at a depth of around 90µm from the Pb-Li exposed surface (Figure 5.36).

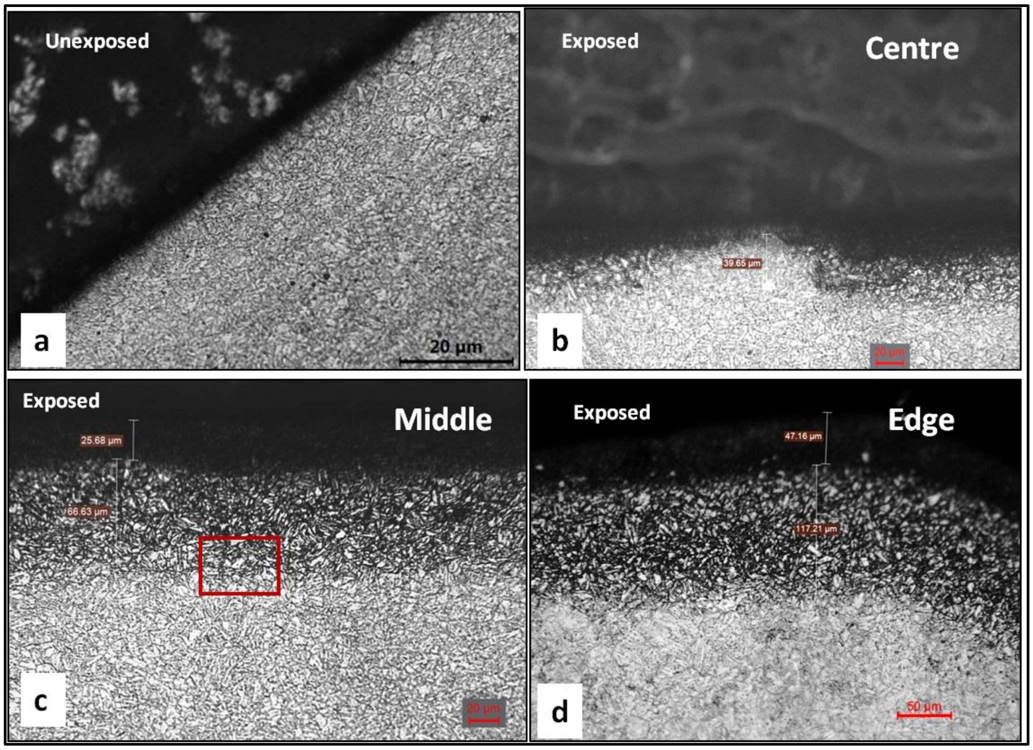

Fig. 5.31: Optical images of the cross-section of IN RAFMS material (a) before exposure and at (b) centre, (c) middle and (d) edge of the disc after exposure to Pb-Li at 773 K for 3, 000 h.

Figure 5.34 shows the SEM images of the cross-section of the etched IN RAFMS sample near the edge of the disc. Two distinct surface layers were prominently visible in these SEM images. The outer layer had a spongy appearance showing a change in microstructure from the inner layer. The inner layer was preferentially etched but retained the original tempered martensitic structure of IN RAFMS. As shown in Figure 5.34 (a), EDS profiles were recorded from the inner matrix across the sample boundary for the elements Fe, Cr, W, Ta, V and Pb. It was observed that the concentrations of iron and chromium decreased gradually from the unaffected matrix towards the inner layer but later decreased sharply at the outer layer. It should be noted that these EDS profiles gave an indication of the variation in actual concentration of the specific elements at different locations and not their normalized values. Due to the comparatively lesser concentrations of Pb, V, Ta and W; their profiles could not be distinguished clearly in Figure 5.34 (a).

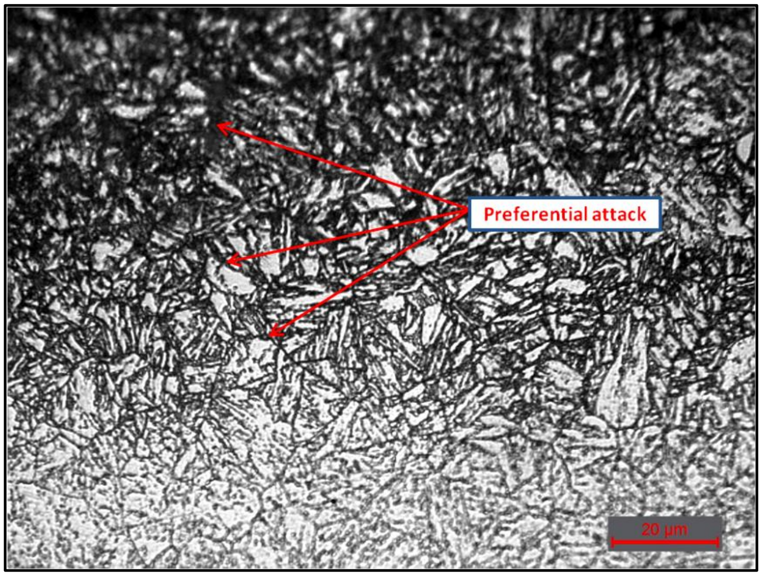

Fig. 5.32: Optical image of the preferentially etched region indicated by box in Figure 5.31 (c).

In order to know whether a penetration of Pb-Li could take place in the IN RAFMS matrix, point EDS analysis was carried out at three different locations near the edge of the sample as shown in Figure 5.34(b). The three locations correspond to the unaffected matrix, the inner preferentially etched layer and the outer spongy layer and has been identified as Spot 1, 2 and 3 respectively (Figure 5.34 (b)). The chromium and lead content obtained from of point EDS analysis has been consolidated in Table 5.11. Since this analysis gave normalized values, the concentration of other minor alloying elements and that of iron had been considered as base. It was noted that the gradual decrease of Cr from the unaffected inner matrix towards the outer exposed surface, as obtained in the EDS profile, matched well with its local concentrations at the three different zones.

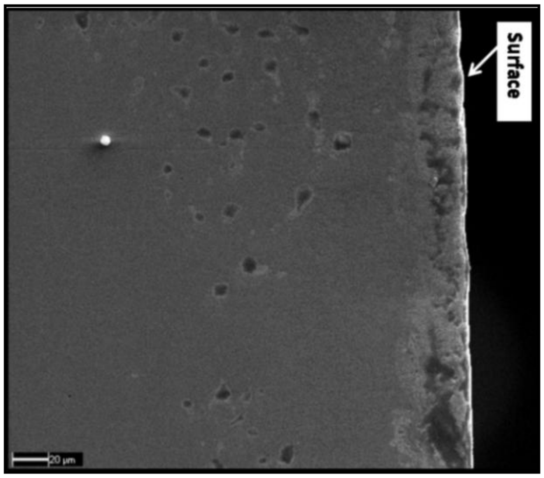

Fig. 5.33: SEM image of the un-etched cross-section of IN RAFMS disc near its edge after exposure to Pb-Li at 773 K for 3, 000 h.

On the other hand, presence of Pb was observed towards the exposed surface of the IN RAFMS indicating Pb-Li penetration as obtained earlier for P91 sample (Section 5.3.1). Although, the reason behind higher concentration of Pb in the inner layer (spot 2) as compared to the outer one (spot 3) needs to be investigated, it may be possible that spot 2 corresponded to a location having preferential Pb-Li attack (pits) leading to accumulation of Pb. The formation of pits due to Pb-Li attack is clearly shown in Figure 5.33. Other than a variation in the depth of the Pb-Li attacked region as observed in the optical images (Fig. 5.31), the SEM images and the EDS profiles at the other locations viz. centre and middle; showed similar results and thus are not being presented here.

The results of EDS analysis were complemented by recording the depth profiles for Pb, Li, V, Mn, W and Ta through GD-OES on the exposed IN RAFMS sample. The GD-OES scans taken from the exposed surface up to a depth of 15 µm into the IN RAFMS matrix near the edge of the disc are shown in Figure 5.35. A higher content of lead and lithium could be observed near the Pb-Li exposed surface which gradually decreased towards the inner matrix thus giving an indication of Pb-Li ingress. Since, Li could not be detected by EDS, the ***GD-OES data gave a first-hand evidence of lithium penetration into the IN RAFMS matrix***. However, the depth of lithium penetration was lesser as compared to that of lead. Similar results have been recorded for F82H steel when exposed to flowing Pb-Li at 823 K [189]. On the other hand, the concentrations of trace alloying elements like V, Mn and W were also found to drop down within near the outer steel surface which might be because of the relative increase in lead and lithium.

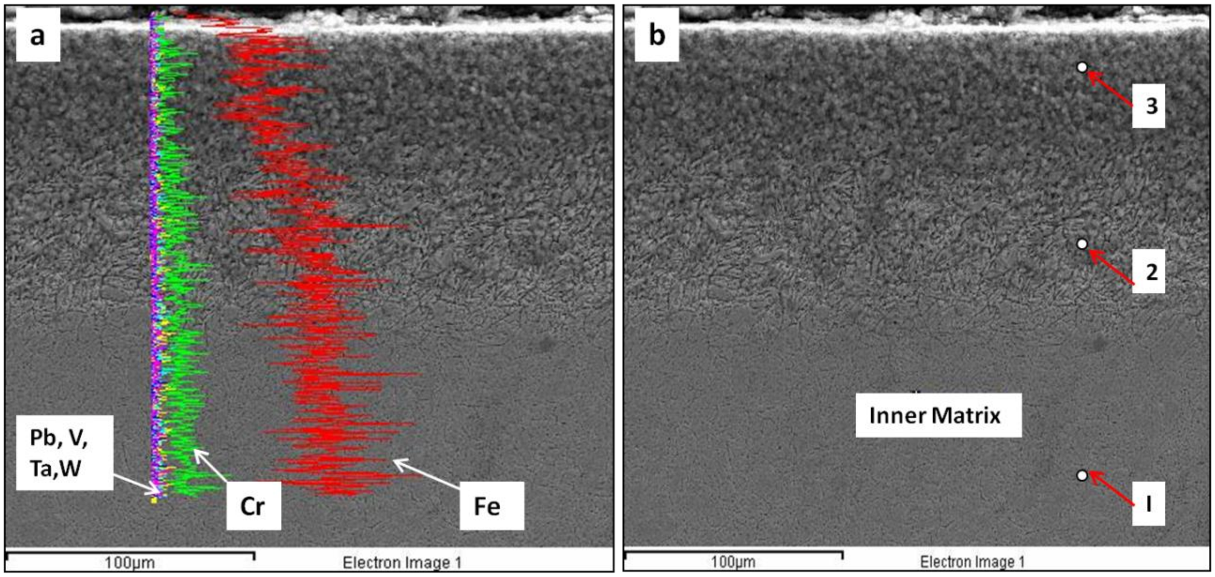

Fig. 5.34: SEM images of the etched cross-section of the IN RAFMS disc exposed to Pb-Li: (a) EDS line scans of Fe, Cr, Pb, W, Ta and V across the exposed surface, (b) Locations of point EDS analysis.

Table 5.11: Composition at different locations near the Pb-Li exposed surface of the IN RAFMS disc measured through EDS (unit: wt %).

Elements	Spot 1 (Unaffected Inner matrix)	Spot 2 (Inner etched layer)	Spot 3 (Outer spongy layer)
Cr	9.42	6.87	4.26
Pb	0	0.58	0.44
Fe, others	base	base	base

Figure 5.36 shows the EBSD mapping of the cross-section of the IN RAFMS sample after exposure to Pb-Li for 3, 000 h at 773 K. Figure 5.36 (a) indicates the EBSD map from the outermost Pb-Li exposed surface and up till a depth of 90 µm whereas the EBSD map of the sample beyond a depth

of 150 μm from the exposed surface is shown in Figure 5.36 (b). Therefore, Figure 5.36 (b) shows the EBSD mapping of the unexposed IN RAFMS material. The change in microstructure from lath type martensite in the inner matrix to spheroidal type grains towards the Pb-Li exposed surface could be clearly observed. Such spherodisation have been observed by Xu et al. in the cross-sectional SEM image of an F/M steel (JLF-1) when exposed to liquid Li [185]. The spheroidal structures have been reported as ferrite which had formed due to the interaction with liquid Li leading to depletion of C from the martensitic structure of the exposed surface. Figure 5.36 (a) also shows dark colored channels penetrating into the top surface which were probably the path of Pb-Li attack along grain boundaries. Similar surface channels were also observed in the SEM image of Figure 5.33. The black spots in the inner matrix were once again an indication of Pb-Li accumulation in the pit type structures as observed in SEM-EDS analyses.

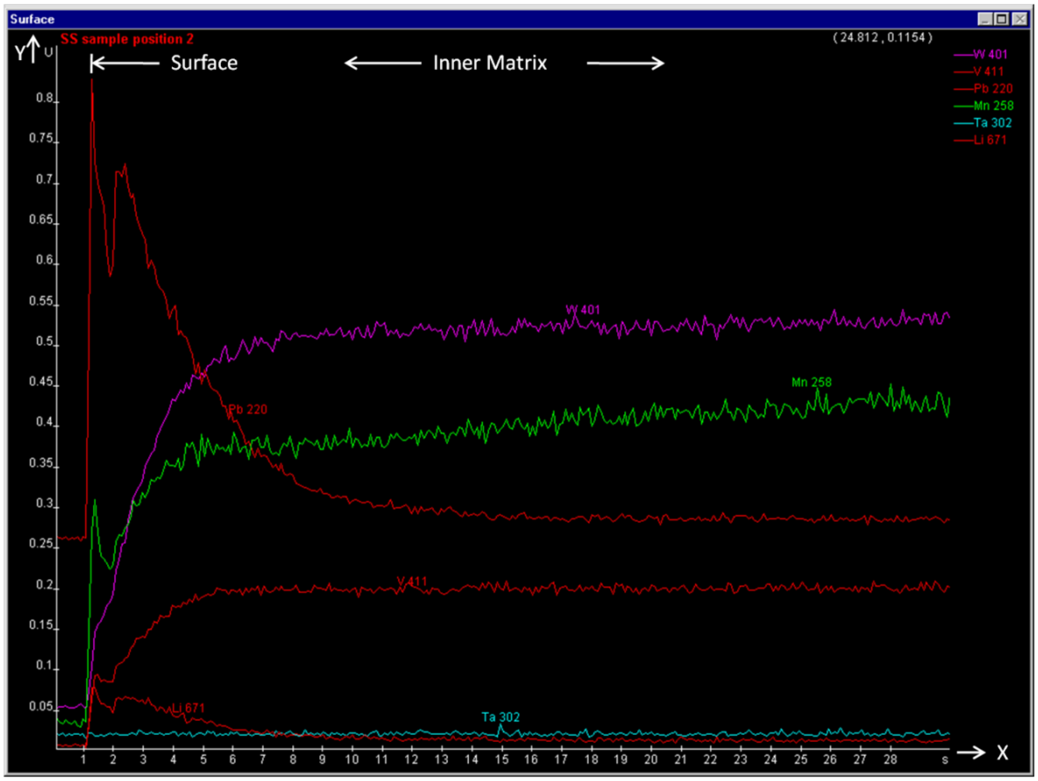

Fig. 5.35: GD-OES profiles for Pb, Li, V, Mn, W and Ta on the IN RAFMS sample up to a depth of 15 µm from the Pb-Li exposed surface. X axis denotes the depth of analysis (a. u.). Y axis denotes the relative concentration (a. u.).

Micro-hardness tests were carried also out on the mounted IN RAFMS sample using a diamond indenter and applying a load of 2.94 N for a dwell time of 5s. The overall hardness of the bulk material (unaffected by Pb-Li) was found to decrease from an original of 250 HV to 214 HV after exposure to Pb-Li for 3, 000 h due to the long term tempering effect of the IN RAFMS disc at 773 K. However, the hardness of the inner preferentially etched layer was noted to be 187 HV whereas that of the outer spongy layer was 143 HV; thus indicating the lowering of strength on Pb-Li exposure (similar to P91) with greater decrease in the outer surface layer. Increase in porosity of the surface layer due to formation of channels as observed in Fig. 5.33, may also be one of the factors responsible for its reduced strength.

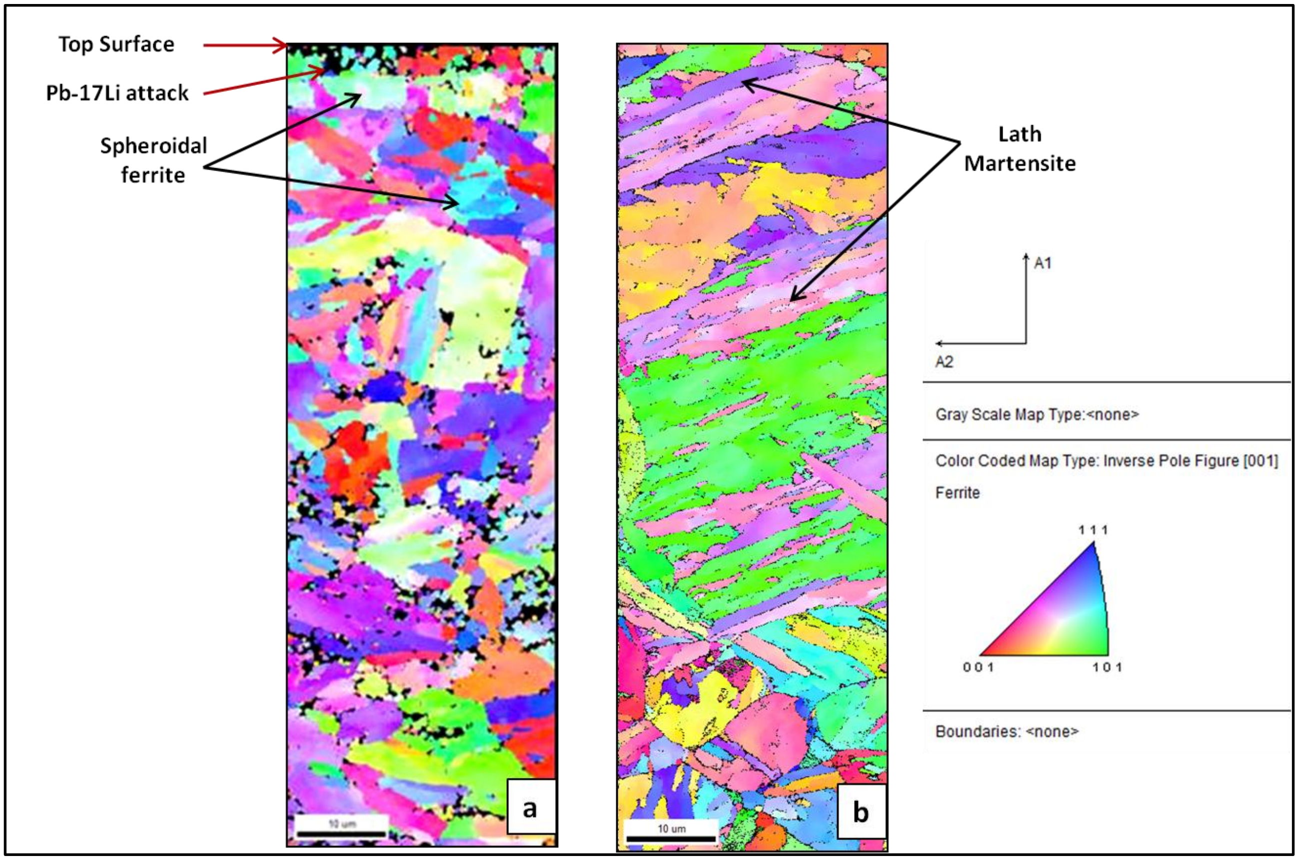

Fig. 5.36: EBSD mapping of the IN RAFMS disc exposed to Pb-Li; (a) From top exposed surface up to a depth of 90 µm ; (b) Beyond 150 µm from the top surface (vertically below).

Table 5.12 shows the content of metallic impurities in Pb-Li eutectic analyzed before and after the corrosion test at 773 K for 3, 000 h. The increase in chromium after exposure indicated its dissolution from the IN RAFMS matrix. Since the Ni content of IN RAFMS is almost negligible and no other nickel containing material was used in contact with Pb-Li, the content of Ni (and Bi) was found to remain almost similar to their initial concentration as present in the unexposed Pb-Li alloy.

Table 5.12: Metallic impurities in Pb-Li before and after the corrosion test at 773 K for 3, 000 h.

	Cr (wppm)	Ni (wppm)	Bi (wppm)
Before	-	6.71	164
After	<0.02	6.86	165

5.3.2.2. Discussion of results

The weight loss suffered by the IN RAFMS material at a rate of 1.02 µg/cm^2.h corresponded to a corrosion rate of 11.45 µm/y considering the entire surface area of the disc exposed to Pb-Li. Nevertheless, it should be noted that the weight loss corresponding to this corrosion rate is a cumulative result of weight losses taking place at varying rates along the radial direction of the IN RAFMS disc. As shown in Figure 4.5 (Section 4.4.2), the linear velocity varies at the three circumferential locations along the disc radius as V_{min} (near the centre) > V_{mid} (near the middle) > V_{max} (near the edge). Since, the increase in velocity will lead to an increase in the extent of Pb-Li attack into the steel matrix and a higher rate of material removal from the exposed surface; the corresponding weight losses (W) will also vary as W_{min}> W_{mid}> W_{max} [124]. This phenomenon is validated by the fact that the depth of Pb-Li attack increased from the centre (30 µm) towards the edge of the of the IN RAFMS disc with the maximum depth being 114 µm at the edge.

It should be kept in mind that the corrosion rate of 11.45 μm/y for IN RAFMS has been calculated considering a linear dependence of weight loss on time of exposure. This was because; the weight loss was measured for the sample only after completion of the present experiment i.e. after 3, 000 h. Nevertheless, Pb-Li compatibility experiments with EUROFER 97 in the forced circulation PICOLO loop; have also resulted in a linear weight loss curve even though the samples were taken out after every 1, 500 h for weight loss measurements [163]. However, similar studies at regular time intervals were required in the present rotating disc test system to build an exhaustive database which may establish the actual dependence of corrosion rate with duration of exposure.

Some compatibility studies in Pb alloys and pure Li have reported the occurrence of erosion-corrosion on specimen surfaces under various flow conditions [220, 222]. In 2005, M. Kondo et al. observed extensive surface damage on various alloys including the potential blanket structural material F82H; when they were exposed at 823 K to liquid lead-bismuth eutectic (Pb-Bi) flowing at 2 m/s in a forced circulation loop [220]. The maximum linear velocity of 1.13 m/s relevant to the rotation of IN RAFMS disc in the present case was lower than that of Pb-Bi in the above mentioned study. Moreover, the characteristic features of erosion-corrosion like surface damage due to material break off and narrow pitting as observed in the materials exposed to Pb-Bi in the above; was not noted in the present case of IN RAFMS. However, some of such features were observed in the case of P91 in Section 5.3.1(due to higher velocity i.e. 1.4 m/s at the edge). It may thus be possible that the range of velocity for IN RAFMS i.e. 0.38 m/s -1.13 m/s; was below the threshold value that is required to trigger its erosion-corrosion in liquid Pb-Li at 773 K. However, further studies at different velocities in a loop type test system were needed to confirm this fact. Nevertheless, the fact reported by Kondo et al., that erosion-corrosion resulting from higher Pb-Bi flow velocities led to higher rate of weight loss; is once again an evidence of direct dependence of corrosion rate on flow velocity which was also inferred from the present experimental results.

The corrosion rate of 1.02 μg/cm^2.h for IN RAFMS was comparatively lower than that obtained in previous experiments conducted with several other ferritic-martiensitic and RAFM steels like Fe-12Cr-1Mo, HT-9, F82H, OPTIFER, MANET, EUROFER-97 etc [177]. In such reported work, the above materials were exposed to flowing lead-lithium especially in loop configurations and the Pb-Li flow rate was in the range of 1 cm/s to 0.5 m/s only [161-163,176,182]. A corrosion rate of 40 μm/y was observed was observed for EUROFER-97 steel exposed to Pb-Li at 773 K for 2500 h in a thermal convection loop with the liquid flowing at 1 cm/s [178]. The Chinese counterpart of RAFM steel; CLAM, exhibited a corrosion rate of about 17 μm/year under a Pb-Li flow velocity of 0.08 m/s at 753 K for 8000 h[164]. On the other hand, the Japanese RAFM steel, JLF-1 underwent weight loss at a significantly low rate of 2.5 gm/m^2 i.e. 0.083 μg/cm^2.h for 3000 h in molten Pb-Li at 873K [221]. This was possibly because the experiment was carried out under static condition.

Other than weight loss, exposure to Pb-Li also caused changes in the structure and composition of the IN RAFMS material in the present study. Dissolution of alloying elements from the steel matrix was found to be associated with the penetration of Pb and Li in the same. The outer surface layer noted on the exposed cross-section of IN RAFMS was significantly depleted of Fe and Cr and contained a number of channels open to the surface, showing the possible path of Pb-Li ingress. Similar solubility driven elemental dissolution have been noted when various other RAFM steels have been exposed to Pb-Li [155, 161, 178, 182,]. However, the enrichment of W near the exposed surface as noted in many other RAFM steels was not observed in the present condition [162]. This might be because of the comparatively lesser corrosion rate which will result in lesser depletion of other major alloying elements like Fe and Cr.

The microstructure of the above mentioned layer depicted a spongy appearance after Pb-Li exposure as compared to the original tempered martensitic structure of IN RAFMS. This was associated with a distinct change in grain structure from the inner lath type martensite to spheroidal ferrite grains towards the Pb-Li exposed surface. Similar observations have been recorded earlier when an F/M steel (JLF-1) was exposed to molten lithium contained in a molybdenum crucible, thereby causing a change of phase from martensite to ferrite over the exposed surface [222, 224]. The major reason for this phase change has been predicted to be the loss of carbon and chromium especially due to the trapping of carbon by the molybdenum crucible. Although, the carbon content of the exposed IN RAFMS material was not analyzed in the present experiment, the decrease in hardness at the surface layer up to 143 HV, matched well with a similar value obtained on the ferrite layer formed on JLF-1 when exposed to static Li [224]. This gives an indication of similar phenomenon occurring in the present case. On the other hand, studies on CLAM steel have shown that Pb-Li exposure can cause the loss of grain boundary carbides either through dislodgement or by decomposition (due to loss of Fe and Cr) [225]. It has been discussed in Section 5.2.2.3 that thermal ageing can lead to the formation of sub-grains in a martensitic structure [216-217]. However, the absence of grain boundary carbides and depletion of carbon at high temperature (773 K) may also push the structure towards equilibrium forming relatively equiaxed sub-grains as discussed in Section 2.5.3. It is possible that the spheroidal structures observed on the surface of the present IN RAFMS are a result of sub-grain formation (Figure 5.36). However, since the carbon content was not analyzed in the present case, it is difficult to predict whether similar extent of carbon depletion have taken place.

It is expected that the concentration gradient of Fe, Cr and other alloying elements existing between the steel matrix and molten Pb-Li initiated their depletion from the grain boundaries thus allowing Pb-Li to penetrate along the same. The association of grain boundary attack with the chromium carbides on the boundary and weakened passive layer has been already discussed in the case static experiments (Section 5.2.2). An additional driving force for preferential grain boundary attack is the reduction in the overall energy of the system, which is achieved when the surface energy of the solid/liquid interfaces (γ_{sl}) is smaller than the energy of the initial grain boundary (γ_{gb}), i.e., when $2\gamma_{sl} \leq \gamma_{gb}$; as has been observed for SS 316L when exposed to lead – bismuth eutectic at 823 K [226]. However, the extent of depletion of the constituent elements also depends on their solubility in Pb-Li at 773 K [195, 227].

Ingress of Pb-Li through the grain boundaries allowed further elemental depletion from the grain interiors into the Pb-Li channels causing spherodisation (due to a possible phase transformation to ferrite / formation of sub-grains) giving this layer a spongy appearance. Later the Pb-Li slowly penetrated into the inner matrix through the prior austenite and lath boundaries. The pit like features found in Figure 5.34 might be a result of Pb-Li accumulation at high energy regions of greater dissolution like triple points. Formation of pits associated with grain boundary attack has been also observed when JLF 1 steel has been exposed to Pb-Li under static conditions [125]. The alloying elements from adjacent areas dissolve in the Pb-Li channels and pits thereby continuing corrosion.

Thus, due to its close proximity from the exposed surface, the outer layer experienced greater elemental depletion and underwent microstructural transformation while the inner preferentially etched layer was still in the initial stage of Pb-Li attack. Since the inner layer still retained its original ferritic/martensitic structure, the microhardness of this layer (187 HV) was in between the value for the outer spongy layer (143 HV) and the un-attacked inner matrix (214 HV).

The following points were noted on comparing the results of P91 and IN RAFMS from RDCTF (Section 5.3.1 and 5.3.2):-

a. The depth of chromium depletion was almost equal to that of iron in the case of IN RAFMS. However, chromium depletion depth was lower than that of iron in P91.

b. No phase transformation in the surface layers of P91 after Pb-Li exposure.

c. The corrosion rate of IN RAFMS has been found to lesser than P91 under similar average velocities (i.e. ~0.7 m/s) and temperature conditions (773 K).

The greater depletion zone for chromium in IN RAFMS might be a result of its slower diffusion as compared to that in P91. This is because; tungsten creates a stronger bond with alloying elements thereby slowing down their diffusion in the matrix [100]. However, this also signifies that the actual content of chromium depleted from IN RAFMS matrix into Pb-Li would be comparatively lesser than P91. This is because chromium replenishment would be difficult in the Pb-Li adjacent surfaces once the initial chromium content has leached out. It has been already discussed for static experiments in Section 5.2 that the presence of tungsten oxides on the surface could be one of the important factor behind the greater corrosion resistance on IN RAFMS material. Another reason might also be result the higher overall bond strength of tungsten alloys (like IN RAFMS) in general as compared to molybdenum based ones (like P91) [228]. The higher strength does not allow the Fe-Cr depleted surface layers to detach away as easily as in P91. This might also be the reason for the absence of phase transformed outer layers in the case of P91. Thus, comparison of the depth of iron and chromium depletion in both the materials will not be a correct indication of corrosion rate; especially in flowing systems; since it is not possible to determine the location of the initial steel-Pb-Li interface.

It is thus evident that Indian RAFMS could be considered as a suitable structural material for the Indian-TBM as far as corrosion rate in isothermal and flowing Pb-Li is concerned. Nevertheless, it should be kept in mind that long term liquid metal/alloy corrosion test under isothermal conditions may lead to saturation of the liquid with metallic impurities and thus may lead to gradual decrease in corrosion rate after a certain duration of time. On the other hand, corrosion tests carried out in non –isothermal systems will evidently lead to a higher corrosion rate as discussed in Section 2.9.

It may be marked here that the calculated corrosion rate of 11.45 µm/y is gross estimate which could be applied for comparison of its characteristic with similar other materials and understanding the corrosion mechanism. However, the corrosion behavior of Pb-Li may be different in the actual Pb-Li flow circuit in the Indian LLCB TBM where a difference in temperature will exist in between the TBM flow channels and other parts of the Pb-Li loop present downstream. Moreover, the flow profile of Pb-Li in the TBM channels in the presence of high intensity magnetic field will be significantly different from that generated inside the RDCTF. Therefore, corrosion rate data generated from experiments in prototype Pb-Li loops in the presence of magnetic field; will be more appropriate from the point of view of design of ITER-TBM as well as the DEMO reactor [229].

5.3.2.3. Summary

1. The corrosion compatibility of IN RAFMS material was investigated in flowing Pb–Li using the rotating disc corrosion test set-up for duration of 3, 000 h at 773 K. The corrosion rate of the exposed IN RAFMS disc as measured from weight loss was found to be of the order of 1.02 µg/cm^2.h at a maximum linear flow velocity of 1.13 m/s, which corresponds to thickness reduction at a rate of 11.45 µm/y.
2. The corrosion mechanism was governed by gradual dissolution of Fe and Cr from the steel matrix and penetration of Pb and Li into the matrix along grain boundaries. Depletion of alloying elements into the Pb-Li caused a change in microstructure up to a depth of 30 µm from the

exposed surface. Pb-Li attack along the grain boundaries and martensitic lath boundaries continued further creating points of Pb-Li accumulations (pits).

3. The extent of Pb-Li attack at various locations along the radial direction of the IN RAFMS disc depended on the linear flow velocity of Pb-Li at that region. Higher velocity towards the edge of the disc was responsible for the maximum depth of the Pb-Li attack in this region.

5.3.3. Corrosion of segmented IN RAFMS disc in Pb-Li at 823 K in RDCTF

After the first experiment on IN RAFMS with a disc type sample, the second experiment was carried out with a segmented sample of the same material in order to establish how corrosion progresses with time. The design of the sample has been already discussed in Section 3.4.1 and the actual sample geometry as well as the experimental procedure has been described in Section 4.4.3. Six segments obtained from a disc (45 mm diameter, 6 mm thick) of IN RAFMS material were exposed to Pb-Li at 823 K at a flow velocity of 0.5 - 0.75 m/s. One of the exposed segments was taken out after every 2, 000 h for analysis over a total duration of 10, 000 h. It may be noted that one particular segment was taken out after 2, 000 h; cleaned off the adherent Pb-Li and afterwards put back again into the flowing Pb-Li. The time period of exposure for this sample will be denoted as 2, 000 h + 2, 000 h for the forthcoming sections.

5.3.3.1. Corrosion Rate

The weight loss data for all the segments exposed for different time intervals in Pb-Li is given in Table 5.13. An increasing trend was generally observed when measured weight loss was plotted against the duration of exposure in Pb-Li as shown in Figure 5.37. The loss was comparatively lesser in the initial 2, 000 h due to a probable incubation period as reported in similar studies on EUROFER steel at KIT, Germany [161-163, 181]. Such incubation period is due to the presence of passive oxide (scales) on the steel surface which dissolves slowly and therefore prevents the attack on bare metal. The presence of oxides of Fe and Cr over the surface of the as-received IN RAFMS material (before Pb-Li exposure) has been already detected through XPS in the present study (Section 5.1). On the other hand, the non-uniform dissolution of these oxides during the initial 1, 000 h of exposure has also been observed in the static experiments (Section 5.2.2). In the present case, the weight loss increased significantly after the initial 2, 000 h till 10, 000 h as shown in Table 5.13.

The weight loss after 6, 000 h was found to substantially higher and was probably due to breaking off of chips from the surface during sample cleaning. Therefore, this point has not considered for plotting the weight loss data in Figure 5.37. The overall corrosion rate was obtained from the slope of the linear fit of the points of weight loss from 2, 000 -10,000 h as shown in Figure 5.37. A similar procedure has been followed for EUROFER samples exposed to flowing Pb-Li [167, 194]. The linear fit (through Origin 8.5) in the present case gave a satisfactory R^2 value of 0.994 and thus a corrosion rate of 159.4μm/y was obtained by dividing the slope of the graph (i.e. 1.34 $x10^{-4}$ gm/h) by the wetted surface area (i.e. 9.43 cm^2) of each segment.

Table 5.13: Weight loss of IN RAFMS segments after exposure to Pb-Li for different time intervals.

Sample No	Time (h)	Initial weight (g)	Final weight (g)	Weight Loss (g)
1	2000	11.9805	11.9489	0.0316
2	4000	11.9560	11.6180	0.3380
3	2000 + 2000	11.9427	11.5082	0.4345
4	6000	11.9234	10.9712	0.9602
5	8000	11.9234	11.1120	0.8114
6	10000	11.1170	11.0134	1.1275

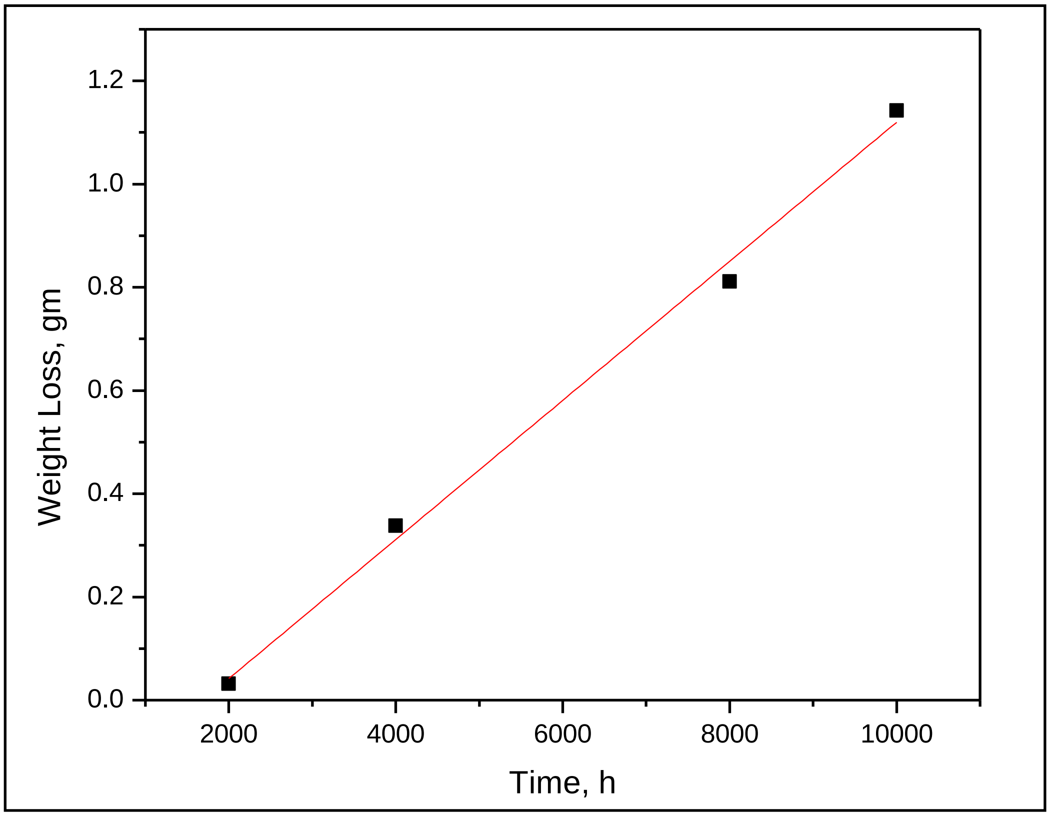

Fig. 5.37: Weight loss of the IN RAFMS segments exposed to Pb-Li at 823K for 10, 000 h.

It may be noted that, the weight loss of the sample exposed for 2, 000 + 2, 000 h have not been indicated in Figure 5.37. The effect of sample cleaning on weight loss has been separately indicated in Figure 5.38 where only the weight losses of the samples exposed for 2, 000 h, 4, 000 h and 2, 000 + 2, 000 h have been indicated. It was clearly observed that interim cleaning of the adherent Pb-Li layer from a sample had caused a significant increase in its weight loss after 4, 000 h. The weight loss of the sample which was cleaned in between (2, 000 h + 2, 000 h) was 0.43 while it was only 0.33 gm for the sample directly exposed for 4000 h. This means around 30 % increase in weight loss was affected by sample cleaning which is probably associated with the complete removal of the Pb-Li boundary layer near the exposed surface. This boundary layer generally contains the alloying elements which have leached out of the steel matrix and thus the concentration of those elements in this layer governs the rate at which further dissolution takes place [140, 215]. However, if this layer is removed/ replaced by some means (i.e. sample cleaning) then accelerated corrosion may take place as observed in the present case.

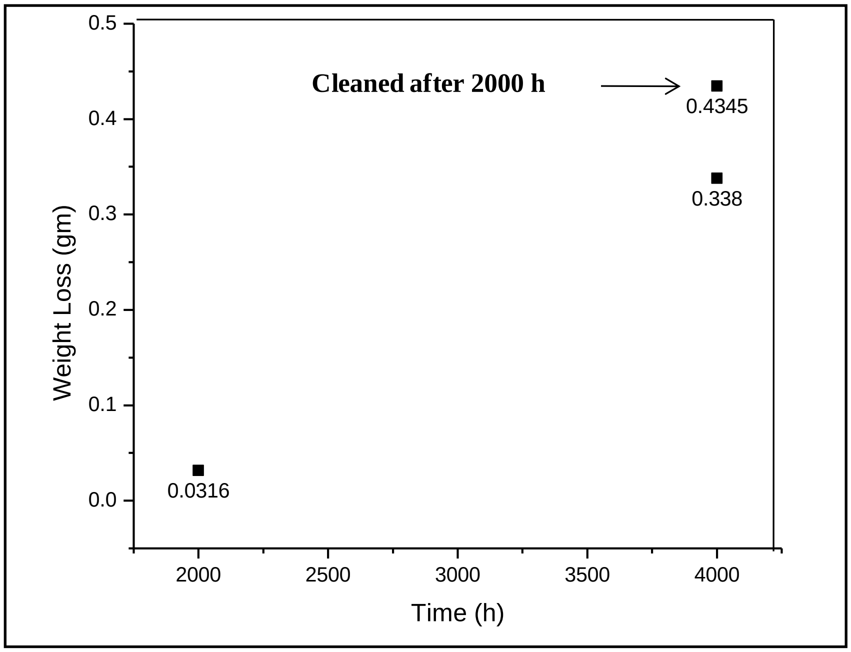

Fig. 5.38: Weight loss of the IN RAFMS segments exposed to Pb-Li at 823K for 4, 000 h.

The corrosion rate of IN RAFMS material obtained from the linear fitting of the weight loss values (Figure 5.37) corresponded to thickness loss at a rate of 159.4 µm/y. This rate was significantly higher than the corrosion rate of IN RAFMS material obtained in the earlier experiment in RDCTF at 773 K (i.e. 11.45 µm/y). This increase (13 times) was most probably because of the higher operating temperature in the present case which was 823 K. An increase in corrosion rate from 128 µm/y to 911 µm/y (6 times) has been reported from MANET steel with a similar increase in operating temperature from 773 K to 823 K [174]. In case of EUROFER 97, an increase in temperature from 753 K to 823 K resulted in an increase in corrosion rate from 90 µm/y to 700 µm/y (~ 7 times) [163,179]. Once again, the reason for this increase has been mainly attributed to the increase in solubility (in Pb-Li) and diffusivity (both in steel and Pb-Li) of alloying elements with temperature [123, 230].

Although the rate of increase of corrosion rate of IN RAFMS with temperature was higher in the present system, the actual values of corrosion rate are lesser than other steels like MANET or EUROFER 97. However, it should be kept in mind that the above reported data on MANET and EUROFER have been obtained through loop tests where an additional factor of temperature gradient generally causes an increase in corrosion rate [161-163].

5.3.3.2. Investigation through SEM-EDS and Discussion

After establishing the corrosion rate, the surface and cross-section of all the exposed IN RAFMS segments was studied through SEM-EDS. In order to further understand the effect of increasing flow velocity on the corrosion behavior, both the surface and cross-section of the segment exposed for the initial 2,000 h was analyzed in greater detail. For this sample; three locations were investigated upon as shown in Figure 5.39. These locations were termed as "inner" (Point A) which was exposed at 0.5 m/s, "middle" (Point B) which was exposed at 0.63 m/s and "outer" (Point C) which was exposed at 0.75 m/s.

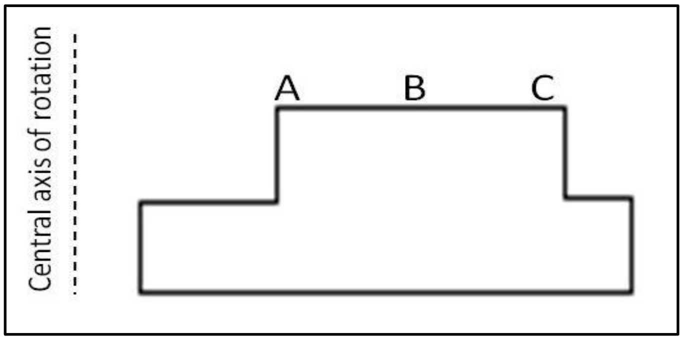

Fig. 5.39: Schematic diagram of the cross-section of IN RAFMS segment.

Figure 5.2 showed the SEM image of the as-received IN RAFMS material thus revealing its tempered martensite structure along with grain boundary carbides ($Cr_{23}C_6$). Figure 5.40 (a), (b) and (c) shows the SEM images of the IN RAFMS sample exposed to Pb-Li for 2,000 h at the inner (point A in Fig.5.39), middle (point B in Fig.5.39) and outer locations (point C in Fig.5.39) respectively.

A clear evidence of grain boundary attack was noted at all the regions and the attack seems preferably over the prior austenite grain boundaries as well as over some boundaries which may belong to very small sub-grains. The extent of grain boundary attack seemed higher near the inner edge as compared to the middle and outer locations. Such a result was apparently against with the general expectation that Pb-Li attack would increase with increasing radial distance due to increase in flow velocity. However, this could be confirmed only by analyzing the cross-section at similar places. Nevertheless, the chromium carbides observed over the grain boundaries in the as-received material (Figure 5.2) were not observed after 2, 000 h of Pb-Li exposure. Similar observations were also recorded for the IN RAFMS samples exposed to static Pb-Li at 773 K (Section 5.2.2.2; Figure 5.19). The dropping of carbides due to preferential grain boundary attack has been earlier noted in the case of CLAM steel exposed to Pb-Li and JLF 1 steel exposed to Li [224-225].

Other than grain boundary attack, a deposit was also observed over the outer edge of the sample where it was held by the molybdenum holder. The SEM image of this region is shown in Figure 5.40 (d). It is expected that slight gap must have remained between the holder and the sample edge where the corroded species got accumulated forming the deposit. Figure 5.41 (a) show SEM image of the deposit over the outer edge at the area indicated by box in Figure 5.40 (d) while Figure 5.41 (b) shows the high magnification image of the deposit in this area. The deposit could be actually demarcated into two regions: - the dark matrix and some white nodules. To analyze these differences, the composition of the region shown in Figure 5.41 (b) was mapped with the help of EDS.

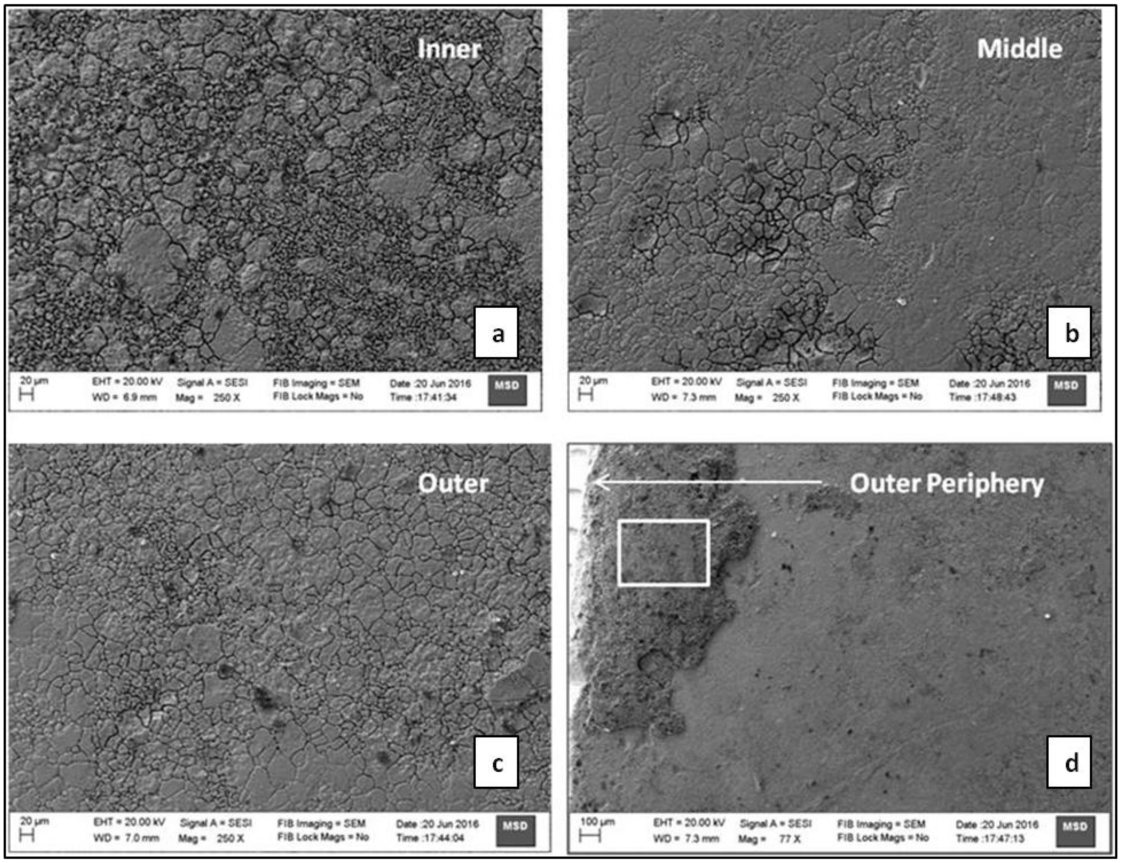

Fig. 5.40: SEM images at the (a) centre, (b) middle and (c) outer locations on the surface of the IN RAFMS sample after exposure to Pb-Li for 2000 h. (d) SEM image of the deposit noted over the outer edge.

These composition maps (of Fe, Cr, W and Ta) are shown in Figure 5.42. It was found that the deposits mainly contained iron and chromium although the locations richer in iron seemed deficient of chromium and vice versa. In order to know the exact composition of the iron and chromium in these deposits, spot EDS analysis was carried out at two different locations shown by spots 1 and 2 in Figure 5.42. The results of spot EDS analysis are shown in Table 5.14 where a distinct difference in composition of the two regions could be observed. The white nodules were found to be rich in iron and chromium and deficient in tungsten while the dark matrix was found to deficient in chromium but enriched in tungsten. It is possible that the dark matrix was a part of corroded surface where depletion of chromium complemented by a relative enrichment of tungsten and tantalum has taken place. Similar depletion of Cr and enrichment of W have been observed over the surface of JLF 1 steel exposed to static Pb-Li at 873 K [125]. This is because of the low solubility of tungsten in Pb-Li [195].

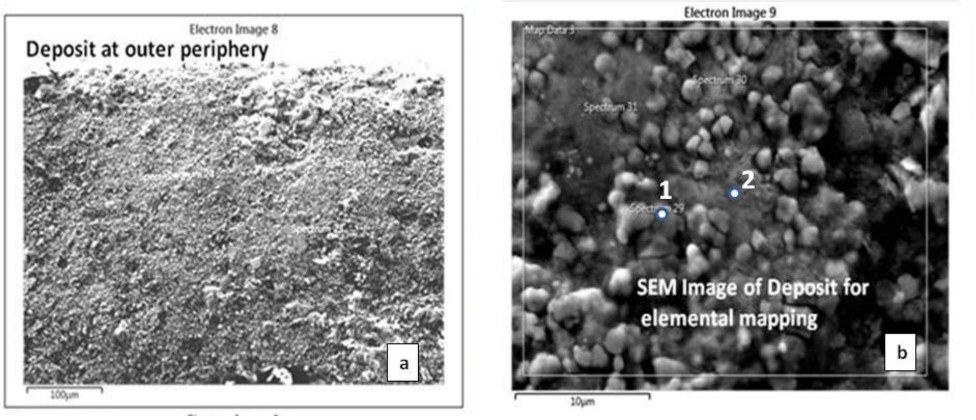

Fig. 5.41: (a) SEM image of the deposit from the area indicated in Figure 5.40 (d) and (b) Spots 1 and 2 of deposit chosen for EDS mapping.

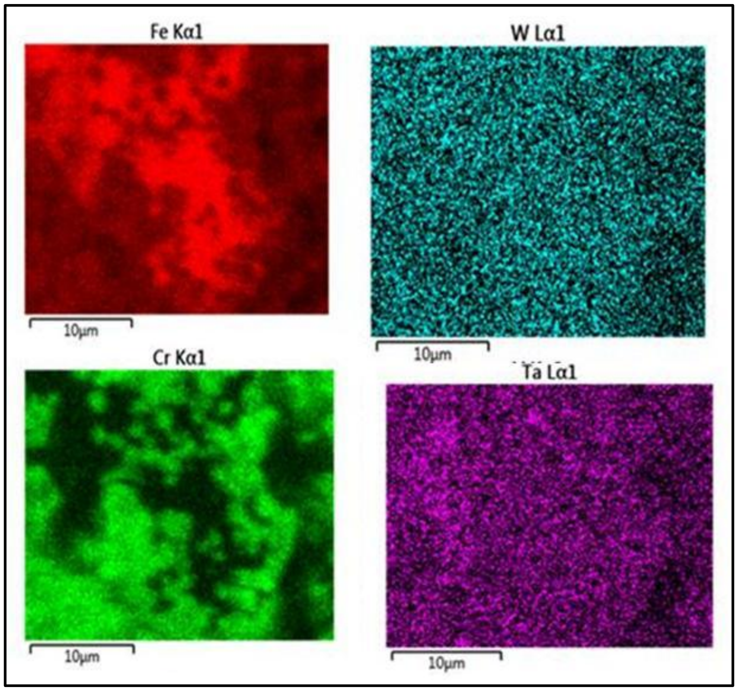

Fig. 5.42: Composition maps of iron, chromium, tungsten and tantalum recorded through EDS over the area indicated in Figure 5.41(b)

On the other hand the white nodules were the deposits formed due to dissolution of iron and chromium from steel into Pb-Li. The higher diffusivity of chromium [215] in Pb-Li results in substantial depletion of the same from the surface layers during the initial period of exposure

[125]. However, since the solubility of chromium in Pb-Li is only 10 ppm at 773 K, most of it gets precipitated as deposits on available surfaces under isothermal conditions [195] which may be represented by the white nodules in the present case. Formation of such Fe/Cr rich deposits have been also observed over the tube walls (MOC :1.4571 steel) of the cooler regions (~ 623 K) of PICOLO loop after exposure of various Ferritic–Martensitic steel samples in flowing Pb-Li at a temperature range of 753 – 823 K [181]

Table 5.14: Composition of various features over the deposit at outer periphery analyzed through EDS.

(Wt %)	**Fe**	**Cr**	**W**	**Ta**	**V**
White Nodules (Spot 1)	54.3	44.6	0.3	0.7	0.1
Dark Matrix (Spot 2)	82.1	5.5	2.9	9.3	0.1

In order to know the nature of grain boundary attack, the line scans of major constituents like iron, chromium, tungsten and tantalum were recorded across the attacked grain boundaries on the 2, 000 h exposed sample through EDS. The first scan was taken at the inner location across a less attacked grain boundary as highlighted by white line in Figure 5.43 (a). The corresponding line scan (Figure 5.43(b)) showed no change in the concentration of constituent elements. On the other hand, the scan taken across a heavily attacked boundary in the same location (inner) showed significant depletion of all alloying elements across the boundary (Figure 5.43(d)).The path of this line scan has been indicated in Figure 5.43(c). Similar depletion of constituent elements was also noted across the attacked grain boundary Figure 5.43(e)) at the outer location. This line scan has been indicated in Figure 5.43(f). The fall in the concentration of all elements at the Pb-Li attacked grain boundary indicates the occurrence of preferential material dissolution. The reasons for this include:-

a. Relatively lesser protection offered by passive oxide layers near the grain boundaries as discussed for static experiments in Section 5.2.2.3 [218].

b. High energy of the grain boundaries (Section 5.2.2.3) [226].

The relative drop in elemental concentration was almost similar over the highly attacked boundaries at both inner and outer locations indicating similar mechanism of corrosion. However, the fraction of highly attacked grain boundaries seemed lesser at the outer locations which were possibly because of dislodgement of loose grains/sub-grains from the exposed surface due to shearing action of Pb-Li (high flow) in this area. Similar results have been observed for JlF-1 steel exposed to flowing Pb-Li in an isothermal stirring test [125]. Thus, at the outer location, the grains which becomes slightly weak/loose due to grain boundary penetration of Pb-Li can erode away even before further attack/penetration to greater depth takes place. This was further verified by analyzing the cross-section of the segment exposed to Pb-Li at 2, 000 h.

Figure 5.44 (a) and (c) shows the SEM image of the cross-section of the IN RAFMS sample exposed to Pb-Li for 2, 000 h at the inner and outer locations respectively. High magnification images of the inner and outer location are shown in Figure 5.44 (b) and (d) respectively. The grain boundary attack of Pb-Li was clearly evident at the inner side which was exposed to a comparatively lower velocity (0.5 m/s) while the outer periphery exposed to a higher velocity (0.75 m/s) did not show such features. The maximum depth of grain boundary attack measured at the inner location was 22 µm. On the other hand, prominent grain dropping as well as chipping was observed at the outer location. The diameter of the dropped grain was around 15 µm which was similar to the prior austenite grain size of the unexposed IN RAFMS sample (Section 5.1). This was thus a signature of complete enveloping of the prior austenite grains by Pb-Li penetration and ***grain dropping*** [186].

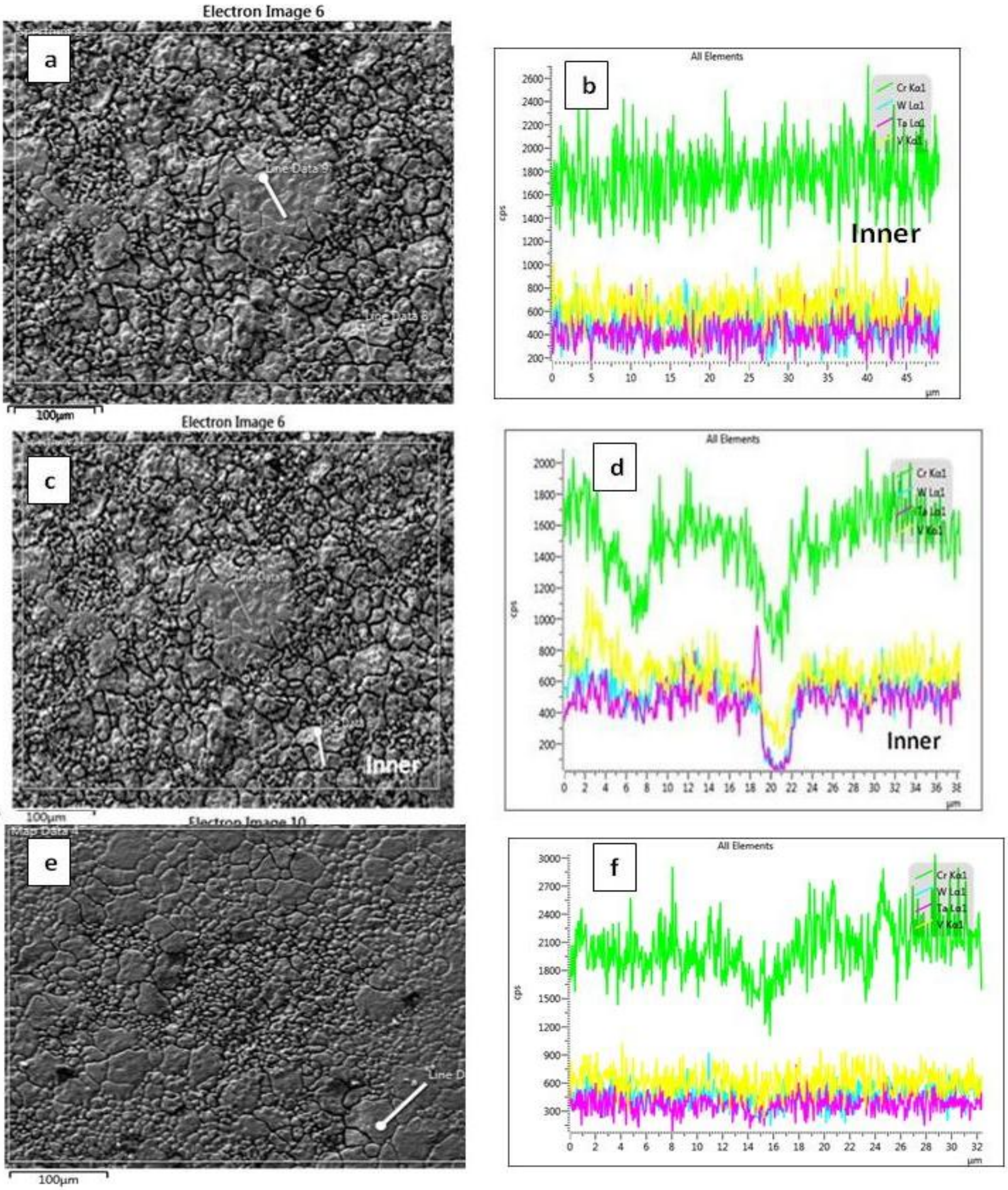

Fig. 5.43: EDS line scans for chromium, tungsten, tantalum and vanadium at various locations (inner, middle and outer) on the surface of the IN RAFMS sample after exposure to Pb-Li at 773 K for 2, 000 h.

The above results indicate that lower velocity at the inner location allows greater Pb-Li penetration although the unaffected matrix in between the attacked boundaries is retained. However, higher velocities at the outer region results in faster removal of the attacked regions by phenomenon grain dropping / exfoliation. An evidence of ***exfoliation*** is also observed from the presence of chips near the exposed surface at the outer locations which are possibly parts of the corroded surface which got dislodged. These results complement with the observations on the exposed surface where greater grain boundary attack and elemental depletion as noted in the inner locations (Figure 5.43).

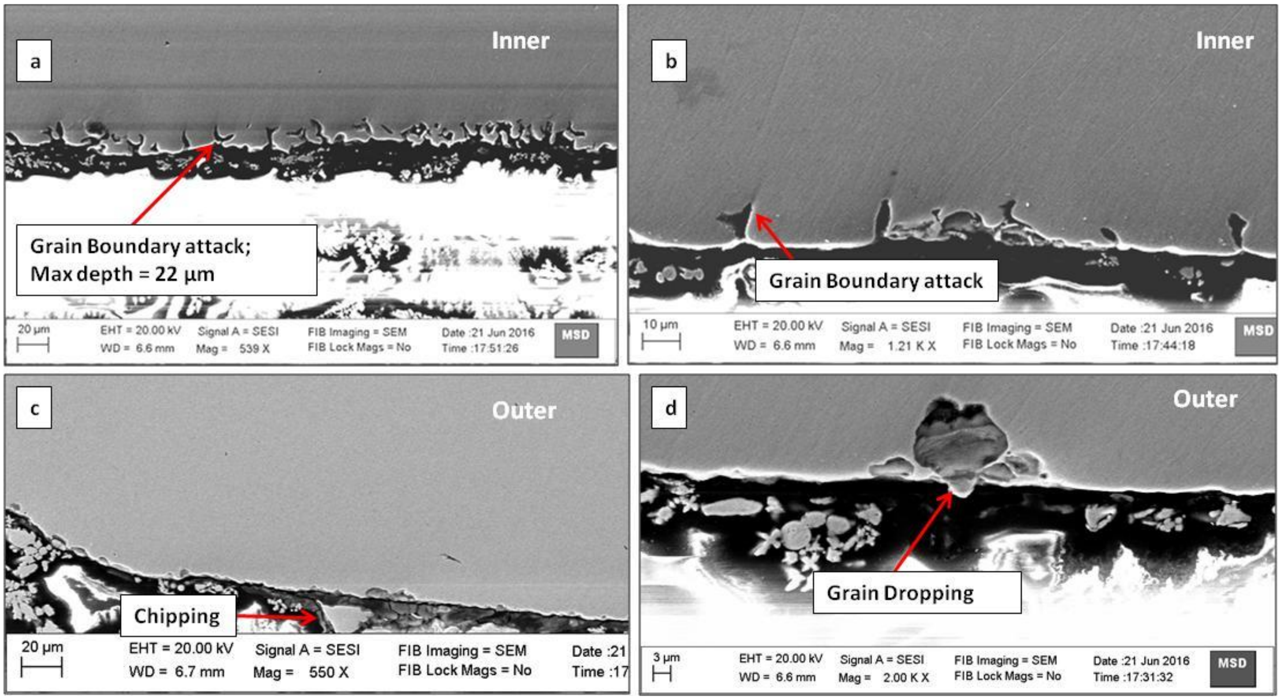

Fig. 5.44: SEM image of the cross-section of the IN RAFMS sample exposed to Pb-Li at 823K for 2, 000 h at (a) and (b) Inner (c) and (d) Outer locations.

The effect of Pb-Li on the composition of the exposed surface was analyzed by taking line scans of major constituent elements on the cross-section at inner and outer locations of the 2, 000 h exposed sample. The path of line scan at inner and outer locations has been shown in Figure 5.45 (a) and (c) respectively. The corresponding elemental profiles at the inner and outer locations have been respectively shown in Figure 5.45 (b) and (d). The maximum depth of elemental depletion (~ 45 µm from Figure 5.45 (b)) suggests that the depletion of alloying elements occurs from a much greater depth as compared to grain boundary penetration (~22 µm) (Figure 5.44(a)). The similarity of line scans at inner (Figure 5.45 (b)) and outer (Figure 5.45 (d)) locations also indicated that dissolution of alloying elements like chromium governs Pb-Li corrosion both at higher and lower velocities. The role of velocity is only to take away the weak surface layers where Pb-Li penetration has taken place. Cross-sectional analysis (Figures 5.44 and 5.45) indicated that the Pb-Li attacked layers / grains on the exposed surface might have been washed away up to a certain depth at the outer location. Therefore it was difficult to identify the exact depth of Fe-Cr depletion at the outer location since the position of the original steel-Pb-Li interface is not known. However; from the similarity in the Cr-depleted layer at both inner (~ 0.5m/s) and outer locations (0.8 m/s), it is evident that the actual depth of elemental depletion might have been higher at the outer location.

In order to get a quantitative estimate, the actual composition over the cross-section was recorded at a number of spots starting from the inner matrix to the exposed boundary. The locations of spots are indicated by Spectrum 6 to 12 at the inner location in Figure 5.45 (a) and Spectrum 15 to 19 at the outer location in Figure 5.45 (c). Table 5.15 gives the composition of various spots in the inner location while Table 5.16 shows the composition of the spots at the outer location. Chromium (Cr) content was found to decrease near the exposed edge at both the inner and the outer locations as indicated by the line scans in Figure 5.45. On the other hand, tungsten (W) got enriched at both the locations due to its low solubility in Pb-Li. Lead was not detected over the exposed surface at either of the locations. This may be probably due to selection of a spot away from Pb-Li attacked grain boundaries. The results of spot EDS (Table

5.14 and 5.15) complement the results from line scans (Figure 5.45) and also support the fact the mechanism of corrosion remains the same at higher and lower velocities.

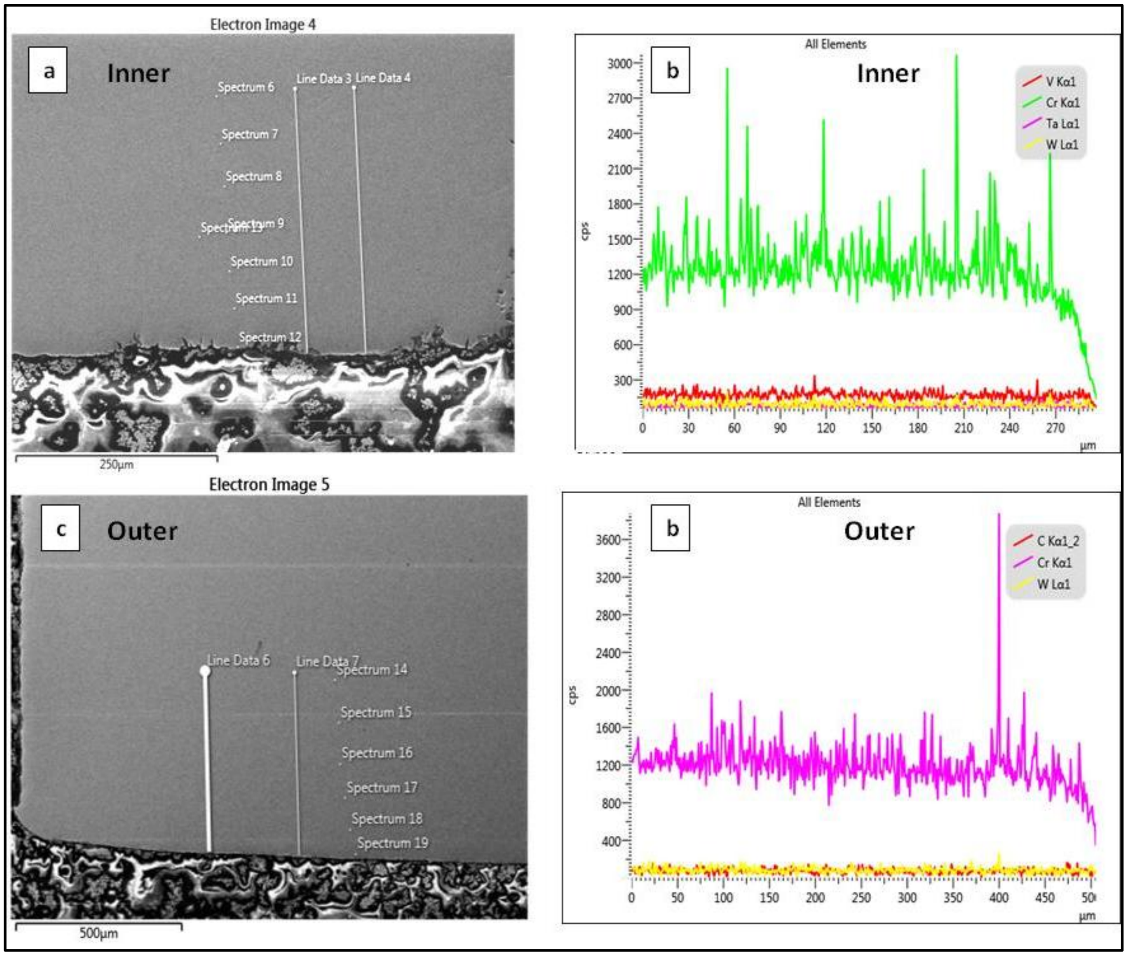

Fig. 5.45: SEM image of the cross-section at the inner edge of the IN RAFMS sample exposed to Pb-Li at 773 K for 2000 h and corresponding EDS line scan.

Table 5.15: Composition at various spots on the cross-section of the inner edge of exposed IN RAFMS sample as indicated in Fig 5.45 (a).

Spectrum	**Fe**	**Cr**	**W**	**V**	**Ta**
6	base	8.8	1.5	0.2	0.1
7	base	9.6	1.8	0.1	0.0
8	base	8.7	1.4	0.3	0.0
9	base	12.7	2.7	0.3	0.1
10	base	9.4	1.3	0.3	0.1
11	base	8.0	1.3	0.2	0.0
12	base	2.2	2.0	0.3	0.6

Table 5.16: Composition at various spots on the cross-section of the outer edge of exposed IN RAFMS sample as indicated in Fig. 5.45 (c).

Spectrum	Fe	Cr	W	V	Ta
15	base	9.0	1.4	0.2	0.1
16	base	8.3	1.4	0.2	0.1
17	base	8.5	1.4	0.2	0.2
18	base	9.0	1.3	0.2	0.1
19	base	3.3	1.7	0.1	0.0

The ***effect of duration of exposure*** on corrosion of IN RAFMS segments was studied by analyzing the surface and cross-section of the segments under SEM-EDS. Figure 5.46 (a) to (f) shows the surface microstructure of the IN RAFMS segments exposed to Pb-Li for 2, 000 h, 4, 000 h, 2, 000 +2, 000 h, 6, 000 h, 8, 000 h and 10,000 h respectively. All images have been recorded at similar magnification. It could be clearly seen that the Pb-Li attack in the first 2, 000 h was confined to the prior austenite grain boundaries only (Figure 5.46(a)). However, formation of very small hexagonal sub-cells inside these boundaries was observed (Figure 5.46(a)) and some sub-cells were found to have dropped off. Thermal exposure (ageing) as well as Stress exposure (creep) results in formation of sub-grains in RAFM steel due to recovery of lath structure as discussed in Section 5.2.2.3 [216, 231-232] . It has been reported that long term tempering (at 823 K in the present case) of a 10Cr1Mo1W steel allowed dislocations present within the martensitic structure (formed during austentization) to anneal out and arrange to form sub-boundaries, leading to the formation of sub-grains [217] . Thus it was initially anticipated that the sub-cells observed in the present case might be such sub-grains which have formed due to continued thermal exposure of IN RAFM steel at 773 K for 2, 000 h. The penetration of Li or Pb-Li along the sub-grain boundaries of JLF 1 steel and subsequent dropping/exfoliation of these weak sub-grains due to Li or Pb-Li flow have been already reported [125]. In the present case;

the dropping off of some sub –cells from the IN RAFMS surface (Figure 5.46 (a)) must be a result of sub-grain exfoliation due to Pb-Li attack along their grain boundaries.

However, it is also true that thermal exposure alone would have created sub-grain formation in the entire matrix including regions not affected by Pb-Li. On the other hand, the first experiment with IN RAFMS (Section 5.3.2) showed the formation of spheroidal sub-grains over the Pb-Li exposed surface only (up to a depth 0f 30 µm). It was predicted that this was mainly due to the loss of chromium and carbon into Pb-Li where carbon loss was mainly associated with its trapping by the molybdenum crucible. In the present case also, the sub-grains were observed only during the initial 4, 000 h of Pb-Li exposure and not afterwards as will be discussed in the following paragraphs. It is thus expected that, the sub-grain formation in both the studies on IN RAFMS in RDCTF (Section 5.3.3 and Section 5.3.2) was probably due to a combined effect of thermal exposure and elemental dissolution in Pb-Li.

The reasons for absence of grain boundary carbides (due to grain boundary attack of Pb-Li) as noted after 2,000 h (Figure 5.46 (a)) have been already discussed in the case of static experiments (Section 5.2.2). It may be noted that carbide disappearance have been also observed for Pb-Li and pure Li attack in the case JLF-1 steel and CLAM steel [125 185, 225]. The reason for this has been attributed to loss of carbon in the case of pure Li exposure (creating carbide instability) [185] and carbide dissolution / spalling in case of Pb-Li exposure [225]. Since the activity of lithium is very low in Pb-Li [233] and formation of Li_2C_2 is the main reason for loss of carbon in pure Li [187]; it is expected that dropping of carbides due to preferential grain boundary attack is the major reason behind disappearance of carbides in the present case of IN RAFMS.

After 4, 000 h, Pb-Li attack took place on the lath boundaries also including greater attack at the sub-grain and prior austenite grain boundaries as shown in Figure 5.46 (b). However the sample which had been cleaned after 2, 000 h and then exposed for a total of 4, 000 h (i.e. 2, 000 + 2, 000 h) showed a uniformly corroded surface where the grain boundary carbides were visible giving rise to an etched appearance. Similar type of uniform corrosion was also noted for the samples exposed for 6, 000 h (Figure 5.46 (d)) and 8, 000 h (Figure 5.46(e)). However, after 10, 000 h the matrix inside the grain boundaries seemed to have been greatly corroded giving rise to a faceted and etched appearance as shown in Figure 5.46 (f).

It is evident that there was a change in corrosion mechanism with increase in the duration of exposure. A reason for initial grain boundary attack (up to 2, 000 h) could be a weaker passive oxide layer over the grain boundaries which facilitate initiation of Pb-Li attack at those points. However, such a case would be valid for both prior austenite as well as lath boundaries since both contain $M_{23}C_6$ type carbides (where M is mostly Cr). Since the Pb-Li attack was mostly confined to the prior austenite grain boundaries up to 2, 000 h; it is possible that the higher energy of PAGBs /sub-grain formation also played a role in initiating attack [234-235].

The grain boundary attack for the first 4,000 h has also led to the dropping of carbides as observed in Figure 5.46(b). It is evident from Figure 5.46 (c) to (f) that continued grain boundary attack led to the detachment of the entire attacked layer from the surface thus creating an etched appearance similar to uniform corrosion. This was first observed in the case of the sample exposed for 2000 + 2000 h (Figure 5.46(c)). This result was in good agreement with the higher weight loss of this sample as compared to the once which is directly exposed to 4, 000 h (Figure 5.38). The uniform corrosion was sustained till 8, 000 h (Figure 5.46(e)) after which a higher attack seemed to have occurred over the grain interiors than the grain boundaries as observed for the 10,000 h exposed sample (Figure 5.46(f)).

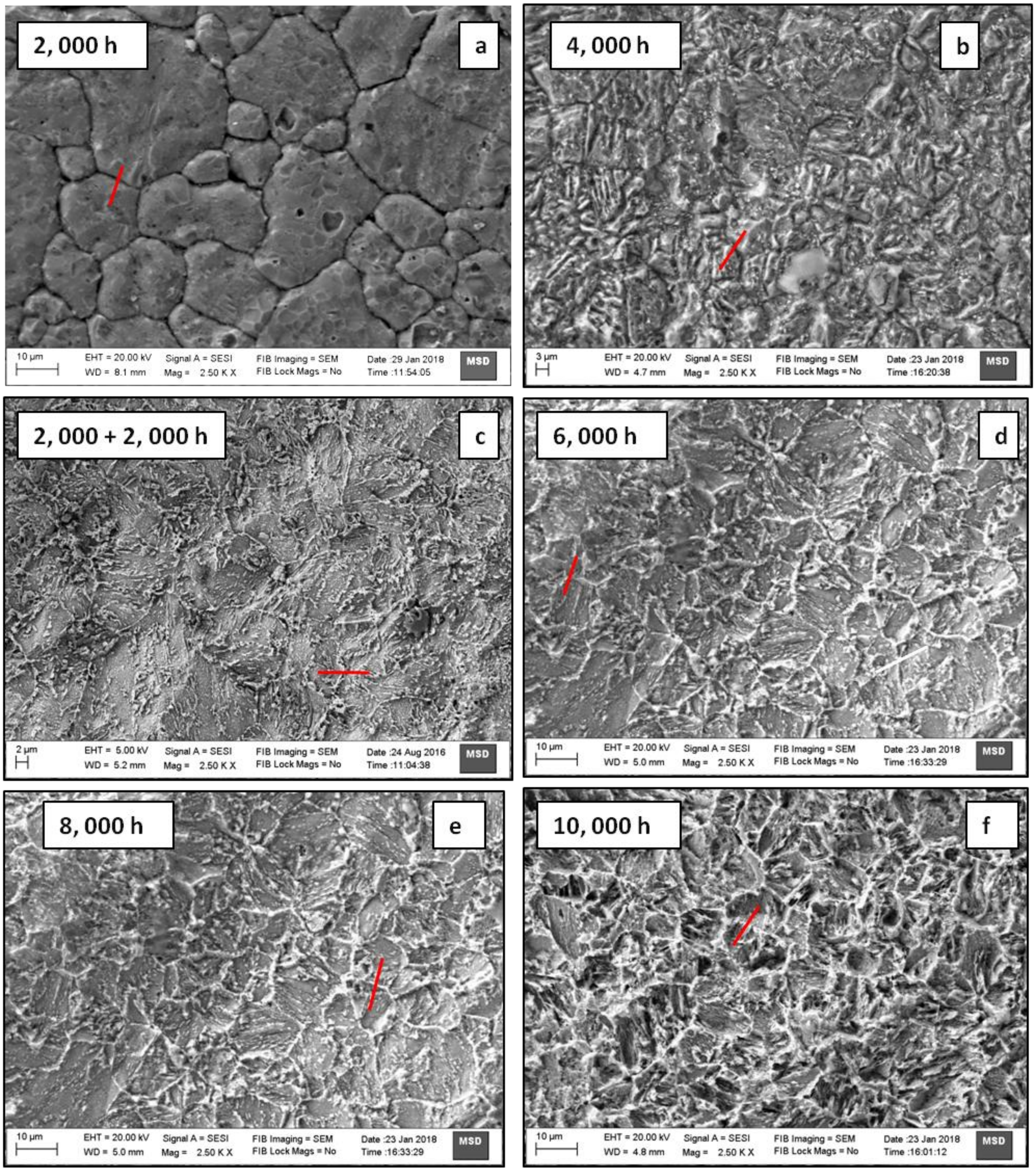

Fig. 5.46 : SEM images on the surface of the IN RAFMS segments exposed to Pb-Li at 823 K for a) 2, 000 h, b) 2, 000+2, 000 h, c) 4, 000 h, d) 6, 000 h, e) 8, 000 h, f) 10, 000 h.

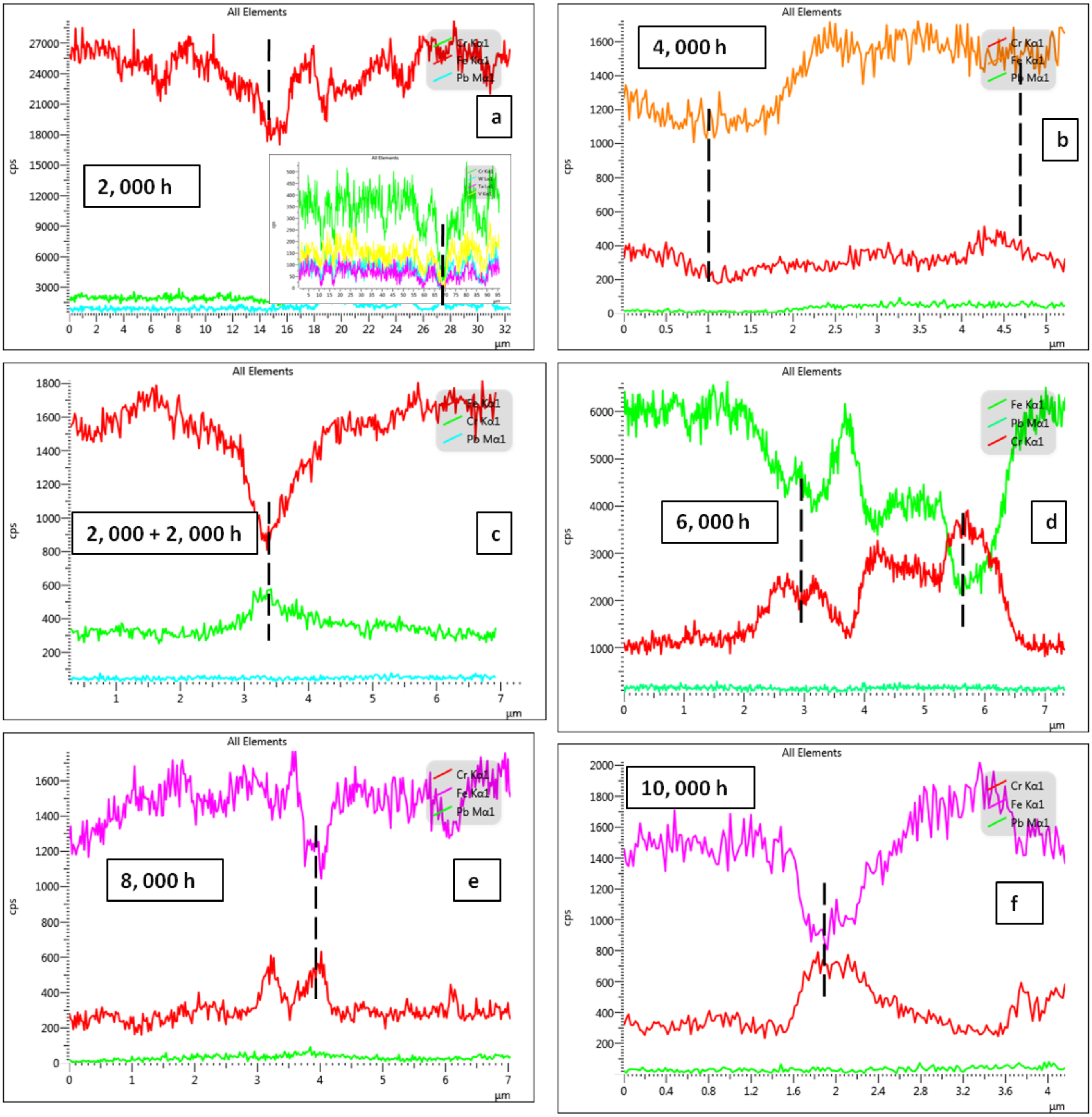

Fig. 5.47: Line scan of iron, chromium and lead taken across the grain boundary of IN RAFMS segment exposed to Pb-Li at 823 K for a) 2, 000 h, b) 2, 000+2, 000 h, c) 4, 000 h, d) 6, 000h, e) 8, 000h, f) 10, 000 h.

In order to further understand the effect of duration of exposure over the grain boundaries, elemental profile of iron, chromium and lead were recorded through EDS across the grain boundaries of the sample exposed for 2, 000 h , 2, 000+2, 000 h, 4, 000 h, 6, 000 h, 8, 000 h, 10, 000 h. These line scans are shown in Figure 5.47 (a) to (f) respectively. The paths of the line scans have been indicated by red lines in Figure 5.46 and the locations of grain boundaries on the line scan have been indicated by dashed lines in Figure 5.47. A drop in concentration of all elements was observed over the attacked grain boundary on the 2, 000 h exposed sample. The sample exposed directly for 4, 000 h showed a similar pattern although the width of depleted zone increased significantly. A definite change in pattern was noted for the sample exposed for 2, 000 + 2, 000 h where a drop in iron and enrichment in chromium was noted across the grain boundary. Similar pattern was noted for all other samples i.e. those exposed for 6, 000 h, 8, 000 h and 10, 000 h. This probably indicated that the nature of Pb-Li attack changed in between 2, 000 h to 6, 000 h where the chromium concentration profile at grain boundary reverses. However since the weight loss was found to increase significantly after 2, 000 h (Figure 5.37); it was thus evident that the incubation period or the period of reduced attack lied somewhere between 2, 000 h to 4, 000 h and matrix dissolution must have already started at 4, 000 h.

It might be possible that the initial Pb-Li attack occurs only at the matrix adjacent to the grain boundaries where the passive layer is weak. Under such a condition, a drop in all constituents might be noted at the grain boundaries as observed in Figure 5.47(a). Similar results have been noted when IN RAFMS have been exposed to static Pb-Li at 773 K (Section 5.2.3). However, the overall weight loss would be lower during preferential grain boundary attack as is observed in the present experiment during the initial 2,000 h (Figure 5.37). With continued exposure constituent elements from the areas adjacent to the attacked grain boundaries start dissolving into the Pb-Li channels causing greater width of elemental depletion as has been observed for the sample expose for 4, 000 h (Figure 5.47(b)). It may be noted that one of the grain boundaries in this sample started showing slight enrichment of chromium (Figure 5.47(b)) and the chromium enrichment later increased significantly in all other samples including the one exposed for 2, 000 + 2, 000 h.

The initial period of exposure is also associated with dissolution of oxide scales along with grain boundary attack as discussed in Section 5.2.3. Once the entire oxide scale gets completely dissolved in Pb-Li, the entire matrix becomes exposed to Pb-Li with equal preference at all locations. This leads to the change of corrosion mechanism of Pb-Li attack over the entire surface as observed in Figures 5.46 (c) to (f).

The removal of passive layer might be accelerated at high flow velocities due to exfoliation of the grains whose boundaries were completely / partially enveloped by Pb-Li. Due to gradual dropping of these grains, the entire top surface containing passive layer gets detached. Since the next layer of grains do not posses any passive layer; Pb-Li attack takes place in the entire matrix and an etched appearance is revealed where grain boundary carbides become clearly visible. This is observed for the samples exposed from 2, 000 +2, 000 h (Figure5.46 (c) till 10, 000 h (Figure 5.46 (f)). Under the above condition a line scan taken across the grain boundary may show an enrichment of chromium due to the presence of chromium carbides at PAG boundaries and lath boundaries as has been observed in Figure 5.47(c) to (f).

The role of passive layer in governing the corrosion mechanism is also revealed from Figure 5.48 which shows the concentration map of oxygen taken over the sample exposed for 2, 000 h and 10, 000 h. It could be seen that significant amount of oxygen was present over the sample exposed for 2, 000 h and oxygen concentration remained nearly constant. However, after 10, 000 h, oxygen content over the matrix considerably reduces although the grain boundaries seemed to have higher oxygen. This is possibly due to the association of oxygen with the chromium carbides which could be observed over the IN RAFMS sample exposed to Pb-Li for 10, 000 h (Figure 5.46 (f)).

In order to investigate the effect of change in corrosion mechanism over the depth of the exposed sample, the cross-sectional SEM images were recorded. From the trend observed in the analysis of sample surface and for the sake of concise discussion; only the images of the sample exposed for 2, 000 h, 6, 000 h and 10, 000 h are shown in Figure 5.49 (a), (c) and (d) respectively. It could be clearly seen that grain boundary attack was prominent on the sample exposed for 2, 000 h only while the sample exposed for 6, 000 displayed a more or less uniform exposed boundary. On the other hand, the 10, 000 h exposed showed widely spaced surface undulations probably due to greater matrix dissolution. It was thus confirmed that Pb-Li attacks only along the grain boundary during the initial phase of corrosion where passive layer might be present over the rest of the surface whereas afterwards, attack takes place over the entire matrix. The surface undulations observed after 10, 000 h may be due to dissolution of large chunks of material from where faster removal of oxide layer had initially taken place (Figure 5.49(f)). This prediction is based on the literature reports where the dissolution of oxide layer has been predicted to be non-uniform in the initial periods of exposure [163].

Line scan of iron, chromium and lead were also recorded across the exposed boundary on the above cross-section of the samples exposed for 2, 000 h, 6, 000 h and 10, 000 h is shown in Figure 5.49 (b), (d) and (f) respectively. The depth of chromium depletion was found to be almost negligible in the samples exposed for 6, 000 h and 10, 000 h as compared to a depletion depth of around 40 μm in case of the sample exposed for 2, 000 h (Figure 5.45). The reason for this might also be related to the change in corrosion mechanism. During the initial 2, 000 h, due to grain boundary penetration, elemental dissolution occurs into the Pb-Li channels inside the grain boundary and thus the elements with higher solubility in Pb-Li may get depleted from a greater depth (Figure 5.45 (b)).

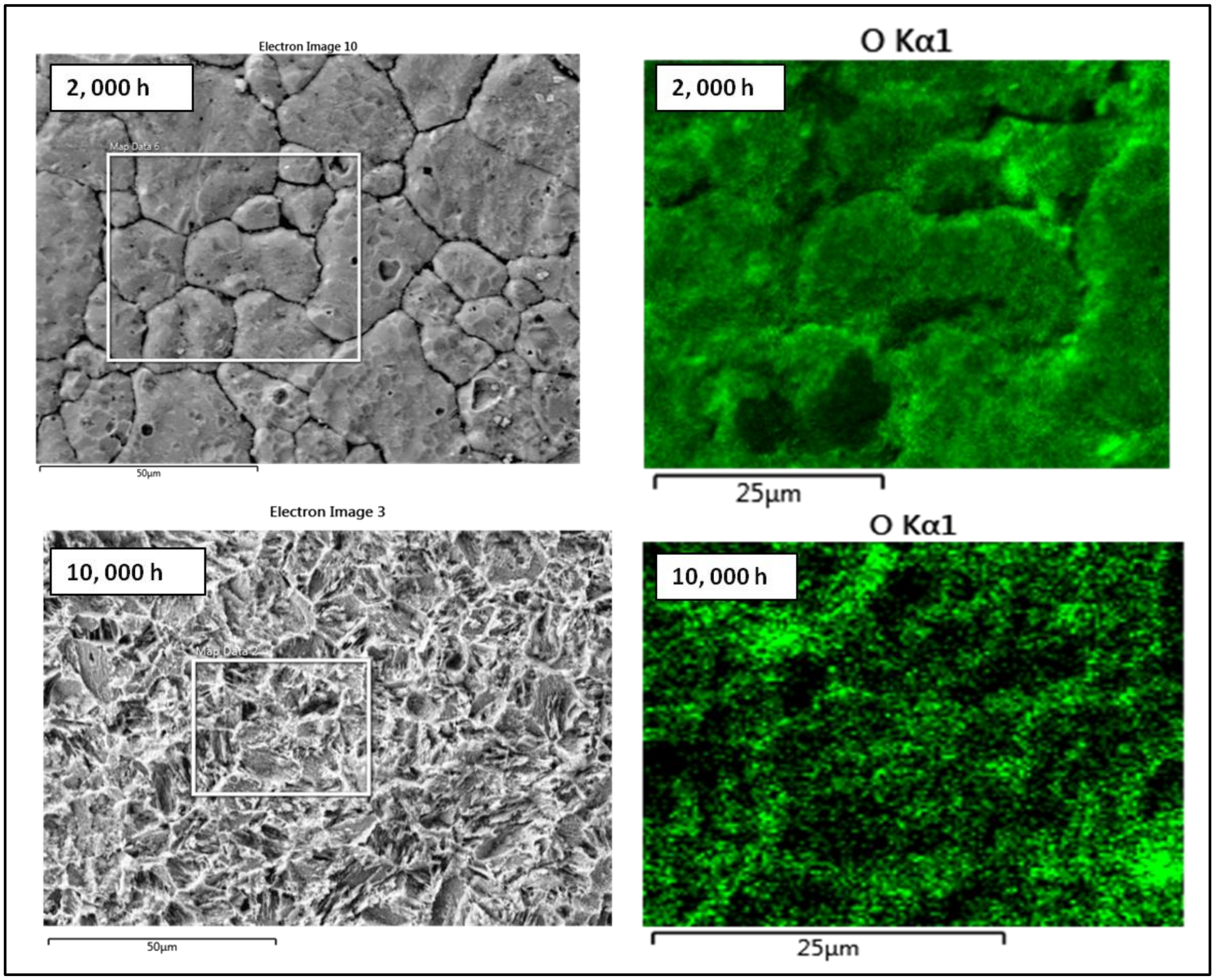

Fig. 5.48: Oxygen concentration maps over the surface of the IN RAFMS sample exposed to Pb-Li at 823 K for 2, 000 h and 10, 000 h.

However, when matrix dissolution predominates afterwards, the entire surface gets equivalent exposure to Pb-Li and in the absence of grain boundary penetration, elemental dissolution occurs from the exposed surface only. This leads to decrease in the overall depth of elemental depletion (Figure 5.49 (f)). Another reason for decrease in the depth of chromium depletion might be associated with its lower solubility in Pb-Li (10 wppm at 773 K) which causes its dissolution rate to decrease after certain duration of exposure [125].

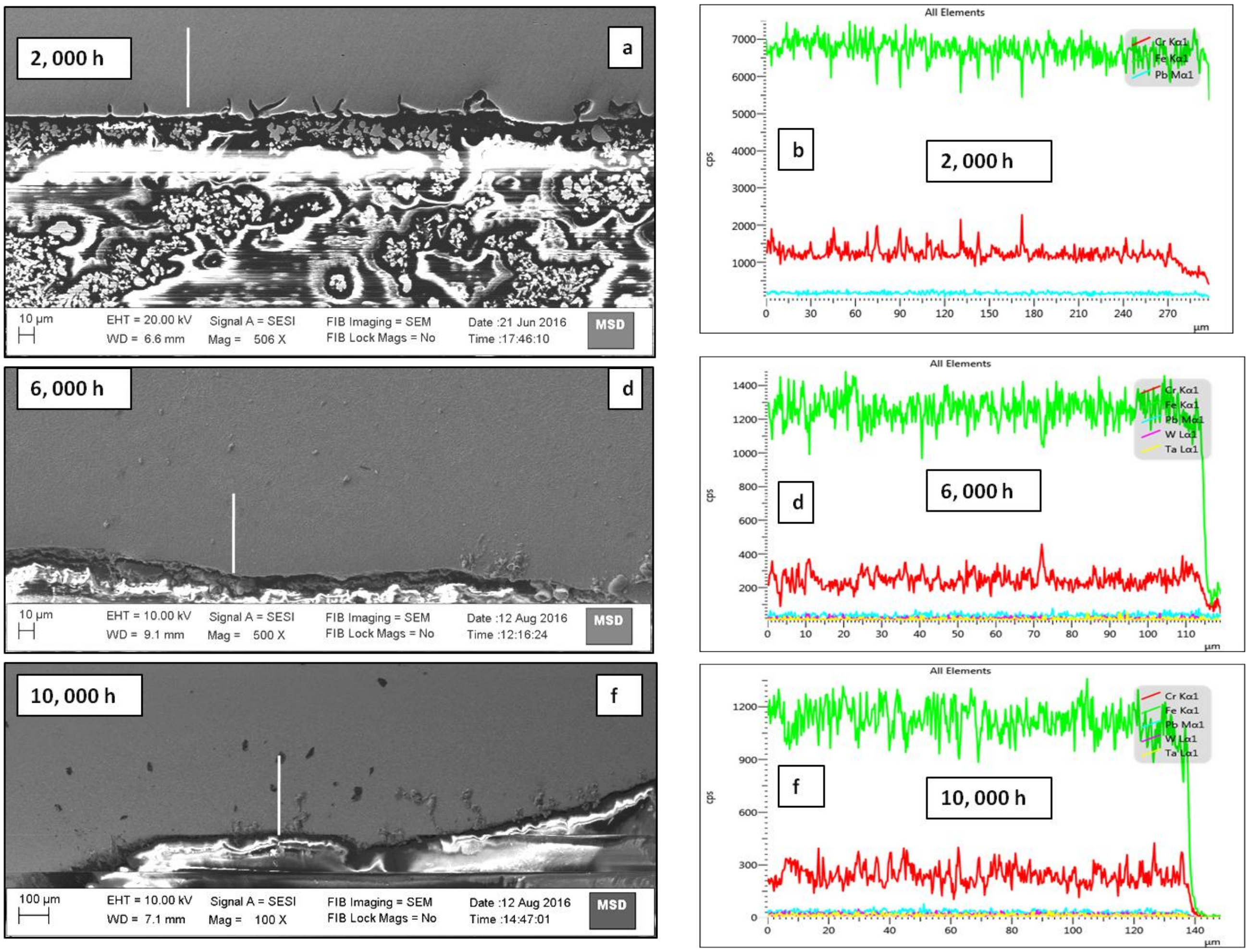

Fig. 5.49: Cross-sectional images of IN RAFMS segment exposed to Pb-Li at 823 K for a) 2, 000 h, c) 6, 000 h, (e) 10, 000 h and line scan of iron, chromium and lead taken across the grain boundary for the sample exposed for (b) 2, 000 h, (d) 6, 000 h, (f) 10, 000 h.

5.3.3.3. Summary

- It was revealed from the present study that; that the existence of passive layer (containing oxides of Fe and Cr) plays a major role in deciding the corrosion mechanism of IN RAFM steel in Pb-Li.
- An initial period of reduced corrosion attack called the “incubation period” which arises from the protective nature of the passive layer generally dominates corrosion till about 2, 000 - 4, 000 h for IN RAFMS at 823 K.

- The major mechanism of corrosion during this “incubation period” involves grain boundary penetration and elemental dissolution into the Pb-Li channels. The grain boundary carbides are removed due to preferential dissolution of the surrounding matrix in Pb-Li
- The passive layer is eventually removed by its slow dissolution in Pb-Li or by removal of the top layer of grains through grain dropping/dissolution.
- Afterwards, the corrosion mechanism changes to matrix dissolution. This leads to the formation of a surface similar to the etched sample before exposure. Matrix dissolution increases with the duration of exposure.
- The corrosion mechanism remains unaffected by flow velocity of Pb-Li although the rate of grain dropping / exfoliation may be accelerated at higher velocities.
- The depth of chromium depletion is higher during grain boundary penetration due to dissolution of the same in Pb-Li channels. The maximum depth of Pb-Li channels have been found to be 22 µm while the depth of chromium depletion has been found to 40 µm in the present case.
- Depth of elemental depletion has been found to be lower at higher velocities.

CHAPTER 6

CORROSION BEHAVIOR OF FERRITIC/MARTENSITIC STEELS IN NON- ISOTHERMAL Pb-Li

---

After having a fair idea of the corrosion mechanism of F/M steels (i.e. P91 and IN RAFMS) under isothermal conditions (static and flowing), the next step was to understand the corrosion phenomenon under actual reactor condition where temperature gradient and magnetic field acts as an additional factors in affecting corrosion. For this purpose, IN RAFMS and P91samples were exposed to Pb-Li loops in the presence and absence of a magnetic field. The first part of this chapter deals with Pb-Li corrosion studies under non isothermal and flowing conditions in the absence of magnetic field which were carried out in the electromagnetic pump driven Pb-Li loop (EMPPIL) installed at BARC, Mumbai and in the forced circulation loop (PICOLO) at KIT, Germany. In the later part, analysis of the effect of magnetic field on the corrosion behavior of P91 and IN RAFMS material has been done and discussed where experiments were carried out in two separate Pb-Li loops at IPUL, Latvia and BARC, Mumbai.

6.1. Corrosion of IN RAFMS in the forced circulation loop Pb-Li loop EMPPIL at 773 K

In the beginning, IN RAFMS coupons were exposed to flowing Pb-Li in the EMPPIL facility at BARC where Pb-Li flowed at an average velocity of 1.5 m/s and the temperature of exposure was 773 K for 5, 000 h. The detailed designs of EMPPIL and corresponding sample / sample holder are given in Section 3.5 (Chapter 3) while the experimental procedure is given in Section 4.5.1 (Chapter 4). It may be noted that these RAFMS samples were of the composition 9Cr-1W-

0.06Ta as mentioned in Section 4.2.1, while the final established composition of IN RAFMS is 9Cr-1.4W-0.06Ta (Table 4.1).

6.1.1. Weight Loss of IN RAFMS in non isothermal and flowing Pb-Li.

After exposure in EMPPIL loop, the IN RAFMS samples were cleaned from adherent Pb-Li and the corrosion rates were calculated from the weight loss measurements after 5, 000 h exposure as given in Table 6.1. It may be noted that the sample placed in the upstream position (i.e. Sample A in Fig 3.20) showed higher corrosion rate as compared to the sample (i.e. Sample D in Fig. 3.20) placed in the downstream position

Table 6.1: Corrosion rate of IN RAFMS exposed to Pb-Li flowing at 0.6-1.5 m/s and at 773 K.

Sample	Initial weight (g)	Final Weight (g)	Weight Loss (g)	Corrosion rate (µm/y)
Upstream (Sample A)	3.4103	3.3010	0.1093	49.98
Downstream (Sample D)	3.2838	3.1950	0.0888	46.67

Similar decrease in corrosion rate (~40%) for the downstream samples as compared to upstream ones has also been obtained in one of our earlier experiments with P91 samples when exposed to flowing Pb-17Li in a thermal convection loop [236]. There could be many reasons for such variation in the corrosion rates:

(1) Differences in flow velocity for the upstream and downstream samples. In this regard, Figure 3.22 clearly shows that the velocity faced by the upstream samples is 1.5 m/s while that for the downstream samples is around 1 m/s.

(2) Reduction in the concentration difference of the elements between the samples and the liquid Pb-Li on moving from upstream to downstream location.

It appears that out of the two reasons; difference in velocity of Pb-Li has contributed more towards the variation in the corrosion rates since the corrosion of Indian RAFMS under stagnant Pb-Li exposure (Section 5.2) has been observed to be much lesser than that under dynamic conditions (Section 5.3). As already pointed out in Section 2.9.2.c, the role of velocity is to bring a fresh liquid to the interface and also to provide an erosive action by the high density Pb-Li (10.5 gm/cc) especially at higher velocities [143]. This effect of velocity has larger implications under the actual reactor conditions, as any disturbances to the lead-lithium flow in the actual coolant circuit (e.g. of TBM) in the form of bends, constriction, probes etc. will generate a localized high velocity zone which will thereby increase the extent of corrosion attack. However, the difference in corrosion rate observed in the present case was 7%, when the velocity varied from 1 m/s to 1.5 m/s.

Thus in the present experiment, the maximum corrosion rate experienced by IN RAFMS (upstream side) at 773 K in flowing Pb-Li was 50 µm/y (Table 6.1). This corrosion rate is comparable to the corrosion rates of other RAFM steels like EUROFER 97, CLAM, etc as listed in Table 2.12 (Section 2.10). Nevertheless, the corrosion rate of IN RAFMS in the present experiment have been calculated based on weight loss data obtained after a single time duration i.e. 5, 000 h. In many reported studies the weight loss of corrosion coupons is measured after taking them out at regular time intervals and then the corrosion rate is calculated from the slope of weight loss vs. exposure time graph [194].

6.1.2. Microscopic investigations

In order to clearly understand the effect of the differences in flow velocity of Pb-Li for the IN RAFMS samples, optical micrographs were recorded over the cross-sections of the exposed samples both along the longitudinal (parallel to flow) and transverse direction (normal to flow). The locations on the sample chosen (sample A) for this microscopy are indicated in Figure 6.1(a). Figures 6.1 (b) and (c) show the micrographs of Sample A taken along the transverse and longitudinal directions respectively. The micrograph in the transverse direction (Figure 6.1(b)) represents the part of sample which has seen the maximum flow velocity (near the edge), while the micrograph along the longitudinal direction (Figure 6.1 (c)) represents the centre of the sample which was exposed to the minimum flow.

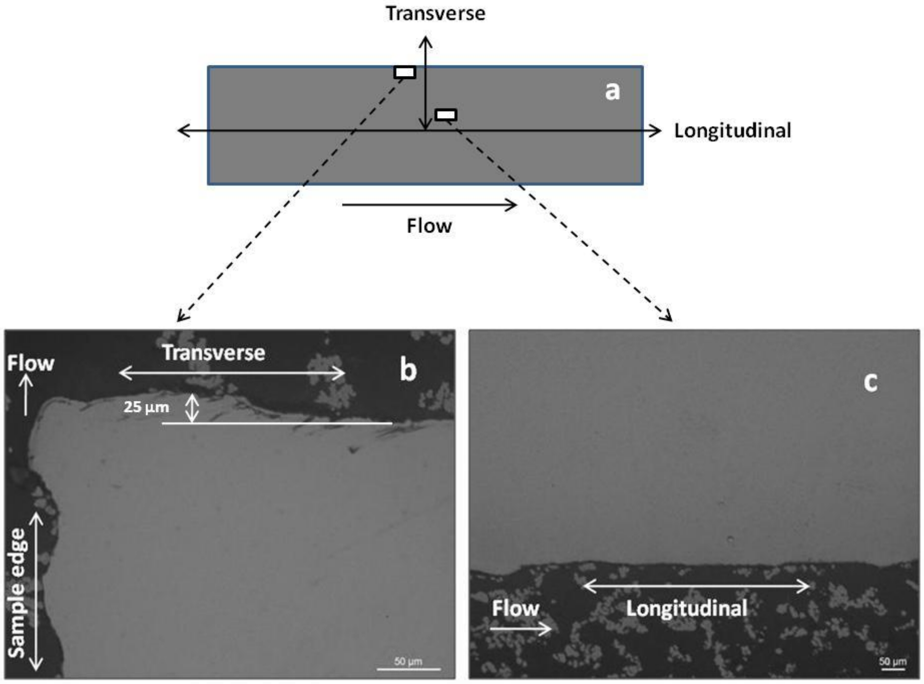

Fig. 6.1: (a) Directions of cut in transverse and longitudinal directions taken over the IN RAFMS samples exposed to Pb-Li at 773 K for 5, 000 h. (b) Optical micrograph of the exposed IN RAFMS sample along the transverse direction. (c) Optical micrograph of the exposed IN RAFMS sample along the longitudinal direction.

The flow velocity distribution along the samples has been already shown in Figure 3.22. Differences on the extent of undulations on the sample surfaces could be noticed in the two micrographs. Higher undulation in Figure 6.1(b) represents non-uniform attack which was prevalent in the transverse direction (depth of attack ~ 25 µm). On the other hand the cross-section of the sample in the longitudinal direction (Figure 6.1(c)) showed relatively lesser non uniformity thus revealing a less aggressive attack. The non uniform nature of lead-lithium corrosion has also been recorded for EUROFER 97 exposed to flowing lead-lithium [161,167]. They have attributed such attack to the non-uniform dissolution of the passive oxide scales present over the steel surface [161-162,167].

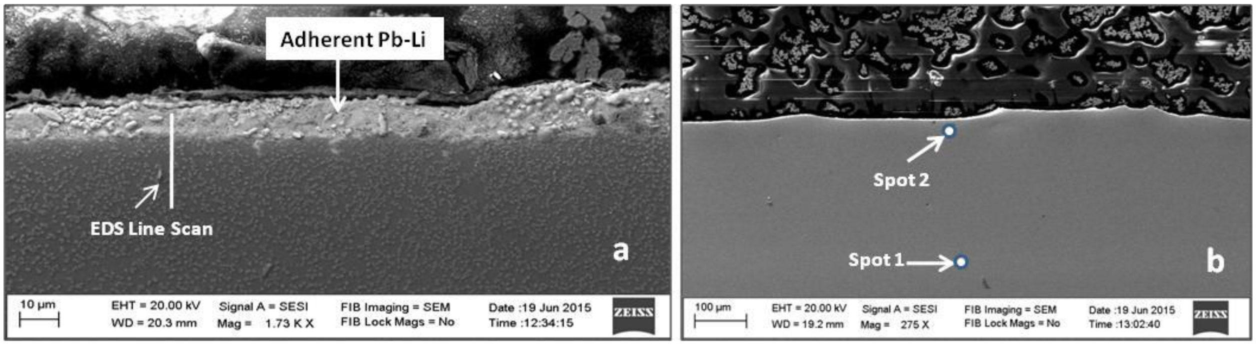

Fig. 6.2: SEM micrographs of the cross-section of IN RAFMS sample after exposure to Pb-Li at 773 K for 5, 000 h (a) before and (b) after cleaning of the solidified Pb-Li. (The dots observed over the sample matrix before cleaning are traces of Pb-Li that had got smeared during polishing).

Figures 6.2 (a) and (b) respectively show the SEM images of the transverse cross-section of exposed sample (sample B in Figure 3.20 (Chapter 3)) before and after cleaning off the Pb-Li remaining on the sample surface after solidification. The presence of this Pb-Li could be noticed as a thick bright layer over the un-cleaned sample in Figure 6.2 (a). Similar to the optical micrograph shown in Figure 6.1 (b), non-uniform surface attack could also be observed in the SEM image of the cleaned sample (Figure 6.2 (b)).

To investigate the effect of exposure of Pb-Li on the composition of the sample, an elemental line scan was taken through EDS over the cross-section of the un-cleaned sample (Figure 6.2(a)). The line scans are shown in Figure 6.3. On moving towards the sample surface, the content of iron (Fe) and chromium (Cr) remained constant until a sharp fall in the concentration of Fe was over a distance of 3-4 µm which was associated with a similarly sharp rise in lead (Pb) content. Similar observations were recorded for EUROFER 97 when the material was exposed to Pb-17Li at 753 K for 3, 011 h where the concentration Fe present in the base material EUROFER 97 was found to drop sharply within a distance of about 5 μm in the solidified Pb-17Li alloy present over the exposed sample surface [163]. Similar to the present RAFMS sample; a crossover of Fe and Pb line scans were obtained within this 5 μm distance. An identical elemental distribution was also noted for the EUROFER 97 material which was exposed to Pb-17Li in the same experimental set-up for 11, 618 h [163]. With respect to these observations, the authors have confirmed that no infiltration of lead had taken into the EUROFER 97 material due to Pb-Li corrosion.

To validate this proposition in the present case, spot EDS analysis was carried out after cleaning the RAFMS sample exposed to Pb-Li for 5, 000 h. As shown in Figure 6.2 (b), the spot for analysis was chosen very close to the sample surface, in order to establish the actual composition of IN RAFMS material near the exposed surface. The results from spot EDS analyses are listed in Table 6.2 and it was observed that lead was not present at the solid-liquid interface. These results were in agreement with those obtained for EUROFER 97 material discussed earlier [163]. However it may be noted that presence of lead was observed after 3, 000 h of exposure of IN RAFMS material to Pb-Li (Table 5.11) in RDCTF (Section 5.3.2). This was possibly because of the fact that the initial duration of exposure was characterized by grain boundary penetration of Pb-Li which may allow lead to be found present inside the grain boundaries. However, as discussed in Section 5.3.3, the corrosion mechanism changes to uniform matrix dissolution after dissolution of the passive oxide layer and therefore the lead penetration was observed in the present case.

In view of the Pb-Li adhering to the surface after solidification, it was difficult to identify the exact position of the Pb-Li-steel interface in the line scan analyses shown in Figure 6.3 However, considering the spot EDS analyses results (Table 6.2), the final position of steel- Pb-Li interface could be assigned to the point where the sharp fall of Fe concentration begins. This interface has been marked in Figure 6.3. Considering the non uniform nature of Pb-Li attack and presence of surface undulations over the exposed sample; the initial position of the pre-test sample surface may be assigned to the point where the concentration of Fe reduces to negligible value and concentration of the Pb begins to drop. However, further investigations are needed to confirm this fact.

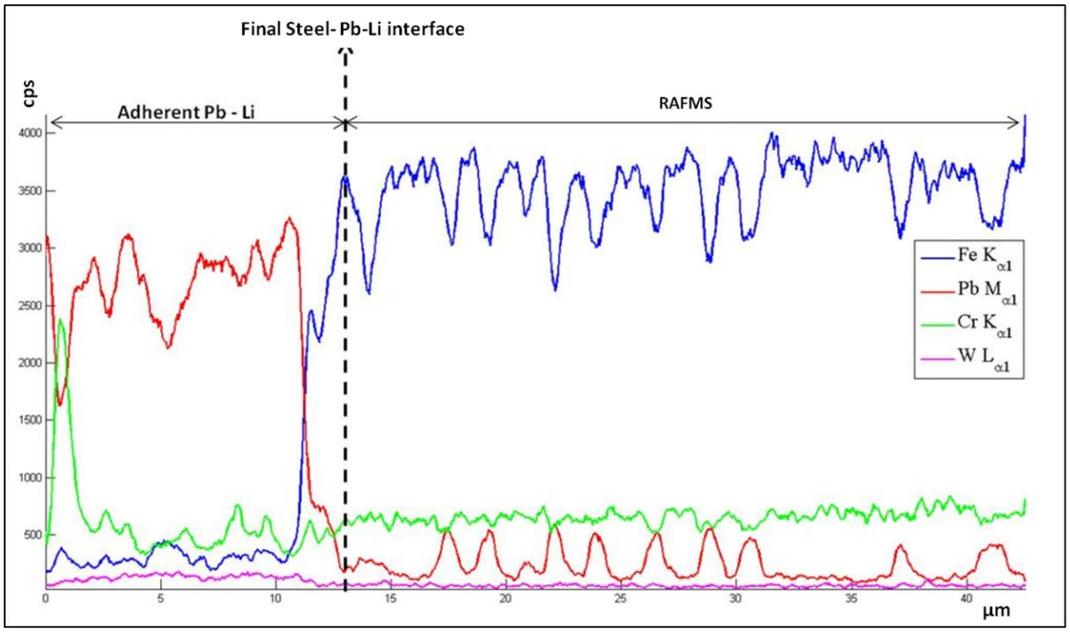

Fig. 6.3: EDS line scans of iron, chromium, tungsten and lead across the cross-section of IN RAFMS after exposure to Pb-Li at 773 K for 5, 000 h. The path of line scan is shown in Figure 6.2 (a).

Table 6.2: Composition of the RAFMS material at the inner matrix and near the top surface (interface) exposed to Pb-Li. The location of the spots are shown in Fig. 6.2 (b)

Element (wt %)	Matrix (Spot 1)	Pb-Li-Steel Interface (Spot 2)
Fe	85	70.2
Cr	9.0	9.6
Pb	-	-
W	1.1	3.6
Mn	0.7	-
V	0.3	0.2

A slight increase in chromium concentration was also noted near the exposed surface through spot EDS analysis (Table 6.2). This was possibly due to the depletion of the major component, Fe and the slower diffusivity of chromium in the steel matrix [215]. It may also be associated with matrix dissolution phenomenon which limits the depletion of alloying elements from the inner matrix (Section 5.3.3). However, the notable enrichment of tungsten at the surface was because of its very low solubility in Pb-Li and similar observations have been recorded for F82H samples exposed to Pb-17Li [161].

6.1.3. Chemical analysis of Pb-Li

Chemical analysis of the lead-lithium alloy before and after exposure in the experiment was carried out through ICP-AES in order to confirm the dissolution of major alloying elements (Cr, W) as well as to analyze the effect of exposure on the eutectic composition. For this purpose, extracts from unexposed Pb-Li alloy and from the alloy drained back to the melt tank after the experiment were used. The results of this analysis are listed in Table 6.3. The increase in chromium content in Pb-Li after exposure confirmed its dissolution from the steels matrix while no change in tungsten content showed its negligible dissolution. This also proved that the effective chromium enrichment (Table 6.2) on the surface layers was mainly due to the comparatively higher dissolution of iron (due to its higher solubility) and not an increase in the actual chromium concentration. The slight increase in oxygen concentration was possibly due to post exposure oxidation. Nickel content was found to be lesser than iron in the exposed Pb-Li alloy.

The absence of nickel in very large quantities (solubility of nickel at 773 K ~3, 000 ppm [195]) points to the fact that the corrosion of SS 316L tube surfaces (generally associated with leaching of nickel into Pb-Li eutectic) did not have a significant effect on the corrosion of RAFMS samples. A lower flow velocity along the walls of the sample holder (0.07 m/s) as shown in Figure 3.22 may be one of the factors that resulted in reduced corrosion of the SS316 L walls. Moreover, a higher geometric factor additionally ensured that the corrosion of the SS316 L tube walls did not affect the corrosion process of the IN RAFMS samples. On the other hand, since nickel was present in negligible quantity in IN RAFMS, the presence of small amount of nickel in Pb-Li (during exposure) is not expected to affect its corrosion behavior. Nevertheless, in order to minimize the interaction between the structural material of the loop and liquid Pb-Li in future, a new loop fabricated out of P91 material is under development.

Table 6.3: Chemical composition of lead-lithium alloy after 5, 000 h of exposure in EMPPIL as analyzed by ICP-AES.

Elements	Li	Cr	Ni	W	O
Before Exposure	0.63 wt %	-	5.71 ppm	<0.1 ppm	11.8 ppm
After Exposure	0.62 wt%	10 ppm	190 ppm	<0.1 ppm	20 ppm

6.1.4. Summary

1. A forced circulation loop (EMPPIL) developed to study the corrosion behavior of IN RAFM steel in flowing Pb-Li was operated for 5, 000 h at 773 K. Corrosion rates of IN RAFMS was found to be 50 µm/y at a maximum flow velocity of 1.5 m/s.
2. The corrosion rate of IN RAFMS in Pb-Li was found change with variation in local flow velocity. Corrosion rate of the IN RAFMS samples was higher (50 µm/y) at the upstream locations (exposed at ~ 1.5 m/s) as compared that obtained for samples placed downstream (47µm/y) due to reduced flow velocity (exposed at ~ (1.0 m/s).
3. The corrosion attack on RAFMS by flowing Pb-Li was found to be non-uniform in nature which resulted in the formation of surface undulations especially at regions facing higher local

velocities (for e.g. Sample edge). The maximum depth of Pb-Li attack was ~ 25 µm at 773 K for 5, 000 h of exposure to Pb-Li.

4. Corrosion of RAFMS in Pb-Li at 773 K was associated with depletion of iron and chromium and enrichment of tungsten at the exposed surface although penetration of lead was not noted after 5, 000 h of exposure which was beyond the incubation period of RAFMS.

6.2. Corrosion behavior of IN RAFMS in Pb-Li at 823 K in PICOLO

Five numbers of IN RAFMS samples were exposed to the electromagnetic pump driven forced circulation loop PICOLO installed at KIT for 8, 000 h [161]. The detailed designs of the PICOLO loop and sample geometry are discussed in Section 3.6. The temperature of exposure was 823 K (550°C) and the Pb-Li flow velocity was 10 cm/s. The details of experimental procedure and corrosion rate measurement have been described in Section 4.5.2. One sample each was taken out after every 2, 000 h for measurement of the radial material loss. The definition of "radial material loss" and its calculation procedure has been described in Section 4.5.2.c.

Figure 6.4 shows the photograph of IN RAFMS samples before and after exposure while Table 6.4 lists the data recorded for measurement of radial material loss for a single sample exposed for 4, 023 h in Pb-Li. Similar charts have been constructed for all the five IN RAFMS samples after exposure to PICOLO. It could be observed from Table 6.4 that for every sample, the diameter before and after exposure were measured at nine points along the length and at twelve turning angles. As described in Section 4.5.2.c, the radial material loss was obtained as per Equation 6.1 and corrosion rate of every sample was obtained by Equation 6.2.

Radial material loss = Final difference in diameter (average) /2 …………………….……...6.1

Radial Corrosion Rate = {Radial material loss/ Duration of exposure} x 8760……………..6.2

Figure 6.5 shows the radial material loss and radial corrosion rate plotted for every sample against their duration of exposure. The data obtained for EUROFER samples exposed to Pb-Li loop under similar conditions have been also plotted for comparison. It could be observed that radial material loss increases with the duration of exposure for both IN RAFMS and EUROFER showing continuous Pb-Li attack. However, the radial material loss and especially the radial corrosion rate after the first 550 h was much lesser for both materials as compared to that in the subsequent intervals.

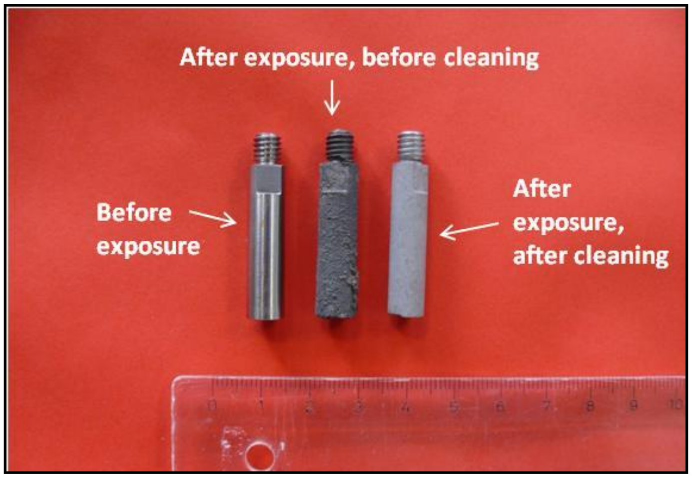

Fig. 6.4: Photographs of IN RAFMS sample before and after exposure to Pb-Li in PICOLO loop at KIT, Germany.

It is possible that this low corrosion rate is because of the passive oxide scale over RAFMS samples which prevents higher corrosion during the incubation period (before complete dissolution of oxides in Pb-Li). Similar results have also been obtained earlier for EUROFER samples exposed to Pb-Li at a temperature of 753 K where incubation period up to 1, 500 h was noted [163]. However, the incubation period has been found to depend on temperature and can come down to 500 h at higher temp of 823 K [167].

The comparison of the corrosion behavior of IN RAFMS and EUROFER was made clear in the final plot of radial material loss with duration of exposure for IN RAFMS and EUROFER which is shown in Figure 6.6. It was clearly seen that the radial material loss for both the materials went hand in hand and led to a corrosion rate of 200 µm/y. This was obtained from the intercept of the linear fit at duration of 1 year (8760 h) (Figure 6.6). Considering EUROFER as reference, it was obvious that IN RAFMS material would be satisfactorily acceptable for the fusion reactor applications from corrosion point of view. It is also observed that during the initial 500 h, the corrosion attack in IN RAFMS is lesser than EUROFER which may indicate its greater corrosion resistance during the initial periods of exposure. This may arise from a stronger oxide scale leading to a higher incubation period at 823 K. Evidence of the greater incubation period for the IN RAFMS samples have been already obtained in Section 5.3.3 in the rotating disc experiment where incubation period ≥ 2, 000 h at 823 K has been predicted.

Table 6.4: Measurement of radial material loss (µm) for the IN RAFMS sample exposed to Pb-Li in the PICOLO loop for 4,023 h at 823 K.

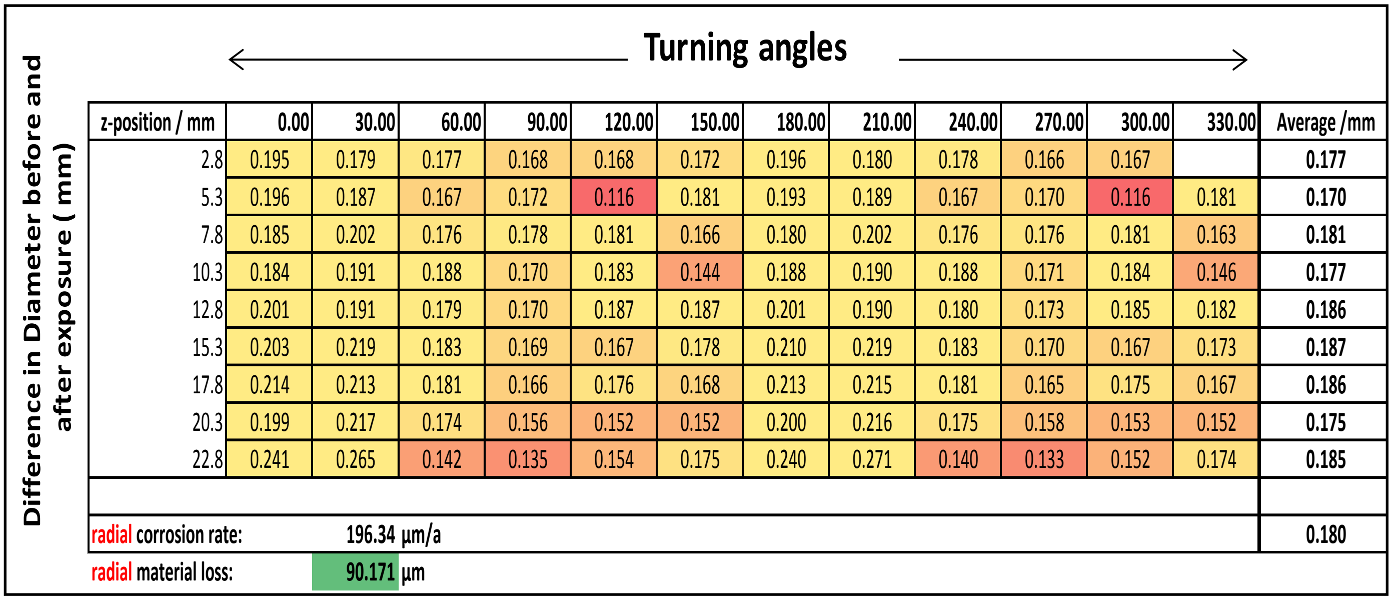

Difference in Diameter before and after exposure (mm)

Turning angles

z-position / mm	0.00	30.00	60.00	90.00	120.00	150.00	180.00	210.00	240.00	270.00	300.00	330.00	Average /mm
2.8	0.195	0.179	0.177	0.168	0.168	0.172	0.196	0.180	0.178	0.166	0.167		**0.177**
5.3	0.196	0.187	0.167	0.172	0.116	0.181	0.193	0.189	0.167	0.170	0.116	0.181	**0.170**
7.8	0.185	0.202	0.176	0.178	0.181	0.166	0.180	0.202	0.176	0.176	0.181	0.163	**0.181**
10.3	0.184	0.191	0.188	0.170	0.183	0.144	0.188	0.190	0.188	0.171	0.184	0.146	**0.177**
12.8	0.201	0.191	0.179	0.170	0.187	0.187	0.201	0.190	0.180	0.173	0.185	0.182	**0.186**
15.3	0.203	0.219	0.183	0.169	0.167	0.178	0.210	0.219	0.183	0.170	0.167	0.173	**0.187**
17.8	0.214	0.213	0.181	0.166	0.176	0.168	0.213	0.215	0.181	0.165	0.175	0.167	**0.186**
20.3	0.199	0.217	0.174	0.156	0.152	0.152	0.200	0.216	0.175	0.158	0.153	0.152	**0.175**
22.8	0.241	0.265	0.142	0.135	0.154	0.175	0.240	0.271	0.140	0.133	0.152	0.174	**0.185**
radial corrosion rate:		196.34 µm/a											**0.180**
radial material loss:		90.171 µm											

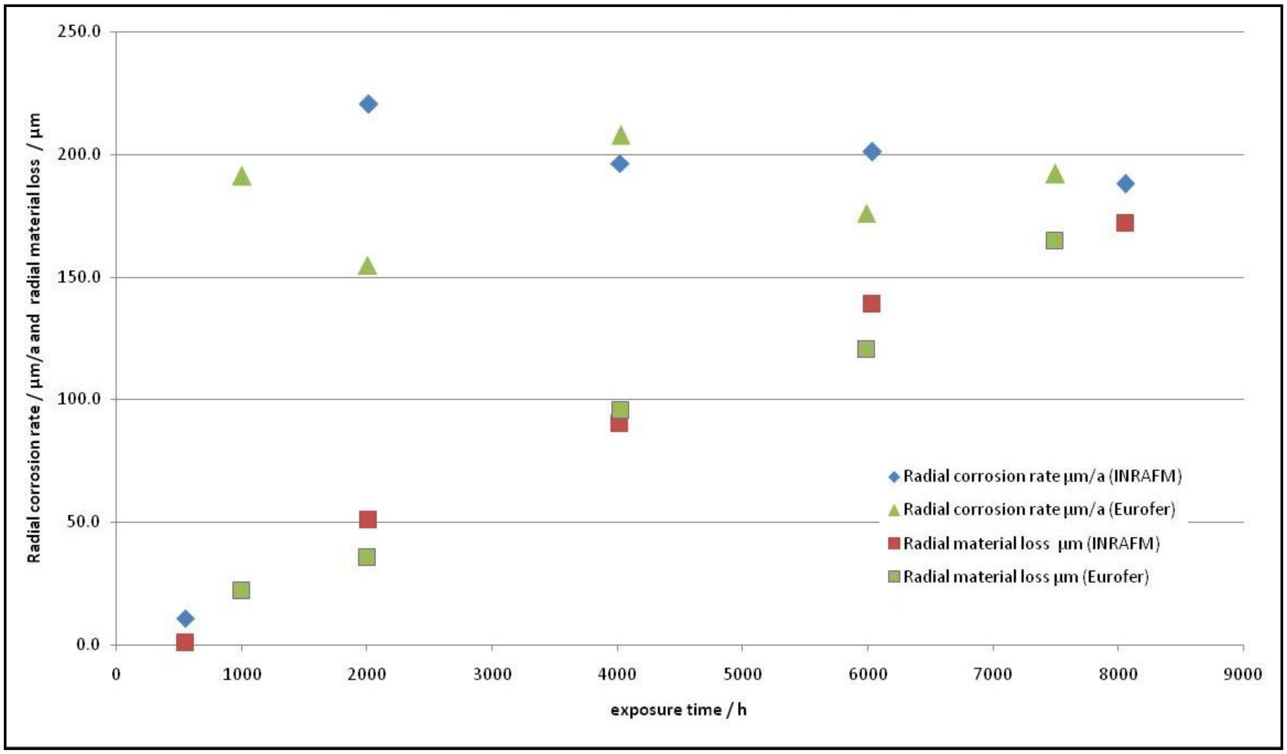

Fig. 6.5: Plot of radial material loss and radial corrosion rate of IN RAFMS and EUROFER samples against the duration of exposure in PICOLO loop at 823 K and Pb-Li flow velocity of 10 cm/s.

However, as we have earlier observed in the static and rotating disc experiment that the incubation period is characterized by grain boundary attack. This phenomenon may be accelerated in a non isothermal system like the present loop where deposition of the corrosion products may take place at cooler regions thus sustaining the corrosive capability of the flowing Pb-Li. This will give rise to a greater rate of dissolution in a non isothermal system even during grain boundary attack and may even reduce the actual span of incubation period.

Another point to be noted is that the radial corrosion rate (Figure 6.5) and the radial material loss (Figure 6.6) was found to increase significantly in the first 2, 000 h and then drop slightly afterwards. Such a decrease in corrosion rate is generally associated with decrease in flow velocity and has been observed earlier for experiments with EUROFER samples in PICOLO [181]. With increase in time of exposure, the pipe walls also start to corrode and thus the flow area is increased which leads to a reduction in flow velocity. Since corrosion attack is directly related to flow velocity (as obtained in the rotating disc experiments) the radial corrosion rate decreases after 2, 000 h in the present experiment with IN RAFMS sample [124]. This case is an example of a realistic situation in fusion reactor where such a reduction in flow velocity can take place. Therefore, it would be advisable to predict the corrosion rate in flowing systems only in terms of long term exposure data as short term exposure date (up to 500 h -1, 000 h) can lead to prediction of a much higher annual corrosion attack [181].

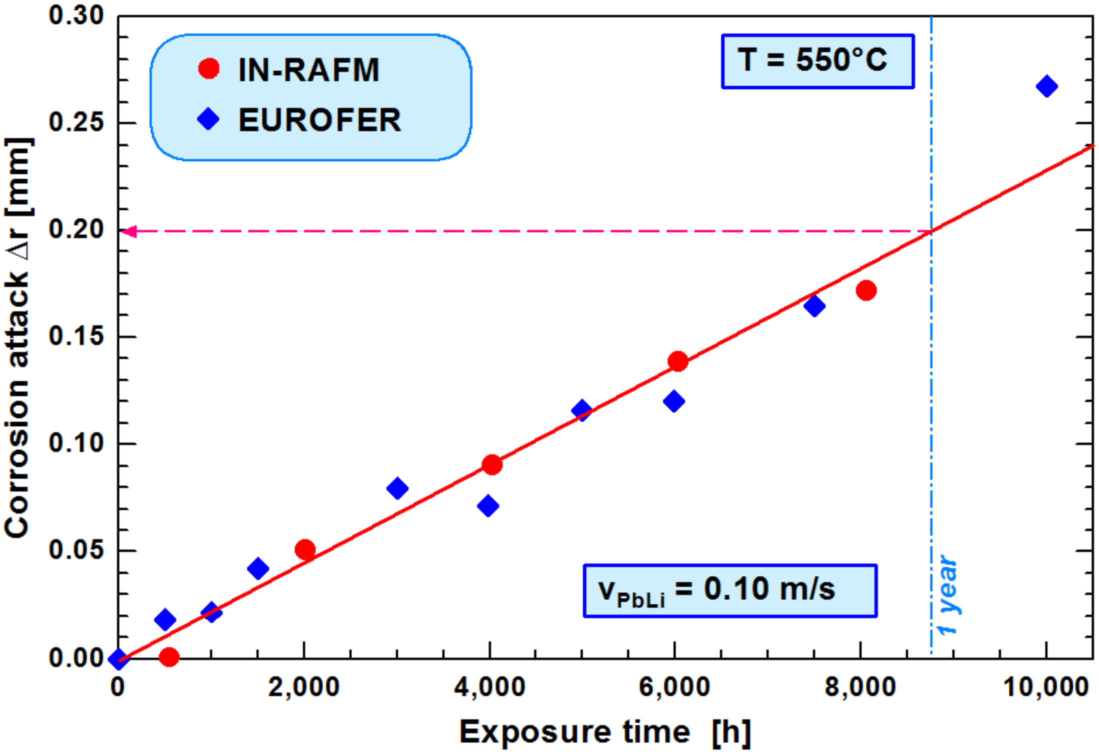

Fig. 6.6: Plot of corrosion attack/radial material loss of IN RAFMS and EUROFER samples against the duration of exposure in PICOLO loop at 823 K and Pb-Li flow velocity of 10 cm/s.

6.3. Corrosion of IN RAFMS and P91 in flowing Pb-Li in the presence of magnetic field

Since all the structural and functional materials in a fusion reactor would be subjected to high intensity magnetic field [11]; the effect of magnetic field on the Pb-Li corrosion process is an important issue to be investigated. The results obtained from corrosion experiments carried out with Pb-Li in the presence of magnetic field have been described in the following sections.

6.3.1. Effect of magnetic field on corrosion of P91 in Pb-Li at IPUL Loop

6.3.1.1. Results and Discussion

The first experiment with magnetic field was carried out in a forced circulation loop at IPUL, Latvia. In this loop, P91 samples were exposed to flowing Pb-Li at a temperature of 823 K under the effect of a magnetic field of 1.7 T. Some samples were also placed outside (i.e. before and after magnetic field) for comparison and the flow velocity of Pb-Li was 15 cm/s. The loop including its components has been described in detail in Section 3.7 (Chapter 3) while the details of the experiment have been included in Section 4.6.1 (Chapter 4). The experiment was carried out for a total duration of 1, 000 h.

Figure 6.7 shows a comparative graph indicating weight losses of all six samples from each of the three regions (i.e. before, inside and after magnetic field) as described in Figure 4.11 (Section 4.6.1). It could be clearly observed that all samples placed inside the magnetic field region experienced higher weight loss than those outside the field. This indicated that magnetic field had a pronounced effect on corrosion by liquid metals. The influence of magnetic field (1.4 T) on the corrosion behavior of austenitic and ferritic/martensitic steels in Pb-Li has been investigated earlier at 733 K. An increase in corrosion rate by 50 % in the case of austenitic steel (SS 316L) and by 30 % in the case of ferritic/martensitic steel (1.4914) inside magnetic field, have been noted [238-238]. The authors have attributed this to the liquid convection movements can occur in the thin boundary layer near the exposed surface which gives rise to high local flow velocities thereby increasing the corrosion rate [239].

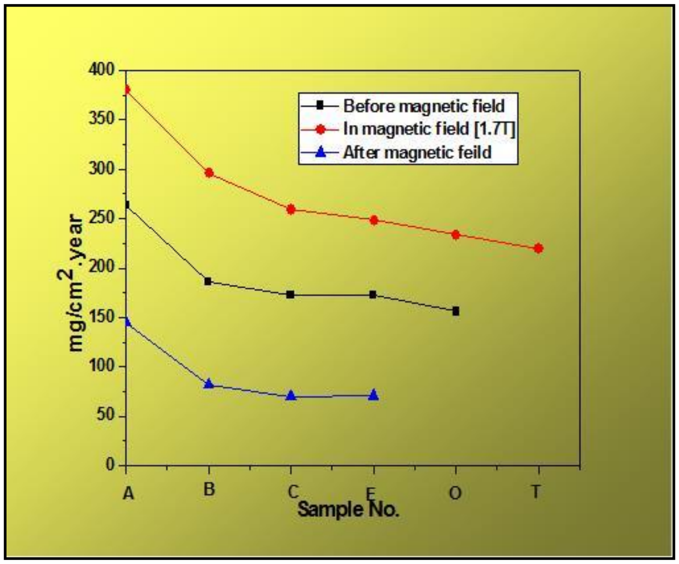

Fig 6.7: Weight Loss of P91 samples in different zones after exposure to Pb-Li at 823 K for 1, 000 h.

It was also observed that the first sample facing the flow in each region (Sample A) experienced greater weight loss than the remaining ones in that region. The different regions of the test section have been already shown in Figure 4.11. This could be possibly because of the sudden change in flow profile in the beginning of each region as observed earlier for EMPPIL (Figure 3.22). The decreasing trend of weight loss in each region was because of flow stabilization towards the end of each region. 3. Similar results were also observed when EUROFER samples were exposed to Pb-Li and magnetic field under similar conditions [182].

The sample arrangement in different regions has been described in Section 3.7. Table 6.5 lists the average corrosion rate of the samples located in the three regions i.e. Region 1(Before magnetic field), Region 2 (Inside magnetic field) and Region 3 (After magnetic field). The corrosion rate in Region 2 (Inside magnetic field) was found to be the highest (304 µm/y), whereas the rate was the lowest in Region 3. The lower rates of Region 3 (After magnetic field) as compared to Region 1 (Before magnetic field) could be attributed to the immediate saturation by the corrosion products in the Pb-Li eutectic after passing through the magnetic field zone where very high corrosion took place.

Table 6.5: Average corrosion rates of P91 samples exposed to flowing Pb-Li at 823 K in the presence and absence of magnetic field for 1, 000 h.

Location	Average corrosion rate[µm/y]
Before magnetic field ((Region 1)	213±11
Under magnetic field (Region 2)	304±20
After magnetic field (Region 3)	96±1

The morphological changes on the sample surfaces after Pb-Li exposure in the presence and absence of magnetic field was studied through stereo microscope (Figure 6.8). As observed from the stereo macrographs in Figure 6.8, the samples inside the magnetic field depicted a distinct wave-like pattern on the surface which was perpendicular to the magnetic field i.e. the Hartmann wall (Section 3.9.3)[184]. The wavy lines were specifically oriented parallel to the flow and perpendicular to the magnetic field. Such patterns were found to be absent in the samples located before and after the zone of magnetic field. According to Muktepavela [240] and Moreau [184], the interaction between the magnetic field and the flow of Pb-Li results in the generation of localized electric currents, which may produce such wave-like patterns on the specimen surface. Similar patterns were noted on the surface of EUROFER 97 samples when exposed to Pb-Li under the presence of magnetic field [182].

In order to further analyze the surface topography observed through stereo micrographs (Figure 6.8), linear profiling of samples was carried out using a Laser Profilometer. Profiles were taken at three different positions on the front and back side of each sample. The scans were taken along the longer edge at every point. The maximum values of profile amplitude (R_L) for each sample were recorded as listed in Table 6.6.

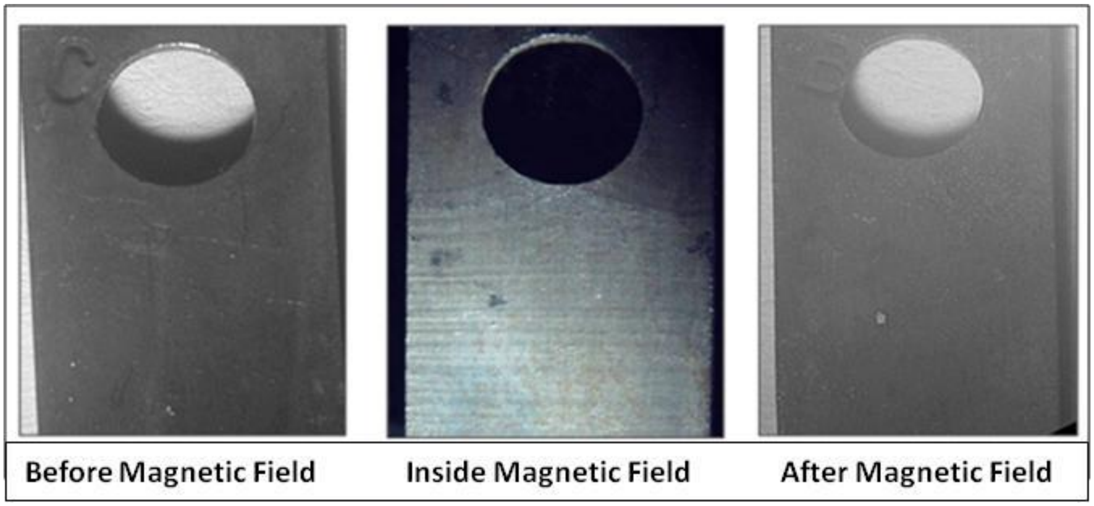

Fig 6.8: Macrographs of P91 samples in different zones after exposure to Pb-Li (Magnification: 4.5x).

An increase in surface roughness (maximum R_L) was observed after Pb-Li exposure both in the presence and absence of magnetic field. In agreement with Figure 6.8, the roughness was found to be highest for the sample placed inside magnetic field, confirming the presence of wave like structures on the surface

Table 6.6: Surface roughness of P91 samples before and after exposure to Pb-Li at 823 K.

Sample	**Maximum R_L (µm)**
As-received	3.1
Before Magnetic Field	7.1
Inside Magnetic Field	14.5
After Magnetic Field	12.0

The microstructural and compositional analysis of the exposed P91 samples was carried out with the help of SEM and EPMA respectively. For all the locations, the first sample facing Pb-Li flow i.e. Sample A (Figure 4.11) was chosen for imaging and analysis. This was because this sample had the highest weight loss as shown in Figure 6.7. The results for the samples placed before magnetic field (Region 1) were similar to those placed after it (Region 3) and thus have not been included here. Figure 6.9 (a) and (b) shows the SEM image of the surface of the P91 samples after exposure to Pb-Li in the presence (Region 2) and absence of magnetic field (Region 3: after magnetic field) respectively. In both cases, Pb-Li attack was characterized by preferential dissolution along certain lines which are most probably the grain /martensitic lath boundaries. The attack was more intense inside magnetic field as observed Figure 6.9 (a). Removal of chunks of material from within the martensite laths was also observed inside magnetic field (Figure 6.9 (a) probably indicating intra lath attack. In this regard, it may be noted that during exposure of EUROFER to Pb-Li in the presence of magnetic field, transformation of the original parent phase (tempered martensite) into fine substructures have been reported. Such phenomenon may also be a consequence of intra-lath attack [183].

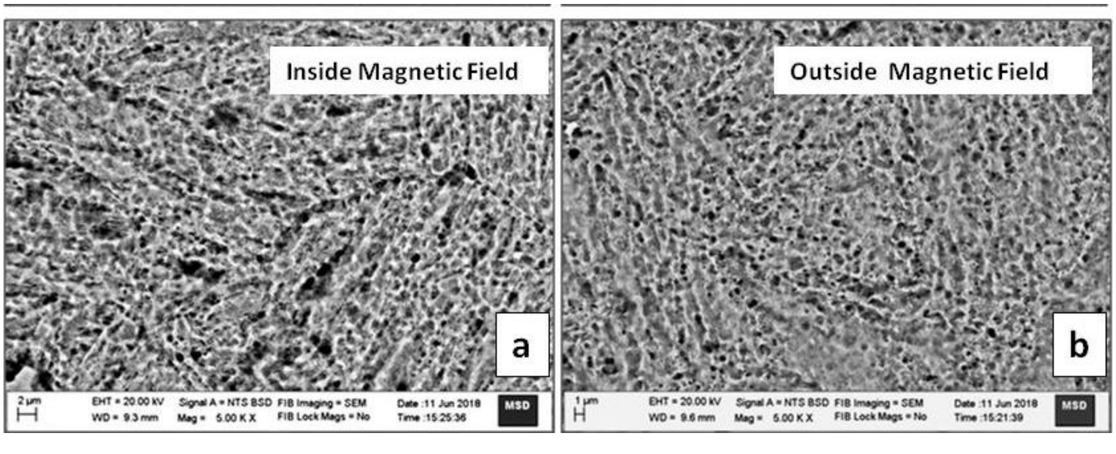

Fig. 6.9: SEM images of the surface of the P91 material after exposure to Pb-Li.

After the surface, cross-section of the P91 samples exposed to Pb-Li was investigated. For this purpose, the cross-sections were cut perpendicular to the flow direction as shown in Figure 6.10.

This was done with an intention to study the wavy lines formed over samples inside the magnetic field. Figure 6.11 (a) and (b) shows the SEM images of the cross-sections of the P91 samples located in the presence (Region 2) and absence (Region3) of magnetic field. Evidences of Pb-Li attack could be noted at both the locations. Nevertheless the attacked channels seemed deeper and mainly confined to grain boundaries in the locations outside magnetic field. On the other hand, the attack was more uniform and grain boundary penetrations were not very prominent/deep inside magnetic field. The increase in local velocity near the walls of Pb-Li carrying channels due to the presence of magnetic field have been already established [241-242]. This might have resulted in higher erosion within magnetic field which results in shallower channels of penetrating Pb-Li (Figure 6.11 (b)).

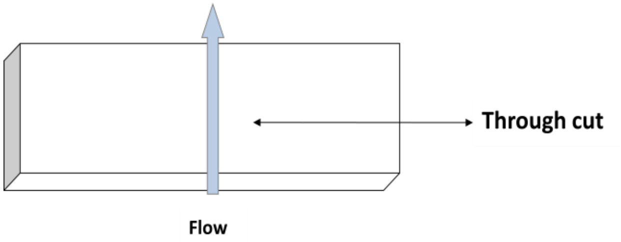

Fig 6.10: Direction of cut for specimen preparation.

The wide spaced undulations (sinusoidal pattern) observed along the cross-section of the sample inside magnetic field contained distinct crest and troughs (Figure 6.11 (b)). The crests actually corresponded to the waves observed over the exposed surface. When the entire sample was scanned, this sinusoidal pattern was observed all over the cross-section although the height and spacing between the waves differed from place to place. The maximum amplitude was observed to be 20 µm while the maximum spacing was 75µm. Similar observations were recorded for EUROFER samples when exposed to Pb-Li in magnetic field [184]. The wavy pattern observed in such case also had amplitude of 20 µm though a larger spacing of about 500 µm was observed.

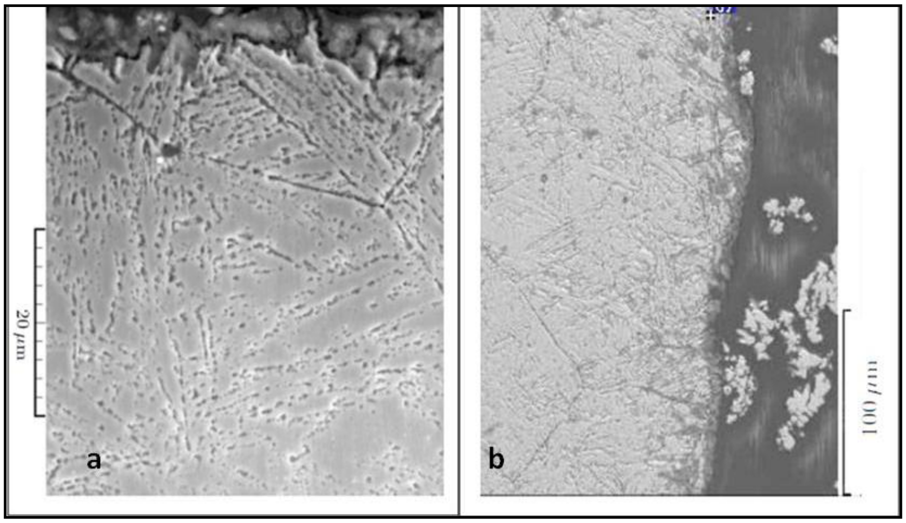

Fig. 6.11: SEM images of the cross-section of P91 samples exposed to Pb-Li in the (a) presence (Region 2) and (b) absence of magnetic field (Region 1).

For a better understanding of the corrosion mechanism, compositional profiles of Fe, Cr, Mo and Pb were taken across corroded samples of P91 with the help of EPMA. The results for the samples placed before magnetic field (Region 1) have been shown in Figure 6.12 while those for the sample placed inside magnetic field (Region 2) is shown in Figure 6.13. Since the values for Fe were much higher than those of the other elements and were difficult to adjust in the same scale therefore they have been shown in separate graphs for each region.

A significant depletion of iron up to a depth of 4 µm was observed inside magnetic field whereas the iron content remained almost constant for the sample outside magnetic field. The greater iron depletion may also lead to greater weight loss inside magnetic field since iron dissolution is the rate controlling step (Section 5.3.2). Depletion of chromium was also observed up to 4 µm from the exposed surface both in the presence and absence of magnetic field. This was accompanied by enrichment of molybdenum due to its lower solubility in Pb-Li [195]. The slight increase in nickel content on the surface was due to its dissolution from the SS316L tubes through corrosion and its subsequent deposition on P91. It was thus clear that exposure to Pb-Li in the presence of magnetic field can lead to enhanced corrosion rate which may be associated with the following reasons:-

a. Higher local flow velocities due to MHD effect.
b. Intra lath dissolution from exposed steel surface.
c. Higher depletion of iron from steel matrix.

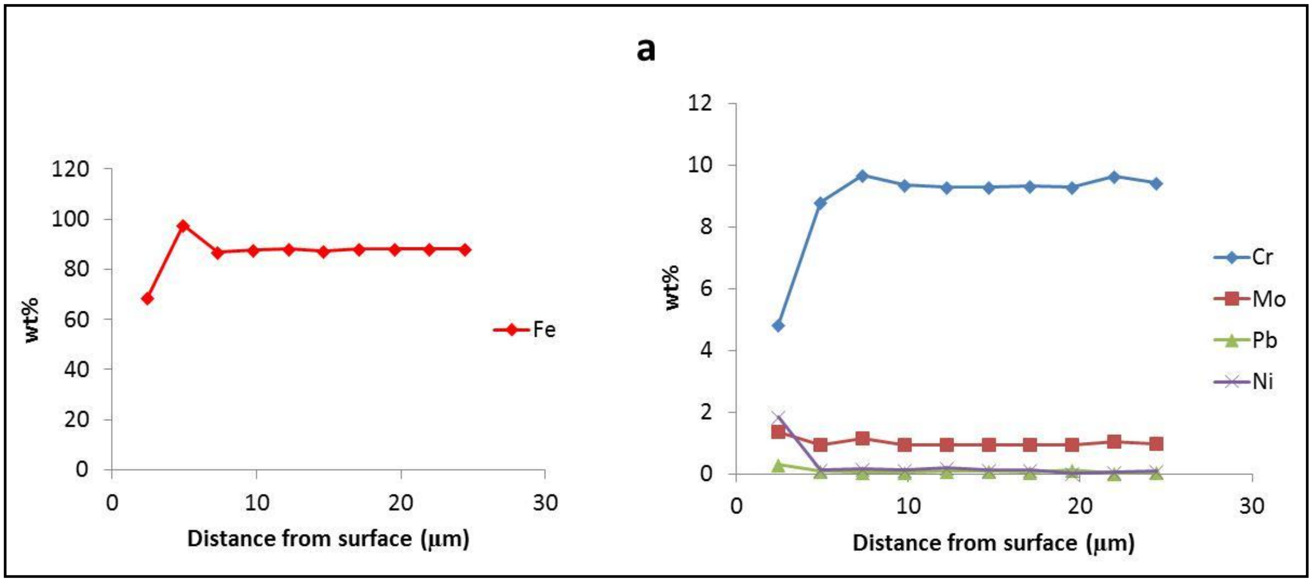

Fig. 6.12: EPMA line scans of Fe,Cr, Mo, Pb and Ni over P91 inside magnetic field.

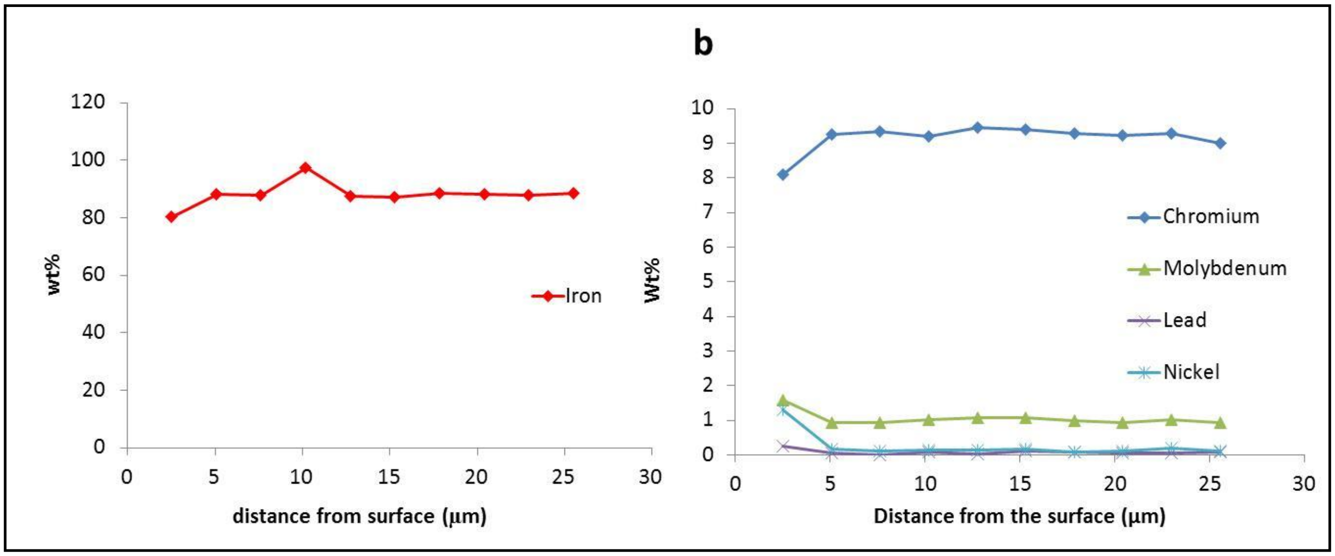

Fig. 6.13: EPMA line scans of Fe,Cr, Mo, Pb and Ni over P91 outside magnetic field.

Another point to be noted is that the higher velocities in the presence of magnetic field may also lead to a faster dissolution of the passive oxide layers. It has been already observed that the incubation period of EUROFER (which is a period of lesser corrosion due to the dissolution of passive oxide scales) depends on the flow velocity of Pb-Li [124]. Thus a faster dissolution of the oxide scales will also lead to comparatively higher corrosion in the presence of magnetic field as observed in Table 6.5. A discussion on liquid flow inside magnetic field in light of the present observations and its effect for higher corrosion has been explained later in this chapter.

6.3.1.2. Summary

a. The corrosion of P91 steel in the Pb-Li eutectic has been studied in the presence of 1.7 T magnetic field at 823 K (550°C). The value of corrosion rate was found to be 2–3 times higher in the preence of the magnetic field.

b. The sample surface inside the magnetic field showed non uniform corroison with a wave-like pattern with an amplitude of 20 μm and a wavelength <200 μm in the direction parallel to Pb-Li flow and perpendicular to magnetic field.

c. Selective dissolution of iron and chromium was found to be responsible for the degradation of P91 in the presence and absence of magnetic field although the extent of dissolution of iron was higher in the presence of magnetic field.

6.3.2. Effect of magnetic field on corrosion of IN RAFMS in Pb-Li in EMPPIL-M

6.3.2.1. Results and Discussion

After studying the compatibility of IN RAFMS with flowing Pb-Li in EMPPIL and with the experience of exposing P91 in Pb-Li within magnetic field at IPUL; an attempt was made to study the effect of magnetic field on the corrosion of IN RAFMS in Pb-Li. For this purpose, the existing EMPPIL facility (Section 3.6) was modified into a new loop called EMPPIL-M as described in Section 3.8. The procedure for testing the corrosion of IN RAFMS samples inside magnetic field in this loop have been described in Section 4.6.2 (Chapter 4). The samples were exposed to Pb-Li at a temperature of 773 K and at an average flow velocity of 1.5 m/s. After an exposure of 2, 800 h, the samples were investigated for analyzing the effect of magnetic field on the corrosion process.

As explained in Section 4.6.2 and illustrated in Figure 4.12, two representative IN RAFMS samples (one outside magnetic field i.e. Sample D and one inside the magnetic field i.e. Sample F) were chosen for the present studies. Table 6.7 shows the weight loss of the samples after exposure to Pb-Li. The sample inside magnetic field clearly showed a greater weight loss than that outside the magnetic field. Since the applied magnetic field was quite small (i.e. 0.5 T), the increase in weight loss inside magnetic field (i.e. 1.3 times) was not as high as that obtained in case of P91 samples (~ 2-3 times) where the applied field was 1.7 T. The greater corrosion attack in the presence of magnetic field was associated with the change in velocity profile of liquid Pb-Li due to Magneto-Hydrodynamic effects (MHD).

Table 6.7: Corrosion rate of IN RAFMS exposed to flowing Pb-Li at 773 K in the presence and absence of magnetic field.

Sample	Initial Weight (g)	Final Weight (g)	Weight Loss (g)	Corrosion Rate ($\mu g/cm^2.h$)	Corrosion Rate (µm/y)
Inside Magnetic Field	6.5673	6.4577	0.1084	5.0086	56.224
Outside Magnetic Field	6.3966	6.3125	0.0828	3.8089	42.71

Figures 6.14 (a) and (b) show the macrographs (recorded through stereo microscope) of the surface of IN RAFMS samples exposed in the presence and absence of magnetic field respectively. The distinct wavy pattern noted on the surface of P91 and EUROFER samples after exposure to Pb-Li in the presence of a high magnetic field of ~1.7 T was not noted in the present case [182]. The possible reason might be the lesser magnetic field i.e. 0.5 T. However, there was a marked

difference in the surface morphology of IN RAFMS in the presence and absence of magnetic field. The sample placed inside magnetic field (Figure 6.14 (a)) seemed to have a significant portion of smooth surface depicting an apparently lesser Pb-Li attack. On the other hand, the surface of the sample outside the magnetic field (Figure 6.14 (b)) looked entirely rough showing uniform attack.

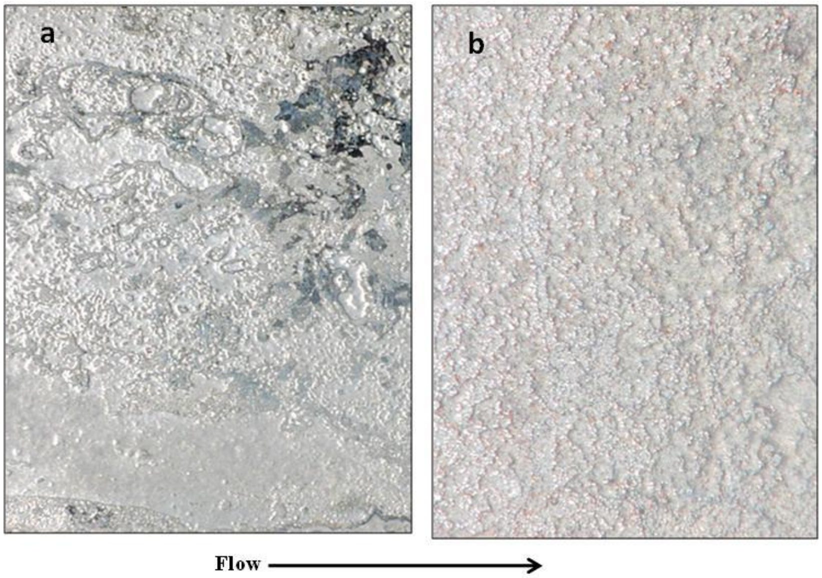

Fig 6.14: Stereo Microscope image (Mag:20x) of the IN RAFMS samples exposed to Pb-Li at 773 K (a) with and (b)without the presence of magnetic field.

Figure 6.15 (a) and (b) shows the optical micrographs of the surface of the IN RAFMS samples after Pb-Li exposure in the presence and absence of magnetic field. The formation of certain surface patterns could be observed in the presence of magnetic field possibly due to the difference in extent of attack at various locations. However, these patterns did not bear any directional similarity with the flow as observed in case of P91 shown in Figure 6.8. Nevertheless, it is expected that change of flow profile due to the effect of magnetic field must have played a major role in formation of these features on IN RAFMS [241]. For further understanding, the roughness parameters of the area denoted by the optical images shown in Figure 6.15 were studied and compared with that of an as-received sample with the help of 3 D Optical Profilometer. It may be noted that all samples were metallographically polished up-to diamond finish before exposure to Pb-Li to keep similar pre-exposure conditions. Figure 6.16 (a), (b) and (c) shows the 2 D surface roughness profile of the IN RAFMS samples before exposure, after exposure without magnetic field and after exposure with magnetic field respectively. The drastic increase in roughness after exposure to Pb-Li could be clearly noted in Figure 6.16 (b) and (c). The maximum difference in surface elevation for the exposed samples both in the presence and absence of magnetic field were almost same (~ 40 μm). However, the fraction of area with maximum elevation was much higher in the presence of magnetic field signifying localized corrosion taking place.

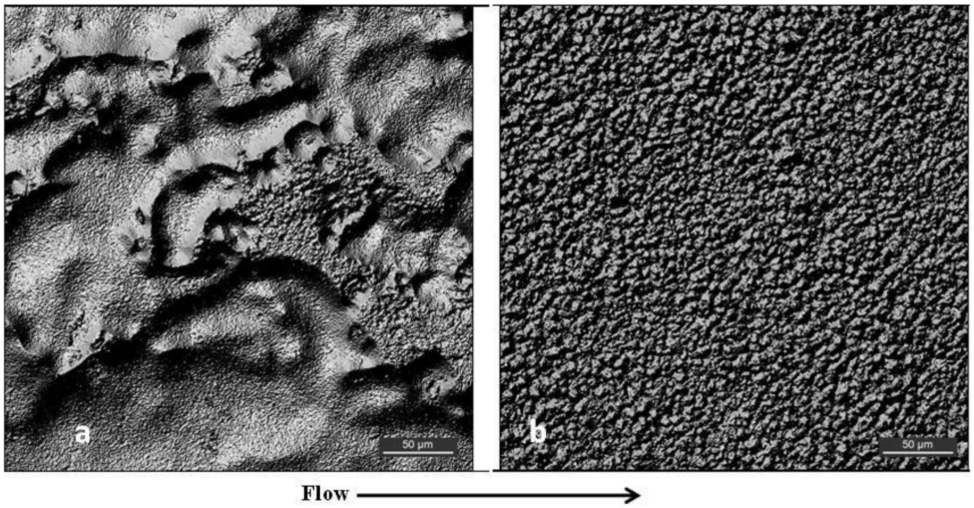

Fig 6.15: Optical image of the IN RAFMS samples exposed to Pb-Li at 773 K (a) with and (b) without the presence of magnetic field; at 20x magnification.

This means a certain part of the surface remained completely un-attacked while the other parts were getting heavily attacked. It may be possible that this pattern (in a low magnetic field of 0.5 T) might be the pre-form of the wavy lines observed in case of the P91 samples (Figure 8.2) exposed to a higher magnetic field (1.7 T). On the hand, only a few points on the surface were found to have the highest elevation in the absence of magnetic field signifying the absence of prominent localized corrosion. The greater difference in surface roughness has been also recorded for EUROFER samples exposed to Pb-Li in the presence of magnetic field [183].

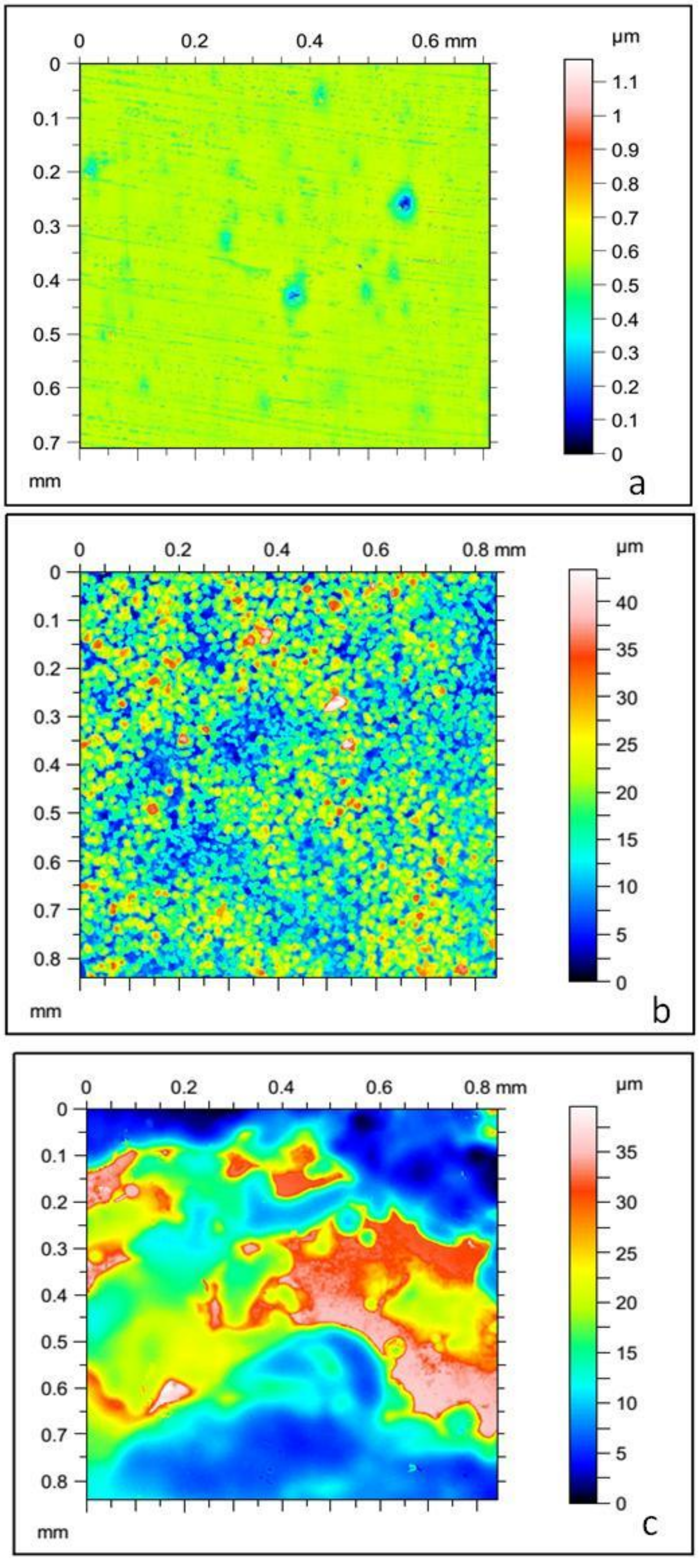

Fig 6.16: 2-D Surface roughness profiles of the IN RAFMS samples (a) before exposure, (b) after exposure without magnetic field and (c) after exposure with magnetic field.

Figure 6.17 (a), (b) and (c) shows the linear roughness profiles over the samples before exposure, after exposure without magnetic field and after exposure with magnetic field respectively. As observed in the 2-D roughness profiles in Figure 6.16, the linear roughness profiles (Figure 6.17) also showed a significant change in surface roughness after exposure to Pb-Li. It has been already observed that Pb-Li attack in the absence of magnetic field begins mostly at the grain boundaries and also depends on the non uniform dissolution of the passive oxide scales [125,163]. This can lead to formation of microscopic non uniformities over the corroded surface even in the absence of magnetic field. These finely distributed non uniformities are clearly reflected from Figure 6.17 (b) which show the surface of the IN RAFMS exposed to Pb-Li in the absence of magnetic field. On the other hand, the profile inside magnetic field (Figure 6.17 (c)) indicated the formation of a preliminary sinusoidal pattern which may intensify on exposure to higher magnetic fields [184].

Figure 6.18 (a) and (b) shows the 3 D surface roughness profile of the IN RAFMS samples after exposure to Pb-Li in the presence and absence of magnetic field respectively. The greater fraction of the un-attacked or less attacked areas was clearly seen for the sample placed under magnetic field. It was also noted that the maximum elevation was slightly lesser within the magnetic field (Figure 6.18) although the corrosion rate of this sample was higher than that outside the field (Table 6.7). This was because of the fact the regions with maximum elevation in both the samples were not un-attacked but actually less attacked. Due to corrosion / dissolution in Pb-Li, the original surface may not be present after 2, 800 h of exposure. Thus it would not be correct to correlate the maximum elevation with corrosion rate. For this reason, another parameter (Sa) was used to quantify the surface roughness. Sa can be appropriately expressed by Equation 6.3 which gives an absolute value of the difference in height of each point compared to the arithmetical mean of the surface.

$$Sa = \frac{1}{A}\iint_{A} |Z(x,y)|dx.dy \quad \text{.......} 6.3$$

Where A is the surface area and Z (x, y) is the difference of each pint with the arithmetic mean surface plane.

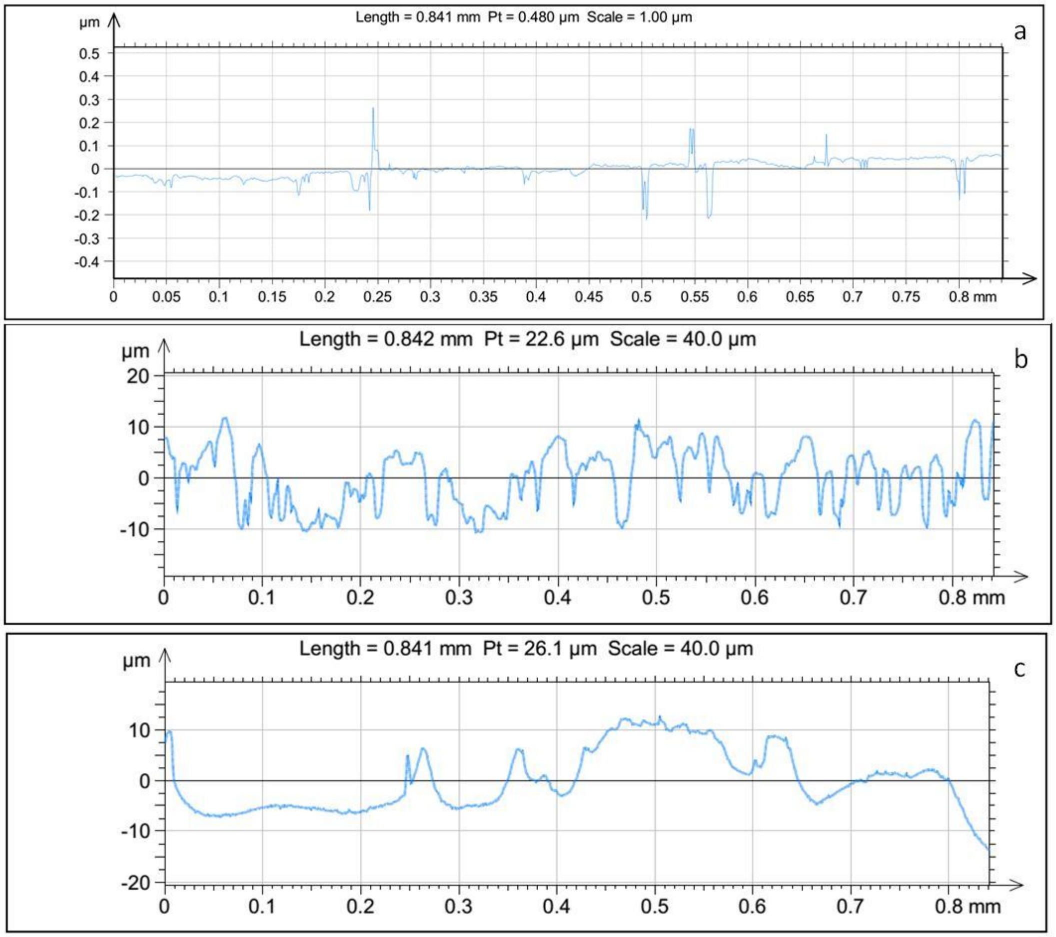

Fig 6.17: Linear Roughness Profile of the IN RAFMS samples (a) before exposure, (b) after exposure without magnetic field and (c) after exposure with magnetic field.

Table 6.8 gives the surface roughness parameter of the IN RAFMS samples before and after exposure calculated through Optical Profilometer as per standard ISO 25178 procedures. The change in “Sa” after Pb-Li exposure is evident as observed from the surface profiling results and the maximum roughness in the presence of magnetic field matches well with the higher value of corrosion rate in this region (Table 6.7). Similar results were also observed for P91 samples exposed to Pb-Li in the presence of magnetic field (Table 6.6).

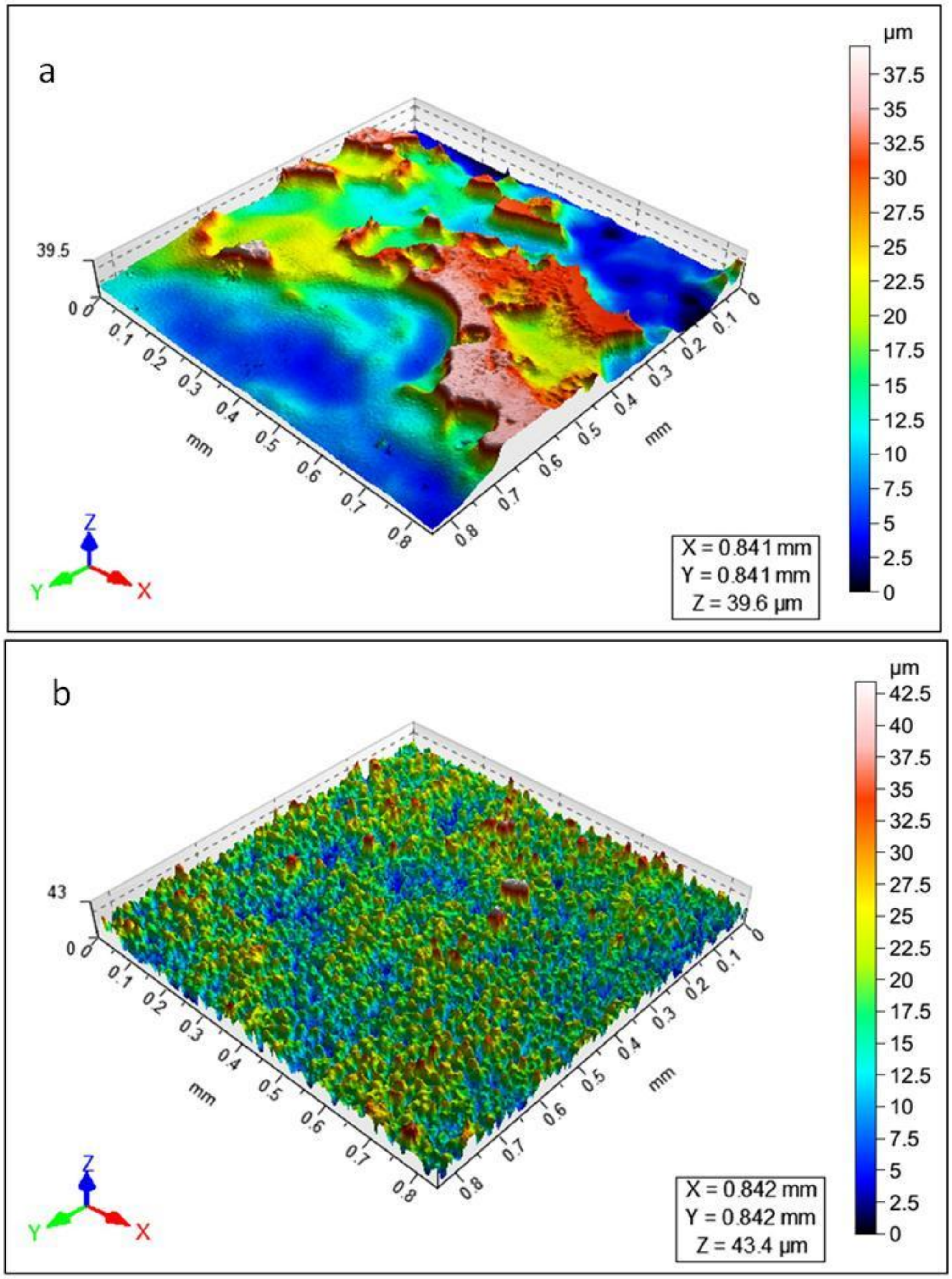

Fig 6.18 : 3-D surface roughness profile of the IN RAFMS samples exposed to Pb-Li at 773 K (a) with and (b)without the presence of magnetic field.

Table 6.8: Surface roughness of IN RAFMS samples before and after exposure to Pb-Li at 773 K.

Sample	Surface Roughness (Sa) (µm)
Before Exposure	0.03
After Exposure (With magnetic Field)	7.79
Before Exposure (Without magnetic Field)	5.23

The difference in surface features observed over the surface of the exposed samples in the presence and absence of magnetic field was prominantly revealed through SEM –EDS analysis. The SEM image of the sample exposed in the presence of magnetic field at magnifications of 100 x and 2500 x are shown in Figure 6.19 (a) and (b) respectively while those for the sample exposed without magnetic field at similar magnifications are respectively shown in Figure 6.19 (c) and (d). The difference in the extent of Pb-Li attack over the surface of sample exposed in the presence of magnetic field was clearly visible as shown in Figure 6.19 (a). On the other hand, a uniformly attacked surface was observed in the absence of magnetic field (Figure 6.19 (c)). At higher magnification, the difference in microstructure of the regions facing various extent of attack was clearly observed for the sample placed inside magneic field (i.e Figure 6.19 (b). In Figure 6.19 (b), the region with lesser attack i.e. highest elevation has been indicated by “1” and the one with higher attack i.e lowest elevation is marked by “2”.

The sample outside magnetic field (Figure 6.19 (d)) showed a clear evidence of grain boundary attack all over it’s surface revealing the martensite lath structure. When EUROFER samples had been exposed to Pb-Li, it was observed that corrosion took place predominantly via the grain boundaries in the absence of magnetic field [183]. However when a magnetic field was applied, the corrosion mechanism changed and the bulk of the steel matrix also started dissolving in Pb-Li [183]. These results were in agreement with the present results on IN RAFMS (Figure 6.19) where a distinct diffrence in the nature of attack is found in the presence and absence of magnetic field. For IN RAFMS, the sample inside magnetic field (Figure 6.19 (b)) did not show the typical grain boundary attack as observed for the sample outside the magnetic field (Figure 6.19 (d)).

In order to understand the exact nature of in Pb-Li attack in the presence of magnetic field, the SEM images of two differently attacked regions (Region 1 and 2) shown in Figure 6.19 (b) were recorded at a higher magnification (~4.5 kx). These were also compared with the SEM image of the sample placed outside magnetic field as well as that with the sample before Pb-Li exposure. All these high magnification images are compiled in Figure 6.20. Figure 6.20 (a) shows surface microstructure of the etched IN RAFMS sample under as-received condition [22-23]. Along with the typical tempered martensite structure and grain boundary carbides ($Cr_{23}C_6$), the prior austenite grain size was found lie within 8 – 15 µm. The surface of IN RAFMS after exposure to Pb-Li in the absence of magnetic field is shown in Figure 6.20 (b).

As observed earlier in Figure 6.19 (c), Pb-Li attack outside magnetic field was confined along the lath boundaries and grain boundaries which resulted in the lath matrix protruding outwards. The carbides found in the as-received sample could not be noted as well, indicating carbide dropping due to grain boundary dissolution/ attack [225]. A number of pits are also noted over the surface mostly over the lath boundaries.These were possibly the Pb-Li channels penetrating the lath boundaries perpendicular to the plane of the paper. However the pits may also be a result of dropping of the larger carbides. Formation of surface pits have also been observed in the case of JLF 1 steel when exposed to Pb-Li at 823 K [125].

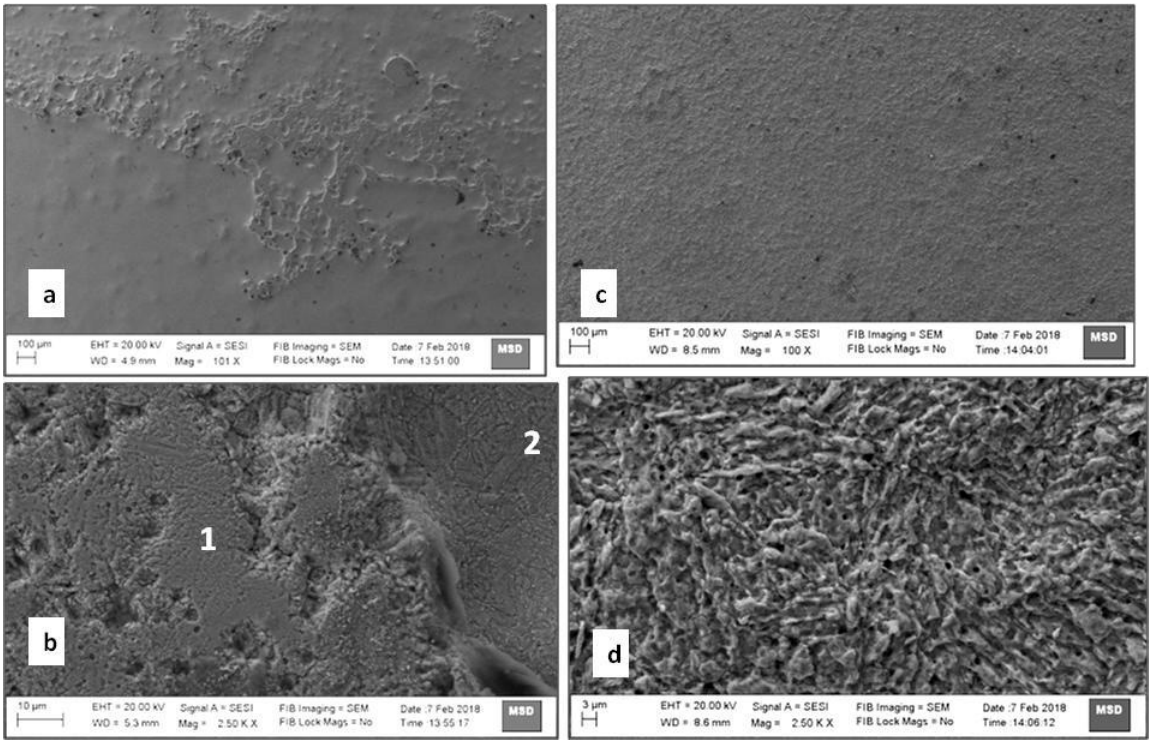

Fig 6.19: SEM images of the IN RAFMS surface after exposure to Pb-Li in the presence of magnetic field at (a) 100x, (b) 2500x and in the absence of magnetic field at (c) 100x, (d) 2500x.

Figure 6.20 (c) and (d) shows the magnified images of the diffrently attacked regions over the surface of the sample exposed to Pb-Li in the presence of magetic field which were indicated by 1 and 2 in Figure 6.19 (b) respectively. As discussed earlier; Region 1 shows the area with lesser attack and Region 2 shows the area with higher attack. This means that the Region 1 indicated the microstructure developed in the initial stages of Pb-Li attack inside magnetic field. As observed in Figure 6.20 (c), the attack in Region 1 was not only confined to lath boundries but also took place in the intra-lath regions. In fact, some of the regions seemed to have been broken into very tiny sub-grains which may have been formed due to fragmentation of the laths during intra lath attack. Such an area has been enclosed by a box in Figure 6.20 (c). A strong fragmentation of the martensite phase over the exposed surface under the combined action of Pb-Li and magnetic field has been also recorded for EUROFER samples when exposed under a field of 1.8 T for 1, 000 h [183]. The authors have confirmed that the corrosion process in the magnetic field was more intensive and involved matrix dissolution resulting in the formation of sub-structures. In that case, the sub-structural size was of 1-3 μm [183].

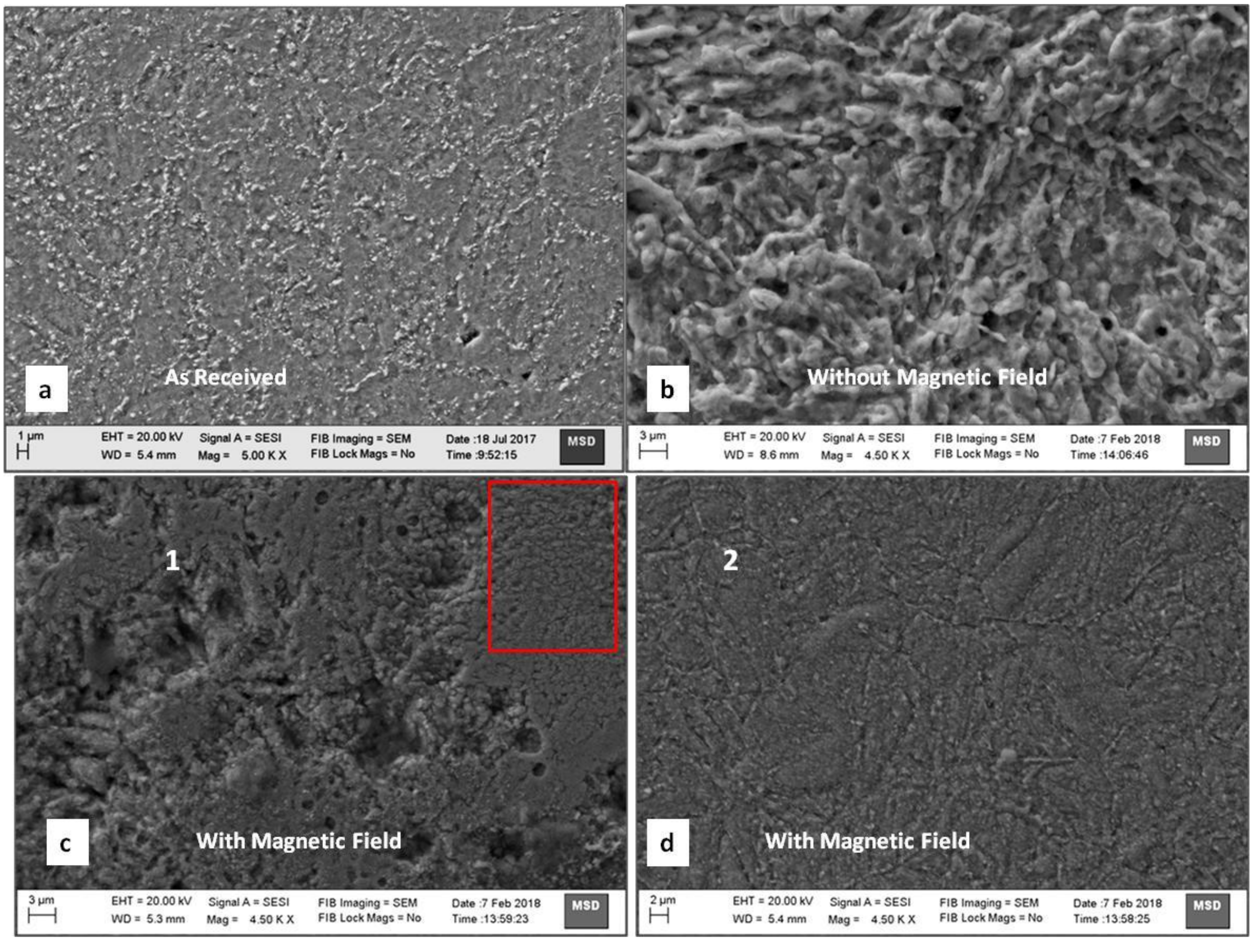

Fig 6.20 : SEM image of the surface of IN RAFMS (a) before exposure, (b) after exposure in the absence of magnetic field, (c) less attacked areas after Pb-Li exposure in the presence of magnetic field [Region 1 in Figure 6.19(c)] and (d) highly attacked areas after Pb-Li exposure in the presence of magnetic field [Region 2 in Figure 6.19(c)].

In Region 2 (Figure 6.20 (d)); the parent microstructure in IN RAFMS was revealed with prior austenite grain size similar to the as-received structure shown in Figure 6.20 (a). The density of grain boundary carbides was less as compared to an unexposed sample which indicated initiation of grain boundary attack. It was possible that this part of the surface had been freshly exposed after the top surface layers above it (containing fragmented grains as observed in Region 1) were washed away by flowing Pb-Li.

In order to know whether the formation of various surface structures were also associated with any difference in composition created by Pb-Li attack, the average compositions of the regions shown in Figure 6.20 were recorded through EDS. Table 6.9 lists the contents of major elements detected in EDS analysis for the IN RAFMS samples placed inside and outside magnetic field and also includes the composition of as-received sample for reference. It was observed that depletion of Fe was predominant in the presence of magnetic field while depletion in chromium content took place outside it. The enrichment in chromium inside magnetic field was possibly due to a comparitively greater decrease in iron content since the EDS ananlysis takes normalized values into account.

Since the contenet of Ni in IN RAFMS was negligible, it is expected that the source of this Ni lies in the corrosion of the SS 316L tube walls [182]. However, the greater deposition of Ni over the sample surface in the presence of magnetic field was possibly due to the higher corroion of SS316 L tube walls in this location due to increase in local flow velocities [237]. On the other hand, greater depletion of Fe in the presence of magnetic field might also be associated with its extensive ferro-magnetic charachteristics as observed in the case of P91 (Section 6.3.1.1). Nevertheless, no major variation of composition was found over the different regions of the sample surface exposed to Pb-Li inside the magnetic field. This indicated the fact that the variation in Pb-Li attack at different regions in the presence of magnetic field was associated only with the higher local flow velocities and not with any change in the dissolution rate of alloying elements.

It was therefore clear that Pb-Li attack on IN RAFMS was more intense inside magnetic field causing both inter and intra lath corrosion. This was associated with a greater dissolution of iron. Moreover, the extent of attack was different at different regions which may have caused faster detachment of the regions with higher attack into the flowing Pb-Li. The detachment of weaker surface layers after attack led to the exposure of fresh surfaces and further attack. Therefore, a continous proscess was established and the non uniform attack was sustained over the entire period of exposure. It was highly possible that under higher magnetic fields like 1.7 T, this phenomenon could give rise to wave like structures as observed in the case of P91 and EUROFER [182].

Table 6.9 : Content of major elements detected over the surface of the IN RAFMS samples before and after exposure to Pb-Li at 773 K in the presence and absence of magnetic field.

Locations/ Elements (wt%)	As-received (Fig 8.15 (b))	Outside Magnetic field (Fig 8.15 (b))	Inside magnetic field (less attacked) (Region1 in fig 8.15 (c))	Inside magnetic field (more attacked) (Region1 in fig 8.15 (c))
Fe	87.9	87	75.1	74.5
Cr	9.5	5.8	11.1	10.6
W	1.5	1.9	1.9	1.7
Ni	0.1	2.7	8.5	10.3

It may be noted that, even in the absence of magnetic field, non uniform dissolution of oxide layer in Pb-Li may gives rise to surface non uniformities. However in that case, the exposed surface morphology at various non uniformly attacked regions would be similar (as observed in Chapter 5 (Figure 5.40) and not different like that for the present sample placed inside magnetic field (Figure 6.20 (c) and (d)).

The diffrences in mode of attack inside and outside magnetic field was also confirmed from the analysis of the cross-section of the exposed samples. It may be noted that the cross-section was cut normal to the length of the samples as demonstarted in Figure 6.21 since the Pb-Li flow was along their length only. This was in order to take in to account all local non uniformities which may be created due to changes in Pb-Li flow pattern inside magnetic field.

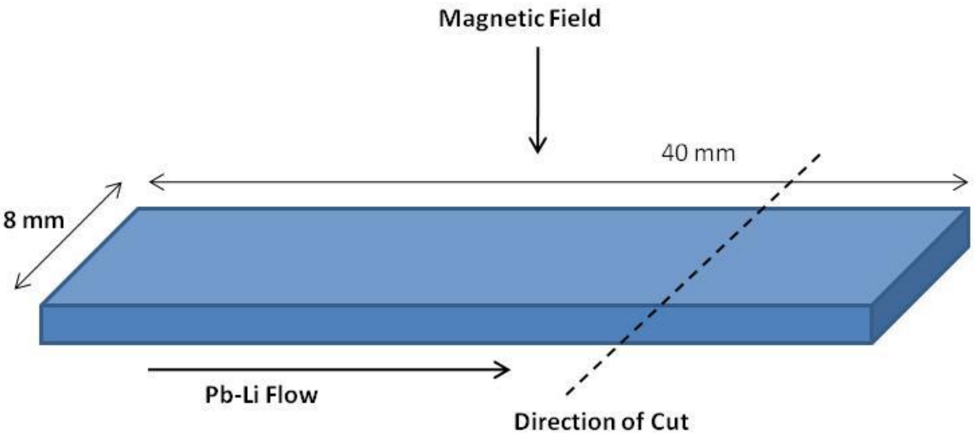

Fig. 6.21 : Direction of cut taken on IN RAFMS sample for study of cross-section.

Figure 6.22 (a) and (b) shows the cross-section of the IN RAFMS sample after exposure to Pb-Li in the absence and presence of magnetic field respectively. The inset in Figure 6.22 (a) shows the high magficication image of the sample placed outside magnetic field. Signatures of Pb-Li attack / penetration could be noted from the non uniform surface in both the samples. However, the greater intensity of corroison attack in the presence of magnetic field was clearly revealed by comparing the width and depth of the regions with maximum attack observed in both the samples. Outside the magnetic field (i.e. Figure 6.22 (a)), the Pb-Li penetration was found to be upto 22 µm and the maximum width of an attacked zone was around 40 µm. The nature of attack gave an impression that it was a result of grain droping as observed for the rotating disc experiments in Section 5.3.3.2 (Figure 5.44).

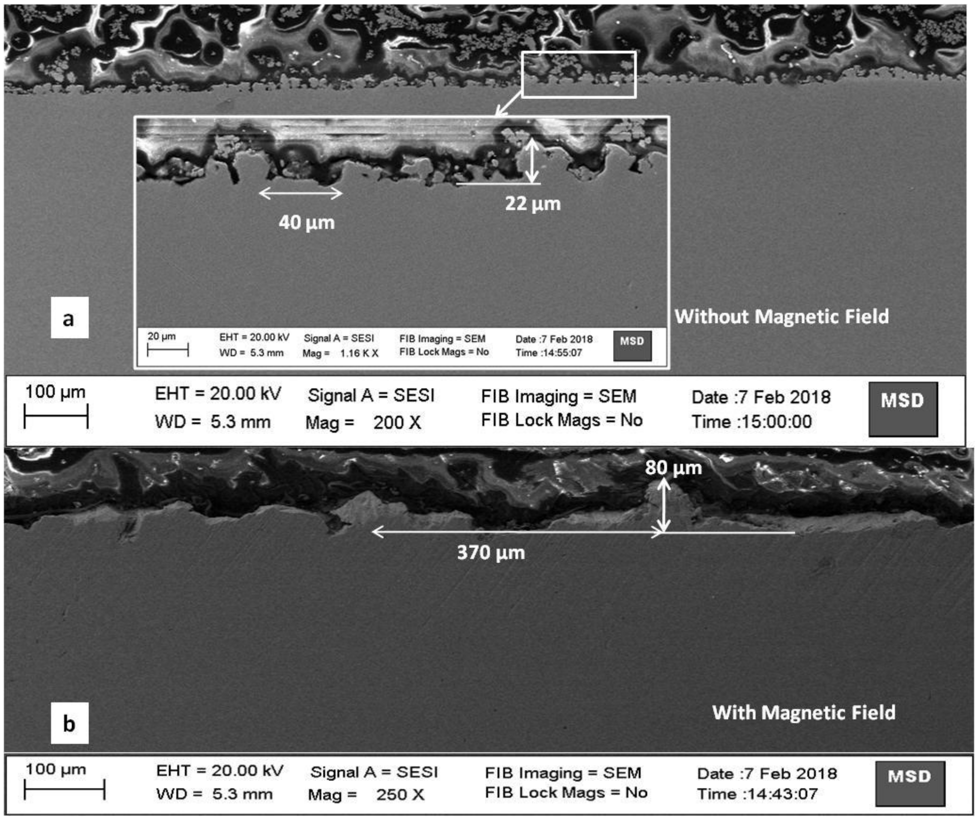

Fig. 6.22: Cross-sections of IN RAFMS samples exposed to Pb-Li in the (a) absence and (b) presence of magnetic field.

In the presence of magetifc field, the maximum depth of attack increased to 80 µm while the width of the greatly attacked zone went up to 370 µm. Although some evidence of grain boundary penetration was also observed inside magnetic field, but the higher intensity (depth and width) of Pb-Li attack was definately due to some additional factors. These were most associated with increase in local flow velocities which may have resulted in removal of large chunks of material at particular locations [241, 243]. This observation complemented the differently attacked zones observed over the surface in the presence of magnetic field in Figure 6.19 (b) and may indicate the formation of wavy pattren at higher magnetic fields [182].

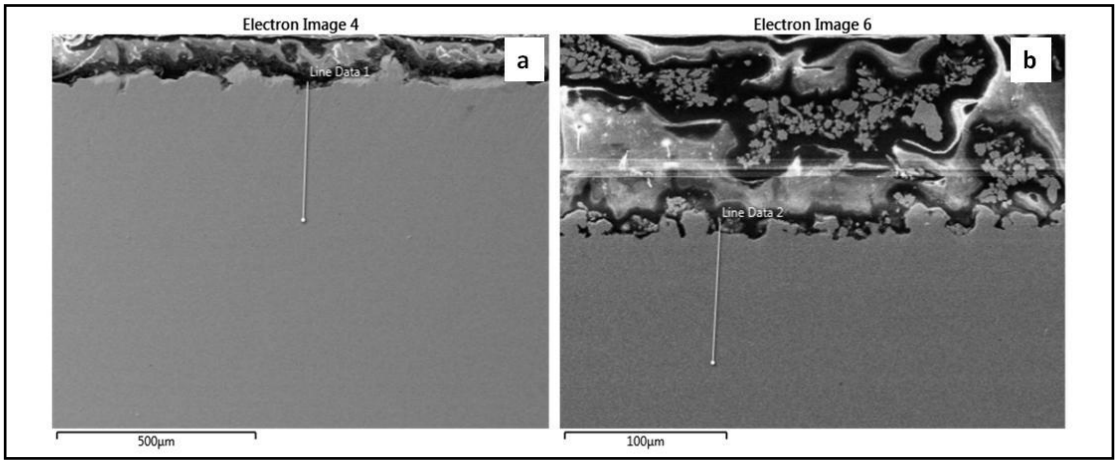

Fig. 6.23: Path of EDS line scans across the cross-sections of the IN RAFMS exposed to Pb-Li in the presence and absence of mangetic field.

It has been already observed through compositional analysis of the exposed surface that the contenets of Cr and Fe varied in the presence and absence of magnetic field (Table 6.9). To know the depth of this compositional variation, EDS line scans for iron, chromium, and lead were taken across the cross-sections of bothe IN RAFMS samples placed inside and outside the magnetic field. Figure 6.23 (a) and (b) shows the path of the line scans taken over the cross-sections of the samples placed inside and outside mangetic field while Figure 6.24 (a) and (b) shows the corresponding line scans. The location of the exposed surface has been indicated by a line marked " Steel-Pb-Li Interface" in Figure 6.24.

It was clearly observed that the sample inside magnetic field underwent depletion of both iron and chromium upto a depth of around 15 µm from the exposed surface. In fact the depletion of iron inside magnetic field was found to occur almost a depth of ~20 µm. On the other hand, although the sample outside magnetic field depicted chromium depletion, the iron content remained almost constant upto the exposed surface. The depth of Cr depletion outside magnetic field was also around 16 µm (similar to that inside magnetic field). The slight increase in iron content after the interface in Figure 6.24 (b) was due to the presence of a small chunk of steel in the mount which might have detached from the surface due to corrosion. Lead penetration was not observed in the IN RAFMS matrix for either of the samples. It may be noted that the compostional profiles recorded through EDS were plotted with actual value and thus the chromium enrichment noted in Table 6.9 for the sample inside magnetic field was not noted in the present case.

The compositional profile in the presence of magnetic (Figure 6.24 (b)) field clearly showed significant depletion of iron along with the general depletion of chromium. Similar results were also observed for P91 in our earlier experiment (Figure 6.12). Since iron dissolution was the rate controlling step for Pb-Li attack, the greater depletion of iron in the presence of magnetic field could have made the IN RAFMS matrix sufficiantly weaker thus allowing it to easily to get dislodged/dissolved in flowing Pb-Li [225]. It has been discussed in Section 5.2.3 that due to the slower diffusivity of chromium in the steel matrix and higher diffusion of the same through the Pb-Li boundary layer, a chromium depleted zone is genrally formed below the exposed surface of RAFM steels even under static conditions [125, 215]. This condition of chromium depletion was reflected for the sample ouside magnetic field in the present case. However in the presence of magnetic field, it was highly possibly that the magnetic forces of attarction acting on the iron diffusing out through the Pb-Li boundary layer made it travel faster causing an increase in its dissolution and formation of a prominant iron depleted zone. Moreover in the presence of magnetic field, the higher local velocities close to the exposed surface also resulted is faster take off of dissolved iron as well as chromium and thus could have accelarated their general dissolution in to Pb-Li (Section 2.9). Therefore there might be localised increase in dissolution rate of both iron and chromium in the presence of magnetic field as have been also reported in the case of EUROFER [183].

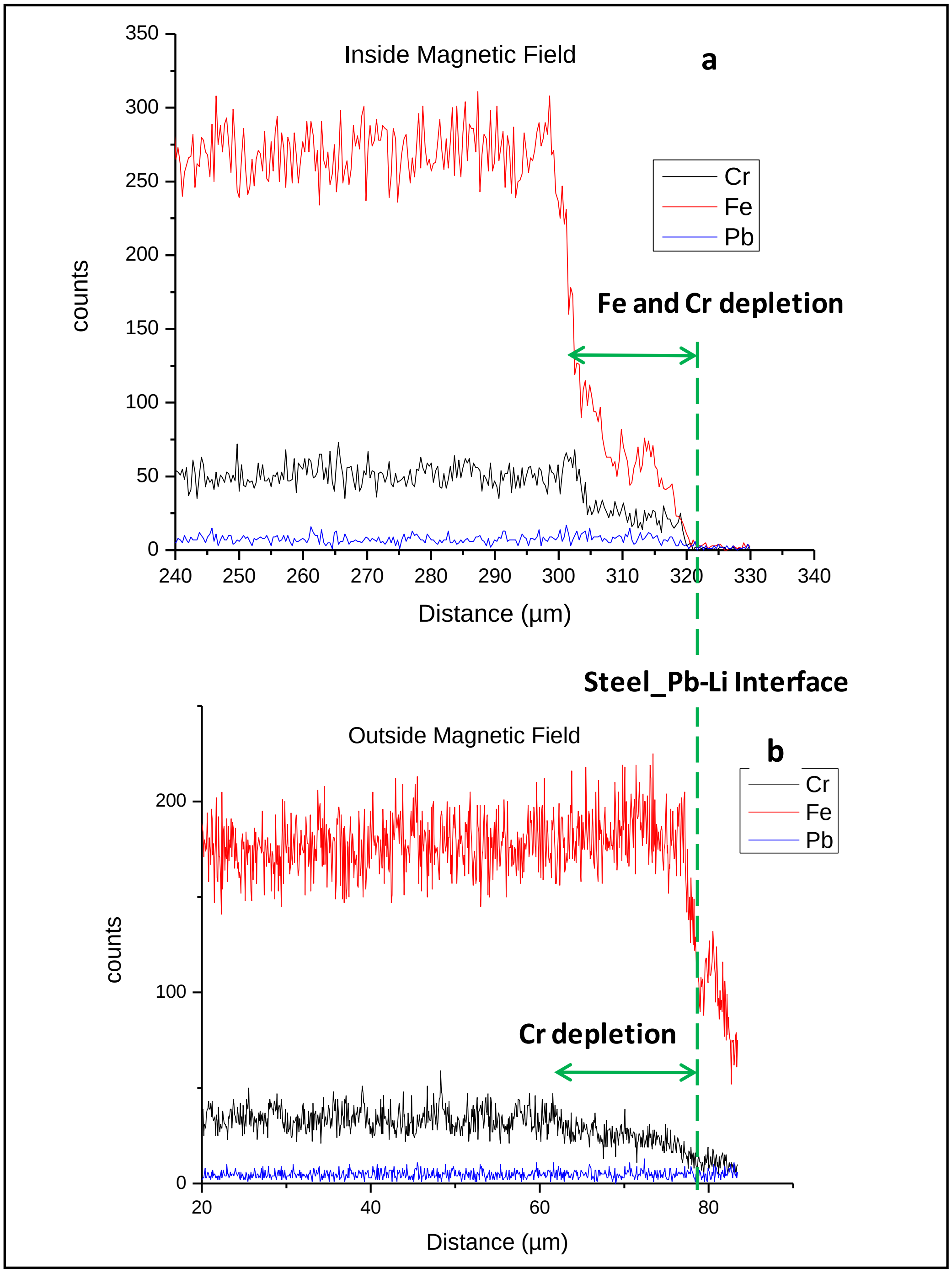

Fig. 6.24: Compostional profiles of iron, chromium and lead over the cross-sections of the IN RAFMS samples exposed to Pb-Li in the (a) presence and (b) absence of magnetic field.

Since iron constitutes almost 90% of the IN RAFMS matrix, the aforesaid local changes in it's dissolution, may also be responsible for formation of surface patterns in the presence of magnetic field. However, the actual reason for higher iron dissolution in magnetic field may involve in-depth analysis of the Magnetohydrodynamic (MHD) effects as well as the interaction of iron with magnetic field as will be discussed in Section 6.3.3 [184].

6.3.2.2. Summary

a. The corrosion of IN RAFMS in the Pb-Li eutectic has been studied in the presence of 0.5 T magnetic field at 773 K. The value of corrosion rate was found to be 1.3 times higher in the presence of the magnetic field.

b. The sample surface inside the magnetic field showed non uniform corroison along with the formation of distinct regions having different surface morphology. However, the wave-like pattern formed in the case of P91 exposed to higher magnetic field was not observed.

c. The Pb-Li attack in the presence of magnetic field was not only confined to the prior austenite and lath boundaries as in the absence of magnetic field but also took place in the intra-lath regions causing formation of sub-grains.

d. Dissolution of iron and chromium was found to be responsible for the corrosion of IN RAFMS. However the dissolution of iron was found to much higher in the presence of magnetic field .

6.3.3. Role of magnetic field in enhancing corroion attack

It has been proved through Magnetohydrodynamics (MHD) that magnetic field causes a change in flow distribution when a conductive fluid is flowing inside it [241]. This has also been discussed in Section 3.9.3. However, the exact nature of flow pattern developed inside magnetic field in the present case is beyond the scope of this study and will be taken up later. Neverthesless, a possible explanation for higher corrosion has been given by R. Moreau considering the experimental results of the EUROFER samples exposed to Pb-17Li in the forced circulation loop at IPUL, Latvia under a magnetic field of 1.8 T [184]. Figure 6.25 (a) and (b) shows surface and cross-section of these EUROFER samples depicting the wavy pattern formed under magnetic field.

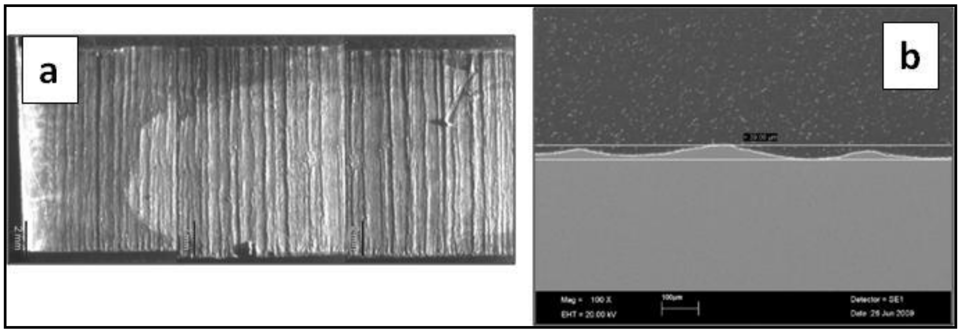

Fig. 6.25: (a) Waves on the surface and (b) Sinusoidal pattern on the cross-section EUROFER sample in the presence of Pb-Li and magnetic field [184].

The corresponding paper [184] reports that an electric current, which short-circuits the humps within the wall (slightly more electrically conducting than the fluid), contributes to the corrosion by a mechanism, which they call electro-dissolution. This has no connection with the initial development of humps and it has been said that a general corroded surface is always slightly irregular and the wavy nature as seen in the present case develops extremely slowly through continued electro dissolution over these areas. In the absence of magnetic field, the net flux of a species from solid into the liquid is dependent on the chemical potential difference. However, in the presence of magnetic field, an additional bias due to a difference in electric fields (created by the applied magnetic field) may occur across the solid-liquid interface (causing generation of electric currents as described above). This bias/force will then act on the diffusing species with an effective charge Ze, causing further dissolution to take place. Thus, an additional electro-dissolution flux is superimposed to the chemical dissolution flux which also gives rise to electro dissolution. The paper introduces two new dimensionless numbers to characterize the process i.e. Dissolution Number (Given by Equation 6.4) and Electro-dissolution number (Given in Equation 6.5)

Dissolution Number (Di*)* = $\left(\frac{Vs}{Uo}\right)\left(\frac{d\Box}{KT}\right)$.. 6.4

Electro-dissolution Number (E_d) = $\left(\frac{\mathrm{Ci}}{\mathrm{Ceq}}\right)\left(\frac{\mathrm{P}}{\mathrm{Ha}}\right)\left(\frac{\mathrm{D.Ze.B}}{\mathrm{KT}}\right)$..6.5

Where B is the applied magnetic field, P stands for Diffusion Péclet number, V_s and Uo are the modified and original velocities respectively. The means that the change in velocity due to the effect of magnetic field will affect the normal dissolution flux while the magnitude of the applied magnetic field (reflected by Hartmann no, Ha [241]) will affect the electro dissolution causing a high corrosion rate. It is obvious that due to its ferromagnetic nature, iron will be the most affected element in the electro-dissolution process. The results obtained on the effect of magnetic field on the corrosion of IN RAFMS and P91 in Pb-Li in the present study could thus be explained in similar lines as above.

CHAPTER 7

SUMMARY

7.1. Factors affecting the corrosion of IN RAFMS and P91 in Pb-Li

The corrosion of IN RAFMS and P91 material has been studied in molten Pb-Li under various conditions of temperature, flow and magnetic field, as described in Chapters 5 to 8. Such studies have been carried out in various test facilities which have generated corrosion rate data depending on the conditions imposed. The four major conditions which were created in order to study the corrosion phenomenon were:-

1. Isothermal static (conducted in Static test facility)
2. Isothermal rotating (conducted in Rotating Disc Corrosion Test Facility (RDCTF))
3. Non isothermal flowing Pb-Li (conducted in Liquid Metal Loops)
4. Non isothermal flowing Pb-Li with Magnetic field (conducted in Liquid Metal Loops)

Table 7.1 is a cumulative database of corrosion rates obtained for IN RAFMS material under different operating conditions investigated in the present work while Table 7.2 lists similar data for P91.The results obtained under specific conditions have been already discussed in Chapters 5 and 6. A comparison of the corrosion rates values listed in Tables 7.1 and 7.2 clearly indicates the effect of material composition, temperature, flow velocity, temperature gradient and magnetic field of the corrosion tack by Pb-Li.

7.1.1. Effect of material composition on corrosion rate

Studies under static condition revealed for the first time that IN RAFMS was more resistant to Pb-Li attack than P91. This was shown from the significant corrosion rate obtained for P91 samples exposed to Pb-Li at 773 K (8.64 μm/y) and 823 K (18.62 μm/y) as compared to the negligible weight loss of IN RAFMS under similar conditions (short term experiments up to 355 h).

Table 7.1: Corrosion Rates of IN RAFMS in Pb-Li under different operating conditions.

Expt . No	Mode	Material of Holder	Sample Geometry	Temp (K)	Velocity (m/s)	Duration (h)	Corrosion Rate	
							$\mu g/cm^2$. hr	µm/y
1.	Static	SS 316 L Crucible and Mo Holder	Flat (12mm x 20mm x 3mm)	773 K	-	355	Nil	Nil
2.	Static	SS 316 L Crucible and Mo Holder	Flat (12mm x 20mm x 3mm)	823 K	-	355	Nil	Nil
3.	Rotating	Mo Crucible and Holder	Disc (60 mm dia, 8 mm thick, 20 mm axial hole)	773 K	0.3-1.1 (Avg. 0.7	3000	1.02	11.45
4.	Rotating	Mo Crucible and Holder	Six Segmented Disc (45 mm dia, 6 mm thick)	823 K	0.5-0.8 Avg. 0.65	10,000	13.9 (sampling after every 2000 h)	159.4
5.	Loop	SS pipes, Mo Holder	Flat (25 mm x 8 mm x 3 mm)	723 K	0.6-1.5	5,000	4.01	47-50
6.	Loop (with Magnetic Field = 0.5 T)	SS pipes, Mo Holder	Flat (40 mm x 8 mm x 2 mm)	723 K	0.6-1.5	2,800	5.0	56
7.	Loop (KIT)	Ferritic Steel	Cylindrical sample	823 K	0.010	8, 000	N.A.	200

Table 7.2: Corrosion Rates of P91 steel in Pb-Li under different operating conditions.

Expt . No	Mode	Material of Holder	Sample Geometry	Temp (K)	Vel. (m/s)	Duration (h)	Corrosion Rate	
							$\mu g/cm^2 . hr$	µm/y
1	Static	SS 316 L	Flat (12mm x10 mm x 2mm)	773 K	-	355	0.77	8.64
2.	Static	Crucible and Mo Holder	Flat (12mm x10 mm x 2mm)	923 K	-	355	1.71	19.2
3	Rotating	Mo Crucible and Holder	Disc (40 mm dia, 6 mm thick)	773 K	0 - 1.4 Avg. 0.7	2000	4.2	47.16
4.	Loop	Ferritic Steel	Flat sample	823	0.015	1000	17.8	200
4. (IPUL)	Loop (with Magnetic Field = 1.8 T)	Ferritic Steel	Flat sample	823	0.015	1000	28.4	320

The corrosion resistance of IN RAFMS was also reflected under dynamic conditions in the rotating disc experiment where the corrosion rate of P91 material was found to be almost four (4) times higher than that of P91 under similar conditions of temperature (773 K) and average flow velocities (~0.7 m/s). Figure 7.1 graphically represents the corrosion rates of IN RAFMS and P91 under static and dynamic (isothermal stirring) conditions. The higher corrosion resistance of IN RAFMS must be related to the difference in its alloying elements w. r. t. P91 and its effect of the corrosion mechanism.

7.1.2. Effect of temperature on corrosion rate

The effect of temperature in increasing the corrosion attack under stagnant condition was observed in the short term exposure test (355 h) with P91 material where the corrosion rate was found to increase by two (2) times on an increase in the temperature of exposure by 50 K. Similar results of increase in corrosion rate with temperature have also noted earlier for EUROFER samples exposed to Pb-Li [167, 181]. However, IN RAFMS showed a negligible weight loss in the initial 355 h and thus the effect of temperature could not be detected.

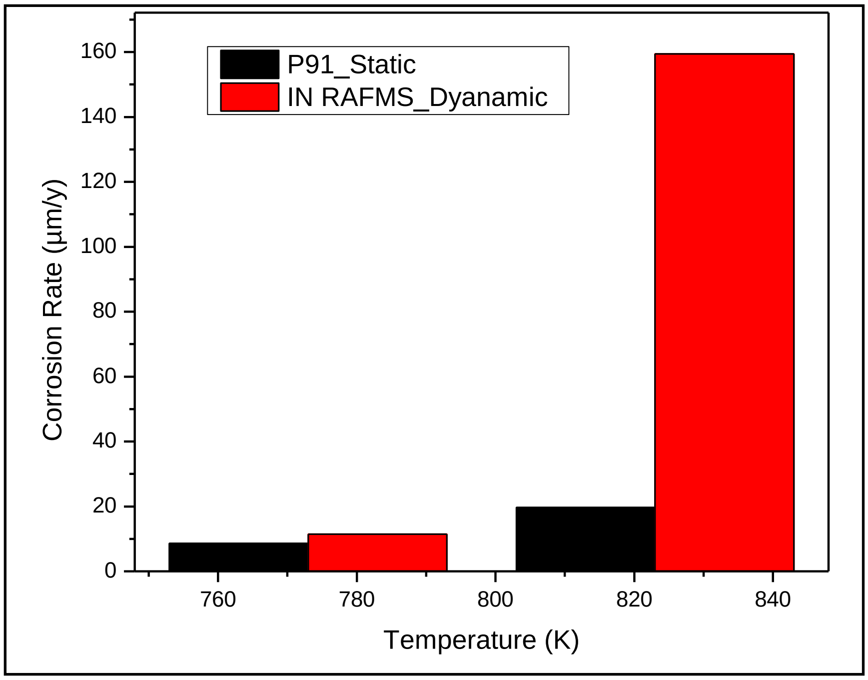

Fig 7.1: Comparison of corrosion rates of IN RAFMS and P91 in static and dynamic systems.

The effect of temperature on the corrosion rate of IN RAFMS under dynamic conditions also validated in the rotating disc corrosion tests where under isothermal stirring conditions, the corrosion rate of IN RAFMS increased by a factor of 13 with temperature increase of 50 K (i.e. from 773 K to 823 K). Increase in corrosion rate up to 10 times on a temperature increase of 70 K has been earlier observed for EUROFER samples [181]. Another possibility might be that the experiment at 773 K was carried out only up to 3, 000 h which may cover most of the incubation period (~2, 000-3, 000 h) as observed in Section 6.3. Incubation period is generally characterized by slow dissolution of passive oxide scales and a comparatively lesser corrosion rate. Nevertheless, even after the incubation period the increase in corrosion rate under isothermal conditions would not be as much as to increase it by 13 times (as observed after increasing the temperature from 773 K to 823 K. This is made clear in Figure 5.37 (Section 5.3.3.1) where the extent of increase in corrosion rate of the IN RAFMS samples after 2, 000 h was ~ 10 times at 823K in the rotating disc experiment.

The effect of temperature on increasing the extent of corrosion attack is mainly due to:-

i. Increase in the diffusivity of alloying elements across the steel matrix (P91 and IN RAFMS) as well as in the Pb-Li especially the boundary layer; with temperature [214, 230].

ii. Increase in solubility of alloying elements in Pb-Li with temperature [195]

Figure 7.2 depicts the effect of temperature on the corrosion rates of IN RAFMS and P91 in Pb-Li under static and dynamic conditions. It could be observed that the rate of increase of corrosion rate with temperature is much higher in the dynamic systems as compared to the static systems. This is possibly because, in the case of dynamic systems, other than an increase in diffusivity, the increase in temperature can also cause a decrease in the boundary layer thickness [223] which in turn speeds up the transport of alloying elements from steel matrix into the bulk Pb-Li. Another point to be noted was that the corrosion rate of IN RAFMS increased by four times when the temperature of exposure was increased from 773 K in EMPPIL to 823 K in PICOLO while the flow velocity was much lesser in PICOLO (0.01 m/s) than EMPPIL (0.6-1.5 m/s). This indicates the fact that corrosion rate is much more sensitive to increase in temperature than an increase in flow velocity.

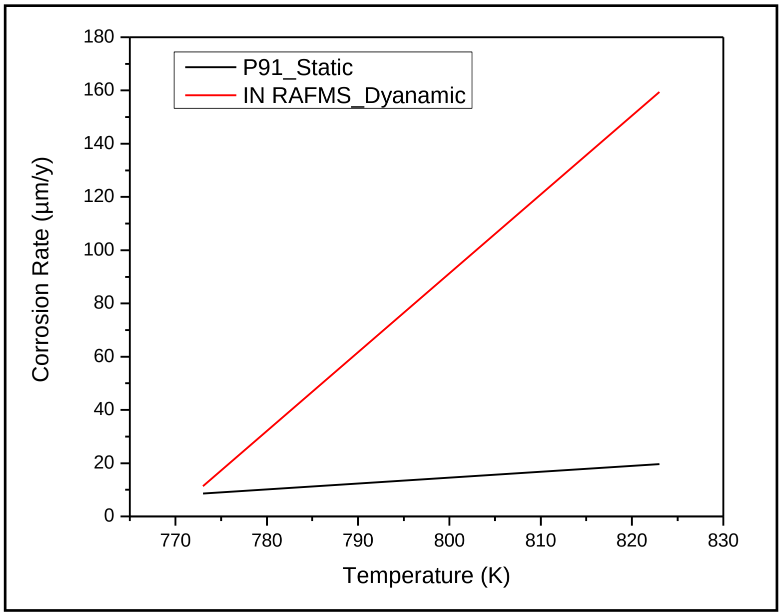

Fig. 7.2: Effect of temperature on the Pb-Li corrosion attack under static and dynamic conditions.

7.1.3. Effect of flow velocity on corrosion rate

The effect of flow velocity in increasing the corrosion attack has been established from the present study in two ways viz:-

i. Higher corrosion rate in dynamic systems (rotating disc and loop) than static system for both P91 and IN RAFMS material.

The corrosion rate of IN RAFMS was found to be almost ten (10) times under isothermal stirring conditions as compared to static conditions. In a similar manner, the corrosion rate of P91 increased by five (5) times when exposed to dynamic (isothermal stirring conditions) as compared to the static exposure. Although the reason for greater increase in case of IN RAFMS is not fully understood but it may be related to the duration of exposure which was 3, 000 h in case of IN RAFMS and 2, 000 h in the P91. Nevertheless, the corrosion rate of IN RAFMS in rotating disc test system has been still found to be lesser than P91 under similar experimental conditions.

ii. Increase in depth of Pb-Li attack for IN RAFMS and P91 with increase in linear velocity along the radial direction of the disc under isothermal stirring conditions.

The RDCTF allowed the study of the effect of flow velocity on Pb-Li attack over the single disc sample. This was done by correlating the depth of attack at various positions along the radius of the disc with the corresponding linear flow velocity. The velocity profile over the disc surface has been discussed in detail in Section 3.4.3. Figure 7.3 shows the variation of depth of attack with increasing velocity from the centre towards the edge of the IN RAFMS disc (60 mm diameter) exposed to Pb-Li at 773 K for 3, 000 h under a flow velocity range of 0.3-1.1 m/s. The depth of attack is found to increase with flow velocity and the increase is parabolic in nature.

The effect of flow velocity mainly in increasing corrosion rate is mainly driven the three aspects:-

a. Faster removal of corroded species from the surface thereby exposing the surface to fresh liquid and thus accelerating the corrosion attack.

b. An increase in flow velocity will also cause a decrease in thickness of the boundary layer which will fasten the transport of corroded species to the Pb-Li.

c. Increase in flow velocity can also lead to erosion corrosion where the mechanical force acting due to high flow velocity will cause faster dislodgement of corroded /depleted layers. This force is directly related to the kinetic energy (K.E.) which in turn is proportional to the square of velocity (v) by Equation 7.1

$$K.E. = m.v^2 \qquad 7.1$$

Where ‘m’ is the mass of the particle carrying the energy (i.e. a constant volume of liquid in this case).

Therefore the force responsible for corrosion/erosion would be directly proportional to the square of velocity as per Equation 7.2.

Mechanical force responsible for erosion α $(\text{velocity})^{2}$ ……………………………..7.2

This may be the reason why the depth of attack has been found to depend on velocity through a second order polynomial as observed in Figure 7.3.

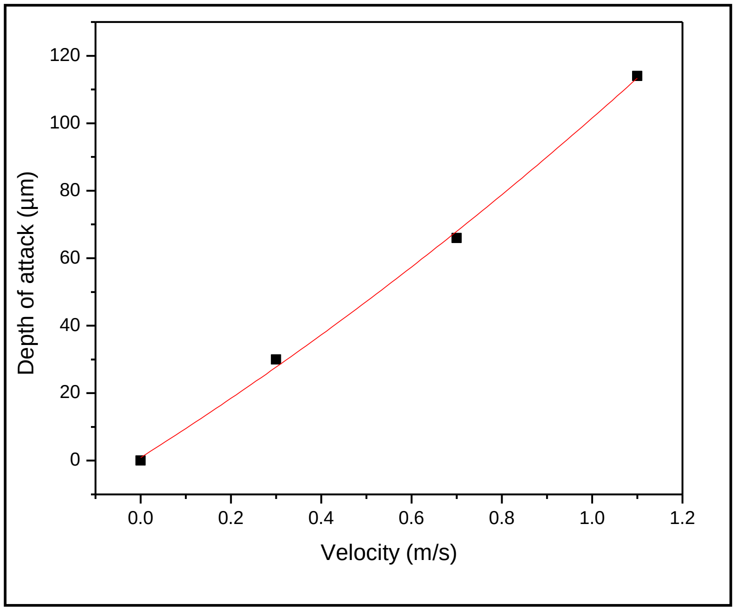

Fig. 7.3 Variation of depth of attack with linear velocity over the IN RAMS disc exposed to Pb-Li at 773 K for 3, 000 h.

7.1.4. Effect of temperature gradient on corrosion rate

The presence of a temperature gradient over flowing Pb-Li (in a Loop) has been found to significantly enhance the corrosion of IN RAFMS and P91as compared to isothermal flow condition (RDCTF). The corrosion rate of IN RAFMS has been found to increase by more than four (4) times in the Pb-Li loop (EMPPIL) than in the RDCTF at 773 K. A temperature gradient of around 200 K existed in between the hot (sample holder) and cold (electro-magnetic pump) regions of this Pb-Li loop which allowed continuous dissolution of corrosion products at the high temperature regions and deposition of the same in the low temperature zones. This phenomenon has been already discussed in Chapter 2 (Section 2.9.2). It is expected that the temperature difference should be directly proportional to the corrosion rate but a few more experiment at different temperature gradients would be needed to confirm this fact. Nevertheless, although the maximum velocities for rotating disc and loop tests might be more or less similar, the minimum velocity is comparatively lesser in rotating disc which may also be a reason behind a lesser corrosion rate in isothermal stirring experiments.

7.1.5.. Effect of magnetic field on the corrosion rate

An electrically conductive fluid (e.g. liquid metal or alloy) flowing in the presence of a magnetic field will experience a force (i.e. Lorentz Force) which will be perpendicular to the flow as well as the magnetic field. This force will once again interact with the external magnetic field to magnetic field to create magneto-hydrodynamic force which significantly changes the flow profile of the liquid metal/alloy. The most significant change lies in the increase in velocity along the walls of the samples and generation of M profile instead of the normal parabolic profile for pipe flows [200]. This has been already discussed in Section 3.9.3. Results from the present study have shown that magnetic field enhances the corrosion rate and the extent of enhancement depends on the magnitude of field. In case of IN RAFMS, presence of 0.5 T magnetic field caused an increase in corrosion rate by 1.3 times while for P91, a higher magnetic field of 1.8 T increased the corrosion rate by 2-3 times. Other than an increase in gross corrosion rate, localized differences in corrosion attack was also observed in the presence of magnetic field which resulted in formation of various surface features both in the case of P91 and IN RAFMS. It is thus evident that the high intensity magnetic field as expected in actual fusion reactors (~5 T) will greatly increase the corrosion rate as well as will change the surface morphology of the Pb-Li carrying conduits made of F/M steel.

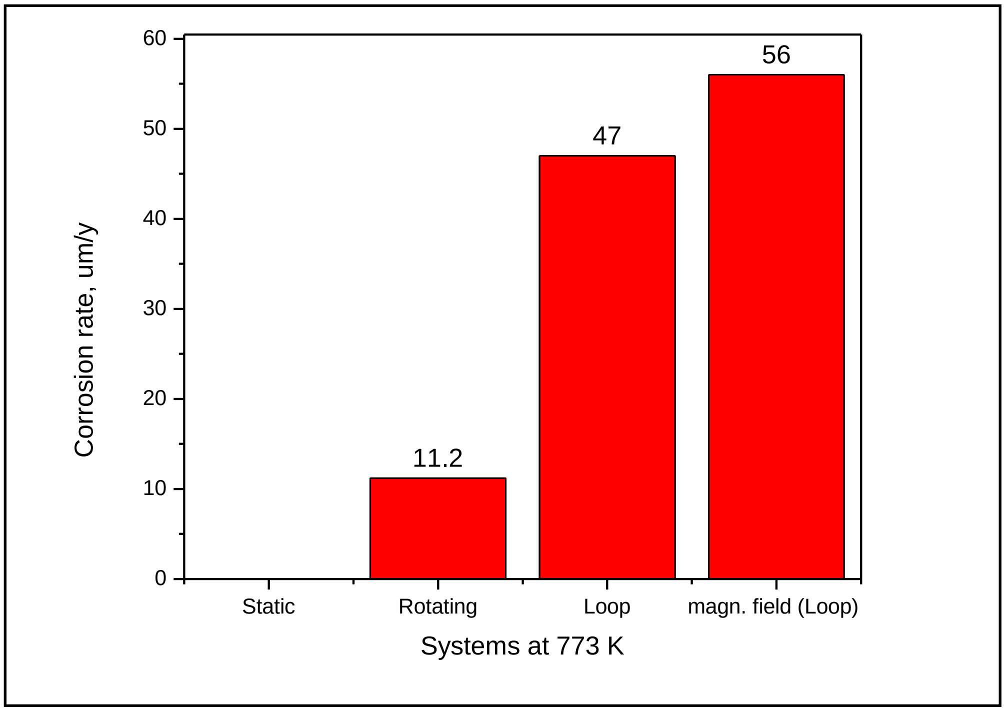

Fig. 7.4: Corrosion Rate of IN RAFMS steel in Pb-Li at 773 K in different test systems [Velocity of Pb-Li: Static – 0 m/s; Rotating – 0 - 1.1 m/s; Loop – 0.6 -1.5 m/s].

Figure 7.4 shows the variation of corrosion rate of IN RAFMS material exposed to various test conditions at 773 K. The increase in corrosion attack could be observed clearly as we move from static to isothermal stirring (i.e. Rotating) to non isothermal flowing (Loop) and to non isothermal flowing in the presence of magnetic field (i.e. Loop with magnet). Having discussed the factors affecting the corrosion rates; it could be summarized that the increase in corrosion rates observed in Figure 7.4 are due addition of an extra driving force for corrosion in each step. This has been listed in Table 7.3. It may be noted that the temperature factor is common for every stage since it decides the diffusivity of alloying elements as well as the solubility of various metals in liquid Pb-Li.

Table 7.3: Driving Force for Pb-Li corrosion in different test set-up.

System	**Driving force for corrosion in Pb-Li**
Static	Temperature + Chemical Potential
Rotating	Temperature + Chemical Potential + Flow Velocity
Loop	Temperature + Chemical Potential + Flow Velocity + Temperature Gradient
Loop with Magnetic Field	Temperature + Chemical Potential + Flow Velocity + Temperature Gradient + Magnetic Field

7.2. Corrosion Mechanism of Ferritic/Martensitic steels in Pb-Li.

Based on the analysis of the various factors affecting the corrosion rate and micro-structural analysis of the exposed IN RAFMS and P91 samples; the overall mechanism of corrosion in Pb-Li have been established. The general corrosion mechanism in the absence of magnetic field for both these materials are similar and are mainly based on the solubility driven dissolution of the major constituent elements i.e. iron and chromium in liquid Pb-Li. However, as observed from long duration experiments (~10, 000 h) carried out in RDCTF with intermittent sample analysis; the corrosion process is characterized by an initial period of reduced attack followed by a longer period of increased attack. Based on the observations and corresponding analysis, the corrosion process was found to be divided into two major steps viz.

a. Dissolution of the passive oxide layer coupled with grain boundary corrosion up to ~2000-4000 h
b. Uniform corrosion through dissolution of chromium and iron from the entire matrix afterwards.

Both P91 and IN RAFMS steel contains an air formed oxide layer over their surface containing a mixed oxide of iron and chromium [$FeO/ (Fe, Cr)_2 O_3$], while IN RAFMS also contains tungsten oxides [WO_2 and WO_3] on its surface layer. This has been already shown from the XPS analysis of the pre – exposed (diamond) polished surface of IN RAFMS/P91 in Section 5.1. It was also observed that the oxide scale in IN RAFMS contained tungsten oxides in the surface layer although molybdenum oxides were not observed in P91 under similar conditions. The dissolution of this oxide scale in Pb-Li was mainly due to the reducing nature of lithium and its tendency to form its own oxide (Li_2O) [219]. This has been confirmed from analysis conducted in Factsage 7.2 software where no feasible reaction of lead with the contents of the oxide layer i.e. (Fe_2O_3, FeO, Cr_2O_3, WO_2 and WO_3) was observed. On the other hand, lithium was found to reduce all these oxides at the general exposure temperature (773 K). The reactions for reduction of these oxides by Li as obtained from Factsage 7.2 along with the associated change in free energy (ΔG) at 773 K are shown in Table 7.4. The reductions reactions for molybdenum (Mo) oxides have also been included to compare the effect of its presence in P91 (if any, after long duration of atmosphere exposure) with that of tungsten oxide in IN RAFMS (already present). It was observed from Table 7.4 that Cr_2O_3 was more stable than Fe_2O_3 / FeO on the presence of lithium (Pb-Li). Thus the subsurface layer of both P91 and IN RAFMS containing Cr_2O_3 up to a depth of 8 nm (Section 5.1) will prevent Pb-Li attack more effectively than the top layer containing mainly Fe-oxides.

However, since the ΔG for reduction of tungsten oxides were the least negative; the stability of tungsten oxides especially WO_3 was highest among all the other oxides i.e. oxides of Fe, Cr as well as Mo. This indicates that the presence of tungsten oxide in the surface layer of IN RAFMS will act as a major factor in preventing its corrosion attack. Since no molybdenum oxide was detected over the present P91 samples before exposure; the stability of its oxide layer will be significantly lesser than that of IN RAFMS. Nevertheless, even if molybdenum oxides (MoO_2/MoO_3) were present in P91, IN RAFMS would still be more resistant to Pb-Li attack due to the comparatively higher stability of tungsten oxides. This explains the reason for lower corrosion rate obtained for IN RAFMS and P91 under static and dynamic conditions in the present study.

Table 7.4: Chemical reactions and free energy change for dissolution of oxides in passive layer of IN RAFMS and P91 at 773 K.

Sl. No.	REACTIONS	ΔG, (KJ)
1	$2Fe_2O_3 + 12\ Li \longrightarrow 6Li_2O + 4Fe$	-1.83
2	$2Cr_2O_3 + 12Li \longrightarrow 6Li_2O + 4Cr$	-1.23
3	$WO_2 + 4Li \longrightarrow 2Li_2O + W$	- 0.576
4	$WO_3 + 6Li \longrightarrow 3\ Li_2O + W$	- 0.89
5	$MoO_2 + 4\ Li \longrightarrow 2Li_2O + Mo$	-0.577
6	$MoO_3 + 6\ Li \longrightarrow 3Li_2O + Mo$	-0.992

It is thus observed that; although the content of chromium in IN RAFMS / P91 is only 9%, it serves as an important component in maintaining the passivity of the oxide layer. However, due to the presence of chromium carbides along the grain boundaries, the adjacent regions may become deficient in chromium and thus the passive layer becomes weaker [218]. Due to this reason whenever a RAFMS / P91 material is initially exposed to Pb-Li, the dissolution of alloying elements first begins from the grain boundary regions which are directly exposed to Pb-Li. It was observed in the EBSD analysis of the unexposed samples (Section 5.1) that the fraction of carbides was greater in case of P91 as compared to IN RAFMS (Table 5.2). This means that the passive layer would be comparatively stronger in IN RAFMS which may also be one of the reasons for its higher corrosion resistance.

Such grain boundary attack during the initial period of exposure has been observed in the case of IN RAFMS both for the static experiment up to 1, 000 h (Figure 5.19) as well as in the rotating disc experiment up to 2, 000 h (Figure 5.37). The high energy of grain boundaries also act as a major reason for initiation of Pb-Li attack in these regions [234]. The dissolution from grain boundary regions lead to formation of Pb-Li channels and thus weakens the carbides precipitated along the boundaries. This leads to carbide dropping which is noted both in the static (Figure 5.20) and dynamic experiments (Figure 5.46 (a)) with IN RAFMS. Dislodgement of carbides further weakens the grain boundaries and also paves way for further grain boundary attack finally enveloping the complete grain. Thus, even in the presence of a protective oxide scale, a complete grain may drop out of the exposed surface which is observed in Figure 5.44 (d) after 2, 000 h of exposure in Pb-Li in the RDCTF.

During grain boundary attack, the iron and chromium from the regions adjacent to grain boundaries and subsequently from the grain interiors leaches out into the Pb-Li channels penetrating through the grain boundaries. In this process, the entire surface region becomes comparatively depleted of the alloying elements although the passive layer might be protecting major parts of the exposed surface. This is why dissolution of Fe and Cr up to 1 μm is noticed even during the 1, 000 of exposure of IN RAFMS under static conditions (Figure 5.23 (d)). It may be noted that formation of a spongy layer over the exposed IN RAFMS in RDCTF has been associated with the depletion of carbon. However, it may be possible this carbon depletion was mainly due to the presence of molybdenum containment (crucible) which helps in trapping of carbon [125]; since similar layers were not noted in the loop experiments where the containment material was SS316 L.

Thus the present study establishes that slow dissolution of oxide scale into Pb-Li leads to a period of delayed wetting or INCUBATION period which is characterized by comparatively lesser corrosion rate as observed in Figure 5.37. Similar trends in the corrosion attack of EUROFER steel have been observed when exposed to flowing Pb-Li where the incubation period is characterized by non uniform corrosion due to the non uniform dissolution of the oxide scales [161, 167]. However, the present study establishes the fact that grain boundary corrosion is also a major phenomenon taking place during incubation period.

After the complete dissolution of oxide scales; the entire surface gets exposed to Pb-Li under similar conditions and thus the corrosion mechanism changes from grain boundary dissolution to matrix dissolution as observed in Figure 5.47 (e) . This leads to leaching of iron and chromium from the entire matrix (other than the grain boundary carbides) and thus gives exposed surface an etched appearance. As the matrix dissolves, the carbides subsequently drop and the entire surface gets dissolved layer by layer. The present study establishes the fact that change of corrosion mechanism from takes place within 2, 000 h to 4, 000 h in the case of IN RAFMS exposed to flowing Pb-Li at 823 K and dissolution from the entire matrix after ~3000 h leads to a significant increase in corrosion rate (Figure 5.37).

During Pb-Li attack, the depleted elements from the steel matrix initially come out into the Pb-Li boundary layer which is present just adjacent to the exposed surface. The alloying elements have to diffuse through this boundary layer in order to reach the bulk liquid. Thus the thickness of the boundary layer and the diffusivity of alloying elements across this boundary layer is an important factor deciding the corrosion kinetics.

In this context, it has been already discussed in Section 5.3.2 that the corrosion rate of IN RAFMS (or P91) is mainly governed by dissolution of iron although the diffusivity of chromium in liquid Pb-Li is higher. This is because of the slow diffusivity of iron in the Pb-Li boundary layer. It has been earlier reported that the slow diffusivity of chromium in Pb-Li will lead to a chromium depleted layer near the exposed surface. Such chromium depletion has been observed in the present study under both static and dynamic conditions for IN RAFMS (and P91) samples. However, if absolute values are taken into consideration, the depletion of iron into Pb-Li (which is the rate controlling step) would also lead to depletion of iron in the surface layer. The comparative decrease in iron might lesser as compared to chromium and would also be difficult to distinguish when compared to the inner matrix since iron is the major constituent (90 wt%) in both IN RAFMS and P91. This is shown by the line scans taken across the P91 (Figure 5.29) and IN RAFMS (Figure 5.34) material exposed to Pb-Li in RDCTF.

7.2.1. Effect of alloying elements on the corrosion mechanism

Since a major part of Pb-Li attack involves the depletion of Fe and Cr from the exposed surface and since the contents of both these materials are similar in P91 and IN RAFMS, the difference in corrosion rates for these two materials must be associated with the minor alloying elements. It known that Mo and Nb in P91 have been replaced by W and Ta in IN RAFMS [23]. Both Mo and W have been known to impart solid solution strengthening to the F/M steels like P91 and IN RAFMS [79]. Moreover, both these elements have very low solubility in Pb-Li and thus generally get enriched in the surface layers [100, 164]. However, the greater corrosion resistant of IN RAFMS over P91 is associated with the following reasons; the most important one being associated with the stability of passive layer:-

1. Higher stability of passive oxide layer due to the presence of tungsten oxide; which can slower down the dissolution of oxide scales and thereby generates a longer incubation period.

2. Lesser solubility of tungsten in Pb-Li as compared to Molybdenum which slows down the matrix dissolution after dissolution of oxide layer [195].

3. Higher solid solution strengthening and slower diffusivity of tungsten than molybdenum which retains the overall strength of the matrix during Pb-Li attack [100].

4. The higher prior austenite grain size of IN RAFMS (Section 5.1) which reduces grain boundary attack.

The present study has shown some differences in the extent of iron and chromium depletion when P91 and IN RAFMS were exposed to Pb-Li under similar conditions in the RDCTF. This is possibly associated with the presence of tungsten and molybdenum which ultimately gives rise to a difference in corrosion resistance. However, further studies with long term experiments with these two materials are being planned in Pb-Li where the reason behind the difference in corrosion process could be established more conclusively.

7.2.2. Effect of Flow velocity on the corrosion mechanism

Results from the present study, especially in RDCTF, have shown that increase in flow velocity accelerates the Pb-Li attack but does not affect the corrosion mechanism. This is revealed from the fact that similar trend of iron-chromium depletion is observed across the exposed grain boundaries at both the inner and outer periphery of the rotating disc exposed at lesser and higher velocities (Figure 5.45). However, experiments in rotating disc test facility as well as Pb-Li loops have shown the reduction/absence of grain boundary attack at high flow velocities (~1.5 m/s). This is because of the following two reasons:-

a. The thickness of the Pb-Li boundary layer decreases with increase in flow velocity [223] which thus accelerates the transport of corroded species (i.e. alloying elements into the bulk Pb-Li). Additionally in case of Pb-Li loop, the corroded species transported to the bulk fluid gets deposited in the cooler regions. This brings fresh Pb-Li to the exposed sample surface which once again enhances the elemental transport across the Pb-Li boundary layer.

Both the above factors lead to a faster rate of Pb-Li attack along grain boundaries and grain dropping occurs much earlier at higher velocity (in loop and rotating disc). This is why the single IN RAFMS segment exposed to Pb-Li in rotating disc test facility for 2, 000 h showed grain boundary attack towards its inner periphery (low velocity~0.3 m/s) (Fig 5.44 (b)) while grain dropping was noted towards the outer edge (high velocity ~0.8 m/s) (Fig 5.44 (d)).

b. Grain boundary penetration makes the grains weaker and then they get easily detached at higher velocities even before complete grain dropping.

The depth of the Fe-Cr depleted layer in IN RAFMS material have been found to be much lesser when exposed to Pb-Li loop and rotating system for longer durations (i.e. ≥ 5, 000 h) than when exposed to static or rotating system for shorter duration (i.e. ≤ 3, 000 h). This is because of the fact that during long term experiments; the corrosion mechanism changes to uniform matrix dissolution and Fe-Cr depletion takes place from the surface layers only. On the other hand, during short term experiments which cover a part of the incubation period, the Fe-Cr depletion takes place into the grain boundary channels which may penetrate deep into the IN RAFMS matrix as observed in Figure 5.49 (a). Moreover, the weak surface layers depleted of Fe and Cr gets easily dislodged; especially at high flow velocities which may also be one of the reasons for their absence in loop experiments. Thus the depth of the Fe-Cr depleted layers present below the original steel-Pb-Li interface cannot be predicted from analysis of samples exposed for longer durations as well at higher velocities.

7.2.3. Effect of magnetic field on the corrosion mechanism.

Results from the present study have indicated that the presence of magnetic field can affect the Pb-Li corrosion mechanism mainly in the following ways:-

i. Causing localized increase in flow velocity creating greater removal of material from these regions which lead to a higher corrosion rate [241].

ii. Causing inter and intra lath attack as compared to only inter lath (and grain boundary) attack in the absence of magnetic field.

iii. Increasing the iron dissolution from steel matrix probably associated with its ferromagnetic nature.

It must be noted that the Pb-Li flow in magnetic field would very different than ordinary flows and would be controlled by one important factor called the Hartmann number i.e. the ratio of electromagnetic forces to viscous forces. The Hartmann number can also be defined by Equation 7.3:-

$$Ha = B_o L_o (\sigma / \rho \upsilon)^{1/2} \quad \ldots\ldots \quad 7.3$$

Where, Bo is the applied field; σ - electrical conductivity, υ - kinematic viscosity and L_o – typical length scale

For usual magnetohydrodynamic (MHD) flows with moderate values of the magnetic field ($0<B<1$ T), Ha ranges from 10 to 100 as was the case of IN RAFMS samples exposed to EMPPIL -M. In the case of the Pb-Li flow under higher magnetic field as was in the present case of P91 (~1.8 T), these parameters (Ha and *N*) are several orders of magnitude higher.

Thus, the electromagnetic forces increase with increasing magnetic field and are expected to create major changes in the velocity profile which can lead to localized corrosion. It has been also reported that the interaction between the external magnetic field and the flowing liquid metal creates induced electric currents which cross the interface between the liquid and the sample thereby accelerating the corrosion processes [184]. Although the exact reason for intra-lath corrosion is not fully understood; it is possible that the electro-dissolution caused by local electric currents [184] may create differences in the dissolution rate between various regions of the matrix over and above the normal grain boundary attack. However, detailed theoretical analysis is required to establish this fact and is not in the scope of the present study.

Based on the overall results from the present study, the corrosion mechanism of ferritic/martensitic steels in the presence and absence of magnetic field is schematically represented in Figure 7.5.

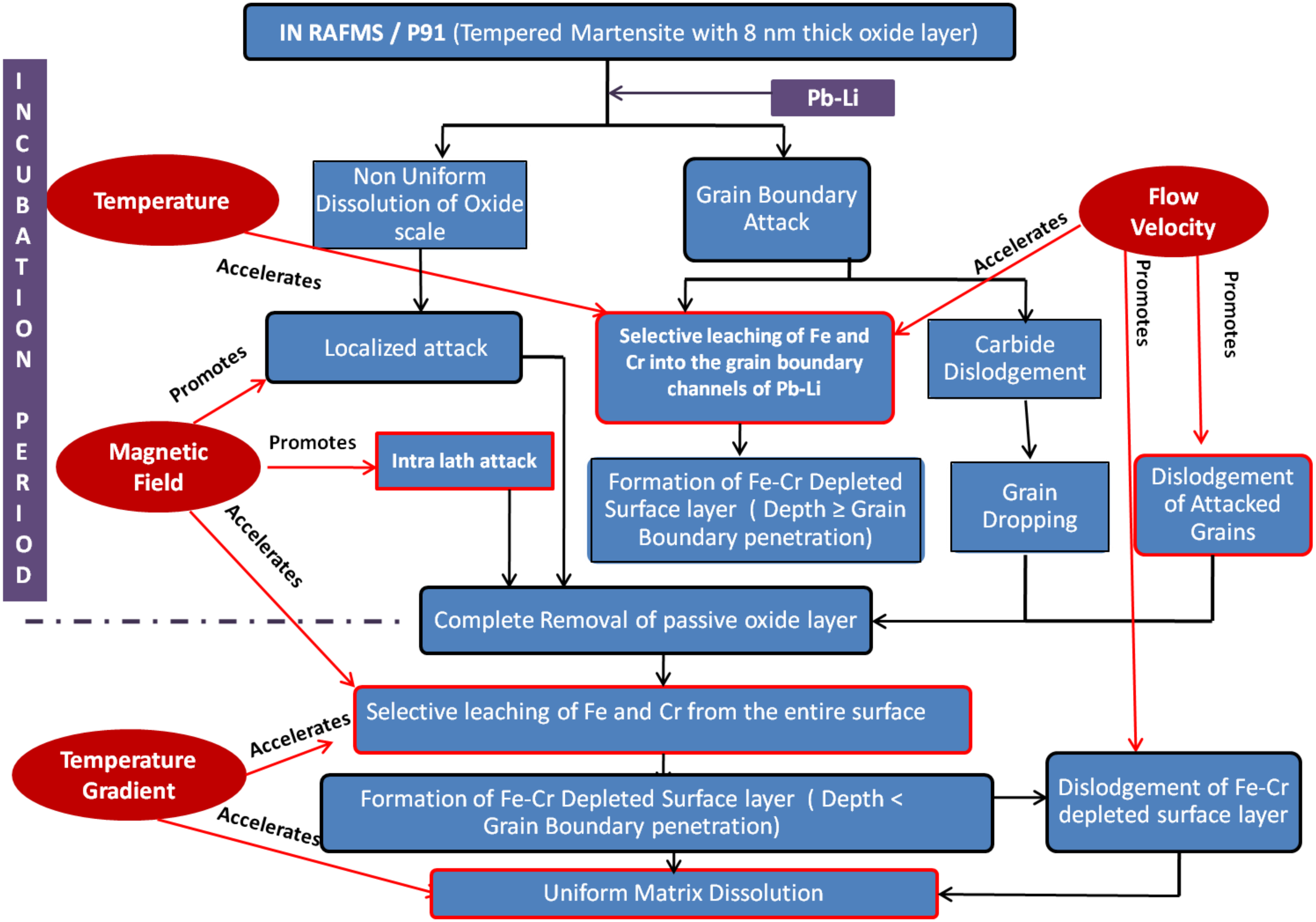

Fig. 7.5: Corrosion mechanism of ferritic/martensitic steels in liquid Pb-Li.

CHAPTER 8

CONCLUSIONS

In the present work, the corrosion behavior of IN RAFMS and modified 9Cr-1Mo steel (P91) has been studied in molten Pb-Li under different conditions of temperature, flow velocity and magnetic field. The studies have been carried out in various test facilities (like static, rotating disc and loop) for generating the required operating conditions. The exposed corrosion coupons have been analyzed through weight loss measurements and multiple microscopic techniques and compared with their pre-test conditions to establish the corrosion rate and the results have been analyzed to establish the corrosion mechanism. The following major conclusions have been obtained from the present study:-

1. The corrosion process of IN RAFMS and P91 in Pb-Li is generally initiated by dissolution of the air formed oxide layer which consists of oxides of iron and chromium ($(Cr, Fe)_2O_3$ /FeO). The air formed oxide layer has been found to be ~8 nm thick on both the materials. Slow dissolution of this layer in Pb-Li accounts for reduced corrosion rate in the so called incubation period which has been found to lie with 2, 000 – 4, 000 h in case of IN RAFMS.
2. Reduction by lithium (in Pb-Li) is mainly responsible for the dissolution the oxide layer. However, the incubation period is also characterized by grain boundary attack probably due to a comparatively weaker passive layer over grain boundary regions.
3. A change in corrosion mechanism occurs after incubation period when the nature of Pb-Li attack changes from grain boundary dissolution to matrix dissolution (due to the complete absence of oxide layer) and uniform corrosion depletion of Fe and Cr takes place from the from entire matrix.

4. In general, corrosion of IN RAFMS and P91 in molten Pb-Li is governed by the dissolution of Fe and Cr from the steel matrix into the Pb-Li. The diffusion of Fe across the Pb-Li boundary layer is the rate controlling step in the case of IN RAFMS.
5. IN RAFMS has been found to be more resistant to Pb-Li corrosion under both static and dynamic conditions than P91. Better corrosion resistance of IN RAFMS was attributed mainly to the presence of tungsten oxides in the passive layer which offers better stability. The corrosion attack by Pb-Li has been found to be grossly non-uniform in nature.
6. Increase in flow velocity causes an increase in corrosion rate of IN RAFMS in Pb-Li mainly due to increased material take off from the exposed surface although the original corrosion mechanism remains unchanged. Grain boundary attack is accelerated at higher velocity and may result in grain dropping (due to faster Pb-Li penetration all around the grains) or grain dislodgement (due to mechanical /shear force of flowing Pb-Li).
7. Increase in temperature of exposure causes an increase in Pb-Li attack which is mainly associated the increase in solubility and diffusivity of alloying elements in liquid Pb-Li. Corrosion rate in Pb-Li has been found to be more sensitive to temperature than flow velocity.
8. Presence of a temperature gradient in a flowing system will cause an increase in Pb-Li attack {due to deposition of leached elements (eg. Fe, Cr) in cooler regions}. However, the actual corrosion mechanism is not altered. The maximum corrosion rate experienced by IN RAFMS at 773 K in flowing Pb-Li was found to be 49.98 µm/y which is a first time data being reported.
9. The corrosion rate of IN RAFMS and P91 in flowing Pb-Li was enhanced in the presence of magnetic field, as magnetic field created local increase / change in flow velocity. Both IN RAFMS and P91 developed distinct surface features in the presence of magnetic field which was also accompanied by intra - lath corrosion other than the usual grain boundary attack.

SCOPE FOR FUTURE WORK

In the present study, corrosion mechanism of ferritic-martensitic steels, P91 and IN RAFMS with molten Pb-Li within a temperature range of 773 K -823 K has been established. In this study it is shown that alloying elements, grain boundaries and passive oxide layer play a major role in initiating the corrosion attack. It has been also established that increasing temperature and velocity can directly increase the corrosion rate. The role of magnetic field in altering the corrosion mechanism and thereby accelerating the corrosion attack have also been shown experimentally. Present work paves the way for several future investigations which can be taken up as independent study. Few of these future works are listed as follows:-

1. Grain boundary engineering could be exploited to identify specific type of grain boundaries which may be highly prone to Pb-Li infiltration and also those which offer highest resistance and tailor the microstructure suitably to develop the steel in such a way that the same the ferritic – martensitic steel matrix offers high corrosion resistance.
2. Fine tuning of alloy composition to alter the nature of passive layer in order to have a longer incubation period. Surface modification techniques over F/M steels may also be explored to modify the surface composition/ microstructure which are more compatible with Pb-Li.
3. Compatibility studies of protective coatings like iron –aluminide with Pb-Li under static and dynamic conditions in the operating temperature.
4. Detailed understanding the effect of magnetic field on the corrosion process through theoretical simulation of MHD interference with the velocity profile as well as the interaction of the Ferritic Martensitic steel with the generated electric currents is needed.

REFERENCES

---

1. V. Zrodnikov, A. D. Efanov, Yu. I. Orlov, P. N. Martynov, V. M. Troyanov, and A. E. Rusanov, “Heavy Liquid Metal Coolant –Lead–Bismuth and Lead – Technology”, Atomic Energy 97(2) (2004) 534-537.

2. E. Mas de les Valls, L.A. Sedano , L. Batet , I. Ricapito , A. Aiello, O. Gastaldi , F. Gabriel, “Lead–lithium eutectic material database for nuclear fusion technology”, Journal of Nuclear Materials 376 (2008) 353–357.

3. IAEA, “Liquid Metal Coolants for Fast Reactors Cooled by Sodium, Lead, and Lead-Bismuth Eutectic”, IAEA Nuclear Energy Series No. NP-T-1.6 (2012).

4. E. P. Loewen, A. T. Tokuhiro, “Status of Research and Development of the Lead-Alloy-Cooled Fast Reactor, Journal of Nuclear Science and Technology 40(8) (2003) 614–627

5. M. Caro, K. Woloshun, F. Rubio, S. A. Maloy, P. Hosemann, “Heavy Liquid Metal Corrosion of Structural Materials in Advanced Nuclear Systems”, The Journal of The Minerals, Metals & Materials Society (TMS), 65(8) (2013)1057 – 1066.

6. W. D. Manly, “Fundamentals of Liquid Metal Corrosion”, Corrosion 12(7) (1956) 46-52

7. M. G. Fontana, “Corrosion Engineering”, McGraw-Hill (1986).

8. U. Schumacher, “Status and problems of fusion reactor development” Naturwissenschaften 88(3) (2001)102-12.

9. J. P. Freidberg, F. J. Mangiarotti, J. Minervini, “Designing a TOKAMAK fusion reactor—How does plasma physics fit in? ”, Physics of Plasmas 22 (2015) 070901.

10. M. A. Abdou, “Tritium Breeding in Fusion Reactors”, Chapter 63: Nuclear Data for Science and Technology”; (1983) DOI : doi.org/10.1007/978-94-009-7099-1_63

11. P. H. Rebut, the ITER Joint Central Team and Home Teams, “ITER: the first experimental fusion reactor”, Fusion Engineering and Design 30 (1995) 85- 118.

12. L. Giancarli, V. Chuyanov, M. Abdou, M. Akiba, B. G. Hong, R. Lässer, C. Pan, Y. Strebkov, the TBWG Team , "Test blanket modules in ITER: An overview on proposed designs and required DEMO-relevant materials", Journal of Nuclear Materials 367–370 (2007) 1271–1280

13. L. M. Giancarli, M. Abdou, D. J. Campbell, V. A. Chuyanov, M. Y. Ahn, M. Enoeda, C. Pan, Y. Poitevin, E. R. Kumar, I. Ricapito, Y. Strebkov, S. Suzuki, P. C. Wong, M. Zmitko, "Overview of the ITER TBM Program", Fusion Engineering and Design 87 (2012) 395–402.

14. C.P.C. Wong, J.-F. Salavy, Y. Kim, I. Kirillov, E. R. Kumar, N.B. Morley, S. Tanaka, Y.C. Wu, "Overview of liquid metal TBM concepts and programs", Fusion Engineering and Design 83 (2008) 850–857.

15. E. R. Kumar, T. Jayakumar, A.K. Suri, " Overview of TBM R&D activities in India", Fusion Engineering and Design 87 (2012) 461–465

16. M. Victoria, N. Baluc, P. Spatig "Structural materials for fusion reactors", Nuclear Fusion 41 (2001) 1047-1053

17. P. M. Raole, S. P. Deshpande and DEMO Team "Structural materials for fusion reactors", Transactions of The Indian Institute of Metals 62(2) (2009) 105-111

18. R. L. Klueh, K. Ehrlich and F. Abe "Ferritic/ martensitic steels : promises and problems", Journal of Nuclear Materials 191-194 (1992)116-124

19. R. L. Klueh, "Ferritic/martensitic steels for advanced nuclear reactors" Transactions of the Indian Institute of Metals 62 (2) (2009) 81-87

20. N. Baluc, R. Schäublin, P. Spätig and M. Victoria, "On the potentiality of using ferritic/martensitic steels as structural materials for fusion reactors", Nuclear Fusion 44 (2004) 56-61

21. L. Tan, L. L. Snead, Y. Katoh, "Development of new generation reduced activation ferritic-martensitic steels for advanced fusion reactors", Journal of Nuclear Materials 478 (2016) 42-49.

22. B. Raj , K. B. S. Rao, A.K. Bhaduri , Progress in the development of reduced activation ferritic-martensitic steels and fabrication technologies in India", Fusion Engineering and Design 85 (2010) 1460–1468

23. S. Saroja, A. Dasgupta, R. Divakar, S. Raju, E. Mohandas, M. Vijayalakshmi, K. B. S. Rao, B. Raj, "Development and characterization of advanced 9Cr ferritic/martensitic steels for fission and fusion reactors", Journal of Nuclear Materials 409 (2011) 131-139.

24. K. Laha, S. Saroja, A. Moitra, R. Sandhya, M.D. Mathew, T. Jayakumar, E. Rajendra Kumar, "Development of India-specific RAFM steel through optimization of tungsten and tantalum contents for better combination of impact, tensile, low cycle fatigue and creep properties", Journal of Nuclear Materials 439 (2013) 41–50

25. S. Banerjee, the Indian Team on Fusion Reactor Materials, "Overview of Indian activities on fusion reactor materials", Journal of Nuclear Materials 455 (2014) 217–224

26. S. K. Albert, C. R. Das, S. Sam, P. Mastanaiah, M. Patel, A. K. Bhaduri, T. Jayakumar, C. V. S. Murthy, E. Rajendra Kumar, "Mechanical properties of similar and dissimilar weldments of RAFMS and AISI 316L (N) SS prepared by electron beam welding process", Fusion Engineering and Design 89 (7–8) (2014) 1605-1610

27. S. Glasstone and A. Sesonske, "Nuclear Reactor Engineering: Reactor Design Basics", Volume 1, Springer (1994).

28. www.wikipedia.org

29. G. McCracken and P. Stott, "Fusion: The Energy of the Universe", Academic Press. (2005)

30. Daniel Clery, "A Piece of the Sun: The Quest for Fusion Energy", The Overlook Press (2013)

31. A. A. Harms, D. R. Kingdon and K. F. Schoef ,"Principles of fusion energy: An introduction to fusion energy for students of science and engineering", World Scientific Publishing Company (2000)

32. W. Bleam, "Soil and Environmental Chemistry", Academic Press (2017)

33. F. Chen, " Introduction to Plasma Physics and Controlled Fusion", Springer (2016)

34. J. P. Freidberg, “Plasma Physics and Fusion Energy”, Cambridge University Press (2008).

35. A. R. Raffray, M. Akiba, V. Chuyanov, L. Giancarli, S. Malang, “Breeding blanket concepts for fusion and materials requirements”, Journal of Nuclear Materials 307–311 (2002) 21–30

36. www.iter.org.

37. D. Steiner and M. Tobias, “Cross-section sensitivity of tritium breeding in a fusion reactor blanket: effects of uncertainties in cross-sections of 6Li, 7Li, and 93Nb”, Nuclear Fusion 14 (1974) 153-163.

38. D. H. Jansen, E. E. Hoffman, D. M. Shepherd “Lead-lithium shielding alloy - metallurgical studies” Journal of Nuclear Materials 3 (1959) 249-268

39. M. Übeyli, “Effect of Lithium Enrichment on the tritium breeding characteristics of Various Breeders in a Fusion Driven Hybrid Reactor” Journal of Fusion Energy 28 (3) (2009) 300–303.

40. Z. Gao, “Compact magnetic confinement fusion: Spherical torus and compact torus”, Matter and Radiation at Extremes 1(3) (2016) 153-162.

41. L. D. Horton, JET Contributors, “8 - Joint European Torus”, Magnetic Fusion Energy-From Experiments to Power Plants (2016) 215–259.

42. K. Tomabechi, “International thermonuclear experimental reactor, ITER”, Fusion Engineering and Design 8 (1989) 43-49.

43. S. Deshpande and P. Kaw, “Fusion research program in India”, Sadhana 38(5) (2013) 839 - 848.

44. E. Rajendra Kumar, C. Danani , I. Sandeep , C. Chakrapani , N. Ravi Pragash ,V. Chaudhari , C. Rotti , P. M. Raole , J. Alphonsa , S. P. Deshpande, “Preliminary design of Indian Test Blanket Module for ITER” , Fusion Engineering and Design 83 (2008) 1169–1172

45. R. K. Choudhary, V. Kain, R. C. Hubli, “Formation of alumina-aluminide coatings on ferritic-martensitic T91 steel”, Journal of Mining and Metallurgy, Section B Metallurgy 50 (2) B (2014) 165-170

46. P. Chaudhuri, C. Danani, V. Chaudhari, R. Srinivasan, E. Rajendra Kumar, S.P. Deshpande, “Current status of design and engineering analysis of Indian LLCB TBM”, Fusion Engineering and Design 85 (2010) 1966–1969.
47. S. J. Zinkle and L.L. Snead “Designing Radiation Resistance in Materials for Fusion Energy”, Annual Review of Materials Research 44 (2014) 241-267
48. H. Bolt, V. Barabash, W.Krauss, J. Linke, R. Neu, S. Suzuki, N. Yoshida, ASDEX Upgrade Team, “Materials for the plasma-facing components of fusion reactors”, Journal of Nuclear Materials 329–333 (A) 1 (2004) 66-73.
49. A. K. Suri, N. Krishnamurthy and I. S. Batra, “Material Issues in Fusion Reactors”, Journal of Physics: Conference Series 208 (2010) 012001 (1-16)
50. M. Araki, M. Akiba, M. Dairku, K. Iida, H. Isi, M. Seki, S. Suzuki and K. Yokoyama, “Thermal Response of Bonded CFC/OFHC Divertor Mock-Ups for Fusion Experimental Reactors under Large Numbers of Cyclic High Heat Loads”, Journal of Nuclear Science and Technology, 29 (9) (1992) 901-908.
51. N. Baluc, D. S. Gelles, S. Jitsukawa, A. Kimura, R.L. Klueh, G. R. Odette, B. Van der Schaaf, Jinnan Yu “Status of reduced activation ferritic/martensitic steel development”, Journal of Nuclear Materials 367–370 (2007) 33–4.
52. Paul, E. Alves, L.C. Alves, C. Marques, R. Lindau, J.A. Odriozola, “Microstructural characterization of Eurofer-ODS RAFM steel in the normalized and tempered condition and after thermal aging in simulated fusion conditions”, Fusion Engineering and Design 75–79 (2005) 1061–1065.
53. G. Benamati, C. Fazio , I. Ricapito, “Mechanical and corrosion behavior of EUROFER 97 steel exposed to Pb–17Li”, Journal of Nuclear Materials 307–311 (2002) 1391–1395
54. D. L. Smith, B. A. Loomis, D. R. Diercks, “Vanadium-base alloys for fusion reactor applications-a review”, Journal of Nuclear Materials 135(2–3) (1985) 125-139.
55. L. L. Snead, T. Nozawa, M. Ferraris, Y. Katoh, R. Shinavski, M. Sawan, “Silicon carbide composites as fusion power reactor structural materials”, Journal of Nuclear Materials 417 (1–3) (2011) 330-339.

56. S. J. Zinkle and N. M. Ghoniem, “Operating temperature windows for fusion reactor structural materials”, Fusion Engineering and Design 51–52 (2000) 55-71.

57. D. S. Gelles, “Microstructural examination of commercial ferritic alloys at 200 dpa”, Journal of Nuclear Materials 233–237 (1996) 293-298.

58. H. Schroeder, H. Ullmaier, “Helium and hydrogen effects on the embrittlement of iron- and nickel-based alloys”, Journal of Nuclear Materials 179–181 (1991) 118-124.

59. M. Rieth, B. Dafferner and H.-D. Röhrig, “Embrittlement behavior of different international low activation alloys after neutron irradiation”, Journal of Nuclear Materials 258-263(1998)1147-1152.

60. K. M. Feng, C. H. Pan, G. S. Zhang, T. Yuan, Z. Chen, Z. Zhao, H. B. Liu, Z. Q. Li, G. Hu, X. Y. Wang, X. F. Ye, D. L. Luo, H. Y. Wang, Z. W. Zhou, C. M. Gao, Y. J. Chen, P. H. Wang, Q. X. Cao, Q. J. Wang, the Chinese HCSB TBM Design Team, “Overview of design and R&D of solid breeder TBM in China”, Fusion Engineering and Design 83 (7–9) (2008)1149-1156.

61. S. Malang, M. Tillack, C. P. C. Wong, N. Morley & S. Smolentsev, “Development of the Lead Lithium (DCLL) Blanket Concept”, Fusion Science and Technology 60 (2011) 249-256.

62. S. Malang, R. Mattas, “Comparison of lithium and the eutectic candidate liquid metal breeder material lead-lithium alloy, two for self-cooled blankets”, Fusion Engineering and Design 27 (1995) 399-406.

63. E. Yachimiak Jr. and M. S. Kazimi, “Safety Analysis of Liquid Lithium-Lead Breeders in Fusion Reactor Geometries”, PFC/RR-84-10, (1984), Prepared for EG&G Idaho, INC. and the U.S. Department of Energy Idaho Operations Office under DOE Contract # DE-APO7-791DO019.

64. A. Atanov, A. Chepovski, V. Gromov, G. Kalinin, V. Markov, V. Rybin, E. Saunin,G. Shatalov, A. Sidorov, Yu. Strebkov, V. Bondarenko, I. Chasovnikov, V. Vinokurov,V. Zemlyanin, V. Prohorenko, A. Kondar, A. Ukhlinov, “Properties and behavior of 83Pb-17Li eutectic”, Fusion Engineering and Design 14 (1991) 213-218.

65. G. M. Gryaznov, V. A. Evtikhin, L. P. Zavyal'skii, A. Y. Kosukhin,I. E. Lyublinskii, N. V. Samsonov and A. A. Gusakov, “A comparative study of the corrosion resistance of an austenitic steel in lithium and the eutectic lead-lithium alloy”, Atomnaya Energiya 59(5) (1985) 355-358.
66. E. Mas de les Valls , L.A. Sedano L. Batet , I. Ricapito , A. Aiello, O. Gastaldi , F. Gabriel, “Lead–lithium eutectic material database for nuclear fusion technology”, Journal of Nuclear Materials 376 (2008) 353–357.
67. V. Coen, “Lithium-lead eutectic as breeding material in fusion reactors”, Journal of Nuclear Materials 133-134 (1985) 46-51.
68. S. J. Zinkle, “Summary of Physical Properties for Lithium, Pb-17Li, and (LiF)n•BeF2 Coolants”, ORNLAPEX Study Meeting, July 27-28 (1998).
69. M. Hansen and K. Anderko, “Constitution of Binary Alloys”, 2nd ed. McGraw-Hill, New York (1958) 900-902.
70. P. Hubberstey, T.Sample and M. G. Barker “Is Pb-17Li really the eutectic alloy? A redetermination of the lead-rich section of the Pb-Li phase diagram (0.0 <Li (at %) < 22.1)”, Journal of Nuclear Materials 191-194 (1992) 283-287.
71. A. I. Barrado, E. Conde, M. Fernández, J. María Gómez-Salazar, A. Quejido, J. Quinones, “Towards the development of technical specifications for the production of lithium–lead alloys for the ITER HCLL TBM”, Fusion Engineering and Design 87 (2012) 1297–1300.
72. X. Xu, “Corrosion susceptibility of structural materials for fusion in liquid and solid breeders”, Master Thesis, University of Madrid (2013).
73. R. Bhattacharyay, Indian TBM Team, “Status of Indian LLCBTBM program and R&D activities”, Fusion Engineering and Design 89 (2014) 1107–11.
74. E. R. Kumar, K. N. Vyas, T. Jayakumar, “Overview of LLCB TBM design and R&D activities in India”, Fusion Engineering and Design 109–111 (2016) 1522–1527.
75. S. G. Khambholja, A. Abhishek, D. D. Satikunvar and B. Y. Thakore, “Thermophysical properties of Pb-Li”, AIP Conference Proceedings 030021 (2018); doi: 10.1063/1.5028602
76. A. Zalkin, W. Ramsey, “Intermetallic Compounds between Lithium and Lead. III. The β1-β Transition in LiPb”, Journal of Physics & Chemistry 61(1957) 1413-1415.

77. U. Jain, A. Mukherjee, S. Sonak, S. Kumar, R. Mishra, N. Krishnamurthy, “Interaction of alumina with liquid Pb83Li17 alloy”, Fusion Engineering and Design 89 (2014) 2554–255.

78. S. N. Rosenwasser, P. Miller, J. A. Dalessandro, J. M. Rawls, W. E. Toffolo, W. Chen,” The application of martensitic stainless steels in long lifetime fusion first wall/blankets”, Journal Nuclear Materials 85 & 86 (1979) 177.

79. R. L. Klueh, “Elevated-temperature ferritic and martensitic steels and their application to future nuclear reactors”, ORNL Report ORNL/TM-2004/176 (2004).

80. R. Viswanathan and W. Bakker, “Materials for ultrasupercritical coal power plants—Boiler materials: Part 1”, Journal of Materials Engineering and Performance 10 (2001) 81-95.

81. F. Masuyama, Advanced Heat Resistant Steel for Power Generation, The Institute of Materials, London (1999) 33-48,

82. R. Viswanathan and W. Bakker,” Materials for ultrasupercritical coal power plants—Turbine materials: Part II”, Journal of Materials Engineering and Performance 10, 96-101 (2001a)

83. R. L. Klueh and E. E. Bloom, “The development of ferritic steels for fast induced-radioactivity decay for fusion reactor applications”, Nuclear Engineering and Design.Fusion 2 (1985) 383-389.

84. R. L. Klueh and P. J .Maziasz, “Reduced-activation ferritic steels: a comparison with Cr-Mo steels”, CONF-871036—4 DE88 000332.

85. B. Van der Schaaf, D. S. Gelles, S. Jitsukawa, A. Kimura, R. L. Klueh, A. Moslang, and G. R. Odette, “Progress and critical issues of reduced activation ferritic/martensitic steel development”, Journal of Nuclear Materials 283-287(2000) 52-59

86. J. C. Chang, B. S. Kim, and N. H. Heo, “Stress Relief Cracking on the Weld of T/P 23 Steel”, Procedia Engineering 10 (2011) 734–739

87. V. Karthik, K. Laha, P. Parameswaran, K.S. Chandravathi, K.V. Kasiviswanathan, T. Jayakumar, B. Raj, “Tensile Properties of Modified 9Cr-1Mo steel by shear punch testing

and correlation with Microstructures", International Journal of Pressure Vessels and Piping 88(10) (2011) 375-383.

88. P. J. Ennis, A. Zieliñska-Lipiec, and A. Czyrska-Filemonowicz, "Microstructural Stability of Creep Resistant Alloys for High Temperature Plant Applications", The Institute of Materials, London (1998) 135-144.
89. W. B. Jones, C. R. Hills and D. H. Polonis, 'Microstructural Evolution of Modified 9Cr-lMo Steel", Metallurgical Transactions A 22A (1991)1049-1058.
90. H. C. Furtado, L. H. de Almeida, I. L. May, "Precipitation in 9Cr–1Mo steel after creep deformation", Materials Characterization 58 (1) (2007) 72-77.
91. T. Gu, M. Wang, Y. Xu, X. Zhou, H. Zhao, L. Chen, "Effect of Long-Term Thermal Aging on Microstructure and High-Temperature Strength of a 10% Cr Martensite Ferritic Steel", Steel Research International 87 (5) (2016) 662-671.
92. W. Wang, S. Liu, G. Xu B. Zhang, Q. Huang, "Effect of Thermal Aging on Microstructure and Mechanical Properties of China Low-Activation Martensitic Steel at 550 °C", Nuclear Engineering and Technology 48(2) (2016) 518-524.
93. A. Strang and V. Vodarek, "Microstructural Stability of Creep Resistant Alloys for High Temperature Plant Applications", The Institute of Materials, London (1998) 117-134.
94. A. Aghajani, F. Richter, C. Somsen, S. G. Fries, I. Steinbach, G. Eggeler, "On the formation and growth of Mo-rich Laves phase particles during long-term creep of a 12% chromium tempered martensite ferritic steel", Scripta Materialia 61(11) (2009) 1068-1071.
95. Y. Hosoi, N. Wade, S. Kunimitsu, T. Urita, "Precipitation behavior of laves phase and its effect on toughness of 9Cr-2Mo Ferritic-martensitic steel", Journal of Nuclear Materials 141–143(1) (1986) 461-467.
96. H. Cerjak, V. Foldyna, P. Hofer, and B. Schaffernak, "Microstructural Development and Stability in High Chromium Ferritic Power Plant Steels", The Institute of Materials, London (1997) 145-158.

97. W. C. Leslie, “Iron and its dilute substitutional solid solutions”, Materials Transactions B 3 (1972) 5-26.

98. T. Fujita, “Advanced High Chromium Ferritic Steels for high temperature”, Metal Progress (1986) 33-40.

99. A. Ravikiran, R Mythili, S Raju, S Saroja, G Paneerselvam, T Jayakumar and E. Rajendra Kumar, “Effect of alloy content on microstructure and microchemistry of phases during short term thermal exposure of 9Cr–W–Ta–0.1C reduced activation ferritic/martensitic (RAFM) steels”, Bulletin of Materials Science 37 (6) (2014) 1453–1460.

100. G. Neumann and C. Tuijn, “Self Diffusion and Impurity Diffusion in Pure Metals: Handbook of experimental data”, Pergamonn Materials Series (2009).

101. J. Nutting, “Advanced Heat Resistant Steel for Power Generation”, The Institute of Materials, London (1999) 12-30.

102. L. Tan, Y. Yang, J. T. Busby, “Effects of alloying elements and thermomechanical treatment on 9Cr Reduced Activation Ferritic–Martensitic (RAFM) steels”, Journal of Nuclear Materials 442(1–3) (2013) S13-S17.

103. J. J. Kai and R. L. Klueh, “Microstructural analysis of neutron-irradiated martensitic steels “Journal of Nuclear Materials 116-124 (1996).

104. R. L. Klueh and P. J. Maziasz, “The microstructure of chromium-tungsten steels”, Material Transactions A 20A (1989) 373-381

105. O. K. Von Goldbeck, “Iron—Chromium Fe—Cr. In: Iron—Binary Phase Diagrams”, Springer (1982).

106. N. Igata, “Ferritic/martensitic dual-phase steel as fusion reactor materials”, Journal of Nuclear Materials 133-134 (1985) 141-148.

107. S.J. Sanderson, “Ferritic Steels for High-Temperature Applications”, Proceedings of an ASM International Conference on Production, Fabrication, Properties, and Application of Ferritic Steels for High-Temperature Applications (1983) 87.

108. C-Y. HSU and T. A. Lechtenberg, “Microstructure and mechanical properties of unirradiated low activation ferritic steel”, Journal of Nuclear Materials 141-143 (1986) 1107-1112

109. G. Dieter, “Mechanical Metallurgy”, McGraw Hill Education (1989)

110. B. Arivazhagan, R. Prabhu, S. K. Albert, M. Kamaraj, and S. Sundaresan, “Microstructure and Mechanical Properties of 9Cr-1Mo Steel Weld Fusion Zones as a Function of Weld Metal Composition”, Journal of Materials Engineering and Performance 18 (2009) 999–1004

111. J.-F. Salavy, L.V. Boccaccini, P. Chaudhuri, S. Cho, M. Enoeda, L. M. Giancarli, R. J. Kurtz, T. Y. Luo, K. B. S. Rao, C.P.C. Wong, “Must we use ferritic steel in TBM?”, Fusion Engineering and Design 85 (2010) 1896–1902.

112. H. Tanigawa, E. Gaganidze, T. Hirose, M. Ando, S.J. Zinkle, R. Lindau and E. Diegele “Development of benchmark reduced activation ferritic/martensitic steels for fusion energy applications”, Nuclear Fusion 57 (2017) 092004 (13pp).

113. M. J. Gorley, “Critical Assessment 12: Prospects for reduced activation steel for fusion plant”, Materials Science and Technology 31(8) (2015) 975-980.

114. Q. Huang, N. Baluc, Y. Dai, S. Jitsukawa, A. Kimura, J. Konys, R.J. Kurtz, R. Lindau, T. Muroga, G. R. Odette, B. Raj, R.E. Stoller, L. Tan, H. Tanigawa, A.-A.F. Tavassoli, T. Yamamoto, F. Wan, Y. Wu, “Recent progress of R&D activities on reduced activation ferritic/martensitic steels”, Journal of Nuclear Materials 442 (2013) S2-S8.

115. B. Van der Schaaf, F. Tavassoli, C. Fazio, E. Rigal, E. Diegele, R. Lindau, G. LeMarois, “The development of EUROFER reduced activation steel”, Fusion Engineering and Design 69 (1–4) (2003) 197-203.

116. A. Kohyama, A. Hishinuma, D. S. Gelles, R. L. Klueh, W. Dietz, K. Ehrlich, “Low-activation ferritic and martensitic steels for fusion application”, Journal of Nuclear Materials 233–237 (1996) 138-147.

117. B. Raj, T. Jayakumar, “Development of Reduced Activation Ferritic–Martensitic Steels and fabrication technologies for Indian test blanket module”, Journal of Nuclear Materials 417 (1–3) (2011) 72-76.

118. A. N. Mistry, C. S. Sasmal, S. Sam, N. Singh, A. Prajapati, J. P. Chauhan, H. M. Tailor, S. K. Albert, K. Laha, S. Saibaba, A. K. Bhaduri, E. Rajendra Kumar, “Status of India-specific Reduced Activation Ferritic-Martensitic steel and fabrication technologies development for LLCB TBM”, Fusion Engineering and Design, 125 (2017) 263-268.

119. ‘U. R. Evans, “An Outline of Corrosion Mechanisms, Including the Electrochemical Theory”, Corrosion Handbook, Wiley (1948).

120. A. S. Brasunas, “Liquid Metal Corrosion”, Corrosion 9(3) (1953) 78-84.

121. E. E. Stansbury and R. A. Buchanan, "Fundamentals of Electrochemical Corrosion”, ASM International (2000).

122. J. E. Draley, “Corrosion by Liquid Metals” Springer US (1970).

123. G. Ilinčev, D. Kárník, M. Paulovič, A. Doubková, “The effect of temperature and oxygen content on the flowing liquid metal corrosion of structural steels in the Pb–Bi eutectic”, Nuclear Engineering and Design 236 (18) (2006) 1909-1921.

124. J. Konys, W. Krauss, H. Steiner, J. Novotny, A. Skrypnik, “Flow rate dependent corrosion behavior of Eurofer steel in Pb–15.7Li”, Journal of Nuclear Materials 417 (2011) 1191–1194.

125. M. Kondo, M. Takahashi, T. Tanaka, V. Tsisar, T. Muroga, “Compatibility of reduced activation ferritic martensitic steel JLF-1 with liquid metals Li and Pb–17Li”, Fusion Engineering and Design 87 (2012) 1777– 1787.

126. M. G. Barker, M. J. Capaldi, “The deposition of corrosion products in Pb-17Li”, Journal of Nuclear Materials 212-215 (1994) 1534-1537.

127. J. W. Nowok, “Mass transport phenomena at the liquid metal/substrate (metal, carbide) interface1”, Materials Science and Engineering: A, 232 (1–2) (1997) 157-162.

128. S. J. Pawel, J. R. DiStefano, E. T. Manneschmidt, “Thermal gradient mass transfer of type 316L stainless steel and alloy 718 in flowing mercury”, Journal of Nuclear Materials 296 (2001) 210-218.

129. T. Gnanasekaran, R. K. Dayal, B. Raj “10 – Liquid metal corrosion in nuclear reactor and accelerator driven systems”, Nuclear Corrosion Science and Engineering: Energy, Woodhead Publishing Series (2012) 301–328.

130. M. Caro, K. Woloshun, F. Rubio, S.A. Maloy and P. Hosemann “Heavy Liquid Metal Corrosion of Structural Materials in Advanced Nuclear Systems”, The Journal of The Minerals, Metals & Materials Society (TMS), 65 (8) (2013) 1057-1066.

131. J. Zhang, P. Hosemann, S. Maloy, “Models of liquid metal corrosion”, Journal of Nuclear Materials 404 (2010) 82–96.

132. R. Distefano, E. E. Hoffman, Atomic Energy Review 2 (1964) 3–33.

133. X. He, N. Li, “A kinetic model for corrosion and precipitation in non-isothermal LBE flow loop”, Journal of Nuclear Materials 297 (2001) 214–219.

134. L. F. Epstein, “Static and Dynamic Corrosion and mass transfer in liquid metal systems”, Liquid Metal Technology 20 (1957) 67–81.

135. I. V. Gorynin, G. P. Karzov, V. G. Markov, V. A. Yakovlev, “Structural materials for atomic reactors with liquid metal heat-transfer agents in the form of lead or lead-bismuth alloy”, Metal Science and Heat Treatment 41(1999) 384–388.

136. Nuclear Energy Agency (NEA), “Handbook on Lead-bismuth Eutectic Alloy and Lead Properties, Materials Compatibility, Thermal hydraulics and Technologies”, OECD (2015), NEA. No. 7268.

137. J. Zhang, “A review of steel corrosion by liquid lead and lead–bismuth”, Corrosion Science 51(60) (2009) 1207-1227.

138. J. Konys, “Corrosion chemistry of Heavy Liquid Metals for Fusion and Nuclear Applications”, INEPT Training course, KIT (2012).

139. J. Konys, G. Milller, "Corrosion and compatibility of structural materials in liquid lead alloys", JAERI-Conference (2003), JP0350241.

140. F. B. Celerier, F. Barbier, "Investigation on models to predict the corrosion of steels in flowing liquid lead alloys", Journal of Nuclear Materials 289 (2001) 227–242.

141. B. Poulson, "Electrochemical measurements in flowing solutions", Corrosion Science 23 (1983) 391-430.

142. K. D. Efird, E. J. Wright, J. A. Boros, T. G. Hailey, "Correlation of Steel Corrosion in Pipe Flow with Jet Impingement and Rotating Cylinder Tests", Corrosion 49 (12) (1993) 992-1003.

143. E. Heitz, "Chemo-Mechanical Effects of Flow on Corrosion", Corrosion 47(2) (1991) 135-145.

144. M. Kondo, M. Ishii, T. Norimatsu, T. Muroga, "Experimental study on corrosion and precipitation in non-isothermal Pb-17Li system for development of liquid breeder blanket of fusion reactor", IOP Conf. Series: Journal of Physics: Conf. Series 877 (2017) 01200.

145. J. Weber, "Flow induced corrosion: 25 years of industrial research", British Corrosion Journal 27 (1992) 193-199.

146. T. Y. Chen, A. A. Moccari, D. D. Macdonald, "Development of Controlled Hydrodynamic Techniques for Corrosion Testing", Corrosion 48 (3) (1992) 239-255.

147. P. F. Tortorelli, O. K. Chopra, "Corrosion and compatibility considerations of liquid metals for fusion reactor applications", Journal of Nuclear Materials 103 (1981) 621-632.

148. O. K. Chopra, P. F. Tortorelli, "Compatibility of materials for use in liquid-metal blankets of fusion reactors" , Journal of Nuclear Materials 123 (1–3) (1984) 1201-1212.

149. C. Park, "Study on Compatibility of Advanced Materials Exposed to Liquid Pb-Li for High Temperature Blanket System", Thesis, Kyoto University (2013).

150. H. Grhbner, H. Feuerstein and J. Oschinski, "Compatibility of metals and alloys in liquid Pb-17Li at temperatures up to 650^{o}C", Journal of Nuclear Materials 155-157 (1988) 702-704.

151. P.F. Tortorelli and J. H. Devan, “Corrosion of ferrous alloys exposed to thermally convective Pb-17 at% Li”, Journal of Nuclear Materials 141-143 (1986) 592-598.

152. P.F. Tortorelli and J. H. Devan, “Compatibility of Stainless Steel with Pb-17 At. Pct Li”, Journal of materials for energy systems 4 (2) (1982) 78-83.

153. H. U. Borgstedt, G. Frees, G. Drechsler, “Corrosion of stainless steel in flowing PbLi eutectic”, Journal of Nuclear Materials 141–143(1986) 561-565.

154. V. Coen, P. Fenici, H. Kolbe, L. Orecchia, T. Sasaki, “Compatibility of AISI 316 L stainless steel with the Li17Pb, eutectic”, Journal of Nuclear Materials 110 (1982) 108-114.

155. O. K. Chopra and D. L. Smith, “Compatibility of ferrous alloys in a forced circulation Pb-17Li system”, Journal of Nuclear Materials 141-143 (1986) 566-570.

156. O. K. Chopra and D. L. Smith, “Compatibility of ferritic steels in forced circulation lithium and Pb-17Li systems”, Journal of Nuclear Materials 155-157 (1988) 715-721.

157. P. F. Tortorelli, Dissolution kinetics of steels exposed in lead-lithium and lithium environments”, Journal of Nuclear Materials 191-194 (1992) 965-969.

158. P. F. Tortorelli, “Deposition behavior of ferrous alloys in molten lead-lithium”, Fusion Engineering and Design 14 (1991) 335-345.

159. J. Sannier, M. Broc, T. Flament and A. Terlain, “Corrosion of austenitic and martensitic stainless steels in flowing Pbl7Li alloy”, Fusion Engineering and Design 14 (1991) 299-307.

160. H. U. Borgstedt and H.D. Rijhrig, “Recent results on corrosion behavior of MANET structural steel in flowing Pb17Li eutectic”, Journal of Nuclear Materials 179-181 (1991) 596-598.

161. H. Glasbrenner, J. Konys, H. D. Rohrig, K. Stein-Fechner, “Corrosion of ferritic-martensitic steels in the eutectic Pb-17Li”, Journal of Nuclear Materials 283-287 (2000) 1332-1335.

162. H. Glasbrenner, J. Konys, Z. Vob, “Corrosion behavior of low activation steels in flowing Pb-17Li”, Journal of Nuclear Materials 281 (2000a) 225-230.

163. J. Konys, W. Krauss, Z. Voss, O. Wedemeyer, “Corrosion behavior of EUROFER steel in flowing eutectic Pb–17Li alloy”, Journal of Nuclear Materials 329–333 (2004) 1379 -1383.
164. Y. Chen, Q. Huang, S. Gao, Z. Zhu, X. Ling, Y. Song, Y. Chen, W. Wang, “Corrosion analysis of CLAM steel in flowing liquid LiPb at 480°C”, Fusion Engineering and Design 85 (2010) 1909 -1912.
165. Q. Huang, Z. Zhu, S. Gao and Y. Song, Y. Wu, “R&D of dragon series lithium-lead loops for material and blanket technology testing”, Fusion Science and Technology 62 (2012) 272-275.
166. H. Steiner, W. Krauss, J. Konys “Calculation of dissolution/deposition rates in flowing eutectic Pb–17Li with the MATLIM code”, Journal of Nuclear Materials 386–388 (2009) 675–677.
167. J. Konys, W. Krauss, J. Novotny, H. Steiner, Z. Voss, O. Wedemeyer, “Compatibility behavior of EUROFER steel in flowing Pb–17Li”, Journal of Nuclear Materials 386–388 (2009) 678–681.
168. J. Sannier, T. Dufienoy, T. Flament, A. Terlam, “Comparison of austenitic and martensitic steels behaviour in semi-stagnant Pbl7Li”, Journal of Nuclear Materials 191-194 (1992) 975-978.
169. V. Coen, H. Kolbe, L. Orecchia, “Effects of Pb-17Li on the tensile properties of steels”, Journal of Nuclear Materials 155-157 (1988) 740-743.
170. T. Sample, P. Fenici, H. Kolbe, “Liquid metal embrittlement susceptibility of welded MANET II (DIN1.4914) in liquid Pb-17Li”, Journal of Nuclear Materials 233-237 (1996) 244-247.
171. G. Coccoluto, P. Gaggini, V. Labanti, M.Tarantino, W. Ambrosini, N. Forgione, A. Napoli, F. Oriolo, “Heavy liquid metal natural circulation in a one-dimensional loop”, Nuclear Engineering and Design 241 (5) (2011) 1301-1309.
172. D. Martelli, G. Barone, M. Tarantino, M. Utili, “Design of a new experimental loop and of a coolant purifying system for corrosion experiments of EUROFER samples in flowing PbLi environment”, Fusion Engineering and Design 124 (2017) 1144-1149.
173. H. U. Borgstedt, G. Frees, M. Grundmann, Z. Peric, “Corrosion and mechanical properties of the martensitic steel X18CrMoVNb121 in flowing Pb-17Li”, Fusion Engineering and Design 14 (1991a) 329-334.

174. V. Coen, “Lithium-lead eutectic as breeding material in fusion reactors”, Journal of Nuclear Materials 133& 134 (1985) 46-51.
175. H. U. Borgstedt, G. Drechsler, G. Frees, Z. Peric, “Corrosion testing of steel X18CrMoVNb121 (1.4914) in a Pb-17Li pumped loop”, Journal of Nuclear Materials 155-157 (1988) 728 -731.
176. N. I. Loginov, A. S. Mikheyev, V. A. Morozov, I. I. Zasorin, A. E. Solomatin, I. R. Kirillov, K. I. Tkachenko, V. I. Engelko, “Results of corrosion test of EUROFER 97 in lead-lithium alloy”, Proceedings of the International Symposium of Fusion Nuclear Technology Barcelona (2013).
177. G. Benamati, C. Fazio, I. Ricapito,” Mechanical and corrosion behavior of EUROFER 97 steel exposed to Pb–17Li”, Journal of Nuclear Materials 307–311 (2002) 1391–1395.
178. K. Splichal, M. Zmitko, “Corrosion behavior of EUROFER in Pb–17Li at 500 °C”, Journal of Nuclear Materials 329–333 (2004) 1384–1387.
179. J. Konys, W. Krauss, Z. Voss, and O. Wedemeyer, “Comparison of corrosion behavior of bare and hot-dip coated EUROFER steel in flowing Pb–17Li”, Journal of Nuclear Materials 367, (2007)1144 -1149.
180. J. Sannier, T. Flament, A. Terlain, "Corrosion of martensitic steels in flowing Pb17Li", Proceedings of the 16th Symposium on Fusion Technology", London (1991) 901–905.
181. W. Krauss, J. Konys, H. Steiner, J. Novotny, Z. Voss, O. Wedemeyer, "Development of modeling tools to describe the corrosion behavior of uncoated EUROFER in flowing Pb-17Li and their validation by performing of corrosion tests at T up to 550°C", FZKA 7295, KIT Report (2007).
182. I. Bucenieks, R. Krishbergs, E. Platacis , G. Lipsbergs , A. Shishko, A Zik , F Muktupavela, “Investigation of corrosion effects of eurofer steel in Pb-17Li stationary flow in the magnetic field”, Magnetohydrodynamics 42 (2006) 237-251.
183. M. C. Gázquez, T. Hernández, F. Muktepavela, E. Platacis, A. Shishko, “Magnetic field effect on the corrosion processes at the Eurofer–Pb–17Li flow interface”, Journal of Nuclear Materials 465 (2015) 633-639.
184. R. Moreau, Y. Brechet, L. Maniguet, “Eurofer corrosion by the flow of the eutectic alloy Pb–Li in the presence of a strong magnetic field”, Fusion Engineering and Design 86 (2011) 106-120.

185. Q. Xu, M. Kondo, T. Nagasaka, T. Muroga, M. Nagura, A. Suzuki, “Corrosion characteristics of low activation ferritic steel, JLF-1, in liquid lithium in static and thermal convection conditions”, Fusion Engineering and Design 83 (2008) 1477–1483.

186. M. Kondo, T. Muroga, T. Nagasaka, Q. Xub, V. Tsisar, T. Oshima, “Mass transfer of RAFM steel in Li by simple immersion, impeller induced flow and thermal convection”, Journal of Nuclear Materials 417 (2011) 1200–1204.

187. Q. Xu, M. Kondo, T. Nagasaka, T. Muroga, O. Yeliseyev, “Effect of chemical potential of carbon on phase transformation and corrosion of JLF-1 steel in a static lithium”, Journal of Nuclear Materials 394 (2009) 20–25.

188. M. Kondo, T. Muroga, A. Sagara, V. Tissar, A. Suzuki, T. Terai, M. Takahashi, N. Fujii, Y. Yokoyama, H. Miyamoto, E. Nakamura “Flow accelerated corrosion and erosion–corrosion of RAFM steel in liquid breeders”, Fusion Engineering and Design 86 (9–11) (2011a) 2500-2503.

189. A. Kanai, C. Park, K. Noborio, R. Kasada, S. Konishi, T. Hirose, T. Nozawa, H. Tanigawa, “Compatibility of Ni and F82H with liquid Pb–Li under rotating flow”, Fusion Engineering and Design 89 (2014) 1653–1657.

190. Q. Huang, M. Zhang, Z. Zhu, S. Gao, Y. Wu, Y. Li, Y. Song, C. Li, M. Kong, the FDS Team “Corrosion experiment in the first liquid metal LiPb loop of China”, Fusion Engineering and Design 82(15–24) (2007) 2655-2659.

191. Q Huang, S. Gao, Z. Zhu, M. Zhang, Y. Song, C. Li, Y. Chen, X. Ling, X. Zhou, “Progress in compatibility experiments on lithium–lead with candidate structural materials for fusion in China”, Fusion Engineering and Design 84 (2009) 242–246.

192. S. Ramya, D. Nanda Gopala Krishna, U. Kamachi Mudali, “In-situ Raman and X-ray photoelectron spectroscopic studies on the pitting corrosion of modified 9Cr-1Mo steel in neutral chloride solution”, Applied Surface Science 428 (2018) 1106–1118.

193. H. U. Borgstedt, G. Frees, Z. Peric, “Material compatibility tests with flowing Pb-17Li eutectic”, Fusion Engineering and Design 17 (1991) 179-183.

194. J. Konys, W. Krauss, Z. Zhu, Q. Huang, “Comparison of corrosion behavior of EUROFER and CLAM steels in flowing Pb–15.7Li”, Journal of Nuclear Materials 455 (2014) 491–495.

195. H. U. Borgstedt and H. Feuerstein, “The solubility of metals in Pb-17Li liquid alloy”, Journal of Nuclear Materials 191-194 (1992) 988-991.

196. American Iron and Steel Institute; “High-temperature characteristics of stainless steels, A Designers Handbook Series No 9004”; Distributed by Nickel Development Institute.

197. The Indian TBM Team, “Conceptual Design Review Report of Indian LLCB TBM submitted to ITER”, 2016.

198. P. A. Davidson, “An introduction to magnetohydrodynamics”, Cambridge University Press (2001).

199. A. Shercliff, “The flow of conducting fluids in circular pipes under transverse magnetic fields”, Journal of Fluid Mechanics 1 (1956) 644–666.

200. P. J. Bhuyan and K. S. Goswami, “Effect of Magnetic Field on MHD Pressure Drop inside a rectangular conducting duct”, IEEE transactions on Plasma Science 36 (4) (2008) 1955-1959.

201. E. R. Kumar, “Status of LLCB TBM R&D activities in India”, Proceedings of the Fusion Energy Conference, FTP/4-4Ra (2012) 1-8

202. P. Satyamurthy, “Experimental Facility to Study MHD effects at Very High Hartmann and Interaction parameters related to Indian Test Blanket Module for ITER”, IIT Kanpur Lecture, (2009).

203. P. K. Swain, A. Shishko, P. Mukherjee, V. Tiwari, S. Ghorui, R. Bhattacharyay, A. Patel, P. Satyamurthy, S. Ivanov, E. Platacis, A. Ziks, “Numerical and experimental MHD studies of Lead-Lithium liquid metal flows in multichannel test-section at high magnetic fields” Fusion Engineering and Design 132 (2018) 73–85.

204. S. Subramanian, P. K. Swain, A. V. Deshpande, P. Satyamurthy, “Effect of Hartmann layer resolution for MHD flow in a straight, conducting duct at high Hartmann numbers”, Sadhana 40 (2015) 851–861.

205. J. Freibergs, J. Klavins, O. Lielausis, A. Mikelsons, J. Zandarts, “MHD technology for the production of Pb-Li eutectic alloys”, The 15th Riga and 6th PAMIR Conference on Fundamental and Applied MHD Fusion (2005) 259-262.

206. S. Swaminathan, C. Mallika, N. G. Krishna, C. Thinaharan, T. Jayakumar, U. Kamachi Mudali, “Evolution of surface chemistry and morphology of oxide scale formed during initial stage oxidation of modified 9Cr–1Mo steel”, Corrosion Science 79 (2014) 59–68.

207. T. Swarr, G. Krauss, “The effect of structure on the deformation of as-quenched and tempered martensite in an Fe-0.2 pct C alloy” , Metallurgical Transactions A 7(1) (1976) 41–48.

208. M. N. Mungole, G. Sahoo, S. Bhargava, R. Balasubramaniam, “Recrystalised grain morphology in 9Cr 1Mo ferritic steel”, Materials Science and Engineering: A 476 (1–2) (2008) 140-145.
209. C. D. Wagner, “Handbook of X-ray Photoelectron Spectroscopy”, Perkin-Elmer (1979).
210. K. J. Laidler, “Chemical Kinetics”, Perason Education Inc. (1987).
211. L. J. Rodríguez-Aragóna, J. López-Fidalgo, “Optimal designs for the Arrhenius equation”, Chemometrics and Intelligent Laboratory Systems, 77 (2005) 131-138.
212. G. Benamati, C. Fazio, I. Ricapito, “Mechanical and corrosion behaviour of EUROFER 97 steel exposed to Pb–17Li”, Fusion Engineering and Design 14(1991) 219-226.
213. M. G. Barker, T. Sample, “The solubilities of nickel, manganese and chromium in Pb-17Li”, Fusion Engineering and Design 14 (1991) 219.
214. N. Simon, T. Flament, A. Terlain, C. Deslouis “Determination of the diffusion coefficients of iron and chromium in Pb17Li”, International Journal of Heat and Mass Transfer 38(1995) 3085-3090.
215. N. Simon, A. Terlain, T. Flament, “The compatibility of martensitic steels with liquid Pb–17Li”, Journal of Nuclear Materials, 254 (1998) 185-190.
216. S. Ye, F. Zhao, F. Huang, J. He and J. L. Wang, “Microstructure evolution of CLAM steel during creep at 923K”, IOP Conference Series: Earth and Environmental Science, 81 (2017) 012041.
217. X. Tao, C. Li, L. Han, J. Gu “Microstructure evolution and mechanical properties of X12CrMoWVNbN10-1-1 steel during quenching and tempering process”, Journal of Materials Research and Technology 5(1) (2016) 45-57.
218. S. K. Bonagani, B. Vishwanath, V. Kain, “Influence of tempering treatment on microstructure and pitting corrosion of 13 wt.% Cr martensitic stainless steel”, Corrosion Science 131 (2018) 340–354.
219. I. Barin, “Thermochemical Data of Pure Substances”, Wiley-VCH (2004).
220. M. Kondo, M. Takahashi, T. Suzuki, K. Ishikawa, K. Hata, S. Qiu, H. Sekimoto, “Metallurgical study on erosion and corrosion behaviors of steels exposed to liquid lead–bismuth flow”, Journal of Nuclear Materials 343 (2005) 349–359.
221. M. Kondo, T. Muroga, “Corrosion Characteristics of RAFM Steels and Unalloyed Metals in Static Pb-17Li”, Plasma and Fusion Research: Regular Articles 8 (2013) 3405053.

222. M. Kondo, V. Tsisar, T. Muroga, T. Nagasaka, O. Yeliseyeva, “Erosion-corrosion of RAFM JLF-1 steel in Lithium flow induced by impeller”, Journal of Plasma and Fusion Research Series 9 (2010) 294-299.
223. H. Schlichting, “Boundary layer theory”, McGraw-Hill Book Company (1960).
224. Q. Xu, T. Nagasaka, T. Muroga, “Compatibility of low activation ferritic steels with liquid lithium”, Fusion Science and Technology 2 (2007) 609-612.
225. X. Chen, Q. Yuan, B. Madigan, W. Xue “Long-term corrosion behavior of martensitic steel welds in static molten Pb–17Li alloy at 550 °C”, Corrosion Science 96 (2015) 178–185.
226. K. Lambrinou, E. Charalampopoulou, T. Van der Donck, R. Delville , D. Schryvers “Dissolution corrosion of 316L austenitic stainless steels in contact with static liquid lead-bismuth eutectic (LBE) at 500 °C”, Journal of Nuclear Materials 490 (2017) 9-27.
227. V. Coen and T. Sample, “Pb-17Li - A fully characterised liquid breeder”, Fusion Technology 1 (1990) 249.
228. B. S. Lement, I. Perlmutter, “Mechanical properties attainable by alloying of refractory metals”, Journal of the Less Common Metals, 2 (2–4) (1960) 253-271.
229. L. Giancarli, V. Chuyanov, M. Abdou, M. Akiba B. G. Hong, R. Lasser, C. Pan, Y. Strebkov, the TBWG, “Breeding blanket modules testing in ITER: an international program on the way to DEMO”, Fusion Engineering and Design 81 (2006) 393–405
230. P. Shewmon, (Ed.), The Minerals, Metals, and Materials Society, “Diffusion in Solids-The Minerals, Metals & Materials Series”, Springer International Publishing (2016).
231. Ravikirana, R. Mythili, S. Raju, S. Saroja, “Effect of alloy content on microstructure and microchemistry of phases during short term thermal exposure of 9Cr-W-Ta-0·1C reduced activation ferritic/martensitic (RAFM) steels”, Bulletin of Materials Science 37 (6) (2014) 1453–1460.
232. R. Mythili, Ravikirana, J. Vanaja, K. Laha, S. Saroja, T. Jayakumar, M. D. Mathew, E. Rajendra kumar, “Microstructural Modifications Due to Tungsten and Tantalum in 9Cr Reduced Activation Ferritic Martensitic Steels on Creep Exposure”, Procedia Engineering 55 (2013) 295-299.
233. H. Tas, S. Malang, F. Reiter, J. Sannier, “Liquid Breeder Materials”, Journal of Nuclear Materials, 155-157 (1988) 178-187.
234. D. Wolf, “Correlation between the energy and structure of grain boundaries in b.c.c. metals. II. Symmetrical tilt boundaries”, Philosophical Magazine A 62(4) (1990) 447-464.

235. N. Nakada, T. Tsuchiyama, S. Takaki and Naoki Miyano, “Temperature Dependence of Austenite Nucleation Behavior from Lath Martensite”; ISIJ International 51(2) (2011) 299–304

236. P. Chakraborty, P. K. Pradhan, R. K. Fotedar, N. Krishnamurthy, “Compatibility of 9Cr–1Mo steel exposed to thermally convective Pb–17Li”, Journal of Materials Research and Technology 2(3) (2013) 206–212.

237. A. Terlain, T. Dufrenoy, “Influence of a magnetic field on the corrosion of austenitic and martensitic steels by semi-stagnant Pb l7Li”, Journal of Nuclear Materials 212-21.5 (1994) 1504-1508.

238. S. Malang, “Influence of a magnetic field on liquid metal corrosion”, Fusion Technology 2 (1984) 979–984.

239. J. C. Hunt and R.J. Holroyd, “Applications of Laboratory and Theoretical MHD Duct flow Studies in Fusion Reactor Technology”, UKAEA report CLM-R169 (1977).

240. R. Krishbergs, F. Muktepavela, E. Platacis, A.Shishko, “Phenomenological Analysis of the Corrosion Processes of EUROFER Steel in Pb17Li Melt Flows”, Proc. the 7th International PAMIR conference of Fundamental and Applied MHD 2 (2008) 565–569.

241. F. Barbier, A. Alemany, S. Martemianov, “On the influence of a high magnetic field on the corrosion and deposition processes in the liquid Pb-17Li alloy”, Fusion Engineering and Design 43 (1998) 199–208.

242. S. Saeidi, S. Smolentsev, “Numerical study of the effect of a magnetic field on corrosion of ferritic/martensitic steel in a turbulent PbLi flow”, Magnetohydrodynamics 50(2) (2014) 109-120.

243. S. Saeidi, S. Smolentsev, M. Abdou, “Study of MHD corrosion of RAFM steel in laminar and turbulent PbLi flows in a wall-normal magnetic field”, Fusion Science and Technology (Proceedings of TOFE-2014) (2015) 1-4.

APPENDIX 1

METHODOLOGY OF CFD MODELING OF Pb-Li FLOW

Computational Fluid Dynamics (CFD) can be explained as numerical solution of the differential governing equations of fluid flows with the help of computers. In the present study, the velocity profile of molten Pb-Li at a temperature of 773 K under stirring and flowing conditions have been simulated by CFD for the Rotating Disc Corrosion test facility (RDCTF) and Forced Circulation Pb-Li loop respectively. The thermo-physical properties of Pb-Li used for this purpose are listed in table A.1.1

Table A.1.1: Thermo-physical Properties of Pb-Li.

Property	**Value**	**Reference**
Density	10, 500 kg/m3	A.1
Kinematic viscosity	1.25x10-7 m2/s	A.2

A1. a. Methodology of CFD Modeling for Rotating Disc Corrosion Test Facility.

The Rotating disc corrosion test facility (RDCTF) was used to expose corrosion samples of IN RAFMS and P91 to Pb-Li under isothermal stirring conditions. The detailed description of this facility and corresponding disc type samples have been given in Section 3.4 (Chapter 3). Figure A1.1 shows the schematic diagram of the liquid metal chamber of this facility along with a segmented disc type sample, including the dimensions, which have been used for CFD modeling.

In order to simulate the Pb-Li velocity profile in the molybdenum crucible as shown in Figure A1.1, a simple disc of 50 mm diameter (12 mm thickness) rotating at a speed of 360 RPM in liquid Pb-Li at 773 K was considered. This geometry was modeled in 3 dimensions and the simplified 2 D geometry is sown in Figure A1.2

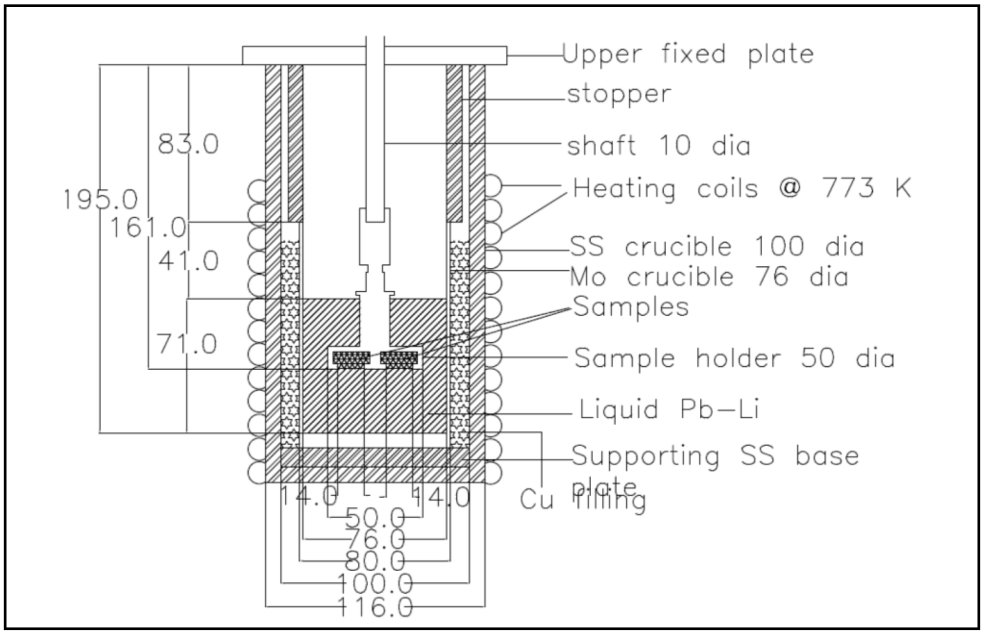

Fig A1.1: Schematic of the liquid metal chamber (molybdenum crucible) of the RDCTF with a segmented disc type sample.

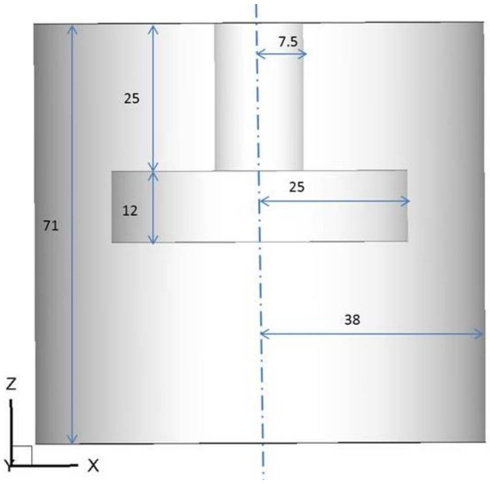

Fig A1.2: Simplified geometry of disc sample and molybdenum crucible considered for modeling.

In order to simulate the Pb-Li velocity profile, the incompressible Navier Stokes equation and the RSM turbulence model have been used [3]. The mass and momentum conservation equations (i.e. Navier Stokes equation) for an incompressible system can be represented by Equations to (i) to (iv) and the same has been used in the present case.

$$\frac{\partial \rho}{\partial t}+\frac{\partial(\rho u)}{\partial x}+\frac{\partial(\rho v)}{\partial y}+\frac{\partial(\rho w)}{\partial z}=\mathbf{0}\ldots\ldots\ldots\ldots\ldots\ldots\ldots\ldots\ldots\ldots\ldots\ldots\ldots\ldots\ldots\ldots\ldots\ldots\ldots\ldots\ldots \text{ i}$$

$$\frac{\partial(\rho u)}{\partial t}+\frac{\partial(\rho uu)}{\partial x}+\frac{\partial(\rho vu)}{\partial t}+\frac{\partial(\rho wu)}{\partial t}=-\frac{\partial \rho}{\partial x}+\ (\square+\square_{t})\ \left(\frac{\partial^2 u}{\partial x^2}+\frac{\partial^2 u}{\partial y^2}+\frac{\partial^2 u}{\partial z^2}\right)+\ \mathbf{F_x}\ldots\ldots\ldots\ldots\ldots\ldots\ldots \text{ ii}$$

$$\frac{\partial(\rho v)}{\partial t}+\frac{\partial(\rho uv)}{\partial x}+\frac{\partial(\rho vv)}{\partial t}+\frac{\partial(\rho wv)}{\partial t}=-\frac{\partial \rho}{\partial y}+\ (\square+\square_{t})\ \left(\frac{\partial^2 v}{\partial x^2}+\frac{\partial^2 v}{\partial y^2}+\frac{\partial^2 v}{\partial z^2}\right)+\ \mathbf{F_y}\ldots\ldots\ldots\ldots\ldots\ldots\ldots \text{ iii}$$

$$\frac{\partial(\rho w)}{\partial t}+\frac{\partial(\rho uw)}{\partial x}+\frac{\partial(\rho vw)}{\partial t}+\frac{\partial(\rho ww)}{\partial t}=-\frac{\partial \rho}{\partial z}+\ (\square+\square_{t})\ \left(\frac{\partial^2 w}{\partial x^2}+\frac{\partial^2 w}{\partial y^2}+\frac{\partial^2 w}{\partial z^2}\right)-\boldsymbol{\rho g}+\ \mathbf{F_z}\ldots\ldots\ldots \text{ iv}$$

The Reynolds number for the given operating conditions was calculated to determine the flow regime existing in the system. For a circular disc rotating in fluid medium, Reynolds number was given by equation (v)

$$Re\ =\omega.R^2/\nu\ =1.88 \text{ x } 10^5\ldots\ldots\ldots\ldots\ldots\ldots\ldots\ldots\ldots\ldots\ldots\ldots\ldots\ldots\ldots\ldots\ldots\ldots\ldots\ldots.. \text{ v}$$

Where R is radius of disc, is rotational velocity in rad/s and is kinematic viscosity of Pb-Li liquid at 773 K. The critical Reynolds number for this system is around 10^5 [A.2]. Since the Reynolds number is in the same range, the flow regime in the vessel for current operating conditions cannot be judged to be either laminar or fully turbulent. So, in the current study turbulence is considered and the Reynolds stress transport model (RSM) has been used [A.4].

A hexahedral mesh with axial symmetry (since, the geometry is axially symmetric) was generated for CFD modeling and the cross-sectional view of the same is shown in Figure A1.3. Higher cell density is used near the wall of disk shaft, disk and vessel to resolve the boundary layer velocity profiles. The boundary conditions imposed on governing equations at various boundaries of solution domain are as follows:-

a. For disc and shaft surfaces, a rotating wall boundary condition is given with 12π rad/s (360 rpm) rotational velocity with respect to central axis (z-axis in current geometry model).
    b. For vessel walls, no slip condition is imposed on velocity.

c. For the free surface of liquid Pb-Li, pressure outlet boundary condition is used to allow flow of liquid into and/or out of the solution domain.

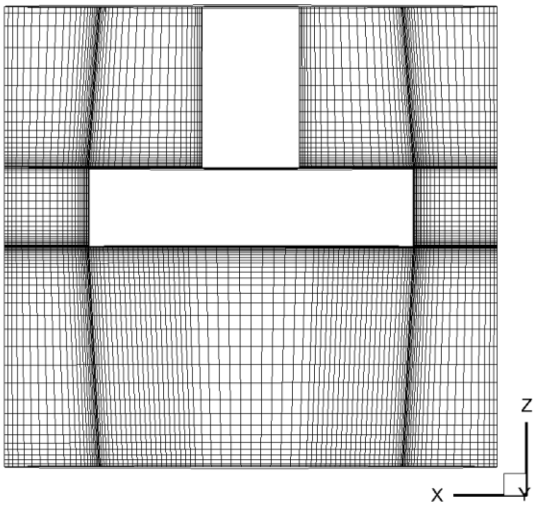

Fig. A1.3: The mesh generated for CFD modeling of the RDCTF.

The axial, radial and tangential velocity profiles of Pb-Li obtained from CFD by solving the Navier Stokes equation and the RSM turbulence model [A.4]. These have been are plotted along the axial direction in the Pb-Li beneath the rotating disc for a radial distance of 20 mm away from central axis and have been shown in Figure 3.13 in Chapter 3 (Section 3.4.3). The RSM turbulence model have been used to plot the 2D velocity profiles at different planes along the radial and axial directions as have been shown in Figure 3.14 and 3.15 in Chapter 3 (Section 3.4.3).

The shear stresses along the radial and tangential direction on the bottom surface of the disc were calculated by CFD with the help of RSM turbulence model and have been plotted along the radial coordinate. This plot is already shown in Fig 3.16 in Chapter 3 (Section 3.4.3). Along with a clear prediction of the velocity distribution of Pb-Li in the RDCTF, the results of CFD analysis showed that the vessel wall does not have any confining effect on the flow around the rotating disc

A1. b. Methodology of CFD Modeling for Pb-Li loop (EMPPIL).

The Electromagnetic pump driven Pb-Li loop (EMPPIL) was used to expose corrosion samples of IN RAFMS to Pb-Li under non isothermal flowing conditions. The detailed description of this facility and corresponding samples have been given in Section 3.5 (Chapter 3). Figure 3.20 shows the schematic diagram of the sample holder of this facility along with the rectangular samples, including the dimensions, which have been used for CFD modeling. The fundamental equations that have been used to calculate the fluid motion are the continuity equation (mass balance) (Equation vi) and Cauchy- momentum equations (momentum balance) which have been represented by Equations vii [A.3]. The equations have been represented in Cartesian tensor with $\mathbf{x} = x_j$ and velocity $\mathbf{u} = u_j$ for j=1, 2,3 represent x, y and z unit vector respectively)

$$\frac{\partial \rho}{\partial t} + \frac{\partial}{\partial x_j}(\rho u_j) = 0 \quad \ldots\ldots\ldots\ldots\ldots\ldots\ldots\ldots\ldots\ldots\ldots\ldots\ldots\ldots\ldots\ldots\ldots\ldots\ldots\ldots\ldots\ldots.. \text{ vi}$$

$$\frac{\partial (\rho u_i)}{\partial t} + \frac{\partial}{\partial x_j}(\rho u_i u_j + p\delta_{ij} - \sigma_{ij}) = 0 \quad \ldots\ldots\ldots\ldots\ldots\ldots\ldots\ldots\ldots\ldots\ldots\ldots\ldots\ldots\ldots..\text{vii}$$

where ρ is the density, ρu_i is the momentum vector and p the pressure. The Stokes viscous stress tensor σ_{ij} is defined by Equation vii.

$$\sigma_{ij} = \frac{\mu}{R_e}\left[\left(\frac{\partial u_i}{\partial x_j} + \frac{\partial u_j}{\partial x_i}\right) - \frac{2}{3}\delta_{ij}\frac{\partial u_k}{\partial x_k}\right] \qquad \ldots\ldots\ldots\ldots\ldots\ldots\ldots\ldots\ldots\ldots\ldots\ldots\ldots.\text{vii}$$

where $u_i = (u, v, w)$ are the wind components, μ is the absolute viscosity, κ is the coefficient of heat conductivity and R_e the Reynolds number.All these equation were simultaneously solved and the following boundary conditions were imposed to calculate the velocity profile of Pb-Li inside the sample holder by CFD:-

a. Average inlet velocity of 1.5 m/s into the sample holder.
b. Isothermal conditions throughout the sample holder at a temperature of 773 K (500°C) over the sample holder.
c. Atmospheric pressure has been selected as outlet boundary condition

Temperature dependent thermo-physical properties of Pb-Li as shown in Table A.1.1 have been used for the analysis. The coupled continuity and momentum equations were solved by a SIMPLE algorithm which is an iterative segregated solution procedure. Rectangular mesh has been generated and mesh independence study has been performed to get an optimum mesh size. On the other hand, the k-ε model was used to incorporate turbulence phenomenon into simulation. The velocity profile obtained by this method has been already shown in Figure 3.22 (Section 3.5 in Chapter 3).

References:-

A.1. S.J. Zinkle, "Summary of Physical Properties for Lithium, Pb-17Li, and (LiF)n•BeF2 Coolants", ORNLAPEX Study Meeting, July 27-28 (1998).

A.2. F. B. Celerier, F. Barbier, "Investigation of models to predict the corrosion of steels in flowing liquid lead alloys", Journal of Nuclear Materials 289 (2001) 227-242.

A.3. J. Cimbala and Y.A. Cengel, "Fluid Mechanics: Fundamentals and Applications", The McGraw Hill Company (2013).

A.4. H. K. Versteeg and W. Malalasekera, "An Introduction to Computational Fluid Dynamics: The Finite Volume Method", PHI (2007).